TECHNICAL UNIVERSITY OF LIBEREC
Faculty of Mechanical Engineering

Hydrofluoroolefins as Working Fluids for Ejector Cooling Technology

Doctoral thesis

Study program	P2301 Mechanical engineering
Study field	Applied Mechanics

Author **Ing. Nguyen Van Vu**

Supervisor **Prof. Ing. Vaclav Dvorak, Ph.D.**
Department of Applied Mechanics

Co-supervisor **Dr. Szabolcs Varga**
Department of Mechanical Engineering, FEUP

Liberec 2020

Prohlášení

Prohlašuji, že svou disertační práci jsem vypracoval samostatně jako původní dílo s použitím uvedené literatury a na základě konzultací s vedoucím mé disertační práce a konzultantem.

Jsem si vědom toho, že na mou disertační práci se plně vztahuje zákon č. 121/2000 Sb., o právu autorském, zejména § 60 – školní dílo.

Beru na vědomí, že Technická univerzita v Liberci nezasahuje do mých autorských práv užitím mé disertační práce pro vnitřní potřebu Technické univerzity v Liberci.

Užiji-li disertační práci nebo poskytnu-li licenci k jejímu využití, jsem si vědom povinnosti informovat o této skutečnosti Technickou univerzitu v Liberci; v tomto případě má Technická univerzita v Liberci právo ode mne požadovat úhradu nákladů, které vynaložila na vytvoření díla, až do jejich skutečné výše.

Současně čestně prohlašuji, že text elektronické podoby práce vložený do IS/STAG se shoduje s textem tištěné podoby práce.

Beru na vědomí, že má disertační práce bude zveřejněna Technickou univerzitou v Liberci v souladu s § 47b zákona č. 111/1998 Sb., o vysokých školách a o změně a doplnění dalších zákonů (zákon o vysokých školách), ve znění pozdějších předpisů.

Jsem si vědom následků, které podle zákona o vysokých školách mohou vyplývat z porušení tohoto prohlášení.

30. listopadu 2020 Ing. Nguyen Van Vu

To my beloved parents, and to beautiful Czech country.

“There is no way to happiness, happiness is the way.”

Thich Nhat Hanh

ABSTRACT

For decades, ejector technology was considered as a potential alternative for conventional compressor cooling technology due to its promising features. For instance, ejector refrigeration cycle can be driven by renewable heat sources with high stability and maintenance. With the current climate change issues, the demand for sustainable cooling technologies using an environmentally friendly working fluid becomes stronger than ever.

The present thesis aims a comprehensive investigation into ejector cooling technology using numerical and experimental methods. The numerical method was employed to understand the influences of various parameters to the system performance, such as the superheating, generator temperature, the heat exchangers size. A theoretical design of an ejector refrigeration system with a novelty environmentally friendly as the working fluid was a major objective of the thesis. Experimental assessments of the solar ejector cooling system were performed to reveal the system behaviors under real conditions.

A prototype of an ejector refrigeration system (ERS) with R600a as the working fluid was used to study the system performance at various working conditions. The behavior of the ejector at on-design and off-design conditions was investigated. The experimental results were used to fine tune and validate the mathematical model of the ejector cooling cycle. The mathematical model developed considers the ejector cooling cycle in detail, including the plate heat exchangers. The model enables to study the cooling cycle from various aspects, such as the influence of heat exchanger design to the performance of the system, or the degree of superheat at the ejector inlets on the system behavior. The mathematical model was used to assess four novel refrigerants of the hydrofluoroolefin group: R1234yf, R1234ze(e), R1234ze(z), and R1233zd(e). A study using computational fluid dynamics was carried out to validate the results from the mathematical model.

The experimental results using a variable geometry ejector (VGE) in an ERS clearly showed the benefit of the design. The improvement of the system performance was up to 42% when compared to a conventional ejector. It was observed that the coefficient of performance was inversely proportional to the secondary inlet pressure when the ejector works at the off-design regime. The results from mathematical work well agreed with the experimental results, within ±15% of tolerance.

The mathematical model also confirmed that a variable geometry ejector is necessary, for all selected working fluids, to obtain desirable cooling performance when the working conditions vary. The influences of the working temperatures to the system performance were considerable. The sizes of the heat exchangers significantly influenced the effectiveness and the pressure drop of the refrigerant flow. The assessment pointed out R1234ze(e) and R1234yf were the most desirable working fluids. The work with computational fluid dynamics supported the results of the mathematical model.

Keywords: ejector cooling technology, variable geometry ejector, renewable energy, plate heat exchanger, R1234ze(e), R1234yf, hydrofluoroolefins, R600a.

Anotace

Ejektorový chladicí technologie je považována za potenciální alternativu ke kompresorové chladicí technologii díky některým svým výhodám. Mezi ně patří možnost ejektorového chladicího okruhu (ECO) být poháněn obnovitelnými zdroji; navíc je ECO stabilní a má jednoduchou údržbu. Silněji než kdy dříve nyní zaznívá požadavek na všechny chladicí technologie používat ekologickou pracovní látku z důvodu rychlých klimatických změn a problémů z nich plynoucích.

Cílem této práce je detailní výzkum ejektorové chladicí technologie prostřednictvím numerických a experimentálních metod. Numerická metoda byla použita k pochopení vlivů nejrůznějších parametrů, např. přehřátí, teploty generátoru, velikost výměníků tepla aj., na výkon systému. Dalším cílem práce je teoretický návrh ejektorového chladicího systému využívajícího ekologická chladiva. Bylo provedeno experimentální vyšetřování ejektorového chladicího systému poháněného solární energií za účelem posouzení výkonu systému za reálných podmínek.

Ke studiu výkonu systému při různých pracovních podmínkách byl použit prototyp ejektorového chladicího systému s pracovním chladivem R600a. Bylo zkoumáno chování ejektoru v návrhových podmínkách (on-design) a nenávrhových podmínkách (off-design). Výsledky experimentu byly použity k doladění a ověření matematického modelu ejektorového chladicího cyklu zahrnujícího všechny součásti systému včetně deskových výměníků tepla. Uvedený model umožňuje studovat chladicí cyklus z různých hledisek, jako je vliv konstrukce výměníků na výkon systému nebo vliv stupně přehřátí na chování systému. Model byl rovněž použit k posouzení čtyř nových chladiv ze skupiny hydrofluoroolefinů: R1234yf, R1234ze(e), R1234ze(z) a R1233zd(e). Jako doplněk byla provedena numerická studie proudění reálného plynu v ejektoru.

Výsledky experimentu jasně prokázaly přínos ejektoru s proměnlivou geometrií. Zlepšení výkonu systému bylo až 42% vůči ejektoru s pevnou geometrií. Výsledky matematického modelu souhlasily s experimentálními výsledky v rozmezí tolerance ± 15%.

Matematický model rovněž potvrdil, že při měnících se pracovních podmínkách je nutné k zajištění požadovaného výkonu použít ejektor s proměnlivou geometrií. Toto platí pro všechna zkoumaná pracovní chladiva. Vliv pracovních teplot na výkon systému byl značný. Velikosti výměníků významně ovlivnily účinnosti přenosu tepla a tlakovou ztrátu. Studie ukázala, že R1234ze (e) a R1234yf jsou pro ejektorový chladicí systém nejperspektivnější pracovní látky. Výsledky matematického modelu byly podpořeny numerickými výpočty (CFD).

Klíčová slova: ejektorový chladící technologie, ejektor s proměnném geometrii, obnovitelný energie, plechový výměník, R1234ze(e), R1234yf, hydrofluoroolefin, R600a.

ACKNOWLEDGEMENTS

I would like to express my sincere gratitude to my supervisor, Professor Václav Dvořák, for his valuable advice and supervision. I am grateful for his countless support, for my professional and personal life, over my study periods in Czech Republic. My research would have not been realized without his persistent help.

I am profoundly grateful to my co-supervisor, Professor Szabolcs Varga, for his constructive guidance and significant contribution throughout the thesis. His outstanding knowledge and supervision have motivated me in many ways. Professor Szabolcs Varga has distributed momentous time helping me in every work of the research.

I am deeply thankful for the financial supports from the Faculty of Mechanical Engineering and the "Studentská grantová soutěž". I feel lucky for being a student at the University of Liberec.

I wish to recognize the valuable assistance of the people in the International Office and the Student service office. Special thanks to Ing. Marcela Válková and Mgr. Radka Dvořáková, who have offered precious help since the first day I came to Czechia.

The Erasmus+ program has given me great chances to enhance my research and experiences of student life. Taking the internships under the Erasmus+ was a turning point in my doctoral program.

I wish to acknowledge Prof. Petr Louda, Prof. Tomáš Vít, Associate Prof. Iva Petríková, Prof. Armando C. Oliveira, and Ing. Petr Novotný CSc. for their kindness and contributions to my academic journey.

I would like to thank the University of Porto for accepting me for the internships. I am thankful for the possibility of using the experimental test rig as well as many other assistances from the Faculty of Engineering. Many thanks to Joao Soares, Behzad Shahzamanian for their willingness to share knowledge and their friendship. I also want to thank Anas Elbarghthi for his collaborations and talks.

I am grateful for the unconditional love and support of my parents and siblings.

Contents

LIST OF TABLES

LIST OF FIGURES

List of Appendices

LIST OF ABBREVIATIONS AND ACRONYMS

List of abbreviations

Abbreviation	**Description**
ABS	Absolute
AC	Air conditioning
ASHRAE	American Society of Heating, Refrigerating and Air-Conditioning Engineers
C	Condenser outlet
CAM	Constant area mixing chamber
CAME	Constant-area mixing ejector
CFD	Computational fluid dynamics
CPM	Constant pressure mixing chamber
CPME	Constant-pressure mixing ejector
D	Diffusor (ejector) outlet
E	Evaporator outlet
ECC	Ejector cooling cycle
EES	Engineering Equation Solver
ERS	Ejector refrigeration system
EU	European Union
F-gases	Fluorinated greenhouse gases
G	Generator outlet
GWP	Global warming potential
HEX	Heat exchanger
ID	Internal diaphragm

ID	Internal diaphragm
IEA	International Energy Agency
INEGI	Institute of Science and Innovation in Mechanical and Industrial Engineering
NIST	National Institute of Standards and Technology
ODP	Ozone depletion potential
P	Pump outlet
PC	Personal computer
PHE	Plate heat exchanger
REFPROP	Reference Fluid Thermodynamic and Transport Properties
rpm	Revolutions per minute
RTD	Resistance temperature detector
SSL	Slope of saturated line
SST	Shear-stress transport
TED	Thermal energy distribution
USA	United states of America
V	Expansion valve

List of variables

Variable	**Description**
A	Heat transfer area, m^2
A_{ratio}	Heat transfer area ratio, *[-]*
AR	Area ratio, *[-]*
Bd	Bond number, *[-]*
Bo	Boiling number, *[-]*

c_p	Specific heat capacity at constant pressure, $J/kg\ K$
c_v	Specific heat capacity at constant volume, $J/kg\ K$
CC	Cooling capacity, W
COP	Coefficient of performance, *[-]*
D_h	Hydraulic diameter, *[-]*
ER	Entrainment ratio, *[-]*
fou	Fouling factor, $m^2 \cdot K/W$
G	Mass velocity, $(kg \cdot m/s)$
Gra	Gravitational acceleration, m/s^2
h	Specific enthalpy, J/kg
h_{lv}	Latent heat of vaporization, J/kg
he	Convective heat transfer coefficient, $W/\ m^2K$
k	Thermal conductivity, $W/m\ K$
$\dot{m}$	Mass flow rate, *kg/s*
Nu	Nusselt number, *[-]*
NXP	Primary nozzle exit position, *mm*
P	Pressure, *Pa, bar*
PR	Pressure ratio, *[-]*
Pr	Prandtl number, *[-]*
Q	Heat energy, *J, kJ*
$\dot{Q}$	Heat rate, *W, kW*
$\dot{q}$	Heat flux, W/m^2, kW/m^2
R	Universal gas constant $J/mol\ K$
r	Specific gas constant, $J/kg\ K$
SP	Spindle position, *mm*

T	Temperature, $K, °C$
t	Plate thickness, m
W	Mechanical work, J
$\dot{W}$	Mechanical power, W
We	Weber number, *[-]*
x_{qua}	Vapor quality, *[-]*

Greek letters

Variable	**Description**
β	Mixing section converging angle, deg
γ	Surface tension, N/m
η	efficiency, *[-]*
θ	Chevron corrugation angle, deg
κ	Specific heat ratio, *[-]*
μ	Dynamic viscosity, $Pa\ s$
ϵ	Effectiveness of a heat exchanger [-]
ϑ	Kinetic viscosity, m^2/s
ϕ	Coefficient, *[-]*

List of subscripts

Subscript	***Description***
2	Hypothetical cross section area
3	Mixed flow before the shockwave
4	Mixed flow after the shockwave
c	Condenser

ch	Channel
co	Cold
cri	Critical point
e	Entrained fluid, secondary flow, evaporator
e2	Secondary flow at hypothetical cross section
ej	Ejector
g	Generator, the primary inlet
g2	Primary flow at section 2
HR	Heat required
in	Inlet
l	Liquid
lv	Liquid-vapor
mol	Molecular
NO	Primary nozzle outlet
p	Pump
Pl	Plate
Po	Port
s	Shockwave
sat	Saturated
sg	Single
sp	Specific
sup	Degree of superheat
t	Throat
tot	Total
tp	Two-phase

va	Vapor
w	Water
y	Hypothetical throat

List of superscripts

Superscript	***Description***
*	ratio

1 INTRODUCTION

1.1 Contextualization of the thesis

Air conditioning (AC) plays an essential role in modern society, as it was clearly stated by Lee Kuan Yew, the first Prime Minister of Singapore in his biography [1]: “Air conditioning was a most important invention for us, perhaps one of the signal inventions of history. It changed the nature of civilization by making development possible in the tropics. Without air conditioning, you can work only in the cool early-morning hours or at dusk. The first thing I did upon becoming prime minister was to install air conditioners in buildings where the civil service worked. This was key to public efficiency.”

Air conditioning of the indoor space is fundamental for well-being and productivity in the hot and humid parts of the World. Whereas the demand for space cooling is driven by economic and population growth. Nowadays, 99% of private dwellings in Singapore are equipped with an air conditioner, which are on for most of the time when the apartment is occupied [2]. In contrast, only 4% of households in India possess an air conditioner, despite having high cooling needs [3]. There are about 1.6 billion air conditioners in use worldwide, dominated by China, United States of America (USA) and Japan. However, the economic growth in developing countries and the global warming will lead to massive expansion of the air conditioning market in the upcoming years. For example, India had nearly 30 million AC units in use in 2016, which was predicted to increase to over 1 billion units by 2050 [4].

Electricity use for space cooling (air conditioners, household fans, dehumidification systems) is becoming the largest share of electricity consumption in buildings as shown in Figure 1.1. Forecasts indicate that air conditioners approximately will reach 5.6 billion installed units on a global scale by 2050. Considering their actual energy efficiency, air conditioning will consume about 620 TWh of electricity, equivalent to about 30% of total electricity use in buildings (see Figure 1.1) [3].

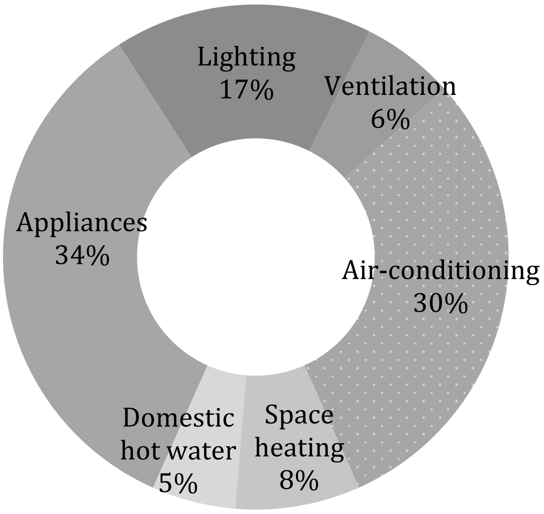

Figure 1.1 Forecast of the share of global electricity use in building by 2050 (data extracted from IEA [3]).

A projection of the electricity consumption for space cooling up to 2050 is shown in Figure 1.2 in comparison to the scenario of 2016 for different regions of the Globe. It is clear from the figure that there is a strong increase in the expected electricity consumption for all the countries indicated. According to this projection, India will be the world leader corresponding to an increase over 40-fold in a period of about 30-years, from 39.5 TWh to 839 TWh. This is equivalent to one-third of the net electricity generation of 28 countries of the European Union (EU-28) in 2018 [5]. Consequently, air-conditioning is one of the major causes of carbon dioxide emissions.

Most current air-cooling technologies use electricity (e.g. vapor compression technology); and over 65% of electricity globally is produced from burning fossil fuels (2016) [6]. Even though the World is moving towards a larger share of renewable energy conversion, electricity generation relies heavily on fossil fuels; e.g. 87.7% and 71.2% in China and EU-28 in 2014, respectively [7]. Space cooling is foreseen to produce 2070 Mt carbon dioxide in 2050, nearly twice as much (1135 Mt) as in 2016 [3]. The total amount of greenhouse gas emissions in carbon dioxide equivalent (CO2-eq) was 4224 Mt in Europe in 2017 [8].

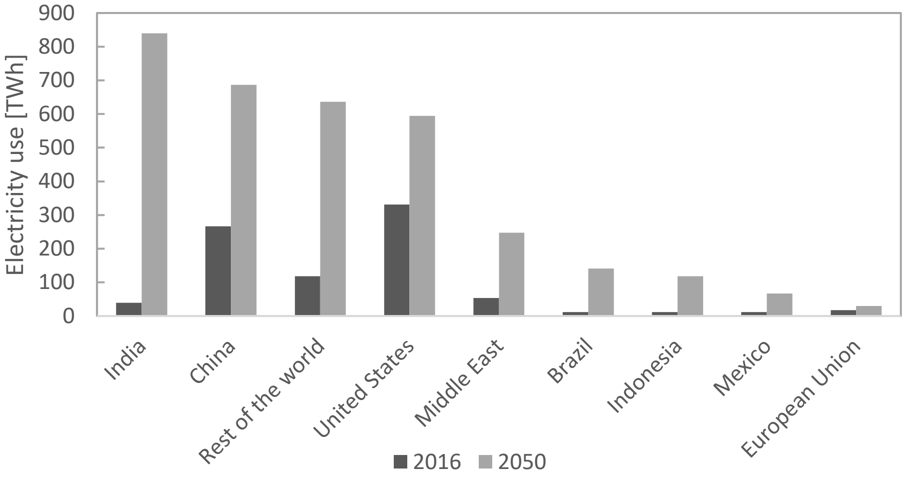

Figure 1.2 Global electricity use for space cooling in building in 2050 (data extracted from IEA [3]).

Considering market expansion and existing air conditioning technologies, space cooling is one of the major causes of global warming on the planet. It is estimated that AC applications alone will be responsible for a temperature rise of 0.5°C [4] in the total projected of 3 - 5°C by the end of this century [9]. Carbon dioxide emissions, by burning fossil fuels, contribute to unwanted greenhouse effects, which in turn provoke unsustainable climate change manifesting on the daily basis by e.g. the rise of sea level, extreme weather events (flood, storm, etc.). Figure 1.3 presents the global risks landscape published by the World Economic Forum [10]. The risks were ranked based on their possibility to happen (likelihood) and their effects to the human life (impact). According to Figure 1.3, extreme weather events (denoted as the green mark at the top-right corner) certainly happen and they strongly impact on human life.

It has been realized by policymakers, scientists, and the public in general that actions must be urgently taken in order to reverse the actual climate trends. These actions include shifting primary energy source usage towards renewables, improving energy conversion efficiency, reducing the emission of greenhouse gases. In other words, the climate change could be slowed down by reducing the emission of CO_2 and other greenhouse gases.

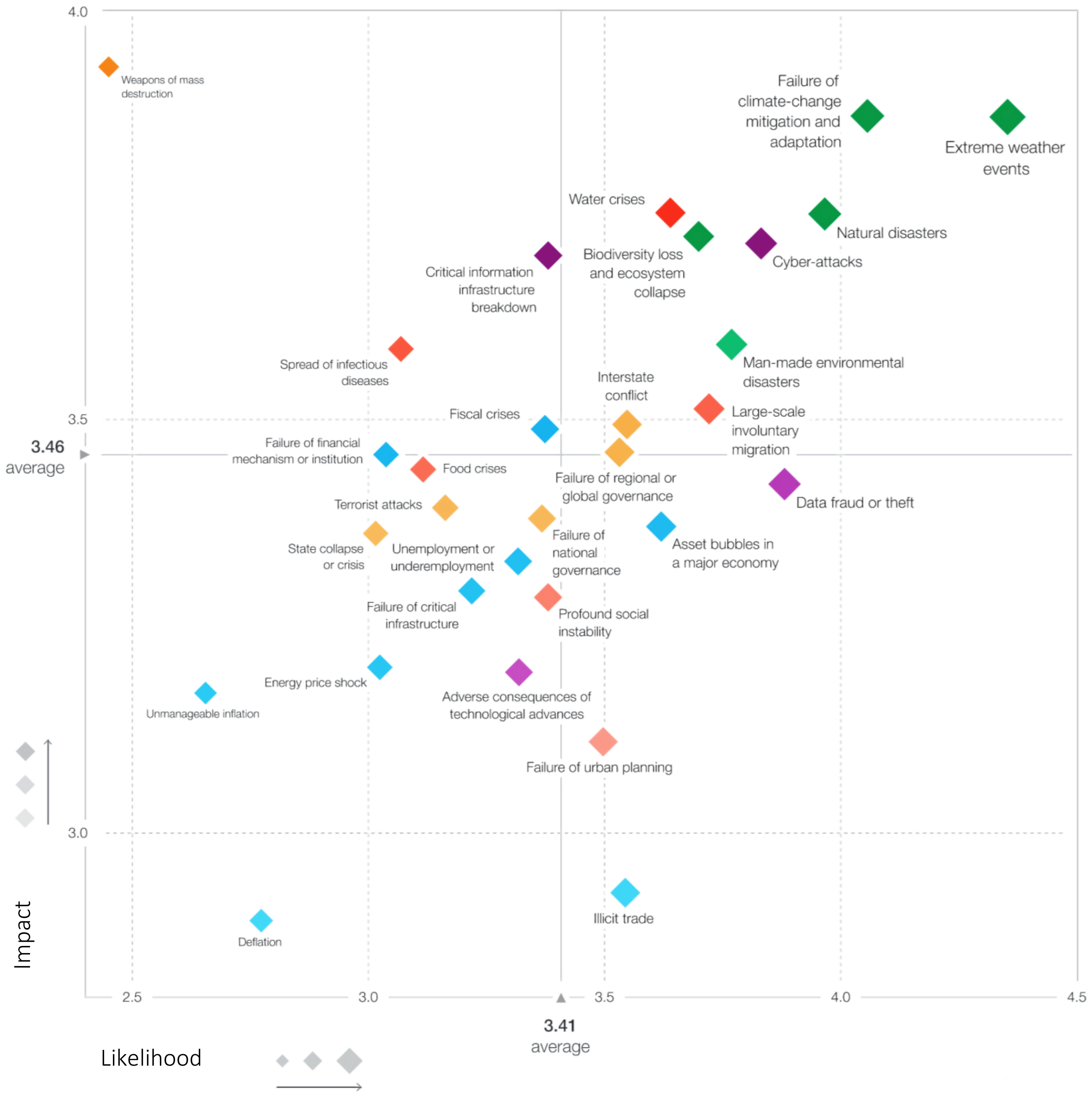

Figure 1.3 The global risks landscape (2019) by World Economic Forum [10].

Besides electricity generation, direct emission of greenhouse gases, such as refrigerants used as working fluids in cooling systems, contribute to the climate change problem. The European regulation 517/2014 [11] on the reduction of fluorinated greenhouse gases (F-gases) emissions is a good example of the efforts to contradict unwanted tendencies in the European Union (EU). According to this regulation, the developed countries should reduce greenhouse gas emissions by 2050 to 80% - 95% of the levels of 1990 [11]. Therefore, a roadmap was defined for replacing 79% of these refrigerants on the market by 2030 (compared to 2015), as shown in Figure 1.4. The regulation states that refrigerators and freezers for commercial use will not be permitted to operate in new installations with working fluids representing a global warming potential index (GWP) of 150 or higher by January 2022. Currently, most commonly used refrigerants have a GWP considerably higher than this limit. For example, HFC refrigerant R134a has a GWP of 1430, while HFC blend R410a has an even higher value of 2088). The regulation no. 517/2014 represents a strong constraint for the refrigeration industry, and thus concerns the research and development of new refrigeration technologies.

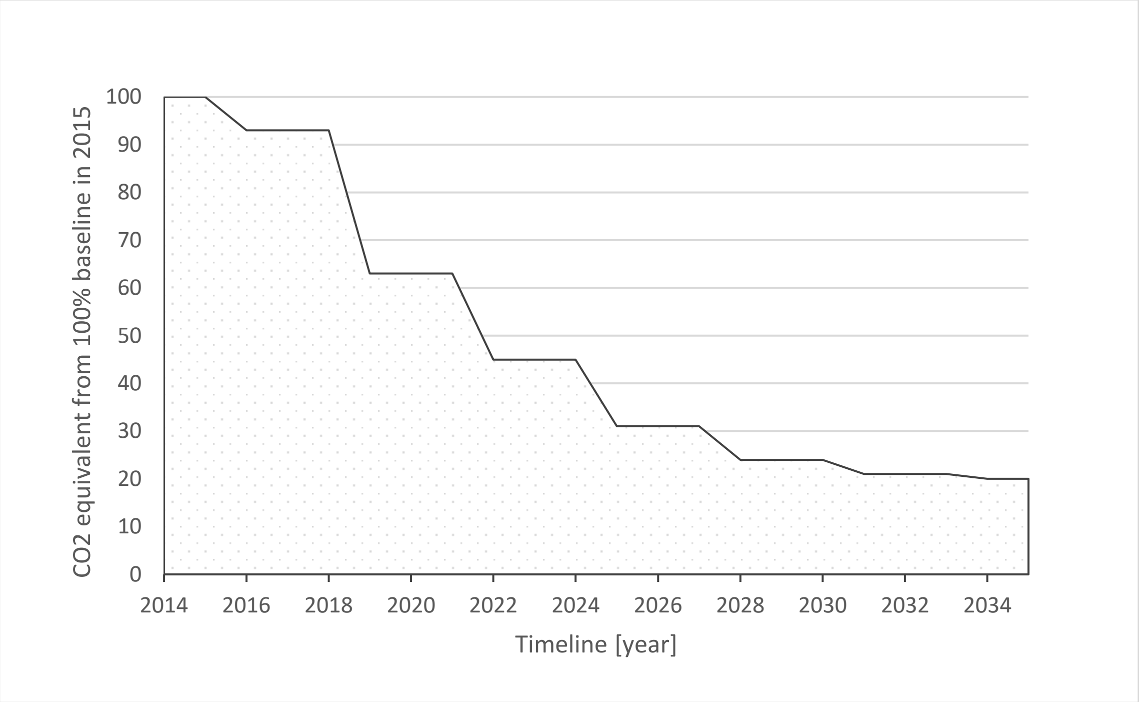

Figure 1.4: Expected phasing out process of the F-gases according to regulation no. 517/2014 of the EU [11].

Cost-effective alternative solutions are required to reduce the electricity stress caused by the increased demand for space cooling because of the unsustainable nature of the current electricity consumption trends. Moreover, renewable energy is abundant in many (hot) regions of the world, but their use for driving air conditioning equipment is rather limited. A heat-driven cooling system, such as ejector refrigeration can play a key role in the air conditioning market of the near future. The most attractive feature of the ejector refrigeration is the possibility of using low-grade thermal energy to drive the system instead of electricity. Widely available low-grade heat sources such as solar heat, geothermal energy, waste heat from power plants, etc. can be used. Solar energy is accessible everywhere, especially in hot regions where air conditioning is needed. Unlike biomass, solar thermal energy is pollution-free, no greenhouse gases are produced during utilization. In addition, the operating and maintenance costs of solar collectors are low. The ejector cooling technologies powered by solar thermal energy offer clean, highly accessible solutions for air-conditioning.

In a study of a solar-driven ejector refrigeration system (SERS) for office buildings, Guo and Shen [12] claimed that the system could save up to 80% electric energy compared to conventional refrigeration. The benefits of using ejector cooling are significant. They are thoroughly presented in the literature review of Chapter 2. The ejector refrigeration has a strong potential to reduce the electric energy stress associated with the fast increase of air-conditioning applications worldwide. The growth of this technology could contribute to the effort towards decelerating the climate change.

1.2 Objectives of the thesis

The work has been carried out focusing on three principal objectives:

1. Development of a simplified mathematical model of ejector cooling cycle (ECC) is aimed that is capable to predict system operation with an acceptable accuracy. This model is then applied to carry out a comprehensive study, addressing the influence of ejector geometry and operating conditions on the overall system performance.
2. Assessment of the application of new environmentally friendly working fluids for ejector cooling technology. Qualified refrigerants must fulfill criteria of thermodynamic performance, and requirements of the regulation 517/2014 of the European Union.
3. Development a design tool for suitable thermodynamic design of the ECC with a qualified refrigerant.

Another objective of the work is to perform experimental assessments of the performance of the solar ejector cooling system (SERS), aiming to reveal the system behaviors under real conditions. Experimental results are also used for validating the mathematical model of the ejector cooling cycle.

1.3 Research methodology

An important aim of the thesis is to develop a capable mathematical model to accurately predict ejector cooling system (ECS) performance for a set of working fluids and operating conditions and then use this model as a design tool for the individual components of the cooling cycle. Additionally, experimental and computational fluid dynamics (CFD) techniques were also employed to support and to validate the mathematical model. In the following text, each means will be individually discussed.

a. Theoretical work

Theoretical analysis was carried out using a mathematical model. Models are fast, cost-effective and flexible tools for assessing different working conditions, refrigerants and system configurations, which would be otherwise difficult or impossible using an experimental approach. The ejector cooling cycle (ECC) model is built by combining sub-models of its major components. The basic ECC consists of an ejector, three heat exchangers (i.e. vapor generator, condenser, evaporator), an expansion valve, and a refrigerant pump. It is believed that the ejector device is quite sensitive to the working pressures, especially the backpressure, (the pressure at ejector diffusor) when the system works at the critical point (detailed discussion is in chapter 2). If the pressure loss through the heat exchangers are well estimated, the system behaviors can be better predicted.

The mathematical model developed is based on basic conservation laws of thermodynamics: energy, momentum, and mass conservation.

It is aimed to address the influences of heat exchanger geometry and operating conditions on the overall system performance. The heat exchangers are comprehensively modeled. Each of these heat exchangers is divided into single-phase sections and phase-change section. Suitable correlations are applied to define the heat transfer coefficients and Fanning friction coefficients for each section. The heat transfer rate and pressure drop are then calculated. By determining the refrigerant pressure drop through heat exchangers, ejector inlets and outlet pressures are more accurately calculated and thus, the model accuracy is improved. Subcooling of the liquid refrigerant at the condenser outlet and superheating at the generator and evaporator outlets are considered in these heat exchanger models.

Thermodynamic design of the major components is proposed depending on required technical demand (e.g. cooling capacity, the temperature of chilling media at the condenser, and refrigerant temperature at generator inlet, etc.) and applied working fluid.

The mathematical model is implemented in commercial software called Engineering Equation Solver (EES - Fchart, USA). All properties of working fluids are obtained from the real-gas database of the software. Since the flow inside the ejector is supersonic and involves a series of shock waves, it is highly compressible. Thus, the use of the real-gas database is an essential requirement for having an accurate mathematical model. Furthermore, the real-gas database is also used in treating the raw experimental data.

Additionally, CFD is applied as a tool for validating the ejector geometry resulting from the mathematical model. A mesh sensitivity study is first performed. The integrated real-gas database (NIST REFPROP) in Fluent (Ansys, USA) is used for the fluid physical properties.

b. Experimental work

Experimental work on a solar ejector cooling system is carried out with the objective to study the influence of key factors such as backpressure and nozzle exit position on the system performance. Thermocouples and pyranometer were carefully calibrated by the team members of the project solar ejector refrigeration system. An uncertainty analysis is performed in EES so that confidence limit for the experimentally obtained data are quantified. These estimates are also needed for the mathematical model validation. Besides, the experimental work provides references for the mathematical model, such as degrees of superheating at ejector inlets and the ejector efficiency.

1.4 Structure of the thesis

The thesis is composed of eight chapters, as presented in the flowchart of Figure 1.5. Chapter 1 is an introductory chapter providing a general context for the work. The objectives of the dissertation are identified, and the followed methodology is presented.

Chapter 2 focuses on the background of ejector cooling technology. A short review of the historical development of ejector refrigeration is presented. A critical review of the existing literature is carried out to support the objectives of the present Ph.D. work.

Chapter 3 describes the details of the mathematical model development for the theoretical analysis of the ejector cooling cycle.

Chapter 4 gives a detailed description of the solar-driven ejector cooling test facility, which was used for the experimental work. The corresponding results are analyzed and discussed in Chapter 5. The validation of the mathematical model with experimental results is presented in the same chapter.

In Chapter 6, a parametric study is carried out for assessing the performance of novel environmentally friendly refrigerants on these types of systems and focusing on a suitable design for the heat exchangers of the cooling cycle.

Chapter 7 is dedicated to the validation of the mathematical model developed in Chapter 3 by the CFD technique.

Finally, Chapter 8 summarizes the most important conclusions of the thesis and provides suggestions for future research dealing with ejector refrigeration technologies.

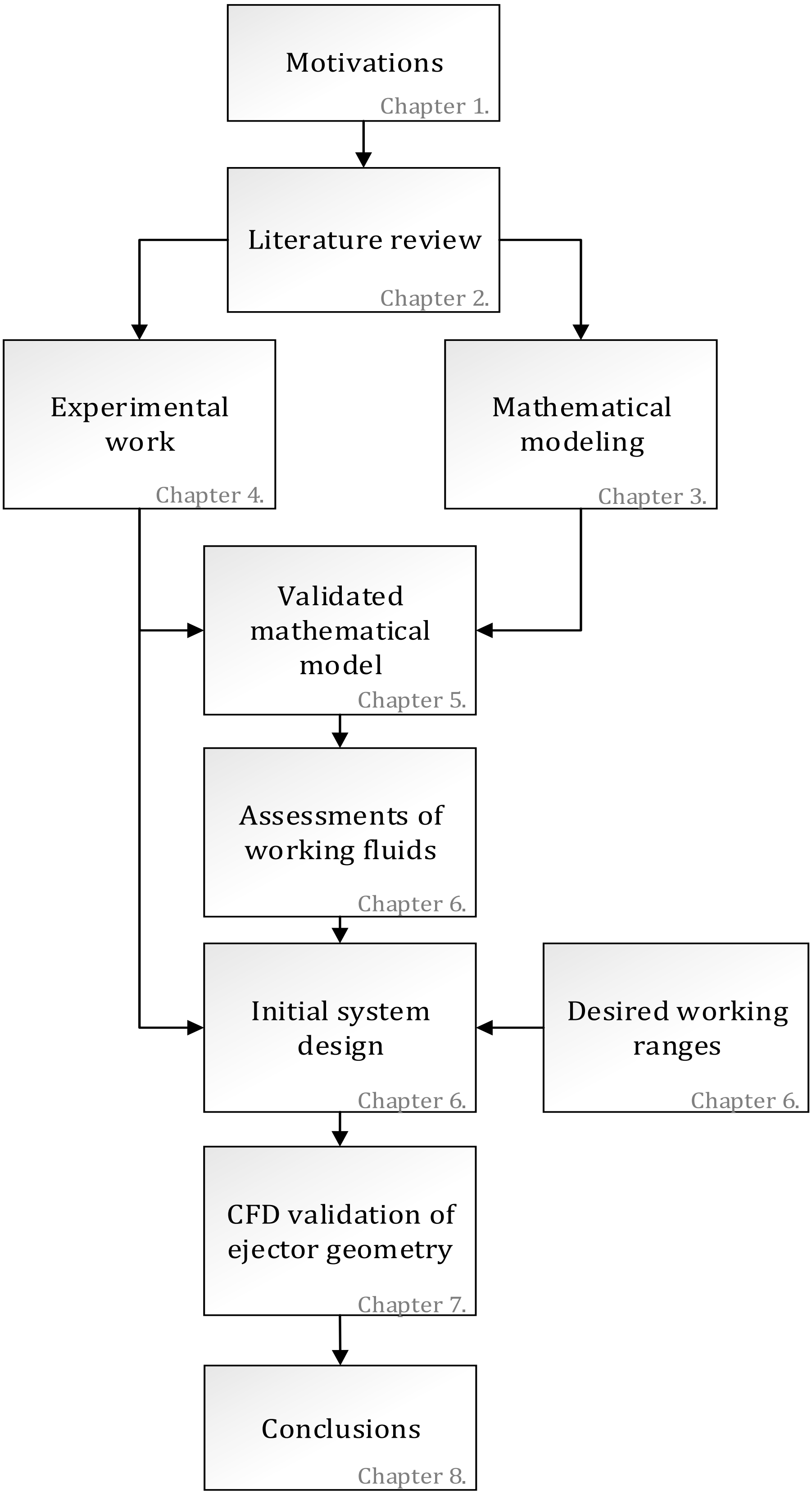

Figure 1.5 Flowchart of the thesis structure.

2 LITERATURE REVIEW

2.1 Background

2.1.1 A brief on the history of ejector cooling technology

Ejector technology has been known for more than a century. In 1858, Henri Giffard obtained a patent for the steam-injector, which uses a steam jet to pump liquid water to a boiler. His theoretical and experimental studies established an initial background for the development of more advanced ejector technology. The invention of the converging-diverging nozzle (de Laval nozzle) in 1889 [13] led ejector technology a step forward, since supersonic state motive jet considerably improved the suction effect.

Ejector technology has been applied in many areas of engineering, such as petrochemical processes, eatable oil deodorization, fertilizer plant, water distillation, etc. Refrigeration was one of the first applications of ejector technology. Maurice Leblanc built the first successful steam jet refrigeration system in Paris in 1908 and obtained the patent in the United State of America (USA) in 1911 [14]. Steam jet refrigeration was installed in some buildings in the USA in the 1930s [15].

Despite the domination of mechanical vapor compressor-based refrigeration technology in the past century, ejector refrigeration remained an attractive topic to researchers. Because of the environmental concerns, increased attention towards the development of improved performance ejector refrigeration can be observed. Over the last decade, several dozens of papers on ERS are published annually in the open literature. Scientists have been trying to improve the stability and performance of the ejector device by focusing on system configuration, ejector geometry, working fluid selection amongst others.

2.1.2 General operating principle of an ejector cooling cycle

The principal components of the ejector cooling cycle are the refrigerant pump, vapor generator, ejector, condenser, expansion valve, and evaporator, as shown in Figure 2.1. Please note that single letters in circles refer to the refrigerant states at the outlet of the components. ERS operation can be roughly described as follows.

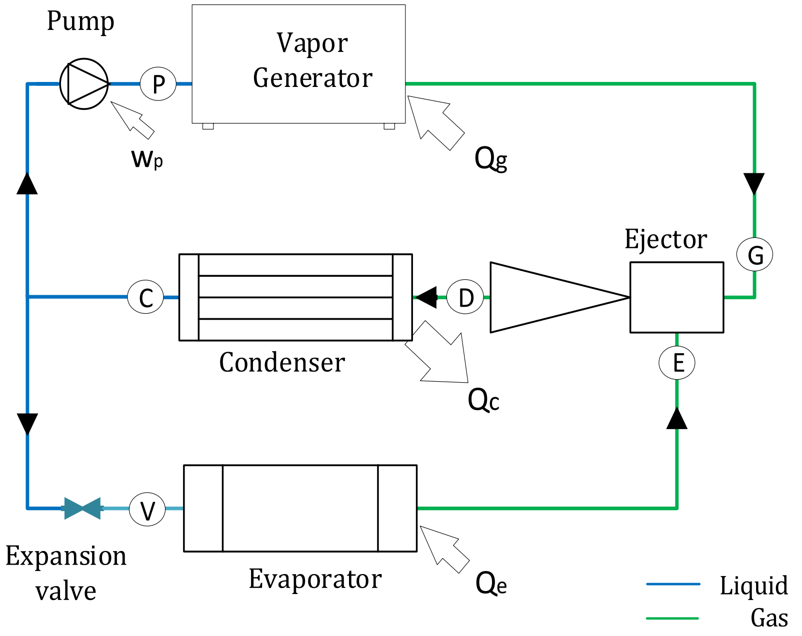

Figure 2.1 Principal components of an ejector refrigeration cycle (single letters refer to refrigerant states).

The vapor generator is used to supply heat to the high-pressure liquid refrigerant using an external heat source. The refrigerant evaporates and it reaches a superheated vapor state at the generator outlet (G). As the high-pressure vapor from the generator (also referred to as primary stream) goes through the primary nozzle of the ejector, it is accelerated to supersonic speed. Because of the expansion, a low static pressure and high-velocity (high kinetic energy) primary jet is obtained around the primary nozzle outlet region. Because of that the working fluid from the secondary inlet (evaporator outlet – E) is entrained into the suction chamber and then accelerated by tangential forces that are generated by the primary jet leaving the nozzle. The cooling effect (Q_e) in the evaporator is proportional to the mass flow rate of the secondary stream. After mixing between the primary and secondary streams, static pressure of the flow increases through a series of shock waves and the flow becomes subsonic. The pressure further undergoes raise in the subsonic diffuser to the required level of the condenser of the ejector cycle (D). the ejector here acts like a compressor device without moving parts, since it increase the pressure of the working fluid from a low lever (E) to a higher lever (D). In the condenser, heat is rejected to the environment or to a coolant so that the working fluid is in a liquid state as it leaves the heat exchanger (C). A portion of the liquid is then pressurized by the refrigerant pump before entering the generator (P), and the remaining liquid expands through an expansion valve and enters the evaporator in a liquid-vapor state (V). This completes the ejector refrigeration cycle.

2.1.3 The ejector and ejector performance indicators

The ejector is a simple device with no moving parts. The principal parts of an ejector are the primary nozzle, suction chamber, constant area section, and diffuser (see Figure 2.2). As it was mentioned before, the basic role of the ejector is to transport and to compress the secondary fluid from the evaporator (suction) pressure to the condenser pressure (backpressure), similarly to a compressor but without shaft work. The lack of moving parts leads to little need for maintenance and long shelf life.

Entrainment ratio (ER) is one of the most important parameters describing the ejector performance. It is the ratio of the secondary mass flow rate ($\dot{m}_e$) and the primary mass flow rates entering the ejector as:

$$ER = \frac{\dot{m}_e}{\dot{m}_g}. \tag{2-1}$$

For a given set of operating conditions and working fluid, the ER depends on ejector geometry. High entrainment ratio indicates better ejector performance.

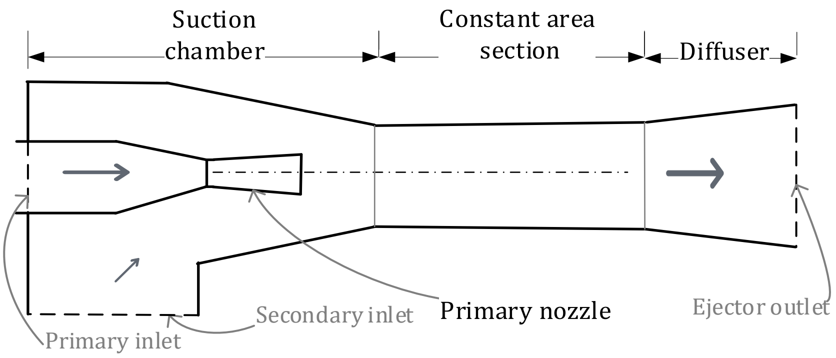

Figure 2.2 Schematic view of a typical ejector.

Under steady-state conditions, the coefficient of performance (COP) is the ratio of evaporator heat ($\dot{Q}_e$) to the total energy input rate required to drive the cycle:

$$COP = \frac{\dot{Q}_e}{\dot{Q}_g + \dot{W}_p} \approx \frac{\dot{Q}_e}{\dot{Q}_g} \tag{2-2}$$

Where, $\dot{Q}_g$ is the generator heat, and $\dot{W}_p$ is the pump work of the pump. Usually, $\dot{W}_p$ is negligible compared to the heat input ($\dot{Q}_g$), as it is shown on the right-hand side of equation (2-2). The COP is directly proportional to the ejector entrainment ratio and the enthalpy difference ratio between the enthalpy change in the evaporator and the generator as: the enthalpy difference ratio is the ratio between the enthalpy difference of evaporator outlet - expansion valve outlet, $(h_e - h_v)$; and enthalpy difference of generator outlet - pump outlet, as shown in the following expression:

$$COP \cong \frac{\dot{m}_e \cdot (h_e - h_v)}{\dot{m}_g \cdot \left(h_g - h_p\right)} = ER \frac{(h_e - h_v)}{\left(h_g - h_p\right)} \tag{2-3}$$

The enthalpy change $(h_e - h_v)$ numerator in equation (2-3) presents the specific cooling effect (specific cooling capacity) generated by one kilogram of refrigerant produced as it goes through in the evaporator (specific cooling capacity); while the denominator $\left(h_g - h_p\right)$ is the amount of specific heat received by the working fluid in the generator from an external heat source. It indicates the amount of required heat for heating one kg of refrigerant to the state at the generator outlet.

2.1.4 Heat exchangers in an ejector refrigeration system

A heat exchanger is a device for thermal energy transfer from a warmer fluid to another colder one [16]. Most of the ejector refrigeration systems (ERSs) found in the literature used plate heat exchangers. Occasionally, other types of heat exchanger (HEX), such as pipe and tube heat exchangers [36], were also applied. Plate heat exchangers (PHEs) consist of a set of thin metal plates that allow for the hot stream to transfers heat to the cold stream with low thermal resistance. The plates are stamped with certain patterns to enhance heat transfer effectiveness. PHEs are preferred for ejector cooling because of their relative compactness and high heat transfer capacity and heat transfer efficiency [17]. Plate heat exchangers can operate with small temperature differences of only 2-3°C between the hot and cold sides [18]. Heat losses are negligible because only the plate edges are exposed to the environment. Fouling in PHE is low due to high turbulence and short residence time. However, high turbulence flow inside PHE causes a higher pressure-drop compared to other heat exchanger types. Plate heat exchangers are lightweight, being about one-sixth compared to the shell-and-tube heat exchanger of equivalent capacity [19].

The heat exchangers in the ERS are called as the generator, condenser, and evaporator, representing their function in an ejector cycle (see Figure 2.1). The generator is the heat exchanger for vapor generating by adding heat to the working fluid. The condenser is the heat exchanger for condensing the vapor to a liquid state by taking the heat energy out of the working fluid. The evaporator is the device where the low temperature working fluid evaporates due to the low-pressure level (vacuum).

2.1.5 The idealized thermodynamic cycle of an ejector cooling system

The ideal (reversible) thermodynamic cycle of an ejector cooling system can be considered as a combination of two thermodynamic cycles: the motive (work) cycle and the refrigeration cycle (as visualized in Figure 2.3). The motive cycle consists of a refrigerant pump, generator, ejector and condenser (P-G-D-C on the temperature-entropy diagram in Figure 2.3). The motive cycle generates work (W_m) that is required to drive the refrigeration cycle. The efficiency of the ideal motive cycle is the Carnot efficiency expressed as:

$$\eta_{m,ideal} = \frac{W_m}{Q_g} = \frac{Q_g - Q_c}{Q_g} = \frac{T_g - T_c}{T_g} \qquad (2\text{-}4)$$

The difference of Q_g and Q_c is the useful work to the ideal motive cycle.

The refrigeration cycle consists of an expansion valve, evaporator, ejector and condenser (V-E-D-C in Figure 2.3, accordingly). It generates the cooling load from the heat energy from the conditioned space and generates the cooling effect. The COP of a reversible refrigeration cycle ($COP_{r,ideal}$):

$$COP_{r,ideal} = \frac{Q_e}{W_r} = \frac{Q_e}{Q_c - Q_e} = \frac{T_e}{T_c - T_e}\,. \qquad (2\text{-}5)$$

The efficiency of the idealized ejector cycle is then [20]:

$$COP_{ej,ideal} = \eta_{m,ideal}\, COP_{r,ideal} = \frac{T_g - T_c}{T_g}\frac{T_e}{T_c - T_e}\;. \qquad (2\text{-}6)$$

Equation (2-6) can be used to establish the maximum limit for the efficiency of a real ejector cycle for given working temperatures. It also indicates that the higher T_g and T_e are, the better the cycle COP since $T_g > T_c > T_e$. The influence of the working conditions at condenser (T_c, P_c) on the system performance is complex because firstly, the influence of T_c to the $COP_{ej,ideal}$ as shown in equation (2-6); secondly T_c and P_c are correlated due to the phase change (P_c is a function of the saturation temperature at the condenser), and P_c strongly influences the ejector performance.

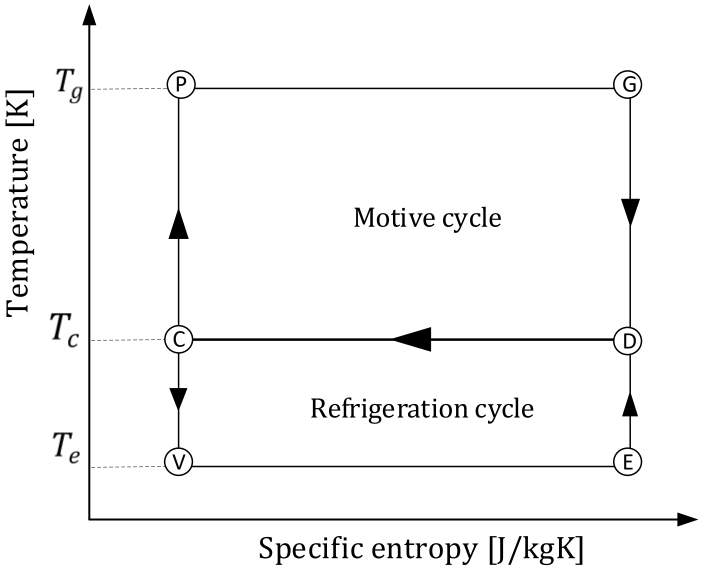

Figure 2.3 Ideal ejector refrigeration cycle in T-s diagram [20, 21].

2.2 Key hypotheses in ejector modeling

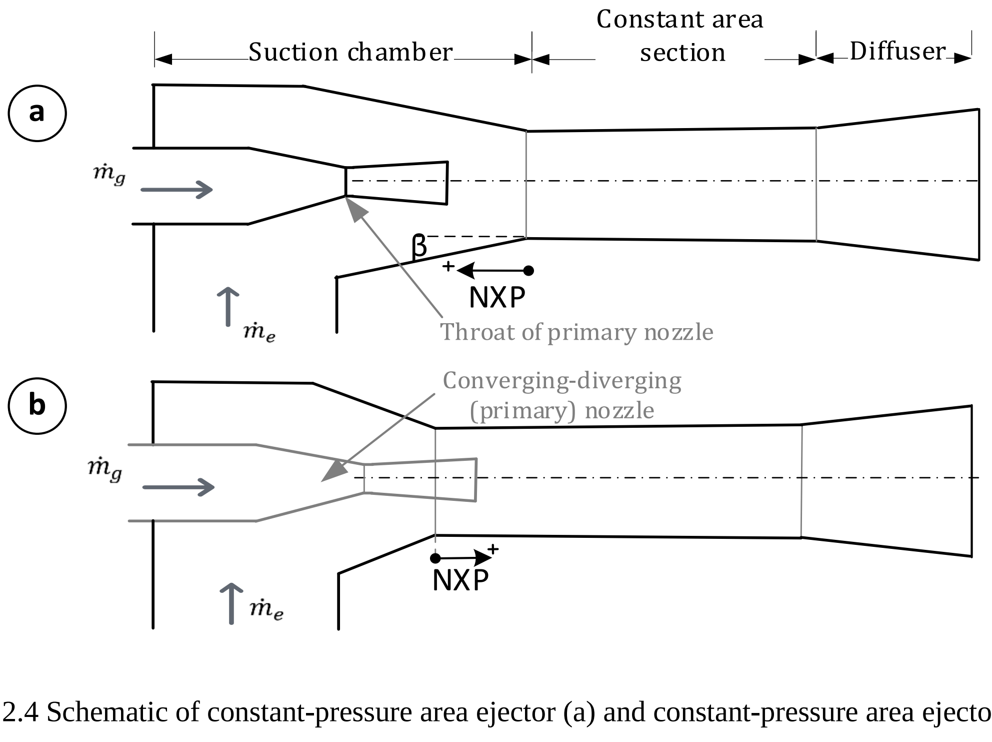

Figure 2.4 Schematic of constant-pressure area ejector (a) and constant-pressure area ejector (b).

Ejector for cooling applications can be classified based on several criteria such as the nozzle position, nozzle design, the number of phrases [22]. Based on the nozzle position, ejectors are classified as constant-pressure mixing ejector (CPME) and constant-area mixing ejector (CAME) [22]. The basic difference between the two is the position of the primary nozzle. The primary nozzle exit of the constant-pressure mixing ejector is located within the suction chamber while in a CAME, it is placed within the constant-area section (see Figure 2.4). The CPME is preferred over the CAME because it can operate with higher backpressure levels without reducing the ejector performance. According to Tashtoush et al. [23], it happens because the shockwave at the downstream of the primary nozzle raises the fluid pressure to a higher level than in the case of CAME. Nevertheless, the CAME is believed to have a better entrainment ratio than CPME [24–26].

The ejector device has been extensively studied, leading to a considerable amount of publications in the open literature. The following text summarizes some of the key hypotheses that are fundamental for the development of the ejector model in this work. Table 2.1 summarizes the important point of the hypotheses.

Table 2.1 Summary of the hypotheses

Hypothesis	**Key Novelties**
Keenan model	• Using conservation laws of mass, momentum, and energy for ejector model. • The processes in the ejector were considered as isentropic, excepts where the transverse shock occurs.
Stoecker model	• Using Fanno and Rayleigh theories to describe shockwave.
Munday and Bagster model	• The primary flow remains as an identifiable jet for some distance after the nozzle exit. • Introduced the concept of the hypothetical throat cross-section. • The two flows complete the mixing process until the end of the constant-pressure mixing section.
Huang model	• Proposed that the hypothetical throat is located in the constant-area section. • The effects of frictional and mixing losses are clearly considered.

2.2.1 Keenan model (1950)

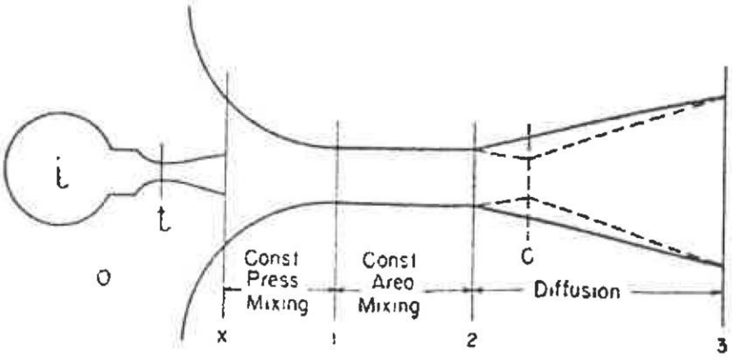

Figure 2.5 Schematic view of the ejector by Keenan et al. [24].

Keenan et al. [24] were one of the firsts to analyze the ejector flow mathematically [20]. Their model was based on ideal gas thermodynamics and the one-dimensional conservation laws of mass, momentum, and energy. During the development of the model, the ejector was divided into a several sections, as shown in Figure 2.5. It was assumed that the inlet pressures of the primary and secondary streams are uniform downstream of cross-section “x” (nozzle exit plane); and the two flows become completely mixed at section “1” (constant pressure mixing). The processes in the ejector were considered as isentropic, excepts in section 2 (see Figure 2.5), where a transverse shock occurs. The shockwave results in the pressure leap of the mixed flow between the points before and after section 2. However, the nature of the shock wave was not described in detail. Instead, the pressure rise of the mixed flow at the cross-section 3 was defined by the energy equation between the fluid states at cross-section 1-3, assuming adiabatic flow. The model did not accurately predict the entrained flow rate and the pressure level at the ejector outlet [27].

2.2.2 Stoecker model (1958)

Stoecker [15] gave a clearer description of the shockwave occurring in a supersonic ejector after the mixing process using the Fanno and Rayleigh theories, as shown in Figure 2.6. Figure 2.6a shows the Mollier chart by Stoecker explaining the pressure profile of flows inside an ejector. Like Keenan model, Stoecker assumed that the mixing process starts from the nozzle exit and finishes by the end of the constant-pressure mixing section (as illustrated in Figure 2.5).The high stagnation the pressure P_G expands through the primary nozzle to the pressure P_{NO} (somewhere in constant pressure mixing section). $P_{NO}$is assumed to be identical with the stagnation pressure at secondary inlet (P_E) and the pressure of the mixed flow (P_M). The shockwave results in the pressure rise from P_M to P_S, somewhere at the diffusion section. The flow is further compressed to P_D as it goes through the diffuser.

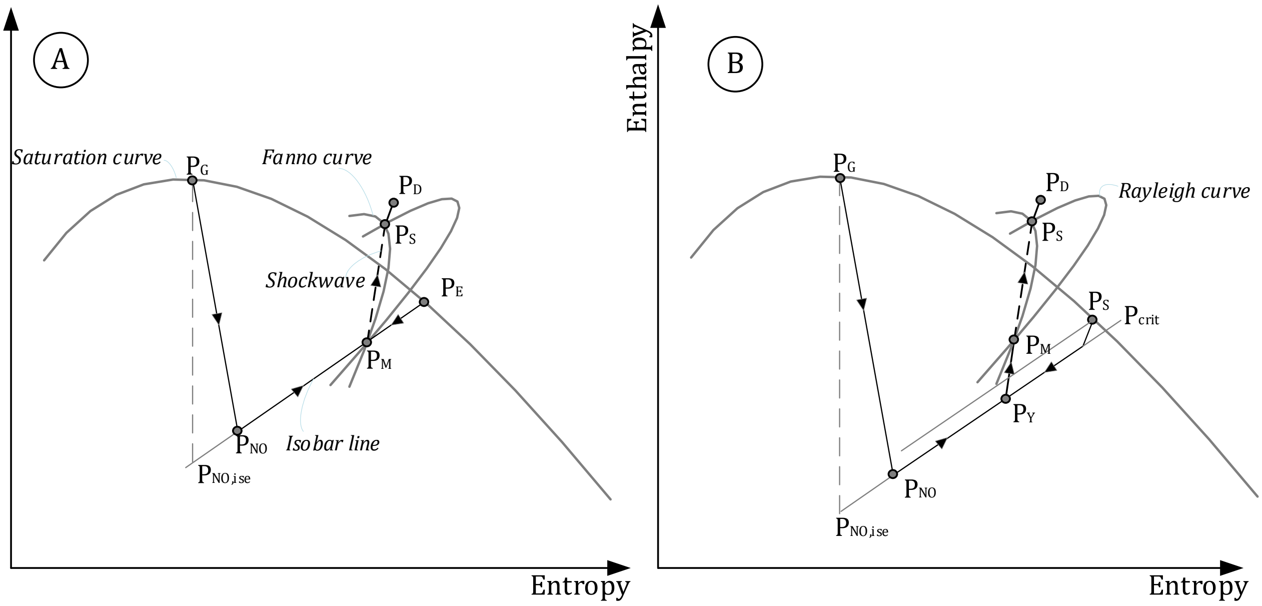

Figure 2.6 Mollier chart by Stoecker theory (A) and Munday & Bagster theory (B) [28].

2.2.3 Munday and Bagster model (1977)

Munday and Bagster [28] argued that when operating with the condenser pressure (P_D) lower than the design value, the actual performance of the system was considerably lower than the one calculated by the Stoecker model. Also, the pressure loss of the secondary flow between secondary inlet P_E and at the hypothetical throat (P_Y) should be taken into consideration, which is not the case of the Stoecker model.

Munday and Bagster [28]proposed that the primary flow remains as an identifiable jet for some distance after the nozzle exit, which confirmed by Fabri and Sienstrunck [29] using the flow visualization method. As shown in Figure 2.7, Munday and Bagster [28] assumed that the two flows start to mix at a hypothetical cross-section (Y-Y) and complete the process until the end of the constant-pressure mixing section. The location so called hypothetical throat is assumed where the secondary flow reaches the sonic velocity. It is not located at a certain place in the converging section, as suggested by Munday and Bagster [28], rather the hypothetical throat varies within the end part of the converging section, depending on the working pressures at the inlets and outlet. Munday and Bagster [28] did not present the procedure to calculate the hypothetical throat area (A_Y). Instead, the ratio between A_Y and the throat area (A_T) was given based on experimental observations. They suggested that for a given steam ejector, the optimal ratio of A_Y/A_T remains approximately constant.

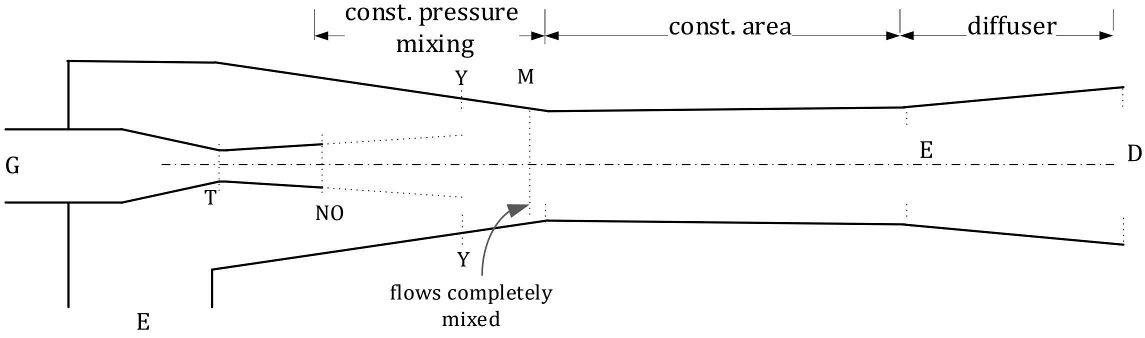

Figure 2.7 Schematic view of an ejector by Munday and Bagster [28].

Both Stocker [15] and Munday & Bagster [28] considered steam as the working fluid. The primary and secondary streams at the inlets were considered as saturated vapors (without superheating). Under such conditions the working fluid would undergo phase change during the flow path as indicated by the different fluid states identified on the Mollier (see Figure 2.6). The influence of the presence of liquid droplets on ejector performance is significant [30–32]. However, the models mentioned above do not consider the effects of the phase-change phenomenon.

2.2.4 Huang model (1999)

Huang et al. [33–35] investigated both theoretically and experimentally an ejector cooling system with R141b working fluid. Based on isentropic relations for an ideal gas, Huang et al. [34] presented a detailed ejector model, where some modifications were proposed to the model of Munday & Bagster [28]. The most important modifications are explained with the help of Figure 2.8. First, the hypothetical throat, where the secondary flow reaches sonic velocity, is assumed to be located in the constant-area section. This hypothesis allows for determining the secondary and primary flow areas at the hypothetical throat in a relatively straightforwardly fashion. Secondly, the mixing process of the two flows occurs in the constant-area section [28-29] with a uniform pressure (instead of the mixing section, as proposed by the earlier works). The Huang model can be used to predict the ejector performance in critical mode (more about the critical mode operation is presented in section 2.3). Ejector operation modes are discussed in details in the subsection 2.1.3. The effects of frictional and mixing losses are considered by applying empirical constants (efficiencies), to be determined experimentally. Ejector efficiencies, however, may depend on the operating temperatures, ejector geometry, working fluid, etc. [36–38]. Huang et al. [34, 35] also found that the degree of superheating at the ejector inlets can influence the performance. However, the superheating was not considered in his mathematical model [34].

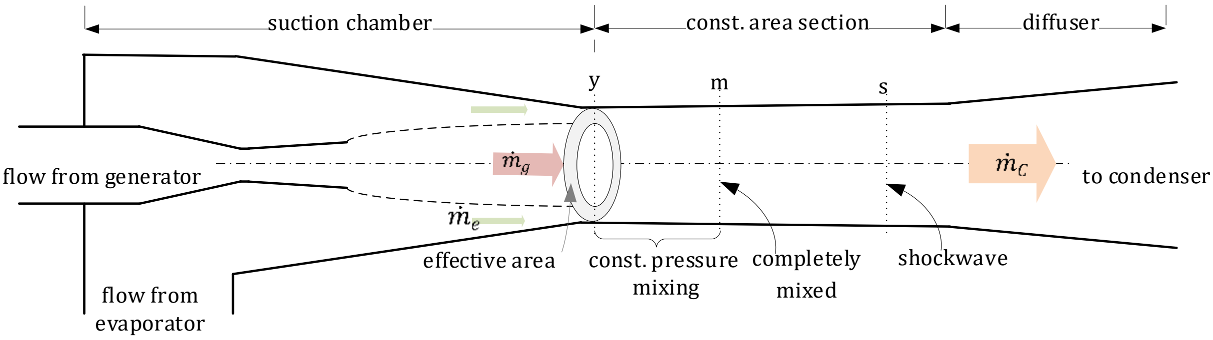

Figure 2.8 Schematic view of the ejector model by Huang et al. [34]

2.3 Working regimes of an ejector

For constant primary and secondary inlet pressures, the performance of a given ejector depends on the backpressure level. A typical ejector operation curve is shown in Figure 2.9. Accordingly, three regimes can be distinguished: on design, off-design, and reverse flow.

For low backpressures, the entrainment ratio remains constant. It is because both primary and secondary flows reach sonic conditions (double choking) along the flow path. Under these circumstances, the entrainment ratio depends on the upstream conditions only, thus becomes independent of the backpressure. This phenomenon is represented by the horizontal part (on design) of the operating curve in Figure 2.9.

The highest limit of the backpressure under which double-chocking remains is called the critical backpressure (P_{crit}). In fact, the critical point is the ejector's optimal performance point, where the working pressures just meet the conditions for the double-choking operation.

Beyond P_{crit}, the secondary stream does not reach sonic velocity and its flow rate becomes a function of the differential pressure between the inlet and outlet. Consequently, ER sharply drops to zero when the backpressure reaches P_{break}. Beyond this point, reverse flow occurs at the secondary inlet and the ejector fails to operate (ER < 0).

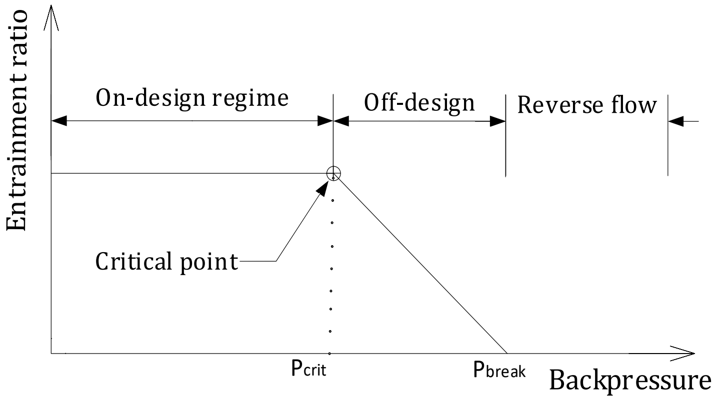

Figure 2.9: Ejector performance curve for constant P_g and P_e.

When the ejector works at on-design regime, the primary flowrate increases as the primary inlet pressure reaches higher value. In case the ejector geometry is fixed, the raise of the primary flowrate reduces the effective area and thus, decreases the secondary flow rate. Detailed discussions on the ejector performance with variation of the working conditions are presented in chapter 6.

2.4 Idealized working principle of an ejector under on-design conditions

Figure 2.10 illustrates the pressure and velocity distribution along an idealized constant-pressure mixing ejector at on-design operating regime The working fluid at the ejector can be characterized three working pressure levels: high-pressure at the ejector primary inlet, low-pressure level at the ejector secondary inlet, and the intermediate pressure level at the ejector outlet. The high-pressure vapor enters the primary nozzle. It is accelerated in the convergent duct until sonic velocity in the primary nozzle throat (denoted as “T”). In the divergent section of the primary nozzle, the working fluid expands reaching supersonic velocity the outlet. The static pressure of the motive stream decreases along with the primary nozzle until its exit point (NO) to a level that is somewhat below the static pressure in the suction chamber (and the secondary inlet). This pressure difference draws the secondary vapor into the suction area. Additionally, part of the kinetic energy of the primary stream is transferred to the secondary stream by momentum exchange. Therefore, the secondary flow is accelerated by primary flow at the downstream of the converging section.

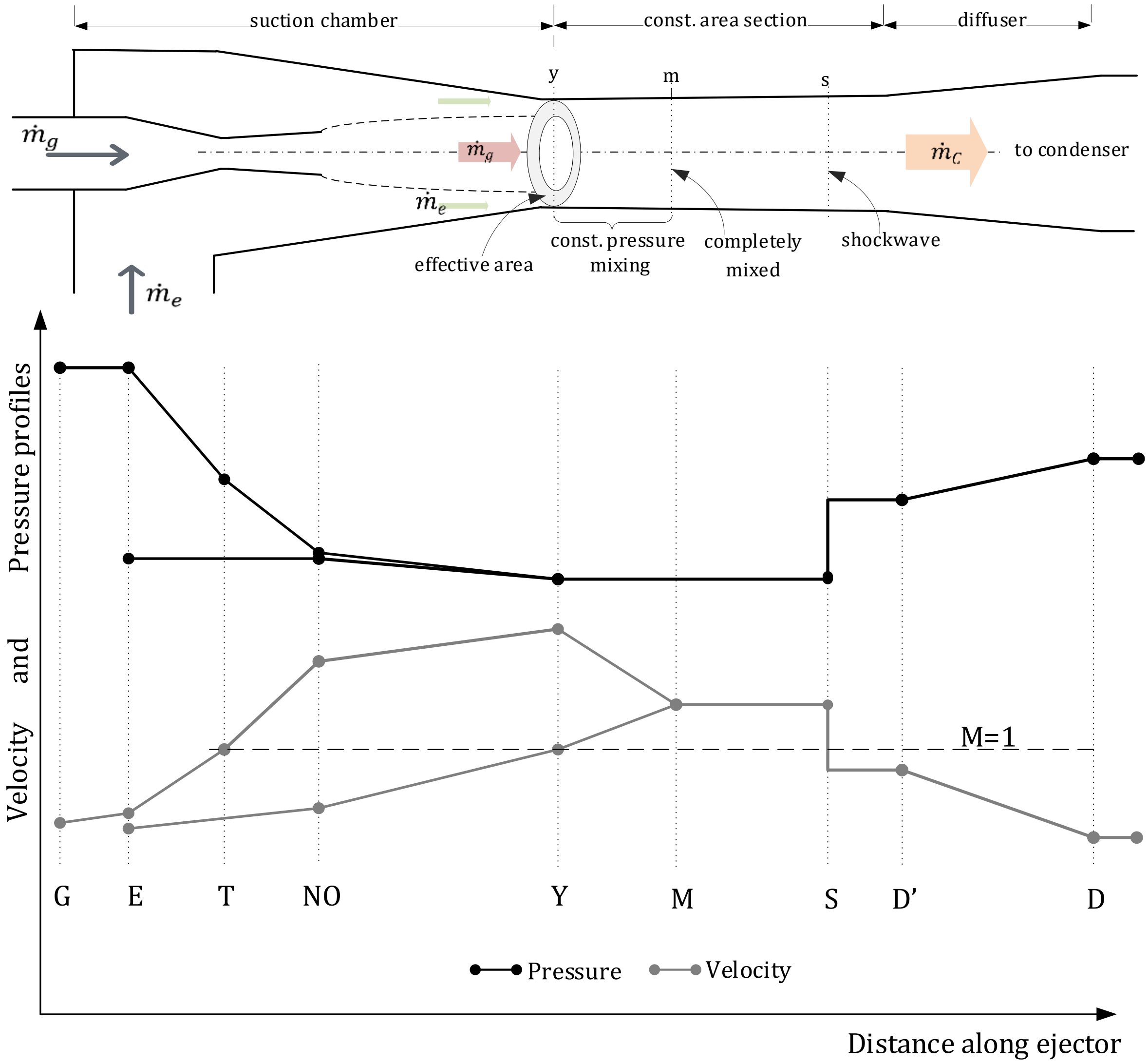

Figure 2.10 The velocity and pressure profiles of the flows as they go through the ejector.

The velocity of secondary flow becomes equal to the speed of sound at the hypothetical throat [28]. The two flows start to mix at the hypothetical throat cross-section (Y) with a uniform pressure [34, 39]. The constant-pressure mixing process is assumed to occur and complete (M) in the constant-area section of the ejector [34] just before the occurrence of a normal shock. The normal shock takes place somewhere downstream of the constant-area section, before the ejector diffuser (the cross-section S in Figure 2.10) [40]. The intensity and location of the shockwave depend on the magnitude of the backpressure [20, 41]. The shock causes the velocity of the mixed fluid to drop below sonic level that is accompanied by a sudden rise of static pressure [28, 42], the pressure recovery. The static pressure of the working fluid is then further recovered in the subsonic diffuser while the flow velocity gradually decreases.

2.5 Heat exchangers in ERS

2.5.1 Heat transfer mechanisms

Conduction and convection are the two major mechanisms of heat transfer in heat exchangers. Thermal conduction occurs due to atomic interactions within a body or between two objects that are physically contacted. Convection is thermal energy transfer between a solid surface and a fluid by in motion. In the ejector cycle, forced convection occurs in the heat exchangers since the fluid motion is usually induced the pump and the ejector itself. In indirect heat exchangers, thermal energy is transferred from the hot fluid to the wall by convection, through the wall by conduction, and from the wall to the cold fluid by convection.

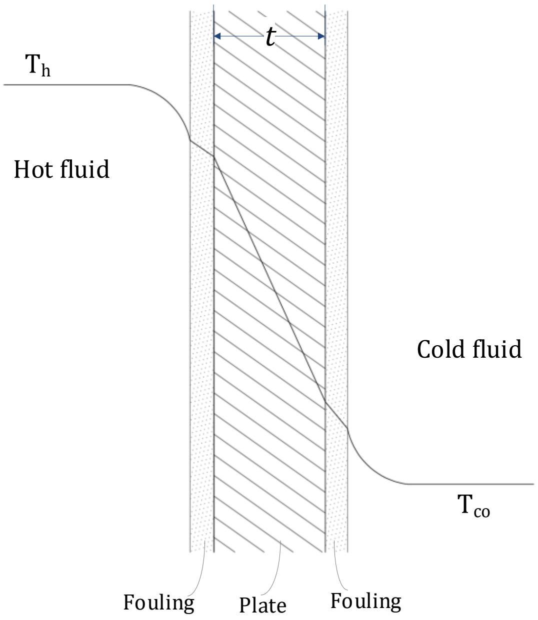

Figure 2.11 Heat transfer mechanisms of plate heat exchanger.

Along with the conduction and convection, the fouling in heat exchanger also influences the overall heat flux. Fouling is caused by the accumulation of fluid impurity on the plate surface. The influence of fouling on heat transfer is expressed by the fouling factor.

This is usually given an empirical value because it is a complex function of numerous factors like fluid density, purity, temperature, etc. Figure 2.11 illustrates the heat transfer mechanisms, including the fouling layers over the two sides of the plate of a plate type heat exchanger. The overall heat transfer coefficient (U), which refers to how well heat is conducted through over a series of resistant mediums, can be expressed as follows:

$$\frac{1}{U} = \frac{1}{he_{co}} + \frac{1}{he_h} + \frac{t}{k} + R_{fou,co} + R_{fou,h}\ , \tag{2-7}$$

where, he_c and he_h are the film heat transfer coefficients of convections on the cold and hot side, respectively. t and k are the thickness and thermal conductivity of the plate heat exchanger. $R_{fou,co}$ and $R_{fou,h}$ are thermal resistances caused by the fouling on the cold and hot side of the plate, respectively.

The overall heat transfer coefficient is one of the key performance indicators. The second indicator is the heat exchanger pressure drop of the working fluid. The third indicator is the effectiveness (ϵ), which is defined as the ratio of the actual heat transfer (q_{act}) to the maximum possible heat transfer (q_{max}):

$$\epsilon = q_{act}/q_{max} \tag{2-8}$$

2.5.2 Plate heat exchanger (PHE)

The flow in plate heat exchanger is highly turbulent with low fouling, which enhances heat transfer. However, the pressure-drop throughout a PHE can be higher compared to other heat exchanger types [17, 19].

Based on the assembling method, plate heat exchangers can be classified into three groups: gasketed plate-and-frame, welded or brazed PHE. Gasketed PHE consists of a stack of pressed plates in a bolted frame. Inter-plate gaskets are used to ensure sealing between flows (as shown in Figure 2.12a). With this configuration, maintenance is relatively simple. Typical operating pressures and temperatures can be up to 25-30 bar and 260°C, respectively [19]. Brazed PHEs (see Figure 2.12b) and welded PHEs offer higher maximum operating pressure levels, up to 40 bar and 30 bar [17], respectively. Also, their operating temperatures can be significantly higher than the gasketed configuration, up to 350ºC [38].

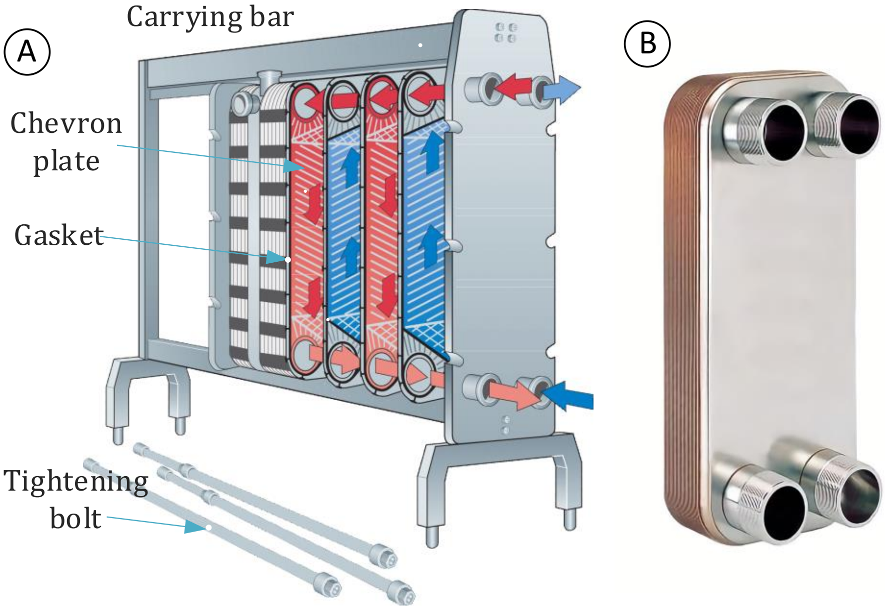

Figure 2.12 Illustration of (A) gasketed plate-and-frame heat exchanger [43] and (B) brazed plate heat exchanger (Alfa Laval [44])

Two widely used arrangements for single pass PHEs are the U-type and Z-type as shown in Figure 2.13. The flow distribution inside the U-type PHE is less uniform than for the Z-type. However, it is preferred because all four ports in this arrangement are fixed on one side of the frame, thus maintenance is simpler [19, 45].

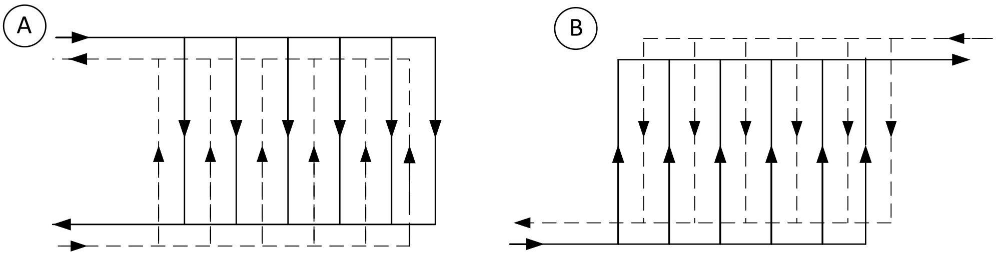

Figure 2.13 Typical pass arrangements used in PHE, U-type (A) and Z-type (B)

Flow in heat exchangers can be arranged into three basic types: counter-flow, parallel-flow, and cross-flow The parallel-flow arrangement can be mostly found in shell and tube HE. This arrangement can be beneficial where the operating temperatures are extreme.

The effectiveness of cross-flow heat exchange is better than parallel-flow [19, 46]. Cross-flow HEX allows for a more compact and multi-pass design. This type of arrangement is preferred when the cooling media is abundant, like air.

The counter-flow arrangement has some key advantages over the parallel flow. First, the temperature difference (gradient) between the hot and cold fluid along the heat exchanger length remains large and more uniform (see Figure 2.14). Thus, the overall heat transfer coefficient is considerably higher [47], and it also produces a more uniform heat flux along with the heat exchanger. Second, the outlet temperature of the cold fluid can reach a higher value, close to the inlet temperature of the hot fluid. Due to these advantages, the counter-flow arrangement is preferred over the others in many applications, including ejector cooling. Thus, the counter-flow arrangement is selected in analyzing the system performance in the present study.

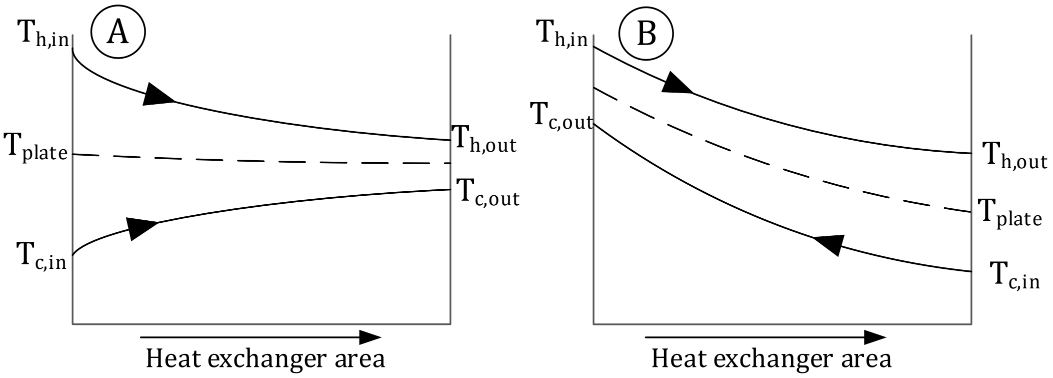

Figure 2.14 Temperature profiles of parallel-flow (A) and counter-flow (B) heat exchanger.

2.6 Classification of refrigerants

A refrigerant is a pure substance or mixture used in refrigeration systems, usually undergoing of one or more phase-change processes. Refrigerants can be classified according to several criteria. One of the possible classification methods considers two categories: synthetic and natural refrigerants. Synthetic refrigerants are substances that do not occur in nature, they were developed by humans for industrial purposes. in contrast, natural refrigerants are those that occur in nature[48].

2.6.1 Synthetic refrigerants

The most typical synthetic refrigerants can be classified according to their chemical composition as halocarbons. A halocarbon is a chemical compound of carbon and one or more elements of the halogen group, usually, fluorine (F) and chlorine (Cl). A halogen has a strong tendency to share a single electron with another atom to create a covalent bond and form a stable compound, as illustrated in Figure 2.15.

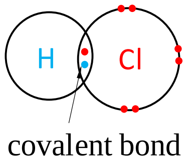

Figure 2.15 Illustration of a covalent bond between atomic Hydrogen and Chlorine.

Generally, using halocarbon refrigerants in refrigeration system offers some favorable properties, e.g., ability to reach sub-zero temperature, under moderate operational pressures. Halocarbon refrigerants can be classified into the following groups: chlorofluorocarbons (CFCs), hydrochlorofluorocarbons (HCFCs), hydrofluorocarbons (HFCs), and hydrofluoroolefins (HFOs).

CFCs consist of chlorine, fluorine, and carbon (R12, R13 etc.). They were widely used for domestic, automotive, commercial cooling purposes since they are non-toxic, non-flammable and stable substances. However, the emission of CFCs into the atmosphere seriously damages to the ozone layer. Consequently, the commercialization of CFCs has been banned since 1987 in developed countries [49], and they are subjected to complete phase out since 2008.

When one or more chlorine element is substituted by hydrogen in a CFC compound, the resulting working fluid is called a hydrochlorofluorocarbon (HCFC). The most common HCFCs are R22, R123, and R141b. They are low-toxic, low-cost, chemically stable and typically non-flammable fluids, developed with the intention to substitute CFCs. Because they may contain chlorine, their ozone depletion potential (ODP) is still relevant (only about 10% compared to CFCs). Because of the negative impact on the environment, HCFCs have been completely banned from the market under European regulation 2037/2000 since 2015 [50], as illustrated in Figure 2.17.

HFCs do not contain chlorine among the constituents; therefore, their ODP is essentially zero. The most common HFCs are R23, R134a, and R410a (a mixture of R32 and R125). They are mostly non-flammable, stable and nonreactive, providing high cooling performance when applied in refrigeration systems. Moreover, they usually have a lower global warming potential (GWP) than HCFCs refrigerants. Because of these properties, HFCs have been widely applied as working fluids in ejector refrigeration systems.

Nevertheless, under the current European regulation 517/2014 [11], these refrigerants are being phased out. The use of HFCs with a GWP index ≥ 2500 are banned since 2020 in the European Union.

Hydrofluoroolefins are considered as the new generation of halocarbons. In terms of chemical compounds, HFOs are similar to HFCs: they are also composed of hydrogen, fluorine, and carbon. The basic difference between them lays in the unsaturated bonds (at least one double bond) that HFOs have in their chemical structure. Unsaturated bond means reduced chemical stability such that their lifespan in the atmosphere is short, typically less than one month. This short lifespan also contributes to their negligible GWP. Figure 2.16 shows the chemical structure of R1234ze(e), R1234ze(z) and R1234yf, each having a double bond

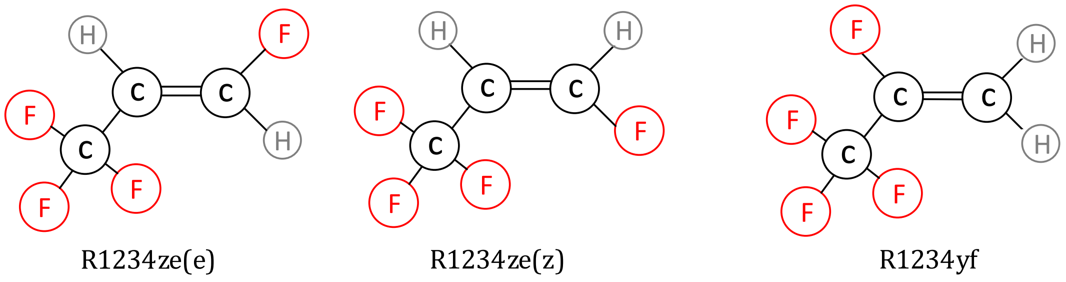

Figure 2.16 Chemical structure of R1234ze(e) and its isomers: R1234ze(z) and R1234yf.

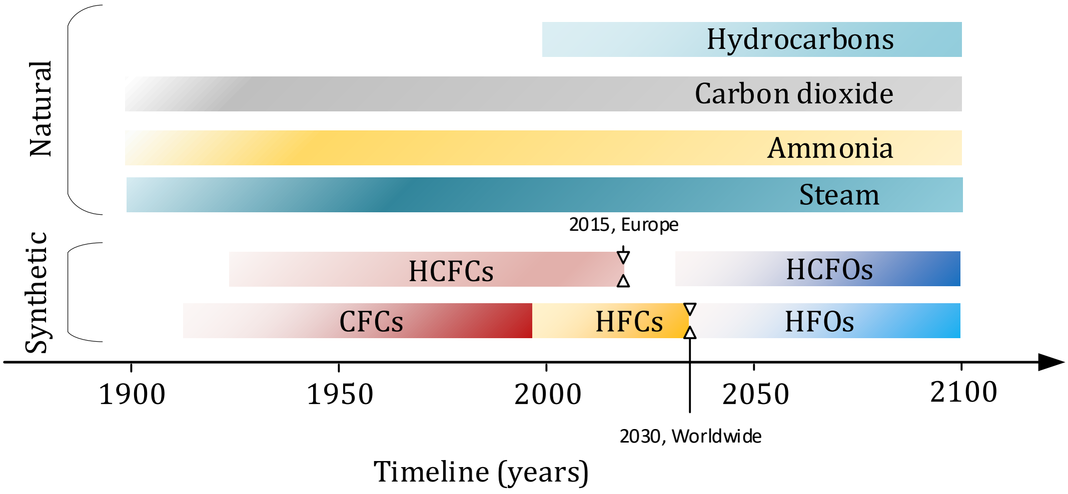

Figure 2.17: Evolution of refrigerants since 1900s, adapted from [49, 50].

2.6.2 Natural refrigerants

Natural refrigerants are environmentally friendly substances when released to the atmosphere. They can be classified into organic and inorganic groups. Organic refrigerants contain molecules of hydrogen and carbon (hydrocarbons), e.g., propane (C_3H_8) and isobutane (C_4H_{10}). Hydrocarbons were introduced as alternatives for halocarbons due to their excellent thermodynamic properties [51–53]. However, they are used with caution because of their flammability.

Inorganic refrigerants were broadly applied before halocarbons became widely available in the 1950s. Typical inorganic refrigerants are ammonia, water, and carbon dioxide. Ammonia (NH_3) has excellent thermodynamic and transport properties compared to halocarbons. However, it is a highly toxic refrigerant classified as a fluid (its safety classification is B2L [54]). Carbon dioxide (CO_2) is non-toxic, non-flammable fluid. As a positive aspect, CO_2 has very high volumetric cooling capacity. Disadvantage of using CO_2 as the working fluid is associated to its very high vapor pressure [55] and low critical temperature, which makes it inappropriate for ejector cooling. Since the end of the 17th century, water has been used as a refrigerant industrial scale in absorption systems [56]. Water is widely availability, low cost, zero impact on the environment, a high heat of vaporization. On the downside, water has a large specific volume, demanding large equipment. Water cannot operate at sub-zero temperatures and requires vacuum conditions at most operating conditions.

2.7 Characterization of refrigerants according to their environmental impact and safety

2.7.1 Ozone depletion potential index

Ozone depletion potential index (ODP) of a given substance is the ratio of integrated loss (over time) of ozone due to that substance and integrated loss of ozone due to trichlorofluoromethane (CFC-11, the reference substance) of the same mass [57].

The Earth is surrounded by the atmosphere, which is composed of several layers. The ozone layer is a thin layer located in the stratosphere, about 12 to 50 km from the surface of the planet. The ozone layer protects all living organisms on Earth by absorbing most of the ultraviolet radiations coming from the Sun. When ozone-depleting substances leak to the stratosphere from human appliances; ultraviolet radiation ruptures carbon-chlorine bonds and releases atomic chlorine. The atomic chlorine acts as a catalyst, breaking down ozone (O_3) to oxygen (O_2).

CFCs are the highest ozone-depleting substances. They are also chemically stable in the troposphere (the lowest layer of Earth's atmosphere). Particularly, CFC-11 has ODP index of 1, and the lifespan is 640 years (see Table 2.2). HCFCs have significant lower ODP index and lifespan in the troposphere, making them much less harmful to the ozone layer compared to CFCs. The two other synthetic halocarbon groups (HFCs and HFOs) have zero ODP index.

2.7.2 Global warming potential index

The GWP index of a gas is defined as its greenhouse effect relative to carbon dioxide [58]. It is also common practice to access GWP100 that is the global warming potential integrated for a 100-year period. In many cases, the abbreviation "GWP" is incorrectly used for GWP100 in published documents. Table 2.2 presents GWP100 values of some common halogens used as refrigerant according to [58].

Table 2.2 Ozone depletion potential and global warming potential index of some commonly used halogen refrigerants.

	ODP [13]	GWP100 [12]	Lifespan (year) [14,15]
CFC-R12	0.73	10200	100
CFC-R11	1	4660	640
HCFC-R22	0.034	1760	12
HCFC-R141b	0.102	782	9.3
HFC-R134a	0	1300	14
HFC-R152a	0	138	1.4
HFO-R1234ze(e)	0	1	0.05
HFO-R1233zd(e)	0	1	0.07

The atmosphere is a mixture of gases. Some gases have the ability to absorb infrared radiation and thus preventing the emission of the infrared radiation from the surface the Earth into space. These gases are called greenhouse gases and their absorption of infrared radiation is called the greenhouse effect, which is directly linked to global warming.

The greenhouse effect of a given gas is characterized by two key properties: the ability to absorb energy and its lifetime (how long its chemical structure lasts) in the atmosphere. The global warming potential index (GWP) was introduced to quantify the greenhouse effect of gases.

Table 2.2 presents ODP and GWP index of commonly halogen refrigerants. The CFCs have extremely high environmental impacts compared with HCFCs and HFCs. In contrast, HFOs have mostly zero impact on the environment.

2.7.3 Refrigerant safety considerations

Toxicity and flammability are the two crucial factors in classifying refrigerant in terms of safety. A toxic substance can damage living organisms in case of exposure. A refrigerant is classified as highly toxic when it causes damage already with short exposure time in a low concentration.

Flammability of a refrigerant is its ability to burn or ignite, causing fire or combustion. It is defined by the flash point, and an upper and lower flammability limits. The flash point is the absolute lowest temperature of the refrigerant at which it vaporizes into a flammable mixture with air. Autoignition temperature is the lowest temperature that refrigerant spontaneously ignites without a source of ignition. The lower flammability limit is the minimum concentration (in volumetric percent) of the refrigerant necessary to support its combustion in air. Similarly, the upper flammability limit is its maximum concentration that can support the flame ignited in air.

According to the American Society of Heating, Refrigerating and Air-Conditioning Engineers (ASHRAE) standard [59], refrigerant safety classes are represented by a capital letter and a number. Toxicity is classified into two groups. The refrigerants in group A have low or nontoxicity when the concentration of the refrigerant is less than 400 ppm. Group B is assigned to the fluids with high toxicity, with harmful effects even in concentrations below 400 ppm. Flammability is classified into four groups: Group 1 – non-flammable; group 2 – mildly flammable; group 2L – mildly flammable with lower burning flame velocity than group 2; and group 3 – highly flammable. For example, R1234yf is classified to A2L group, which stands for low toxicity (“A”), and low and difficult to ignite (2L). In practical terms, an A2L fluid leaking from a running air conditioner does not represent a fire hazard (for more details, the reader is referred to [60]).

2.7.4 Slope of the saturated-vapor line

Typically, ejector in ERS works in the superheated region in order to ensure system stability operates. A more detailed discussion on the influence of superheating is presented in section 2.11. The superheated region is the area on the right-hand side of the saturated-vapor line in the temperature-entropy diagram (see Figure 2.18). Based on the slope of the saturated-vapor line (SSL), refrigerants can be classified into three types: wet, dry, and isentropic. Wet fluids are those that have a saturation vapor curve of negative slope (e.g., R134a – see Figure 2.18). Dry fluids have a positive slope saturation curve, and in case of an isentropic refrigerant SSL is nearly vertical. This is important since an isentropic expansion of a saturated vapor, which appears inside the supersonic ejector, may lead to partial condensation [34]. For example, it can be seen in Figure 2.18 that the isentropic expansion process from 1 to 2s of a wet fluid (R134a) ends at the liquid-vapor region.

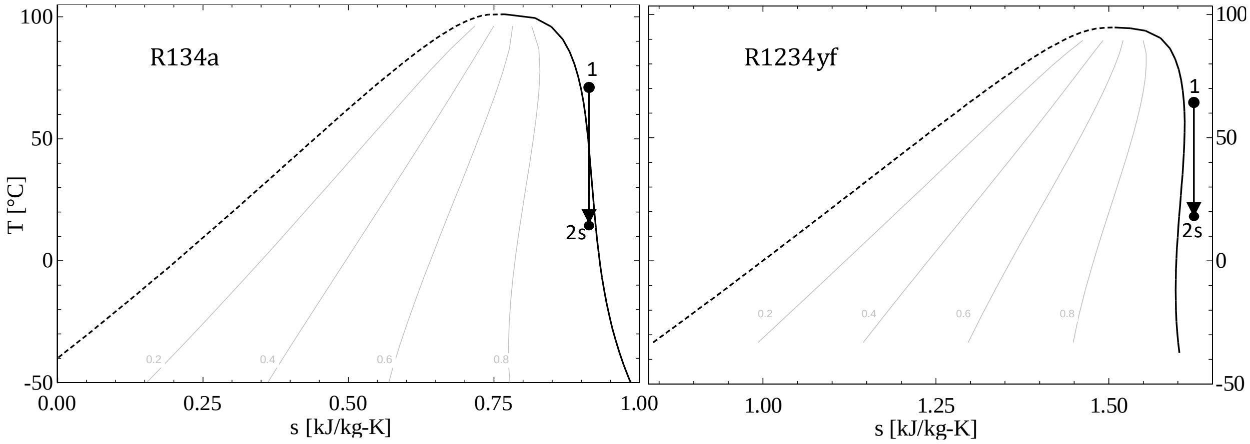

Figure 2.18 Temperature-entropy diagrams of R134a and R1234yf.

In contrast, the expansion in the dry fluid (R1234yf) ends in the superheated region. The condensation could lead to unstable ejector operation when the ejector is designed to work in a single-phase mode. Thus, depending on the nature of a refrigerant, some degrees of superheat are required to avoid this problem. It was reported that the superheat of the primary inlet flow can increase the ejector entrainment ratio [61, 62]. For example, superheating was applied in an ERS with R600a, which has positive-slope of saturated line, as working fluid in the works of Varga et al. [63, 64].

2.8 The influence of ejector geometry on its performance

One of the fundamental factors influencing the ejector refrigeration system (ERS) performance is the ejector geometry [65], leading to a considerable number of publications on this subject over the last two decades. He et al. [66] used the so called “the grey relation analysis” for studying the ejector geometry, more specifically the area ratio and the primary nozzle exit position (NXP). Area ratio of an ejector is the ratio of the constant area section to the primary nozzle throat area (see Figure 2.4). When the ejector works at its optimal performance point (critical point), the area ratio is considered the optimal area ratio. It was concluded that although AR was the dominating factor for the cycle performance, NXP also was relevant. Zhu and Cai [67] studied NXP and convergence angle of the mixing section (β) (see Figure 2.4) by using CFD technique. It was found that both parameters had a significant impact on system performance. The results indicated that the entrainment ratio (ER) varied as much as 26.6% by changing θ alone. Yan and Cai [68] emphasized the influence of AR on the ejector performance in a study considering R134a as the working fluid. In another study by Yan et al. [69] using CFD method concluded that θ influenced the ejector performance up to 15%.

Most studies indicate that geometrical factors AR and NXP have the highest impact on the ejector performance. Based on the theoretical study, considering six commonly used working fluids, Varga et al. [70] quantified the extent in which optimal AR varies under non-constant operating conditions depending on the type of the refrigerant. Experimental data [65, 71, 72] also confirms that ejector AR strongly influences its performance. However, there is little consensus regarding the contribution of NXP, converging angle, etc. to the ejector performance, as cited above. This lack of agreement is most likely because previously mentioned these studies employed different working fluids and operational pressure levels, which led to different flow structures inside the ejector. In an optimization study, Hewedy et al. [73] concluded that for a particular operating condition, there is only one single optimal ejector geometry. This statement is supported by numerical analysis by Varga et al. [70]. Sun et al. [74], therefore, suggested using an ejector with variable geometry. It was found to perform better under varying operating conditions when compared to a fixed geometry device.

2.9 Alternative system configurations of ERS

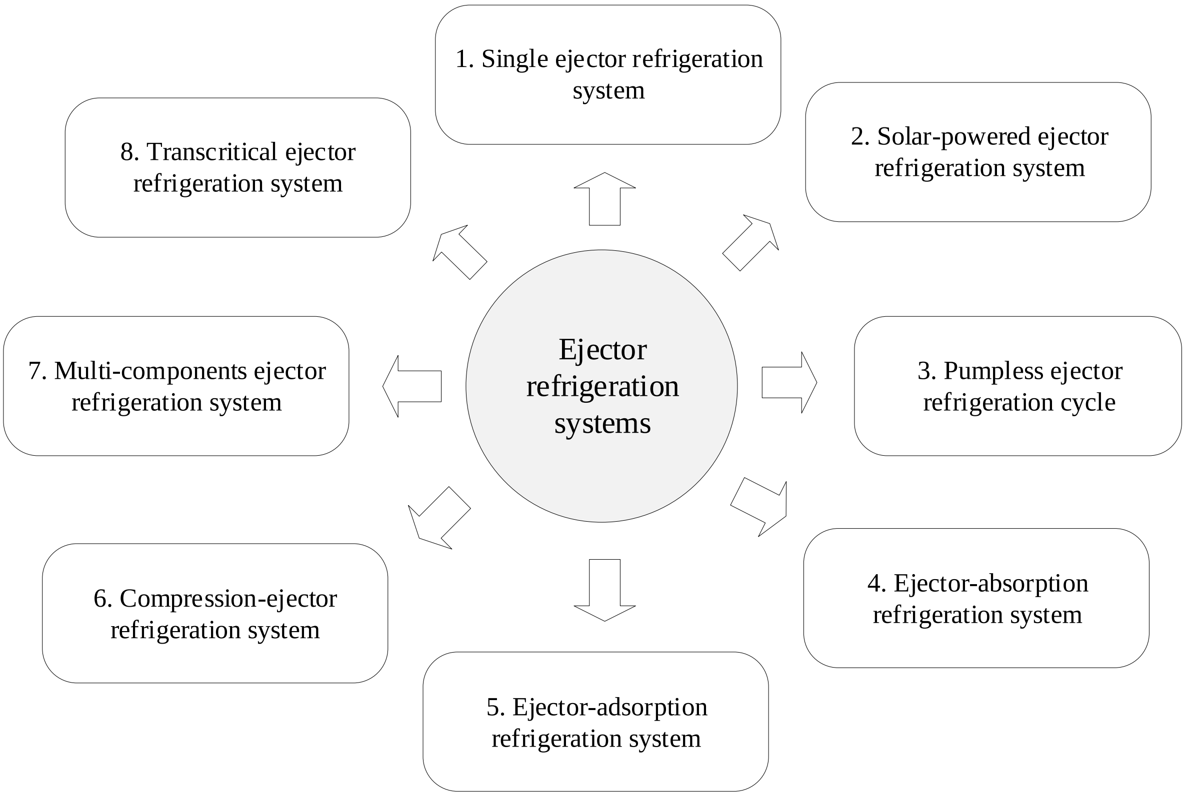

Figure 2.19 Classification of system configurations of ejector refrigeration [75].

Figure 2.19 gives a general overview regarding the diversity in existing ERS configurations. The standard ejector refrigeration system was discussed in section 2.1.2. It is the most used in experimental studies because of its simplicity. A few alternative technological solutions are discussed in the following subsections.

2.9.1 Solar-powered ejector refrigeration system

Solar-powered ERS configuration is a combination of a standard ERS with a solar collector cycle (as shown Figure 2.20). The overall COP of the solar-powered ERS is the product of the COP of the standard ERS and the solar collector-efficiency as:

$$COP_{tot} = COP\ \eta_{solar} \tag{2-9}$$

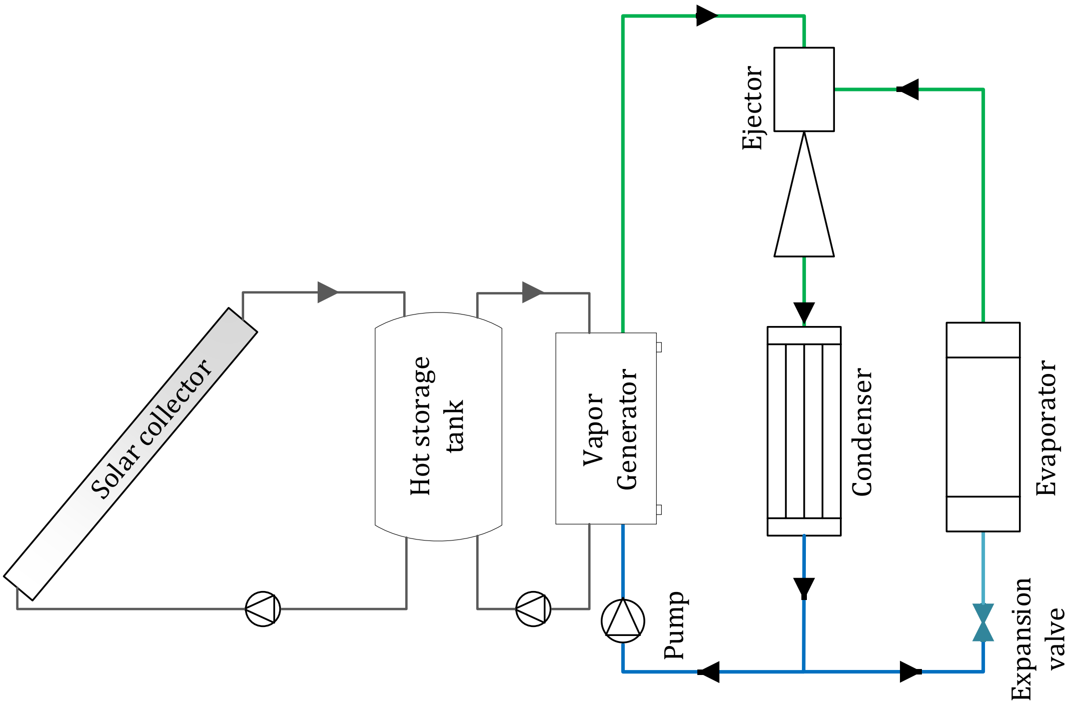

Figure 2.20 Schematic of a solar-powered energy driven ERS with a hot storage tank integrated.

Huang et al. [33] assessed a solar-powered ERS using refrigerant R141b. The authors claimed that the COP of the standard ERS could reach 0.5 at a generator temperature of 90°C, condenser temperature of 28°C and evaporator temperature of 8°C. The overall system efficiency (including COP and the solar thermal efficiency of the solar collector) of the system could be as high as 0.22. Varga et al. [63] presented an experimental study on solar-powered ERS with R600a as the working fluid, claiming that the average overall COP was 0.26. The system showed high operation stability for generator temperatures above 70°C and the condenser temperatures up to 34°C. The condenser temperature was limited by the pressure head of the circulator pump in the ejector cooling cycle.

Variation of solar radiation during operating period of the system is inevitable. Without an auxiliary heat, this variation directly influences the generator temperature level and therefore the performance of the cooling cycle. Integrating of a hot/cold thermal storage system to the solar-powered ERS is one of the solutions to mitigate the issue [63, 65, 76]. Cold storage tank with the use of phase change material (PCM) was proposed to obtain a desired energy storage density [77, 78].

In addition, auxiliary heater and cooler (also called pre-heater and pre-cooler) can be employed to maintain the stability of the cooling supply, for example in the works of Huang et al. and Pridasawas [33, 65].

2.9.2 Pumpless ERS

Another interesting system uses no mechanical pump to increase the pressure level of the primary fluid from the condenser to the generator. The refrigerant pump requires the most maintenance in the ERS cycle because of its moving parts. Pumpless ERS would be of great value especially in isolated locations where electrical energy is not available. Researchers proposed several solutions to materialize this concept. Nguyen et al. [79] studied a steam ejector with a cooling capacity of 7 kW. The working fluid is transferred from the condenser to the boiler by using the gravity head, as shown in Figure 2.21.

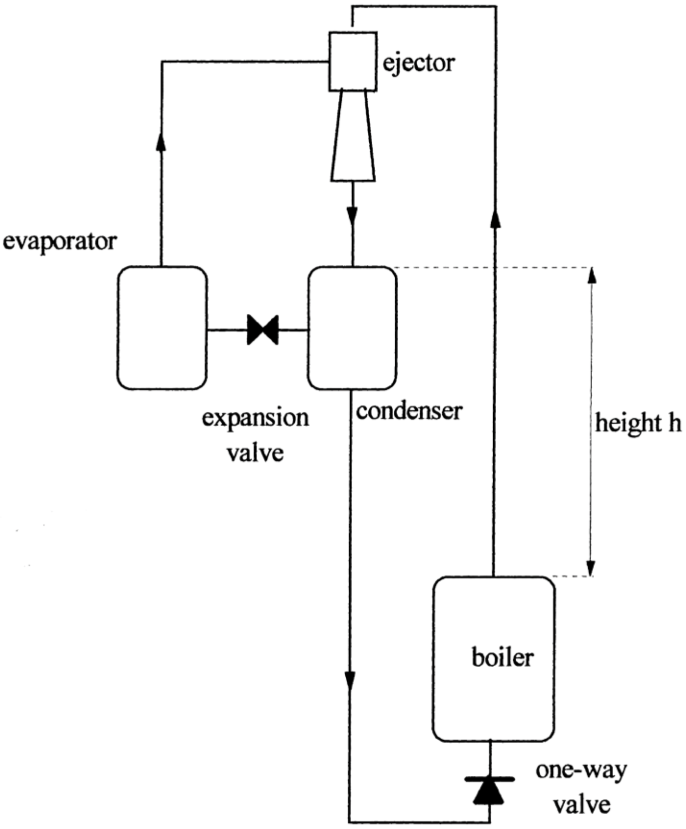

Figure 2.21 Pumpless ERS using gravity as the driving force [79].

The vertical distance (h) between the condenser and the boiler was about 7 m. The system achieved the COP up to 0.3. Despite of the clear advantages, the system has several drawbacks. Because of the configuration, the equipment requires a considerably larger space compared to conventional systems. In addition, the large system volume means large thermal inertia, which increases start-up and shut-down times to an impractical level. The cycle works under high levels of vacuum, which causes system failure every time that air leaks into the system.

Riffat and Holt [18] introduced a novel heat pipe/ejector cooler. The ejector is constructed of a heat pipe with internal wick (see Figure 2.22). The tube has high thermal conductivity, being filled with a refrigerant. As heat is applied to the generator section of the closed heat pipe, the refrigerant inside the wicked structure gains pressure. The refrigerant evaporates and expands though the primary nozzle. The expanded primary flow entrains the working fluid from the evaporator. The mixture from the ejector outlet reaches the condenser, where the heat is released from the cycle. The working fluid condensed on the pipe wall of the condenser section. The condensed refrigerant is absorbed back to the wicked pipe. Due to the wicked structure, the liquid refrigerant returns through the wick by capillary force to the generator section of the pipe. Using mathematical analysis, the authors emphasized the practicability of this cooling system. They claimed that the system could reach a high COP, (e.g., COP $\cong 0.4$ at $T_g = 80°\mathrm{C}$, $T_e = 10°\mathrm{C}$, $T_c = 28°\mathrm{C}$, ethanol as the working fluid).

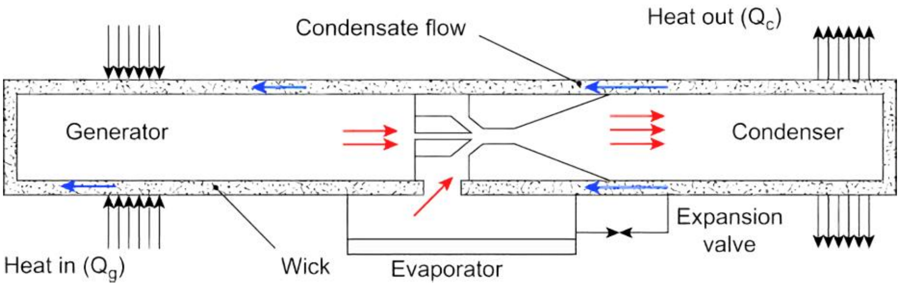

Figure 2.22 Pumpless ERS - heat pipe/ejector cooling system [18].

Another variant of pumpless ERS was proposed by Wang and Shen [80]. In their system, two ejectors were mounted at the inlet and outlet of the generator. The work was carried out was a theoretical approach; however, this concept has not been validated using experimentation.

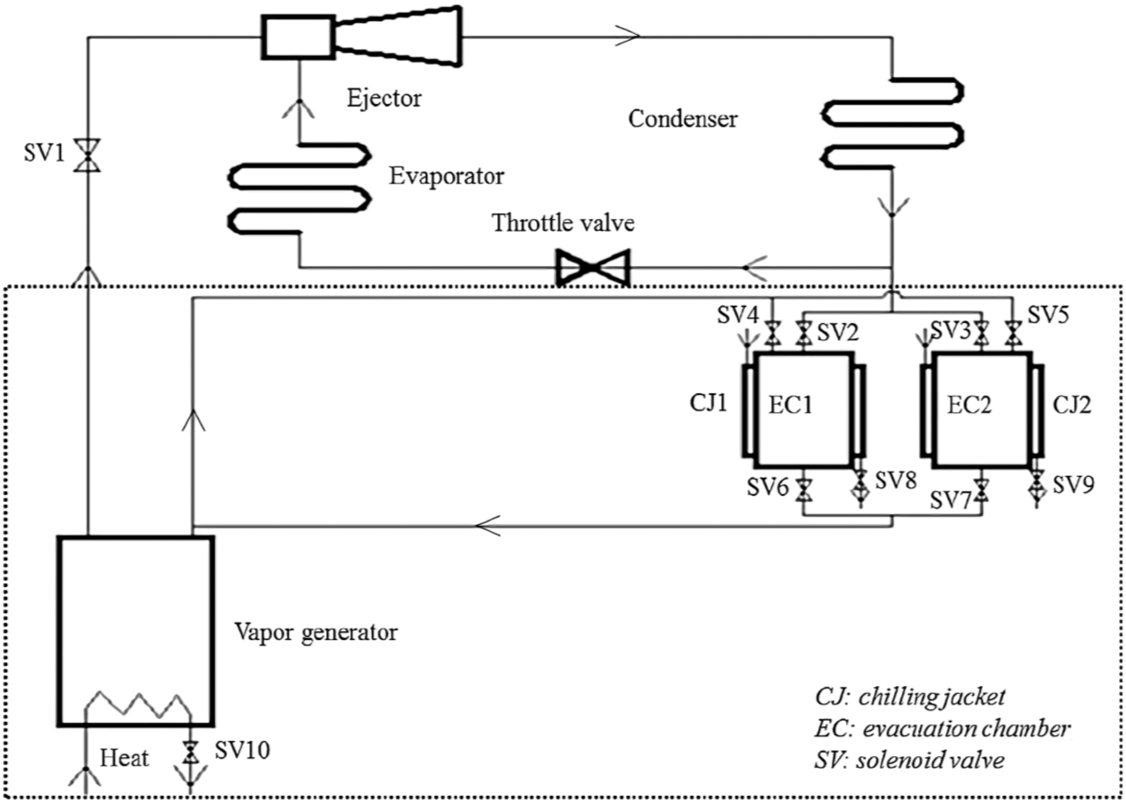

Figure 2.23 Schematic of double-evacuation-chambers ejector cooling system [81].

Ejector cooling system with thermal pumping effect is another interesting solution. Huang et al. [82] introduced a prototype using a multi-function generator to eliminate the need for a mechanical pump. The multi-function generator serves as both a pump and a vapor generator. The experimental results indicated that the coefficient of performance reached 0.185. Zhang and Cheng [81] used thermal pumping effect by applying two parallel evacuation chambers shown in Figure 2.23. The evacuation chambers were installed between the condenser and generator with a set of nine solenoid valves. By evacuating the refrigerant at the condenser outlet, the pressure at the ejector outlet can be reduced and thus, improving the ejector performance. Also, this configuration makes use of the heat from the ejector outlet flow and reduce the heat input to the generator. The study was based on mathematical modeling and was validated by experimental data from the works of Huang et al. [82] and Wu et al. [83]. The model developed was based on the mass and energy conservation laws without detailed mathematical description of the individual cycle components. The authors claimed that the average model predictions error for the entrainment ratio was only 2.7% in comparison with experimental results of Selvaraju and Mani [84] .

2.9.3 Absorption-ejector refrigeration system and adsorption-ejector refrigeration system

Other interesting hybrid solutions are the absorption-ejector refrigeration system and adsorption-ejector refrigeration system. These systems can be considered as two distinct cycles, an ejector cycle and an absorption/adsorption cycle. The coupling of an absorption/adsorption cycle to an ejector cycle tries to exploit the advantages of the two systems. It results in a higher temperature, lower pressure of adsorbent and increased system performance than the standard ERS. For examples, the increase of the COP up to 10% and 60% were reported in the absorption-ejector systems by Chen et al. [85], and Majdi [86], respectively. It is noted that all studies on this topic in the open literature are theoretical works [86–88] without experimental verification.

2.9.4 Compression-ejector refrigeration cycle

Sokolov and Hershgal [89–91] presented a mathematical and experimental study on a hybrid mechanical compressor and ejector cycle for air-conditioning. This cascade refrigeration system is composed of a compression cycle and an ejector cycle, which are linked together by an intercooler (Figure 2.24). The conventional vapor compression cycle transfers the heat from the evaporator to the intercooler; the heat is then transferred to the condenser by the ejector cycle. The indicated that the system operated with an electric COP of 6 using with R114 refrigerant and operating temperatures at the generator (T_g) of 98°C, and at the evaporator (T_e) of 8.8°C. The authors concluded that the proposed system is highly competitive due to its high efficiency, despite of any temperature fluctuation at the ejector primary inlet. However, coupling the ejector cycle with the vapor compression cycle can be challenging and may cause control issues, as reported in another study by Dorantes et al. [92].

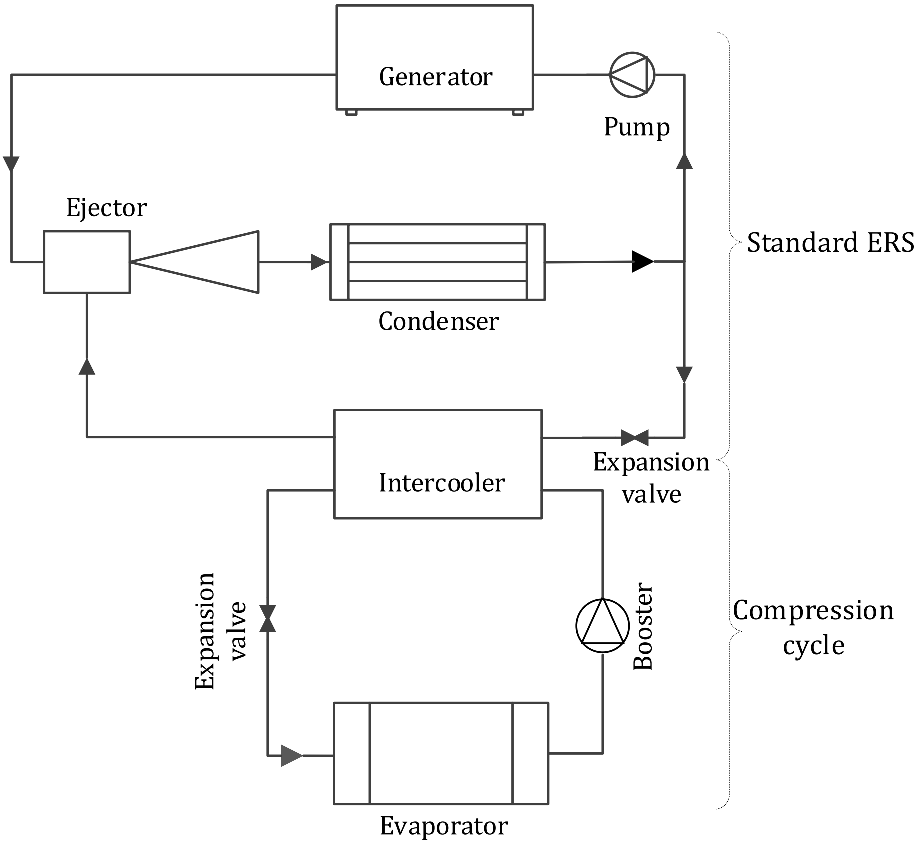

Figure 2.24 Schematic view of a compression enhanced ejector cooling system.

2.9.5 Multi-components ejector refrigeration system

Jianlin Yu et al. [93] introduced an ejector cooling system with an additional ejector, as shown in Figure 2.25. The pressurized liquid at the pump outlet is divided into two flows: one going to the generator (4A) and another going to the jet-pump ejector (4B). The secondary inlet for the jet-pump is the outlet stream from the conventional single-phase ejector. Based on mass, momentum, and energy conservation equations, a mathematical model was developed to study the system performance. Compared with the conventional configuration, the COP was improved up to 57% and 46% with R134a and R152a as the working fluids, respectively.

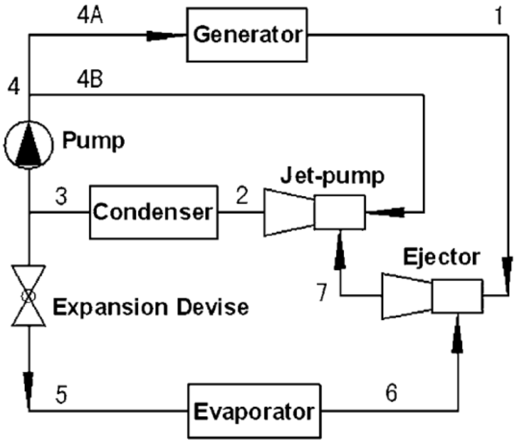

Figure 2.25 Schematic of ejector cooling cycle with an additional ejector [93].

Performance improvement of using multi-ejector systems was confirmed by a number of studies. Zhu et al. [94] claimed that their system outperformed the conventional ejector refrigeration cycle by 5.5% and 8.6% with R152a and R22 as working fluids, respectively. Wang et al. confirmed that their solution was able to reduce total energy consumption by up to 7.4% for nominal conditions [95]. Lin et al. [96] experimentally studied an ERS with one compressor, two ejectors, three evaporators, aiming for high performance at various evaporator temperatures. One of the ejectors is variable ejector, which maintains the primary inlet pressure in design value when the primary flowrate varies with the cooling load. However, the authors reported that the pressure recovery fails when the spindle blocks 50% or higher the cross-section area of the primary nozzle.

2.9.6 Transcritical refrigeration system with an ejector for expansion work recovery

A transcritical refrigeration system may use an ejector for expansion work recovery. Figure 2.26 shows the schematic view of a transcritical ejector cooling system and the corresponding pressure-specific enthalpy diagram. The major components are the compressor, gas cooler, ejector, gas separator, expansion valve, internal heat exchanger, and evaporator. The ejector is used to recover expansion work otherwise lost during the expansion process. Through the action of the ejector, the compressor suction pressure is higher than it would be in a standard cycle, resulting in required compression.

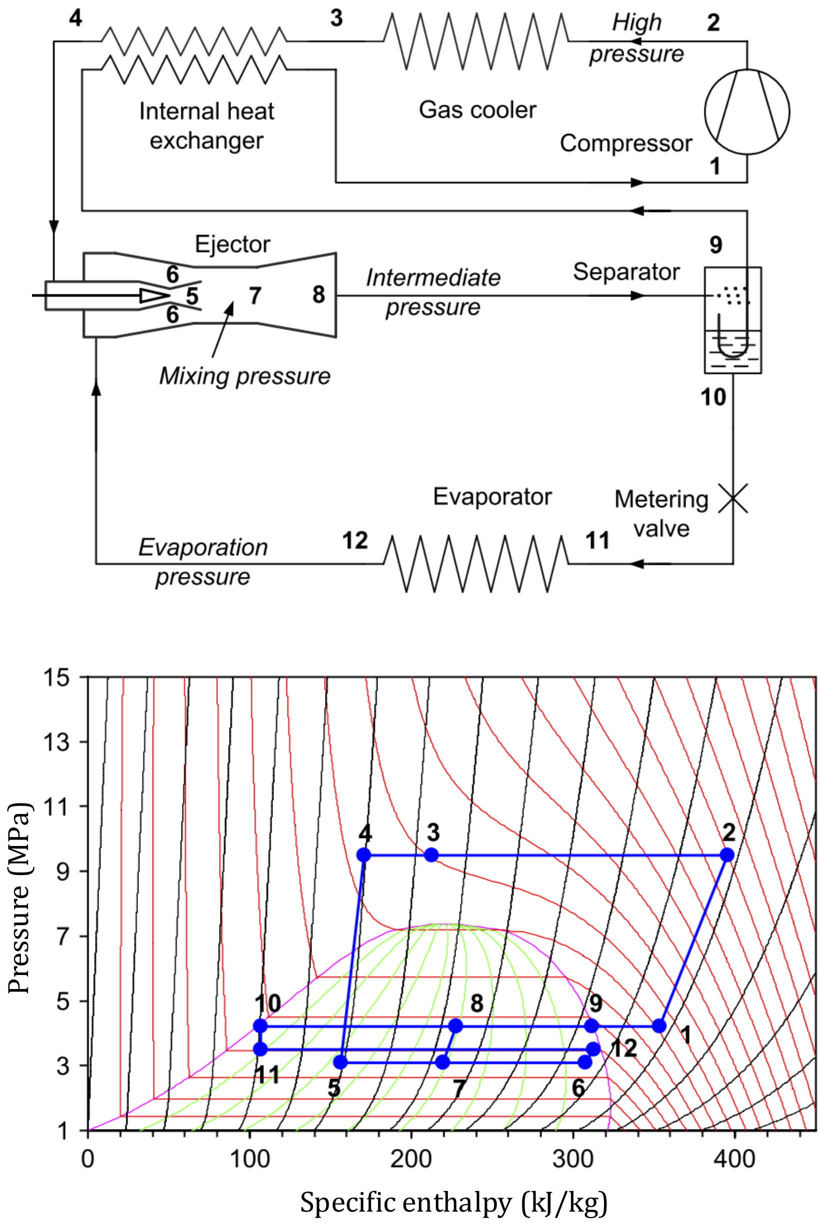

Figure 2.26 Schematic view of a transcritical CO2 ejector cycle (upper) and the corresponding pressure-specific enthalpy diagram (lower) [97].

The high-pressure refrigerant flow at the gas cooler outlet, is expanded to the wet vapor state as it passes the primary nozzle of the ejector, becoming the driving force to entrain and compress the vapor refrigerant from evaporator outlet. The flow inside the ejector is two-phase and phase-change processes occur along the flow path. A liquid/vapor separator is installed in order to separate the flow at the ejector outlet. The saturated vapor from the separator enters the internal heat exchanger and the compressor to become the ejector primary flow. The saturated liquid enters the expansion valve and evaporator and becomes the ejector secondary flow.

A theoretical study of Li and Groll [98] showed that the transcritical CO_2 refrigeration cycle with ejector-expansion device (EVCS) offered a 17% higher COP than the conventional transcritical compression cycle. Wang and Zhou [99] compared the performance of low critical temperature refrigerants, including CO_2, R143a, R32, R1270, using simulations. It was found that R1270 (Propylene) yielded the best performance amongst them. However, in practical applications carbon dioxide (CO_2) is usually preferred for transcritical EVCS, e.g. [99–101]. Danfoss (Denmark) is known as a pioneer in developing and applying transcritical ERS using CO_2. A transcritical CO_2 system was commercially operated since March 2007 in a small supermarket, and approximately 50 systems more were installed in the same year [102]. The systems showed desired reliability and energy consumption. Transcritical CO_2 consumed about 96% energy compared with a conventional compressor-based refrigeration system with R404a as the working fluid [102].

2.10 Overview of the refrigerants previously applied in ERS

The choice of the working fluid has a strong impact on the ejector design and other system components. Nevertheless, one of the advantages of ejector cooling is the relative freedom for the selection of the refrigerant, e.g. when compared to an absorption machine [75, 103]. This led to published studies applying a wide range of working fluids, Table 2.3 introduces some studies on ejector cooling technology with the use of various working fluids. It summarizes the operating conditions and system performance of each studies. A detailed discussion on the refrigerants used in ejector cooling technology is given in the following sections.

2.10.1 Natural refrigerants

Ammonia (R717) has high performance, better than R134a (HFC) and most CFCs [104]. An experimental study of Sankarlal and Mani [105] showed that R717 could work with a rather low-temperature source ($T_g = 60 \div 72°C$). The corresponding COP was $(0.1 - 0.21)$ for $T_c = 33°C, T_e = 10°C$. However, the use of ammonia is limited due to its high toxicity.

Water (R718) has been used as the working fluid in a number of studies on ERS, e.g. [25, 74, 106–108]. Water could be an attractive choice since it is highly available, zero-cost, non-toxic and environmentally friendly. However, the pressure levels in a system using water are well below the atmospheric pressures. Any air infiltration leads to system fault [79]. Some of the studies concluded that water did not yield desirable performance [70, 104]. The optimal area ratio of ejectors that uses water as the working fluid significantly varies with the operating temperatures [70, 108]. Also, R718 is not suitable for application where evaporator temperatures below 0°C are needed.

As mentioned before, carbon dioxide was usually used in transcritical refrigeration systems, where ejectors are used for expansion work recovery. Transcritical cycles using carbon dioxide achieve a favorable performance, with COPs of 3-5 [98, 109, 110]. Nevertheless, the system requires a robust construction since the ERS using carbon dioxide operates at high pressures, up to 12.4 MPa [97, 100, 111]; and the heat transfer process is challenging as the phase-change phenomenon of the working refrigerant does not occur in the gas cooler.

Hydrocarbon refrigerants (e.g., R290, R600 and R600a) are considered as suitable suitable substitutes for the halocarbons. Hydrocarbons have zero impact on the ozone layer, very low GWP, non-toxicity, good thermodynamic performance under moderate operating pressures. On the other hand, they are classified as flammable gases [112]. Thus, particular care must be taken when manipulating a system using a hydrocarbon fluid and specific safety measures must comply. There are several theoretical studies about hydrocarbons as working fluids for ERS, including the work of Pridasawas and Lundqvist [113], Petrenko and Volovyk [114], Roman and Hernandez [115]. According to their results, the performance of R290 and R600a are comparable with HFCs, e.g., R134a, R152a. Smierciew et al. [116] claimed that their system obtained the COP of $0.15 \div 0.2$ for low generator temperatures ($\sim 55 \div 63°C$) and $T_c = 24 - 34°C$. They suggested that ERS with R600a is competitive to absorption cooling since the required heat source temperature can stay below 80°C.

Pereira et al. [117] presented an experimental study on ERS with a variable geometry ejector using R600a. The work demonstrated that by adjusting the ejector geometry, the system was able to achieve near optimal performance for different ejector outlet pressures. Later, this unit was integrated into SERS for air-conditioning, which was believed as the first variable geometry ejector application working under real operating conditions [63]. The results showed good stability and performance of the system.

2.10.2 Synthetic refrigerants

Before the early 2000s, CFCs have been applied in several studies on ERS. For example, mathematical and experimental studies in [21, 76, 118] using R11, R12, R113. Despite of having a favorable performance, these refrigerants were abandoned due to their negative impact on the environment.

Hydrochlorofluorocarbons (HCFCs) and hydrofluorocarbons (HFCs) were frequently used in ejector refrigeration system because of their relatively high performance. HFCs are the most common refrigerants that can be found in both experimental units and commercial applications, including R134a, R410a, R245fa, and R407c. Without being exhaustive, R134a was used in a theoretical study by Khalil et al. [119] and in an experimental work by Yan and Cai [69]. R245fa was applied by Huang et al. [120] in their experimental work. Several studies using HCFCs can also be found in literature, such as the experimental study by Yapici [121] with R123, the theoretical work by Zhu and Jiang [94] using R22, and Huang et al. [33] applying R141b. Generally speaking, these working fluids yielded good system performance; however, due to their negative environmental impact, they will be phased out and eventually banned according to the current refrigerant regulation 517/ 2014 of the European Union [11].

Among HFCs, R134a and R152a are the most favorable refrigerants used in ERS. They provide high performances with all types of ERS technologies [75, 115, 122]. R134a is probably the most commonly used fluid in the refrigeration industry due to its high thermal performance[69, 123–125]. The major drawback of applying R134a is its high GWP index, which resulted in the phasing out by the latest refrigerant regulation, as mentioned previously. In contrast, R152a has a relatively low GWP index of 138 (based on AR5). This refrigerant yielded similar performance to R134a [52] or even slightly outperformed R134a under the same conditions [93, 126]. These both refrigerants are wet, thus require a certain amount of superheat at the ejector inlets.

HFOs are considered as the fourth-generation halogen refrigerants. They have zero OPD and extremely low GWP indexes. Some HFOs are still not widely available, e.g., R1234ze(e). Only a few studies on ejector refrigeration with HFOs as working fluid were found in the open literature. Fang et al. [127] presented an experimental study using R1234ze(e) for an ERS, which was originally designed for R134a. Replacing a working fluid to a system designed for another working fluid is also called as drop-in technique. According to the authors, system performance with replaced refrigerant was only slightly affected since important properties (e.g., working pressures, critical temperatures) of these refrigerants are not very different.

Table 2.3 Previously applied working fluids in ejector refrigeration and their operation characteristics.

Refrigerant	**Dry/wet**	**Method**	T_g (°C)	T_c (°C)	T_e (°C)	ΔT_{sup} (K)	***COP*** *(-)*	***CC*** *[kW]*
R717 [105]	dry	exp	60-72	30-36	5-15	-	0.1-0.21	-
R718 [128]	wet	exp	40-70	12-32	10	-	0.18-0.27	up to 0.7
R600a [63, 117]	dry	exp	87	29	6	5-15	0.2-0.31	1-2
R600 [129]	dry	the	60-200	40	10	-	0.05-0.32	-
R11 [130]	wet	the	60-90	30-35	-5-14	-	0.15-0.4	-
R113 [21]	dry	exp	65-100	42-50	5-18	-	0.1-0.2	-
R134a [68]	wet	exp	72-78	31	10	-	0.1-0.35	0.25-1.3
R152a [115]	wet	the	70-100	25-35	5-15	5	0.35-0.75	1
R245fa [131]	dry	exp	80-105	24-42	4-20	5-7	0.25-0.45	4-7
R141b [33]	dry	exp	90-100	30-32	6-8	-	0.5-0.6	10.5

2.11 The importance of superheating and subcooling of the working fluid at the ejector inlets and outlet

One of the issues concerning single-phase ejectors is the possibility of condensation during the expansion in the primary nozzle or in the mixing section. Generally speaking, condensation should be avoided, especially in the primary nozzle, in order to ensure stable system operation [106]. Thus, a certain degree of superheat at the primary inlet of the ejector is required [132, 133]. The amount of superheat of a working fluid is the temperature difference between its vapor temperature and its saturation temperature. The degree of superheating depends on refrigerant properties. Wet fluids require a higher value of superheating compared to dry or isentropic fluids [34]. Wang and Gao [61] presented a numerical work on the effect of superheat on the ejector performance in the range of 5-30 K and concluded that increasing the degree of superheat of the primary flow increased the entrainment ratio and system stability. Working with a mathematical model of ERS with R134a as working fluid, Khalil et al. [119] showed that when the degree of superheating varied from 0 to 15°C, , ER increased by 13.3% while COP remained essentially constant. Zegenhagen and Ziegler [134] experimentally proved that by increasing the superheat degree up to 14 K at the primary inlet using R134a , the entrainment ratio slightly increased. In contrast with a low level of superheat, phase-change may occur [135], especially at the outlet of the primary nozzle, where strong shockwaves occur. The refrigerant density intensively shifts between low to high as droplets are formed. The shear momentum can change abruptly, leading to instability. However, a very high-degree of superheating is also not recommended because it increases the heat input needed to drive the system without further increase of the entrainment ratio [61, 136].

Despite the significance of superheat on the system performance, few studies gave adequate attention to superheat. As can be seen in Table 2.3, only a few studies mentioned about superheat.

3 MATHEMATICAL MODEL OF THE EJECTOR COOLING CYCLE

In this chapter, the details of the developed mathematical model for the simulation of the ejector cooling cycle is presented. Specific models for the ejector and heat exchanger components were elaborated. The expansion valve and refrigerant pump were modeled by fundamental thermodynamic relations considering losses.

The mathematical model was implemented in the Engineering Equation Solver (EES) software (Fchart, USA). EES solves a set of linear and non-linear algebraic and differential equations. Unlike other widely used software packages in engineering,, equations in EES program may be entered in any order without effect on the solution [137]. Another key advantage of EES is the high accuracy database of thermodynamic and transport property database of hundreds of substances is integrated [137].

3.1 Ejector model

3.1.1 Assumptions of the ejector model

The ejector model of the current work was developed based on the Huang model [34], with two additional assumptions on the pressure and the superheating of primary and secondary inlet flows. The Huang model was discussed in Chapter 2, the two assumptions are: (i) The pressures of the secondary flow at the inlet (P_e) and at the nozzle exit cross-section ($P_{e,NO}$) are identical. This assumption is valid when the ejector steadily works at the critical regime. (ii) A certain degree of superheat at the ejector inlets are assumed in order to avoid the phase change during the processes in the ejector.

Figure 3.1 shows the schematic view of the current ejector model. Ejector inlet and outlet velocities at the two inlets (points G and E) and outlet (point D) of the ejector are neglectable.

Flow irreversibility inside the ejector tackled considering empirical efficiency constants from the literature. It was further assumed that ejector walls are adiabatic. The flow inside the ejector is steady and one dimension. The kinetic energy at the ejector inlets and outlet are negligible.

The hypothetical throat (2), where the secondary flow reaches sonic velocity, is assumed to be in the constant-area section, as shown in Figure 3.1. Downstream this location, the mixing process of the two inlet streams starts with a uniform pressure level and finishes at point 3. The shockwave of the mixed stream occurs at the end of the constant-area section (4).

The mathematical model assumed that the system works at a steady-state; transient operating conditions are not considered.

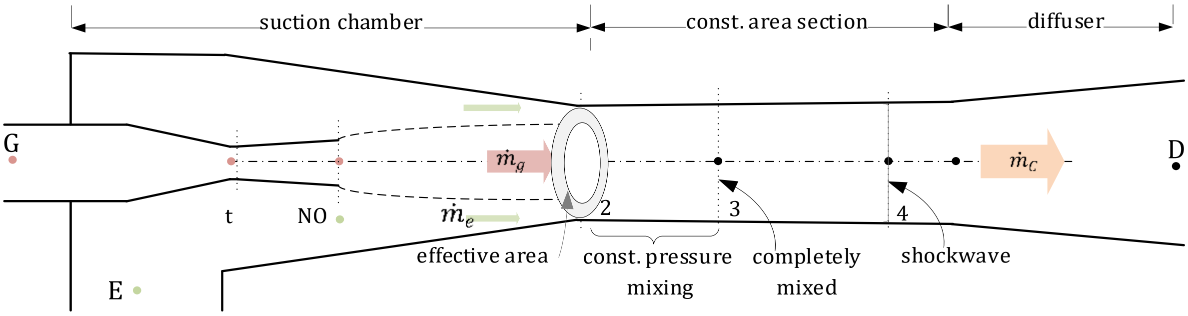

Figure 3.1 Schematic view of the current ejector model

3.1.2 The limitations of the mathematical ejector model

The ejector geometry acquired from the mathematical model the optimal geometry, which allows the ejector to operate at the critical point. The thermodynamic performance of selected refrigerants is compared under the same operating conditions, the mathematical model.

The energy losses in the ejector due to irreversible processes are accounted for by using empirical isentropic coefficients. The specific value of these coefficients may vary depending on the working fluid used, ejector geometry, operating conditions [37, 138]. In the developed model, fixed isentropic coefficients were applied for direct comparison.

The models of the heat exchangers were validated with the data found in the literature. The model was validated for separate components, i.e., ejector and heat exchangers.

3.1.3 Detailed description of the mathematical model

Figure 3.1 shows the different sections inside the ejector that were considered to formulate the problem. The fluid flow at these sections are governed by the conservation laws of mass (continuity), momentum, and energy that can be written as follows:

Continuity equation:

$$\sum\rho_i A_i v_i = \sum\rho_{i+1} A_{i+1} v_{i+1} \quad . \tag{3-1}$$

Linear momentum equation

$$p_i A_i + \sum\dot{m}_i v_i = p_{i+1} A_{i+1} + \sum\dot{m}_{i+1} v_{i+1} \quad . \tag{3-2}$$

Energy equation:

$$\sum\dot{m}_i\left(h_i + \frac{v_i^2}{2}\right) = \sum\dot{m}_{i+1}\left(h_{i+1} + \frac{v_{i+1}^2}{2}\right) \ . \tag{3-3}$$

In the equations above, p refers to the absolute pressure, ρ and h are fluid density and enthalpy. $\dot{m}$ and v are the mass flow rate and average fluid velocity, respectively. i is the location along the ejector axis.

3.1.3.1 Primary and secondary flow in the suction chamber

The primary mass flow rate through the nozzle throat under chocking condition is defined by the following ideal gas dynamic equation:

$$\dot{m}_g = A_t \frac{p_g}{\sqrt{T_g + T_{sup}}} \sqrt{\eta_t \frac{\kappa}{R}\left(\frac{2}{\kappa+1}\right)^{\frac{\kappa+1}{\kappa-1}}} \quad , \tag{3-4}$$

In equation (3-4), p_g is the primary inlet pressure and T_g is the saturation temperature at pressure p_g. T_{sup} is the degree of superheat in the primary flow. In the equation, constant η_t presents the isentropic efficiency of the primary nozzle. In equation (3-4), κ and R denote the heat capacity ratio and gas constant of the working fluid.

The relationship between the nozzle outlet area (A_{NO}) and throat area (A_t) is obtained by the following equation:

$$A_{NO} = (A_t/Ma_{NO})\left[\frac{2}{\kappa+1}\left(1 + \frac{\kappa-1}{2}Ma_{NO}^2\right)\right]^{\left(\frac{\kappa+1}{\kappa-1}\right)/2} \quad , \tag{3-5}$$

Ma_{NO} is the Mach number at the nozzle outlet.

The pressure at the nozzle outlet is a function of the primary inlet pressure (p_g) and Ma_{NO} by the following equation:

$$p_{NO} = p_g \left(1 + \frac{\kappa - 1}{2} Ma_{NO}^2\right)^{\frac{-\kappa}{\kappa-1}} \quad . \tag{3-6}$$

When the ejector works at the critical point (see Figure 2.9), the static pressure after the primary nozzle outlet ($p_{g_{NO}}$) is approximately equal to the secondary inlet pressure and the secondary stream at the same cross-section ($p_{e_{NO}}$) [15, 24, 28], as illustrated in Figure 2.10.

The pressure at the secondary inlet of the ejector (p_e) is at saturation state. Therefore, it can be obtained for a given working fluid by:

$$p_e = f\left(T_{e,sat}\right) . \tag{3-7}$$

3.1.3.2 Hypothetic throat

The secondary flow at the hypothetical throat (section 2 in Figure 3.1) is assumed to be choked under at critical mode [28]:

$$Ma_{e2} = 1 \; . \tag{3-8}$$

The secondary flow pressure at the hypothetical throat (p_{e2}) can be determined the following expression:

$$p_{e2} = p_e \left(1 + \frac{\kappa - 1}{2} Ma_{e2}^2\right)^{\frac{-\kappa}{\kappa-1}} \quad . \tag{3-9}$$

According to the constant pressure mixing assumption, the primary (p_{g2}) and secondary (p_{e2}) pressures at the hypothetical throat area taken as equal[28]

The cross-section area that the primary jet occupies at section 2 (A_{g2}) can be determined from the isentropic relation:

$$A_{g2} = \frac{\phi_p \, A_t}{Ma_{g2}} \left[\frac{2}{\kappa + 1}\left(1 + \frac{\kappa - 1}{2} Ma_{g2}^2\right)\right]^{\left(\frac{\kappa+1}{\kappa-1}\right)/2} \quad . \tag{3-10}$$

In equation (3-10), Ma_{g2} is Mach number of primary stream at section 2, and ϕ_p is the efficiency of the primary flow from the nozzle outlet to the hypothetic section.

From the required cooling capacity ($\dot{Q}_e$), an input parameter of the model, the secondary flow rate ($\dot{m}_e$) can be defined as

$$\dot{m}_e = \frac{\dot{Q}_e}{(h_e - h_v)} \ , \tag{3-11}$$

h_e in equation (3-11) is the enthalpy at the outlet of the evaporator and h_v is the enthaly at the outlet of the expansion valve. These parameters are called from the real gas database.

The hypothetical area of the secondary flow A_{e2} assuming choking can be calculated by:

$$\dot{m}_e = A_{e2} \frac{p_e}{\sqrt{T_e + T_{sup,e}}} \sqrt{\eta_e \frac{\kappa}{R} \left(\frac{2}{\kappa + 1}\right)^{\frac{\kappa+1}{\kappa-1}}} \ , \tag{3-12}$$

In equation (3-12), T_e and $T_{sup,e}$ are the saturation temperature of the working fluid and the applying degree of superheat, respectively. η_e is the isentropic efficiency defined for the entrained flow between points *E* and *2*.

The temperature of the primary flow at section 2 can be computed from the temperature at the primary inlet using:

$$T_{g2} = \frac{T_g + T_{sup}}{1 + \frac{\kappa - 1}{2} Ma_{g2}^2} \ . \tag{3-13}$$

Stream velocities at the hypothetical throat can be obtained as follows:

$$v_{g2} = Ma_{g2} \sqrt{\kappa R \ T_{g2}} \tag{3-14}$$

and

$$v_{e2} = Ma_{e2} \sqrt{\kappa R \ T_{e2}} \ . \tag{3-15}$$

The required cross-section area of constant area section ($A_2 = A_3$) is obtained by total of the two jet cross sections as:

$$A_2 = A_{g2} + A_{e2} \ . \tag{3-16}$$

3.1.3.3 The mixing process in the constant-area section

The mixing process takes place between section *2* and *3* at a constant and uniform pressure while the primary flow transfers kinetic energy to the secondary stream. The mixing process is assumed to be completed at section 3. The resulting flow is supersonic ($Ma_3 > 1$). The velocity of mixed flow (v_3) is calculated by the relation that was proposed by [139]:

$$v_3 = \left(v_{g2} + ER\ \ v_{e2}\right)\frac{\sqrt{\phi_3}}{1+ER}\ , \tag{3-17}$$

Φ_3 is the isentropic efficiency of the mixing process.

The Mach number at section *3* is given by:

$$Ma_3 = \frac{v_3}{\sqrt{\kappa\ R\ T_3}}\ . \tag{3-18}$$

The temperature of mixed flow (T_3) is obtained by applying the energy balance between section *2* and *3*:

$$\begin{aligned}\left(\dot{m}_g + \dot{m}_e\right)\left(T_3\ c_{p_3} + \frac{v_3^2}{2}\right) \\ = \dot{m}_g\left(T_{g2}\ \ c_{p_{g2}} + \frac{v_{g2}^2}{2}\right) + \dot{m}_e\left(T_{e2}\ \ c_{p_{e2}} + \frac{v_{e2}^2}{2}\right)\ .\end{aligned} \tag{3-19}$$

3.1.3.4 Normal shockwave

The mixed flow is assumed to undergo a normal shockwave between section 3 and 4. The shockwave occurs along an infinitely short ejector length accompanied by a sudden change of the fluid properties such as pressure, temperature, velocity, and density.

The mathematical relationship between the static pressure before and after the shockwave (p_3 and p_4) can be written as:

$$p_4 = p_{g2}\left(1 + \frac{2}{\kappa+1}\ \kappa\ (Ma_3^2 - 1)\right)\ , \tag{3-20}$$

In equation (3-20) it is considered that $p_3 = p_{g2}$

The Mach number after the shockwave has relation is given Ma_3 by:

$$Ma_4 = \sqrt{\frac{1 + \frac{\kappa-1}{2}Ma_3^2}{\kappa\ Ma_3^2 - \frac{\kappa-1}{2}}}\ . \tag{3-21}$$

3.1.3.5 Ejector diffuser section

Assuming that the process of mixed flow through the diffuser is an isentropic process with accounting an isentropic coefficient of the diffuser section η_D, the pressure at the exit of the diffuser p_D is defined by:

$$p_D = p_4 \left(1 + \eta_D \frac{\kappa - 1}{2} Ma_4^2\right)^{\frac{\kappa}{\kappa - 1}} \quad . \tag{3-22}$$

3.2 Heat exchangers

Heat exchangers are important components of the ejector refrigeration cycle. The performance of heat exchangers could influence the overall performance of the ejector cooling system. The pressure variations drop in the condenser, generator and evaporator influences ejector inlet and outlet conditions and thus the entrainment ratio which is directly related to the cycle COP (see equation (2-3).

3.2.1 Heat exchanger model assumptions

Both sensible and latent heat transfer occurs in the heat exchangers on the working fluid side. It is common practice to model these processes separately in order to simplify their model description. The actual thermophysical properties of the refrigerant vary along the heat exchanger length, primarily depending on local temperature, pressure, vapor quality and heat transfer coefficient. In the simplified approach, the heat exchanger is treated by considering three distinct sections along the heat exchanger length: sensible heat exchange in gas phase, latent heat exchange and sensible heat transfer in liquid phase.

Each section of the heat exchanger is treated as an individual heat exchanger connected in series. In the model, appropriate correlations are applied to each. The correlations were selected according to the flow properties and thermo-physical properties of the working fluid. This approach is illustrated in Figure 3.2 for the generator. In the figure, $L_{v,l}$, $L_{v,tp}$, and $L_{v,va}$ represent the heat exchanger length of the liquid, two-phase, and vapor sections, respectively. The two-phase process occurs in the two-phase section, where the saturated liquid refrigerant changes to saturated vapor. The added heat to the refrigerant is in the latent form. The refrigerant temperature does not vary in the process. The temperature refrigerant is called the saturation temperature, which is a function of the working pressure and the working fluid. On the contrary, the absorbed heat in the two single-phase processes results in the temperature gain of the refrigerant in the liquid-phase and vapor-phase section (see the temperature-entropy diagram in Figure 3.2). The accumulated thermal energy is in the form of sensitive heat.

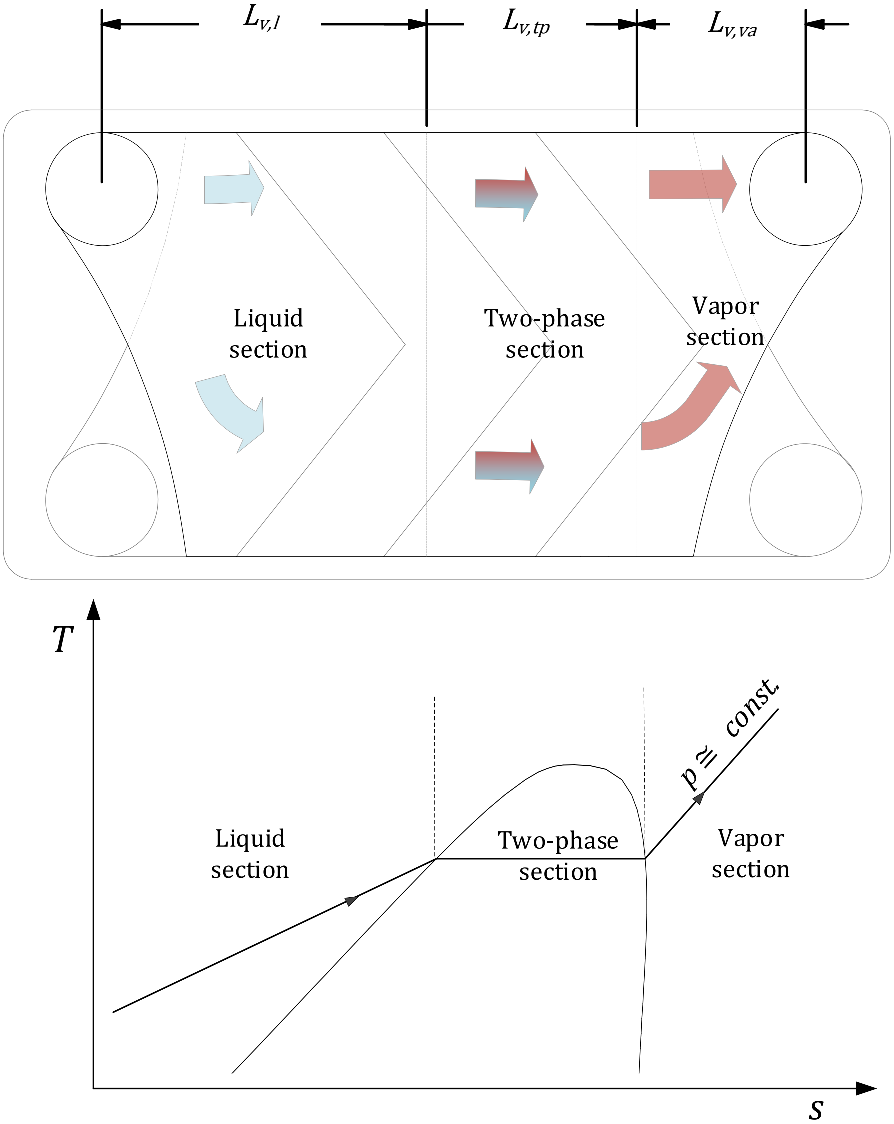

Figure 3.2 Illustration of the considered hypothetical heat exchanger sections for the generator.

Also, two other major assumptions considered during the development of the model: (i) steady-state operation and (ii) no heat loss to the environment.

3.2.2 Overall heat exchanger energy balance

Under steady-state conditions, the first law of thermodynamics can be written as:

$$\dot{Q} = \dot{m}_h(h_{h_{in}} - h_{h_{out}}) = \dot{m}_{co}\left(h_{co_{out}} - h_{co_{in}}\right) . \qquad (3\text{-}23)$$

In equation (3-23), $h_{h_{in}}$ and $h_{h_{out}}$ are the inlet and outlet enthalpies of the hot fluid; $h_{c_{in}}$ and $h_{c_{out}}$ are the inlet and outlet enthalpies at the inlet and outlet of the cold fluid, respectively.

3.2.3 Mathematical description of the heat exchanger plate geometry

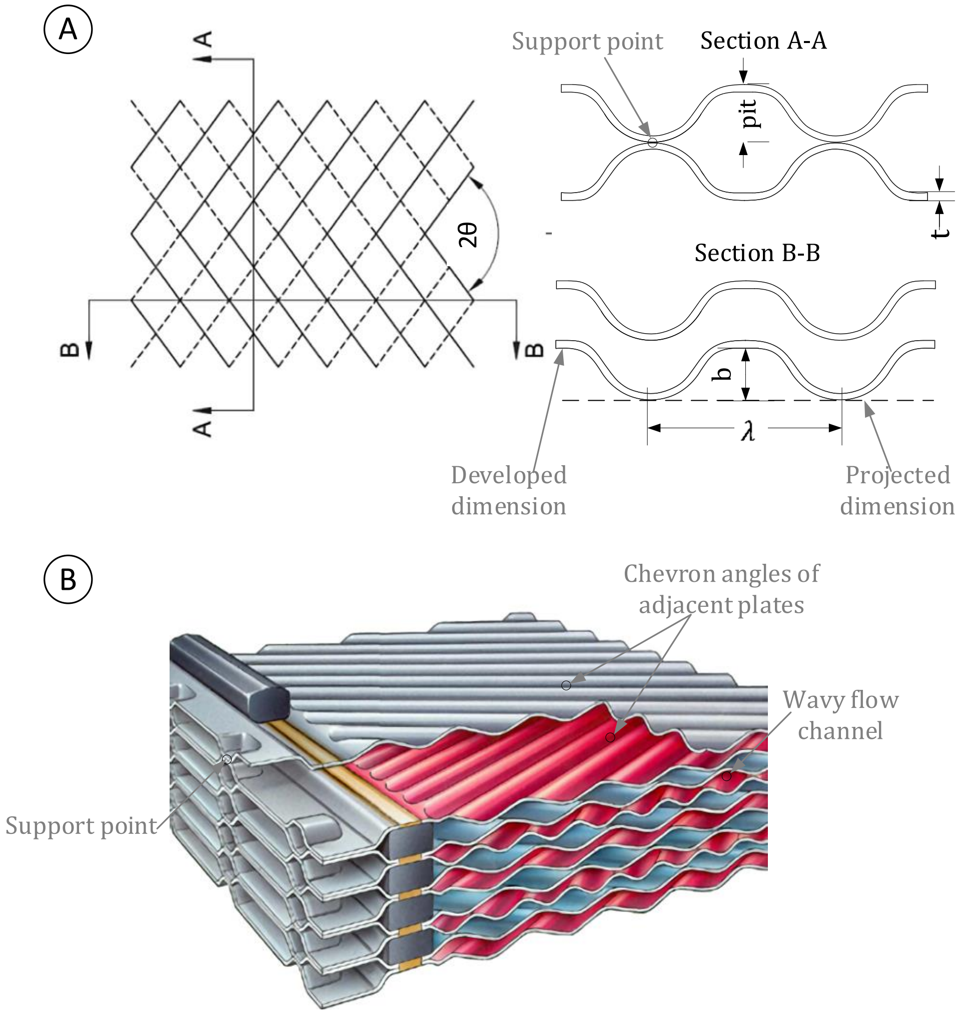

Figure 3.3 Schematic 2D view of chevron corrugated plate heat exchanger (a) and corresponding 3D model (b)[44].

Plates are available in a wide range of corrugation types on the market; however, the chevron type is perhaps the most common. Adjacent chevron plates are reversely assembled, resulting in two key characteristics. First, the plates are clamped together with many support points, as illustrated in section A-A in Figure 3.3a. These points ensure increased mechanical resistance with reduced plate thicknesses (t) when compared with other corrugation types. Second, the generated flow channels have a wavy shape, as shown in cross-section B-B in Figure 3.3, so that the flow between the plates is highly swirled, and turbulent even for low flow velocities leading to up to five times higher Nusselt numbers compared to flat-plate channels [19]. It should be noted that the pressure drop is also higher, 1.3 - 44 times higher than in flat-plate channels [19], thus optimal design should be selected depending in the requirements of a given application.

The heat transfer coefficient depends on many factors including: the surface enlargement (ϕ_{pl}), corrugation profile, gap (b), the chevron corrugation angle (θ), size of chevron pitch (λ), plate thickness (t), and others. The geometrical factors are shown in Figure 3.3.

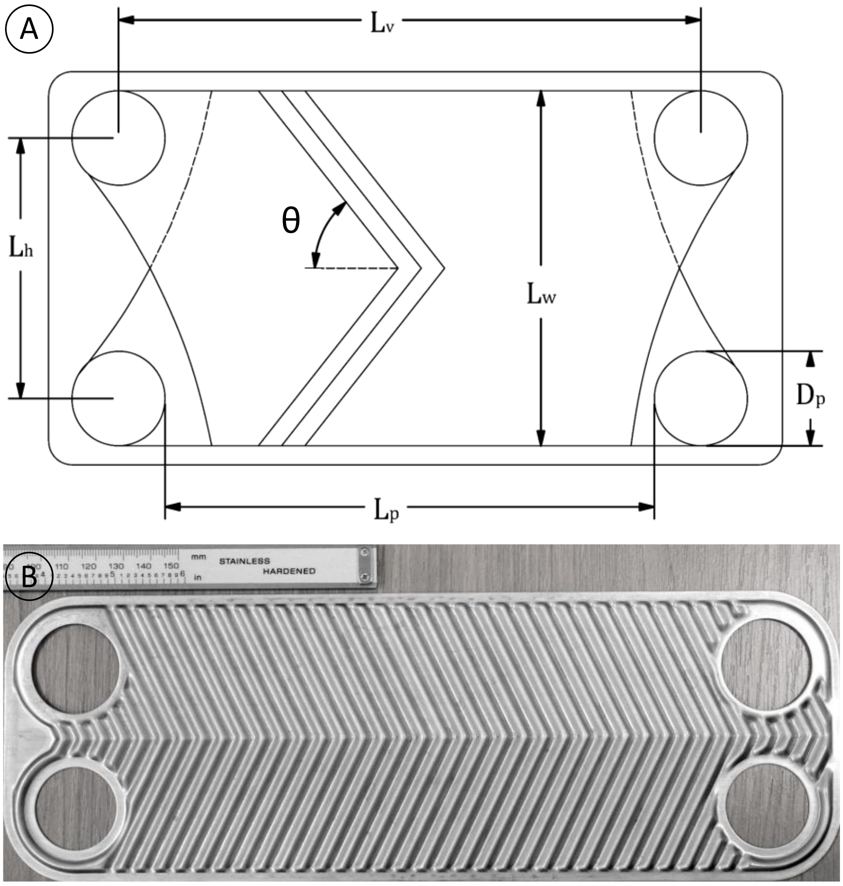

Figure 3.4 Schematic view with the basic dimensions and the photograph actual chevron plate considered in the thesis.

Figure 3.4 shows the basic geometry of a chevron corrugated plate. The surface enlargement factor of the plate (ϕ_{pl}) is defined as the ratio of the real heat transfer area (A) to the projected are (A') as:

$$\phi_{pl} = \frac{A}{A'} \ . \tag{3-24}$$

A is typically given by the plate manufacturer. A' is approximately the product of the port distance L_p and the plate width L_w, and it can be determined from:

$$A' = L_p\, L_w \cong (L_v - D_p)(L_h + D_p) \ . \tag{3-25}$$

Chevron corrugated plate is characterized by the dimensionless parameter (X) that is defined as:

$$X = \frac{\Lambda}{\lambda} = \frac{2\pi\, b}{\lambda} \ . \tag{3-26}$$

In equation (3-26), the ratio of developed dimension (Λ) being the circle circumference with radius b is the projected dimension of the corrugated area. Parameters λ and b are illustrated in Figure 3.3. X can be applied to determine the surface enlargement factor as [17]:

$$\phi_{pl} \cong \frac{1 + (1 + X^2)^{0.5} + 4\left(1 + \frac{X^2}{2}\right)^{0.5}}{6} \ . \tag{3-27}$$

The channel hydraulic diameter (D_h) is defined by:

$$D_h = \frac{4\, b\, L_w}{2\left(b + L_w\, \phi_{pl}\right)} \ . \tag{3-28}$$

Finally, the number of channels per pass (N_{cp}) is given by:

$$N_{cp} = \frac{N_{pl} - 1}{2N_p} \ . \tag{3-29}$$

In equation (3-29), N_p is the number of passes. The present mathematical model was developed for a single pass ($N_p = 1$) configuration for all ejector cycle heat exchanges.

3.2.4 Definition of the chevron corrugated dimensionless numbers

Dimensionless numbers provide a physical understanding of the essential characters of the flows in heat exchangers [140]. They also permit to simplify the governing equations by reducing the number of total variables [141, 142].

3.2.4.1 Reynolds number

The Reynolds number is the ratio of the inertia forces to the viscous forces of the fluid and it is defined as:

$$Re = \frac{\text{inertia forces}}{\text{viscous forces}} = \frac{\rho\ \mathrm{v}\ L_c}{\mu}\ , \tag{3-30}$$

L_c is the characteristic length, μ is the dynamic viscosity, v is the average velocity of the fluid.

The Reynolds number is used to characterize the flow regime. Flow in PHE reaches a turbulent state at a relatively low Reynolds numbers in the range of 10 to 400. The Reynolds number can also be expressed as a function of by the mass velocity (G) as:

$$Re = \frac{G\ D_h}{\mu}\ , \tag{3-31}$$

3.2.4.2 Nusselt number

The Nusselt number (Nu) is the ratio of convection to conduction heat transfer at a boundary in the fluid boundary layer [17, 19]

$$Nu = \frac{\text{convection heat transfer}}{\text{conduction heat transfer}} = \frac{he\ D_h}{k}\ . \tag{3-32}$$

In equation (3-32), he is the film coefficient $(W \cdot m^{-2} \cdot K^{-1})$ and k is the thermal conductivity of the fluid. D_h is the characteristic length, which is channel hydraulic diameter of the heat exchanger in this case.

A Nusselt number of value 1 represents heat transfer across the boundary layer by pure conduction. A larger Nusselt number indicates more dominating effective convection over the conduction.

3.2.4.3 Prandtl number

Prandtl number is the ratio of kinetic viscosity (ϑ) (momentum diffusivity) to the thermal diffusivity (α).

$$Pr = \frac{\vartheta}{\alpha} \ . \tag{3-33}$$

Heat of the working fluid diffuses quickly if Pr is less than 1, and slowly if Pr is greater than 1.

3.2.4.4 Bond number

Bond number (Bd or Eotvos number) is used to measure the importance of gravitational forces compared to surface tension forces in two-phase flows. It is defined as:

$$Bd = \frac{\Delta\rho \ Gra \ L_c^2}{\gamma} \ . \tag{3-34}$$

In equation (3-34), $\Delta\rho$ is the density difference of the two phases, Gra is gravitational acceleration, γ is surface tension.

If Bd < 4, the heat exchanger channel is considered as microscale; if Bd ≥ 4, as macroscale [143, 144]. Accordingly, an appropriate correlation is applied to estimate the two-phase Nusselt number.

3.2.4.5 Boiling number

Boiling number (Bo) is used to account for the effect of the heat flux, mass flux, and latent heat on the heat transfer rate in the phase-change process of the refrigerant. The boiling number is defined as used in the phase-change process of the refrigerant:

$$Bo = \frac{q_{r,tp}}{G \ h_{lv}} \ . \tag{3-35}$$

In equation (3-35) $q_{r,tp}$ is the heat flux, of the refrigerant in the two-phase section. h_{lv} is the latent heat required of vaporization of the refrigerant.

3.2.4.6 Weber number

Weber number is a dimensionless number used in analyzing interacting flows of two different fluids (or phases of a single fluid) that interfere with each other. Weber number is the ratio between the inertial (kinetic) force and the surface tension force of the two-phase flow. It indicates whether the kinetic or the surface tension energy is dominant. The homogenous Weber number (We_m) is defined by:

$$We_m = \frac{\mathrm{G}^2 \ d_h}{\gamma \ \rho_m} \ . \tag{3-36}$$

The homogeneous density (ρ_m) is calculated from the vapor quality (x_{qua}), the density of saturated vapor ($\rho_{sat.va}$) and the saturated liquid ($\rho_{sat.liq}$) as follow:

$$\rho_m = \left(\frac{x_{qua}}{\rho_{sat.vap}} + \frac{1 - x_{qua}}{\rho_{sat.liq}}\right)^{-1}, \tag{3-37}$$

3.2.4.7 Fanning friction factor

Fanning friction factor (f) is the ratio between the local shear stress and the local kinetic energy density as:

$$f = \frac{2\tau}{\rho\, \mathrm{v}^2}, \tag{3-38}$$

v is the average flow velocity, and τ is the local shear stress.

3.2.5 Brief review of existing heat exchangers models

The heat transfer efficiency and pressure drop of flow in heat exchangers are functions of many factors. A number of empirical correlations are proposed in the literature, resulting from experimental data obtained under a well-defined range of operating conditions. The validity of these correlations is, therefore, limited to cases within these conditions. The following subsections provide a short review of published correlations, with the intuition to select the most suitable correlations for the ejector cycle heat exchangers.

3.2.5.1 Single-phase heat transfer

Several sensible heat transfer and pressure drop correlations for plate heat exchangers can be found in the open literature, e.g. [145–147]. Kumar [145] introduced the first empirical correlations for plate heat exchangers, which was considered in many later studies. The author proposed various correlations to cover wide range of operating conditions. In later work, Neagu et al. [148] experimentally validated the correlations by Kumar [145] and Muley [147] with many working fluids at various operating pressures and flow rates. It was concluded that the correlations by Kumar significantly overpredicted the pressure drop, up to 191%. Experimental validations by Akturk et al. [149] came to a similar conclusion. Besides, Kumar’s model considerably underestimates the heat transfer coefficient. The reasons may be that Kumar’s model does not account for geometrical details of the plate, as the corrugation pitch and the surface enlargement factor.

Muley and Manglik [147] proposed correlations for the heat transfer coefficient (he) and pressure drop (ΔP) for heat exchangers with chevron angle of 30° and 60°, and Reynolds numbers in the range of 30÷1000. Surface enlargement factor and viscosity ratio were also considered in the correlations. Muley's correlations [147] were validated in [148, 150, 151]for a wide range of geometry configurations and flow conditions. These correlations were experimentally proved to be suitable for predicting single-phase process in plate heat exchanger. For example, Nusselt number correlation by Muley's model was about 114% error [144]; the predicted error of the pressure drop was -2%÷11.7% [149].

3.2.5.2 Empirical correlations during the phase-change

Amalfi [144] employed a high-precision experimental setup using high-resolution infrared cameras to measure the heat transfer coefficient and pressure drop during phase-change in PHEs. Thousands of measurements on a wide range of test conditions and plate geometry configurations were performed, e.g., chevron angles from 27° to 70°, phase-change temperatures from -25°C to 39°C, various working fluids, and mass fluxes were performed. The author claimed that the developed correlation approximated the experimental pressure drop data with a maximum and relative error of ± 30%, and 10%, respectively. The Nusselt number correlation during phase-change predicted 92.3% of total data points within ± 50% error, mean absolute error of 22.1%, as shown in Figure 3.6.

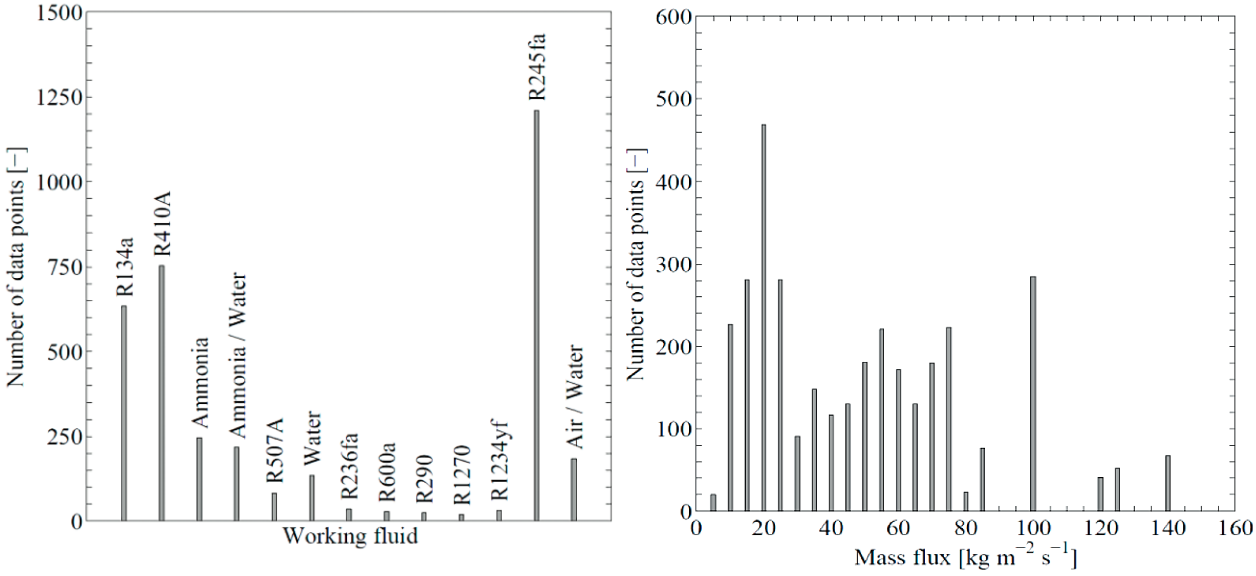

Figure 3.5 Mass flux distribution and working fluids used and working fluids used in the experimental study of Amalfi [144].

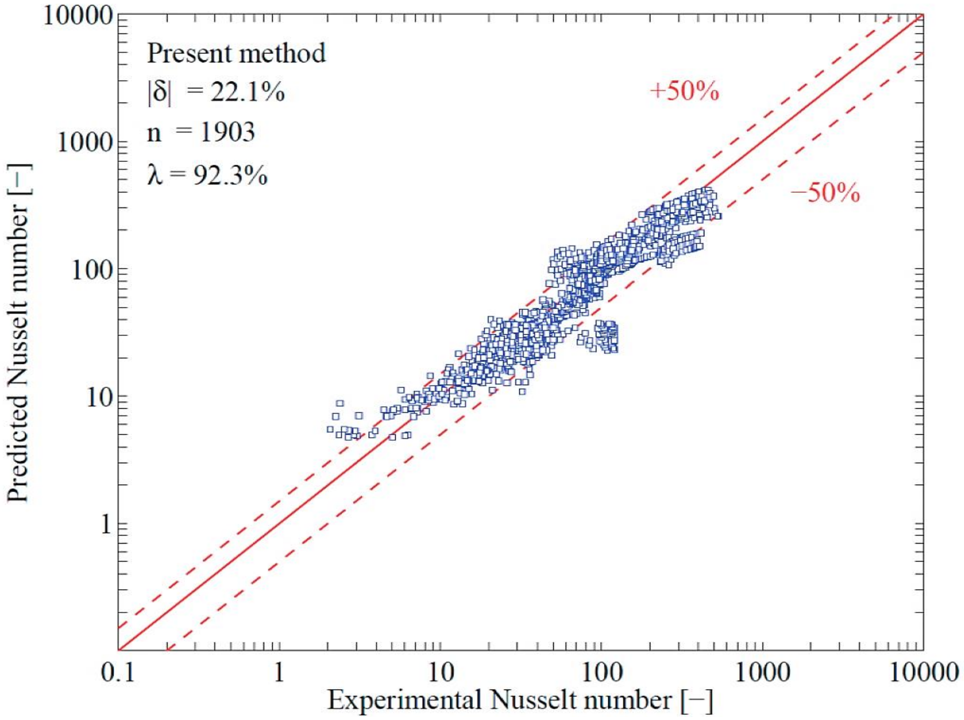

Figure 3.6 Predicted against experimental Nusselt numbers during the phase-change by Amalfi [144].

The later work of Tao and Ferreira [152] developed correlations of he and ΔP of the condensation process in PHEs These correlation were based on a large experimental dataset using various working fluids, including HFCs, HCs, HFOs, at a wide range of mass flow rates, chevron angles. The correlations of the work well agreed with Amalfi correlations [144]

In this thesis, the correlations of Muley [147] and Amalfi [144] were adapted for single-phase and phase change process, respectively.

3.2.6 Heat transfer analysis of plate type heat exchangers

3.2.6.1 Heat transfer analysis methods

The two commonly used methods for heat transfer analysis are the LMTD and the effectiveness-NTU methods. Whichever is the best suited for a given analysis depends on the available input. The application of the LMTD method is preferred when the inlet and outlet temperatures and flow rates are known. In contrast, when the outlet temperatures are unknown, the effectiveness-NTU method is preferred, because of its ability to predict these temperatures without using an iterative procedure.

LMTD method is based on the calculation of the logarithmic mean temperature difference between the hot and cold sides of the exchanger. In the developed model, it was assumed that the temperature at the heat exchanger inlets and outlet are known. Therefore, the LMTD method was selected. For more details on the effectiveness-NTU method, the reader is referred to [19]

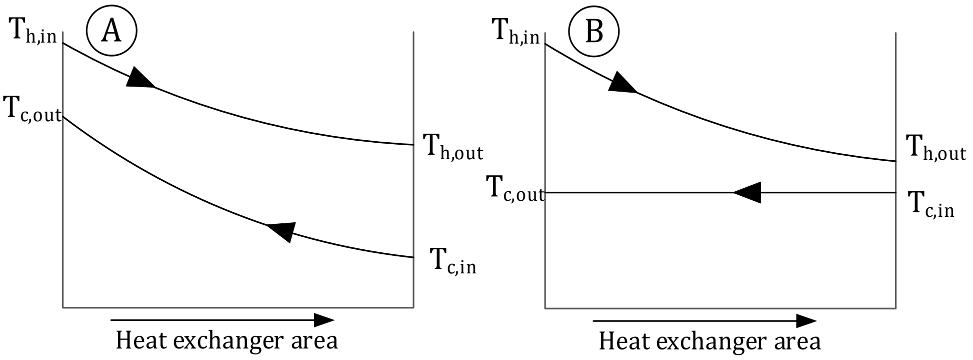

Figure 3.7 Temperature profiles inside a counter-flow heat exchangers for sensible heat transfer (a) and with phase-change on the cold side (evaporation) (b)

Figure 3.7a illustrates the temperature profiles inside a counter-flow heat exchanger undergoing sensible transfer only. Figure 3.7b illustrates the temperature profiles when the cold stream undergoes phase-change, namely evaporation. When the hot stream undergoes the phase-change from vapor to liquid state (at the condenser), it is called condensation. A detailed modeling of the three heat exchangers in the ejector cooling system are presented in the Appendices. The logarithmic mean temperature difference calculated depending on whether sensible or latent heat occurs in the heat exchanger. Without phase-change, the LMTD is calculated as follows [45]:

$$LMTD_{sg} = \frac{\left(T_{h,out} - T_{co,in}\right) - \left(T_{h,out} - T_{co,out}\right)}{ln\left(\frac{T_{h,out} - T_{co,in}}{T_{h,out} - T_{co,out}}\right)} \, . \qquad (3\text{-}39)$$

In case of latent heat transfer, LMTD is given by [45]:

$$LMTD_{tp} = \frac{T_{h,in} - T_{h,out}}{ln\left(\frac{T_{co,tp} - T_{h,in}}{T_{co,tp} - T_{h,out}}\right)} \, . \qquad (3\text{-}40)$$

The heat transfer rate between the hot and the cold stream can be calculated by:

$$\dot{Q} = U \cdot A \cdot LMTD \tag{3-41}$$

3.2.6.2 Heat transfer analysis in a heat exchanger with simultaneous latent and sensible heat transfer

In heat exchangers where both sensible and latent heat transfer occurs can be modeled by the total heat transfer area of three sections: liquid section, two-phase section, and superheated vapor section. These sections are modeled separately as individual units connected in series [19].

In this section, the procedure applied for the vapor generator is presented as an example. In the generator of the ejector cooling cycle, heat is transferred from the hot fluid (for example, water) to the refrigerant. The temperature profiles of the hot and cold streams along the generator length (also called heat exchanger area) are shown in Figure 3.8. Assuming no thermal losses to the environment, the heat transferred from the hot stream to the refrigerant is given by:

$$\dot{Q}_g = \dot{m}_w \left(h_{w,in} - h_{w,out}\right) \; ; \tag{3-42}$$

$\dot{m}_w$ is the mass flow rate of hot water, and $\left(h_{w,in} - h_{w,out}\right)$ is the enthalpy difference between the inlet and outlet. The total generator heat ($\dot{Q}_g$) transferred between the two streams can be considered the sum of the individual heat rates corresponding to the sections where the refrigerant is liquid, two-phase, and vapor states as:

$$\dot{Q}_g = \dot{Q}_l + \dot{Q}_{tp} + \dot{Q}_{va} \; . \tag{3-43}$$

The energy balance can be applied to compute the temperatures at the inlet and outlet of each section. On the hot side, the heat transfer fluid usually is in the liquid phase thus, assuming constant specific heat capacity. The heat flow within each section is function of the temperature variation as:

$$\dot{Q}_l = \dot{m}_w \, c_{p,l} \left(T_{w,tp,out} - T_{w,out}\right) \tag{3-44}$$

$$\dot{Q}_{tp} = \dot{m}_w \, c_{p,w,tp} \left(T_{w,tp,in} - T_{w,tp,out}\right) \tag{3-45}$$

$$\dot{Q}_{va} = \dot{m}_w \, c_{p,w,va} \left(T_{w,in} - T_{w,tp,in}\right) \; . \tag{3-46}$$

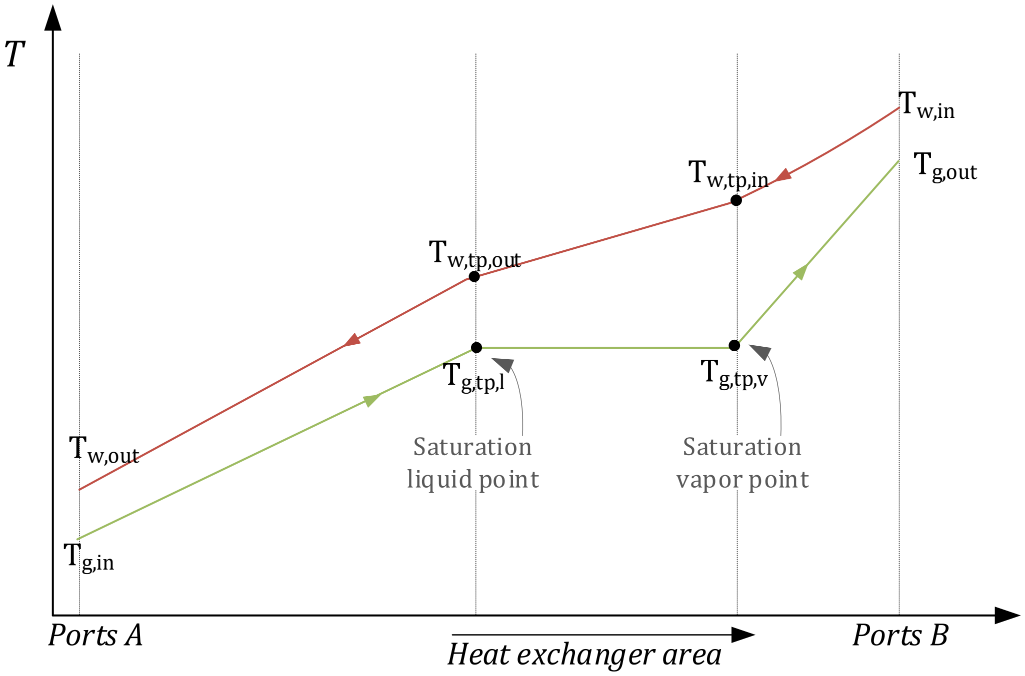

Figure 3.8 Temperature profiles in a counter-flow generator.

On the refrigerant side the heat is given by:

$$\dot{Q}_l = \dot{m}_g\left(h_{g,tp,l} - h_{g,in}\right) \tag{3-47}$$

$$\dot{Q}_{tp} = \dot{m}_g\left(h_{g,tp,v} - h_{g,tp,l}\right) \tag{3-48}$$

$$\dot{Q}_{va} = \dot{m}_g\left(h_{g,out} - h_{g,tp,v}\right) \ . \tag{3-49}$$

where $h_{g,in}$ and $h_{g,out}$ are the enthalpies of the primary flow at and generator inlet and outlet. $h_{g,tp,l}$, and $h_{g,tp,v}$ are the refrigerant enthalpies of saturation liquid and saturation vapor.

3.2.6.3 Empirical correlations for single-phase heat transfer in plate type HEX

The heat transfer in plate heat exchanger depends on a number of factors, including the chevron angle (θ), the surface enlargement factor, corrugation profile, and the gap b. The selection of suitable correlations in this particular application was discussed in section 3.2.5. For the developed model, the selected empirical were based on the expected working conditions. The procedure applied for the vapor generator is presented as an example.

For Reynold number less than 400 and 30° $< \beta < 60°$, Nusselt number by Muley correlation [19, 147] is:

$$Nu = 0.44\left(\frac{\beta}{30}\right)^{0.38} \; Re^{0.5}\, Pr^{\frac{1}{3}} \;, \tag{3-50}$$

Under the operating conditions considered, preliminary results indicated that the Reynolds number in the liquid section of the heat exchanger is always below 400. In contrast, the Reynolds number in the vapor section is greater than 1000. Thus, the Mulley correlation implemented was:

$$\begin{aligned} Nu = \; & (2.668 - 0.006967\beta + 7.244 \times 10^{-5}\,\beta^2) \\ & \times \left(20.78 - 50.94\phi_{pl} + 41.16{\phi_{pl}}^2 - 10.51{\phi_{pl}}^3\right) \\ & \times \; {Re_{g,va}}^{\left(0.728+0.0543\times sin\left(\pi\frac{\beta}{45}+3.7\right)\right)}\, {Pr_{g,va}}^{\frac{1}{3}} \left(\frac{\mu_w}{\mu_{ce}}\right)^{0.14} \end{aligned} \tag{3-51}$$

The correlation is valid for *Re* > 10^3, 30° < β < 60°.

In equation (3-51), $\phi_{pl,g}$ is the plate expansion ratio, usually less than 1.5. The viscosity ratio μ_w/μ_{ce} is evaluated at wall and the channel center. Its value is assumed to be 1 as the flow in the plate heat exchanger is highly turbulent.

3.2.6.4 Nusselt correlations for the heat transfer during phase change

The phase-change process is more complex, and it is more difficult to accurately predict the Nusselt number. Several dimensionless numbers are included in existing formulas, including the Bond, Weber, Boiling numbers. These numbers were introduced in section 3.2.4.

In two-phase flow, an equivalent Reynolds number is defined from the Reynolds numbers of the liquid and vapor phases of the refrigerant as:

$$Re_{g,tp} = Re_{g,va}\left(\frac{\mu_{g,va}}{\mu_{g,l}}\right)\left(\frac{\rho_{g,l}}{\rho_{g,va}}\right)^{0.5} + Re_{g,l} \;. \tag{3-52}$$

In equation (3-54), $\mu_{g,va}$ and $\mu_{g,l}$ are the dynamic viscosities of refrigerant at vapor and liquid states, respectively.

Amalfi proposed two different Nusselt correlations depending on the value of Bond number. If Bd < 4, the heat exchanger channel is considered as microscale and the prediction of the two-phase Nusselt correlation is the function of homogeneous Weber number (We_m):

$$Nu_{g,tp} = 982\,\theta^{*\,1.101}\,We_m^{0.315}\,Bo^{0.32}\,\rho^{*-0.224} \;. \tag{3-53}$$

If $Bd \geq 4$, the heat exchanger channel is considered as macroscale and the prediction of the two-phase Nusselt correlation is [144]:

$$Nu_{g,tp} = 18.495\,\theta^{*0.248}\,{Re_{g,va}}^{0.351}\,{Re_{g,l}}^{0.351}\,Bd^{0.235}\,Bo^{0.198}\rho^{*-0.223} \;, \tag{3-54}$$

In equation (3-54), θ^* is the dimensionless chevron angle, defined as the ratio between the current chevron angle (θ) and the maximum chevron angle given, θ_{max} = 70° [144].

3.2.6.5 The overall heat transfer coefficient (U)

The overall heat transfer coefficient for the sensible and latent heat transfer sections in the heat exchanger is given by:

$$\frac{1}{U} = \frac{1}{he_w} + \frac{1}{he_g} + \frac{t}{k_{pl}} + fou_w + fou_g \;, \tag{3-55}$$

In equation (3-55), he_g and he_w are the firm coefficients of the refrigerant and water. fou_g and fou_w are the fouling factors on the refrigerant side and water side; and t and k_{pl} are the thickness and the conductive heat transfer coefficient of the plate, respectively.

Fouling factors for PHEs are much lower (up to 100 times) than for shell-and-tube heat exchangers [19]. This is because of the highly turbulent flow resulting from the plate geometry. Nevertheless, fouling can considerably increase with time. For example, Genic et al. [153] experimentally found that the total fouling factor in a PHE used for domestic hot water production increased by almost triple after one year operation, from 8.8×10^{-5} to 25.2×10^{-5} ($m^2\ K\ W^{-1}$). Fouling factor has a significant impact on the determination of the suitable the heat exchange area [154]; thus, the selection of fouling factors must be done with caution.

Consequently, the required heat transfer area of each section is determined from:

$$\dot{Q} = U \cdot \mathrm{A} \cdot LMTD \;. \tag{3-56}$$

The heat transfer area ratio (A_{ratio}) between the total used area and the actual required area at a given operating conditions is given by:

$$A_{ratio} = \frac{A_{tot}}{A_{va} + A_{tp} + A_l} \ . \tag{3-57}$$

The total used area (A_{tot}) is calculated from the geometry inputs of the heat exchanger. The A_{ratio} must be greater than 1 for an adequate design. It is often recommended to design the heat exchanger for an A_{ratio} > 2, because of the development of fouling over the lifecycle of the PHE [153].

3.2.7 Calculation of the pressure drops inside the heat exchangers

Fanning friction factor and Prandtl number are the key parameters influencing the head loss and the overall heat transfer coefficient in heat exchangers. Typically, specific empirical correlations are needed for each type of heat exchanger and fluid flow characteristics. This section presents the procedure applied for computing the pressure drop inside the plate heat exchangers considered for the ejector cooling system.

Total pressure drop inside of a PHE is the sum of channel (δP_{ch}) and port pressure drops (δP_{Po}). The hydrostatic pressure drop due to gravitational force is neglected. Here, only the pressure drop on the refrigerant side is considered as it has direct influence on the performance of the ejector cycle.

3.2.7.1 Calculation of the port pressure drop

The port pressure drop on the refrigerant side is obtained using an approximating function, assuming that the refrigerant is in liquid phase at one port in vapor phase at the other. The approximating function can be written as:

$$\delta P_{Po} = \frac{3}{4} \ N_{pl} \left(\frac{{G_{Po}}^2}{\rho_l} + \frac{{G_{Po}}^2}{\rho_{va}} \right) \ . \tag{3-58}$$

In equation (3-58), N_{pl} is the number of plates of the heat exchanger and G_{Po} is the mass velocity at the port given by:

$$G_{Po} = \frac{\dot{m}}{\pi \ \frac{{D_{Po}}^2}{4}} \ . \tag{3-59}$$

D_{Po} is the port diameter.

3.2.7.2 Calculation of the channel pressure drop

Similarly to the procedure followed for the heat transfer analysis, the channel pressure drop was estimated as the sum of the individual pressure drops calculated for the sensible heat transfer in liquid phase, latent heat transfer and sensible heat transfer in vapor phase section, as shown in Figure 3.2. In liquid phase, the refrigerant flow results in a pressure drop given by:

$$\delta P_{ch,l} = 2\, f_l\, L_{v,l}\, N_{pl}\, \frac{{G_{ch,l}}^2}{\rho_{ch,l}\, D_h}\ . \tag{3-60}$$

In equation (3-60), $L_{v,l}$ represents effective length of the liquid fluid flow path with taking to account the corrugation enlargement factors [19]. $G_{ch,l}$ is the mass velocity of refrigerant in a single channel. f_l is the Fanning friction factor.

Similarly, the pressure drop in the two-phase flow and vapor flow regions of the HEX are given by:

$$\delta P_{ch,tp} = 2 f_{tp}\, L_{v,tp}\, N_p\, \frac{{G_{ch,tp}}^2}{\rho_{ch,tp}\, D_h} \tag{3-61}$$

and

$$\delta P_{ch,va} = 2 f_{va}\, L_{v,va} N_p\, \frac{{G_{ch,va}}^2}{\rho_{ch,va}\, D_h}\ . \tag{3-62}$$

The total channel pressure drop is then obtained from:

$$\delta P_{ch} = \delta P_{ch,l} + \delta P_{ch,tp} + \delta P_{ch,va}\ . \tag{3-63}$$

The Muley correlations [147] were selected for calculating the Fanning friction factors of the single-phase sections (liquid and vapor). Plate geometry parameters β and ϕ_{pl} also considered in these correlations. Since the Reynolds number of the liquid refrigerant is usually lower than 200, and the Reynolds number in vapor is usually greater than 1000, the following empirical correlation were implemented:

$$f = \left(\frac{\beta}{30}\right)^{0.83} \left(\left(\frac{30.2}{Re}\right)^5 + \left(\frac{6.28}{Re^{0.5}}\right)^5\right)^{0.2} \tag{3-64}$$

$$\text{for Re} < 400$$

$$f = (2.917 - 0.1277\beta + 2.016 \times 10^{-3}\,\beta^2) \times \left(5.474 - 19.02\phi_{pl} + 18.93{\phi_{pl}}^2 - 5.341{\phi_{pl}}^3\right) \times {Re_r}^{-\left(0.2+0.0577\,\sin\left(\pi\frac{\beta}{45}+2.1\right)\right)} \tag{3-65}$$

for Re > 1000

The correlation of Amalfi [144] was used to compute the Fanning friction factor for the two-phase flow section given by:

$$f_{r,tp,g} = C_{coef}\, 15.698\, {We_m}^{-0.475}\, Bd^{0.255}\, \rho^{*-0.571}\ . \tag{3-66}$$

In equation (3-66), C_{coef} is called the leading coefficient, which is used to take into account the effect of the chevron angle on the pressure drop according to the following expression:

$$C_{coef} = 2.125\, \theta^{*9.993} + 0.955\ . \tag{3-67}$$

3.3 Overall cycle component energy balance equations

Section 3.1 and 3.2 presented the mathematical model for the ejector and the heat exchangers. To complete the mathematical model of the ejector refrigeration cycle, the energy balance equations for the main ejector cooling cycle components are needed.

The total heat transferred to the refrigerant in the generator is given by:

$$\dot{Q}_g = \dot{m}_g\left(h_g - h_p\right)\ , \tag{3-68}$$

h_g is the refrigerant energy at the generator outlet. The enthalpy at the pump outlet (h_p) is the sum of the enthalpy at the condenser outlet and the enthalpy generated by the pump,

$$h_p = h_c + \dot{W}_p/\dot{m}_g\ . \tag{3-69}$$

The pump work in equation (3-69) is needed for the pressure lift to the generator pressure:

$$\dot{W}_p = \dot{m}_g\,(p_g - p_c) \tag{3-70}$$

The heat rate that the refrigerant transfers to the water in the condenser is given by:

$$\dot{Q}_c = \left(\dot{m}_g + \dot{m}_e\right)(h_c - h_d)\ , \tag{3-71}$$

where h_d and h_c is the enthalpy at the outlet of ejector (diffusor) and condenser, respectively.

The process through the expansion valve is assumed as an isenthalpic process. Thus, the enthalpies at the condenser outlet (h_c) and at the expansion valve outlet (h_v) are assumed to be equal. The cooling capacity of the cycle is:

$$\dot{Q}_e = \dot{m}_e(h_e - h_v) \ . \tag{3-72}$$

4 EXPERIMENTAL WORK ON THE SOLAR EJECTOR COOLING CYCLE

4.1 The test rig description

The solar ejector cooling system is located at the University of Porto, Portugal, featuring a variable geometry ejector (VGE) and high-efficiency solar collectors for driving the cooling cycle. Figure 4.1 shows the layout of the solar ejector refrigeration system. The air-conditioned space and the equipment room were constructed using a structural insulated panel. The structural insulated panel is a sandwich structured composite, consisting of construction foam material sandwiched between two layers of composite fiberglass. The structural insulated panel enables us to develop lightweight, high-durable, well-insulated constructions. The air-conditioned space has a floor area of 15 m^2. The equipment room, where the cooling cycle, pumps, hot water tank, and control system are located, has a floor area of about 4 m^2.

The test facility is composed of four cycles: (i) the variable geometry ejector cooling cycle (*in short* ejector cycle *or* main cycle), and three auxiliary cycles, (ii) the solar heat supply cycle, (iii) heat dissipation, and (iv) heat distribution cycles, as shown in Figure 4.2. The green and dark blue lines in the ejector cycle represent the refrigerant in the vapor and liquid phase, respectively. The black lines represent the water circulations of the auxiliary cycles. The ejector cooling cycle and the auxiliary cycles transfer heat through the heat exchangers: generator, condenser, and evaporator. The red squares represent the major measuring sensors. The following text gives brief descriptions of the four cycles.

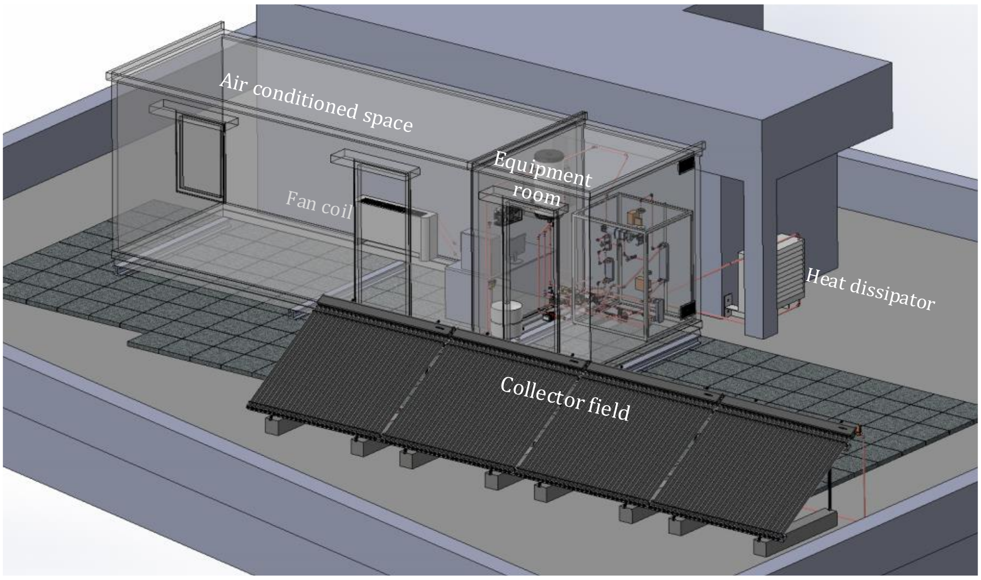

Figure 4.1: 3D model of the test rig.

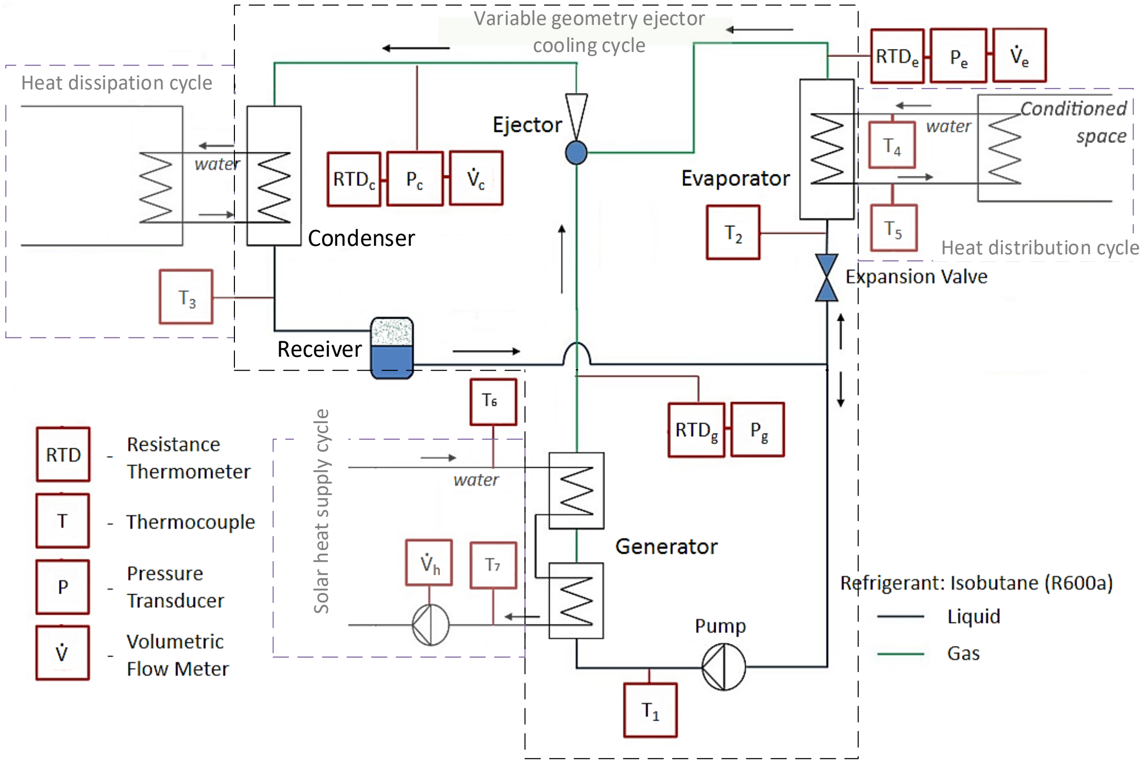

Figure 4.2: Schematics of the SERS unit with indicating data acquisition points.

4.1.1 The solar heat supply cycle

The solar heat supply cycle consists of two sub-cycle, the heat solar collecting cycle, and the heat supply cycle. The solar collector field supplies the necessary thermal energy to drive the SERS. It consists of four evacuated tube type solar collectors (Baxi AR30), connected in series, with a total absorber area of about 13 m^2. The image of the installed solar collectors is shown in Figure 4.3. The collector field can supply about 7.5 kW heat at an outlet temperature of 85°C for solar radiation of 800 W/m^2.

Figure 4.3 The four evacuated tube type solar collectors installed in series.

The outlet of the solar collector field is connected to the top of a 50-liter thermal storage tank. The tank is used to ensure operational stability under a short-term variability of the solar radiation. The circulation pump is located at the outlet of the thermal storage tank, circulating the water back to the solar collectors. Excess heat from the solar collectors is dissipated to the environment by an outdoor fan coil (heat dissipator – as shown in Figure 4.1) in order to protect them from overheating. A check valve was placed at the circulation pump outlet to avoid backflow of the hot water when the pump is not operational. The heat supply cycle circulates the elevated-temperature water from the thermal storage tank to the vapor generator, where the heat is transferred to the primary flow of the ejector cooling cycle (refrigerant cycle).

4.1.2 The heat dissipation cycle

The heat dissipation cycle is used to transfer the heat from the condenser to a large capacity water reservoir. The condenser pressure can be adjusted by regulating the cooling water flow rate. Detailed discussion on this is presented in the next chapter.

4.1.3 The heat distribution cycle

The water is chilled in the evaporator then pumped into the indoor fan coil located in the air-conditioned space (see Figure 4.1). The fan coil is used to remove heat from the air-conditioned space. The circulation pump consumes only about 11 W electric power. Two ultrasonic flow meters and four T-type thermocouples are used to calculate the useful heat generation in the collector field cycle and the cooling capacity in the test room.

4.1.4 The variable ejector cooling cycle

The principal components of the ejector cycle are the vapor generator, variable geometry ejector (VGE), condenser, liquid receiver, expansion valve, pump, and evaporator. A photograph of the whole unit is shown in Figure 4.4.

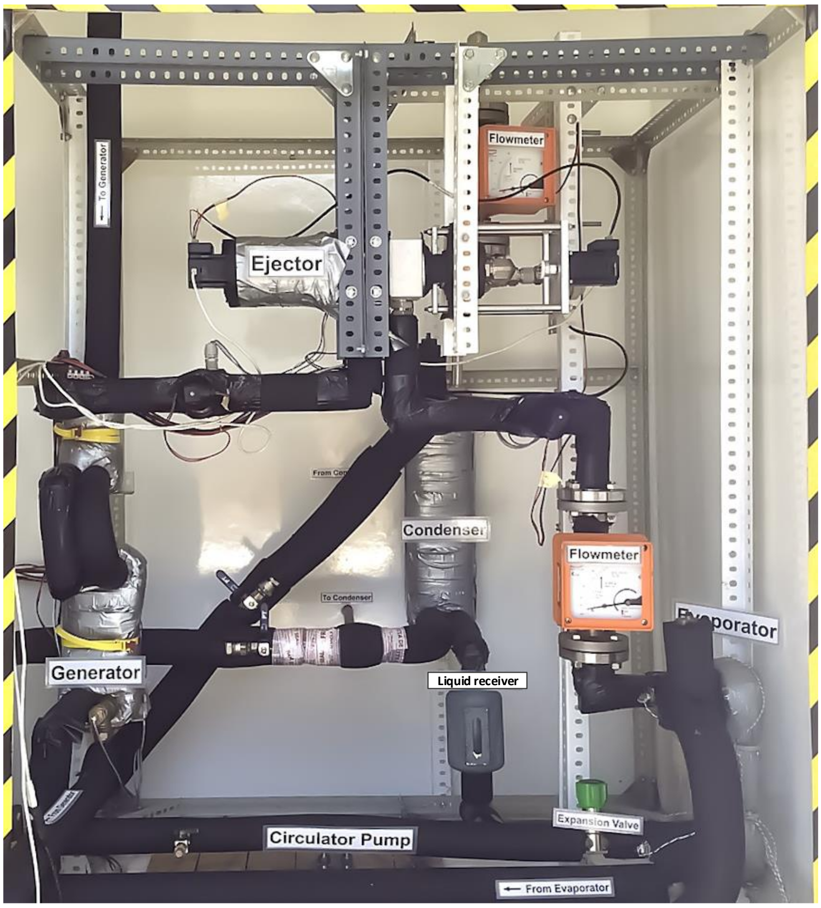

Figure 4.4: Photograph of the variable geometry ejector cycle.

4.1.4.1 The variable geometry ejector

The variable geometry ejector is the heart of the system. It was designed for a nominal cooling capacity of 1.5 kW using R600a as the working fluid. Design operating temperatures were 85°C for the generator, 10°C for the evaporator, and 37°C for the condenser. The spindle position (SP) and nozzle exit position (NXP) can be independently adjusted for optimizing SERS performance at various operating conditions.

The reference point for nozzle exit (NXP = 0 mm) was defined as the position where the nozzle exit touches the converging part of the mixing chamber wall (see Figure 4.5) and thus entirely blocks the free passage for the secondary flow. Likewise, SP was considered to be 0 mm when the spindle touches the primary nozzle wall. The positive directions for both SP and NXP were defined as the spindle and primary nozzle move away from the primary nozzle throat and the constant area section, respectively. They both are adjusted by high precision stepper motors (servomotors).

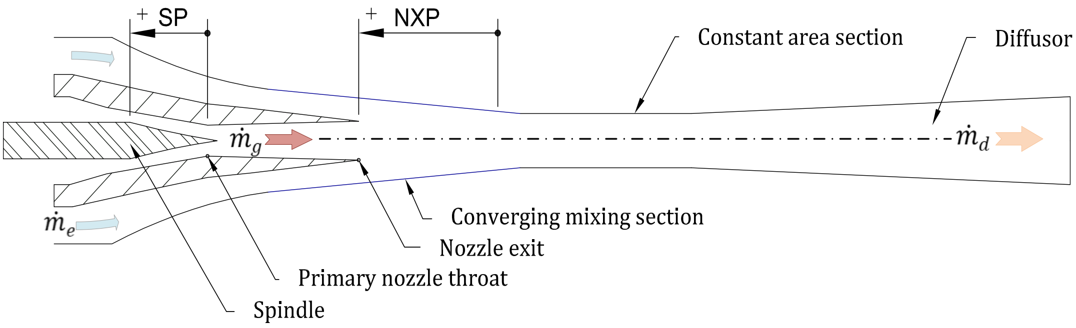

Figure 4.5: Schematic cross-section view of the variable geometry ejector.

4.1.4.2 The refrigerant pump

A magnetic drive rotary vane pump-motor (Fluid-o-Tech) is used to pressurize the primary flow to the required levels. The motor of this integrated pump-motor unit has no moving parts [155], results in a compact, low energy consumption, and silent operation pump system. The pump has the capability of continuous speed control. However, experimental studies in this work were on purpose carried out at constant pump speeds at predefined values. The speed range of the pump is 1100-3500 rpm, the pressure head is up to 16 bar. Figure 4.6 shows a photo of the pump and the typical hydraulic performance at the speed of 2000 rpm.

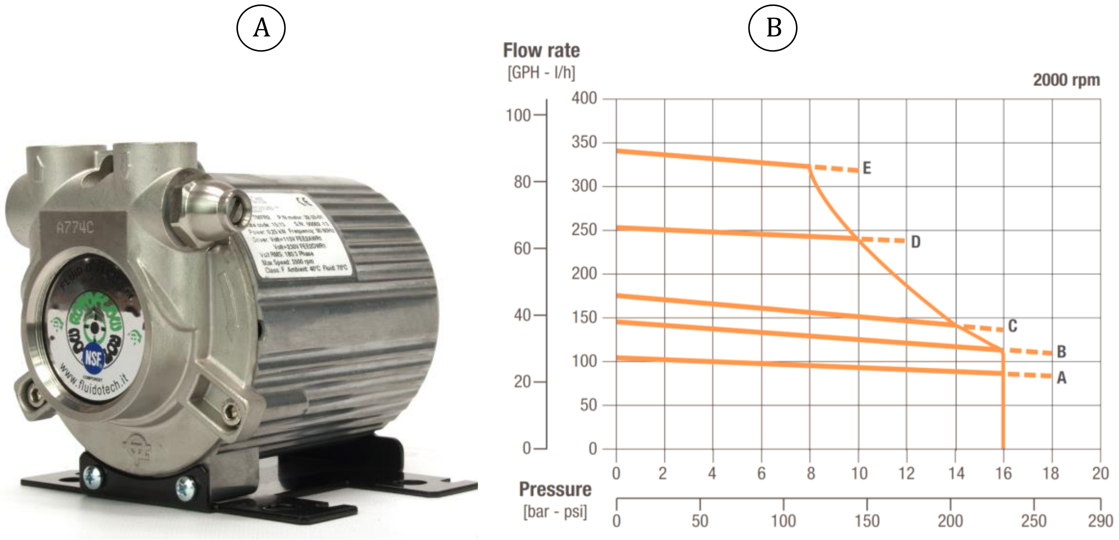

Figure 4.6 The refrigerant pump (A) and its typical hydraulic performance at the speed of 2000 rpm [155].

4.1.4.3 The vapor separator

A vapor separator (also called a liquid receiver) is installed at the condenser outlet to assure that the working fluid is in the liquid state when entering the suction side of the pump. The refrigerant at the condenser outlet is not purely liquid. The liquid receiver separates the vapor that still presents so that the fluid at the outlet is entirely liquid. For that, the device is also called a vapor-liquid separator. Pure liquid flow at the receiver outlet is one of the requirements in preventing the possibility of cavitation that may happen in the pump. A glass window is installed for monitoring the liquid level in the vapor separator, as seen in Figure 4.7.

Figure 4.7 The vapor separator with a glass window

4.1.4.4 The heat exchangers

The high-pressure side of the pump is connected to the vapor generator, consisting of two plate heat exchangers in series. The first heat exchanger elevates the working fluid temperature to near saturation, while phase change takes place in the second one. The stream leaves the generator with some degree of superheat. This high temperature and pressure vapor enters the ejector as primary flow, with the objective to entrain and compress the stream from the evaporator, where the cooling effect takes place. At the condenser, the heat of the total refrigerant flow is transferred to the chilling water. Thus, the pressure at the condenser remains low. Both evaporator and condenser are plate heat exchangers (Alfa Laval) with a nominal capacity of 2.5kW and 10 kW, respectively.

4.1.4.5 The expansion valve

The expansion valve (Swagelok) is located at the evaporator inlet. The expansion valve is a pressure-reducing regulator, which controls outlet (evaporator) pressure by balancing an adjustable spring force against the forces caused by inlet (condenser) and outlet pressures. The desired evaporator pressure is manually adjusted by turning the green knob (see Figure 4.8).

Figure 4.8 Manually adjustable expansion valve Swagelok [156].

4.2 Monitoring and controlling system

4.2.1 Sensors

The ejector cooling system is equipped by a number of sensors and transducers, as presented in Figure 4.2, to monitor the system behavior and performance.

4.2.1.1 Pressure transducers

Three pressure transducers Kobold SEN 86, as shown in Figure 4.9, measure the pressures at the inlets and outlet of the ejector: two are positioned at the ejector primary inlet and outlet (with the pressure range of 0-25 bar), and the ejector secondary inlet (with the pressure range of 0-6 bar). By using internal diaphragm (ID) technology, these sensors could guarantee high accuracy. The manufacturer claimed that the characteristic deviation (precision) is $\leq \pm 0.3\%$ of full scale, and the repeatability is $\leq \pm 0.15\%$ of the full scale [157]. The absolute errors of the pressure sensors are listed in Table 4.1. All the readings from the transducers were obtained in the relative pressure scale. For the performance analysis, the pressure data was then converted to the absolute scale.

Figure 4.9 Pressure transducer Kobold SEN 86.

4.2.1.2 Temperature sensors

High precision RTDs and thermal couples are used for measuring temperatures of the working fluids (R600a and water).

Three Resistance Temperature Detectors (RTDs), also called resistance thermometers, are used to measure the refrigerant temperatures at the inlets and outlet of the ejector, as indicated in Figure 4.2. These RTDs (Kimo) are featured by sensor class B, 4-wire connection with platinum resistor PT100. Their working range is 0-100°C with an accuracy of 0.8°C.

Seven thermocouples (Tecnisis) are used to measure temperatures at the inlets and outlets of the heat exchangers on the water side and refrigerant side, as illustrated in Figure 4.2. The thermocouples are firmly attached to the wall of the tubes by thermal adhesive tape, or by fixing to the hole by using thermal adhesive, as shown in Figure 4.10. The thermocouples are T-type thermocouples (copper/constantan *or* Cu/Cu-Ni). They are very stable, linear, and has excellent repeatability between -200 to 200°C. The entire ejector cooling cycle is well insulated by rubber foam insulation pipe, as shown in Figure 4.10b. Insulating minimizes the heat losses and ensures the accuracy of temperature measurements. Each thermocouple was carefully calibrated, and the calibrating function was added to the LabVIEW program. Hence, high accuracy of thermocouples was archived, as with a maximum standard error of 0.35°C.

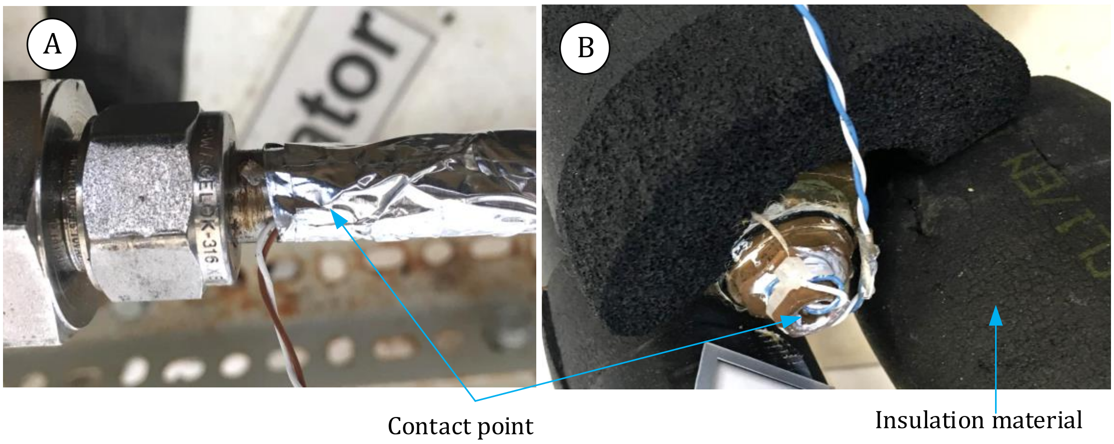

Figure 4.10 Installation of a thermocouple.

4.2.1.3 Flowmeters

The refrigerant flow rates in the ejector cycle are measured by two variable area flowmeters (Kobold BGN-S). These flowmeters are positioned at the ejector outlet (diffusor outlet) and the ejector secondary inlet, as indicated in Figure 4.2.

The flowmeters are equipped with an analog display, as shown in Figure 4.11. The flowmeters are for directly monitoring and an electric-magnetic transmitter for obtaining digital signal to the acquisition system. The flowmeters were particularly calibrated by the manufacturer for the working fluid R600a at the normal pressure (1 bar) and temperature (15ºC) conditions. The mass flow rates are defined by:

$$\dot{m} = \rho(T,p)\sqrt{\frac{\rho_n}{\rho(T,p)}}\,\dot{V} \tag{4-1}$$

In equation (4-1), $\dot{V}$ the is measured volumetric flow, ρ is the refrigerant density at temperature and pressure that $\dot{V}$ is measured, and ρ_n is the nominal density (ρ_n = 2.51 kg/m^3). Their measurement ranges and the corresponding absolute errors of the sensors are shown in Table 4.1.

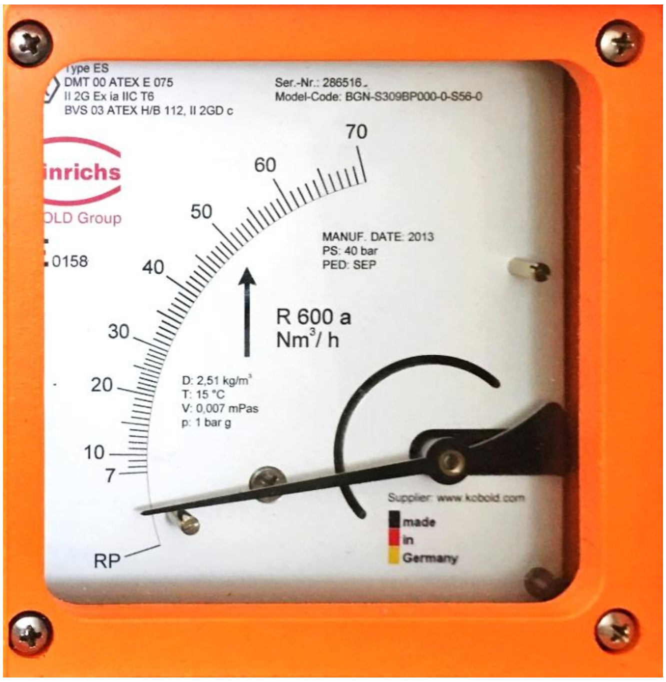

Figure 4.11 Analogue display of the variable area flowmeter at the ejector outlet.

The water flow rates in the other cycles are measured by ultrasonic flowmeters (Kobold DUK), with a maximum measuring error of 1.4% of full scale [158]. The electromagnetic flowmeter is a transducer that measures fluid velocity by the voltage induced across the fluid by its flow through a magnetic field. Figure 4.12 shows the positions of the ultrasonic meters of the solar heat supply cycle (heat supply sub-cycle - between the generator and the thermal storage tank) and the heat distribution cycle.

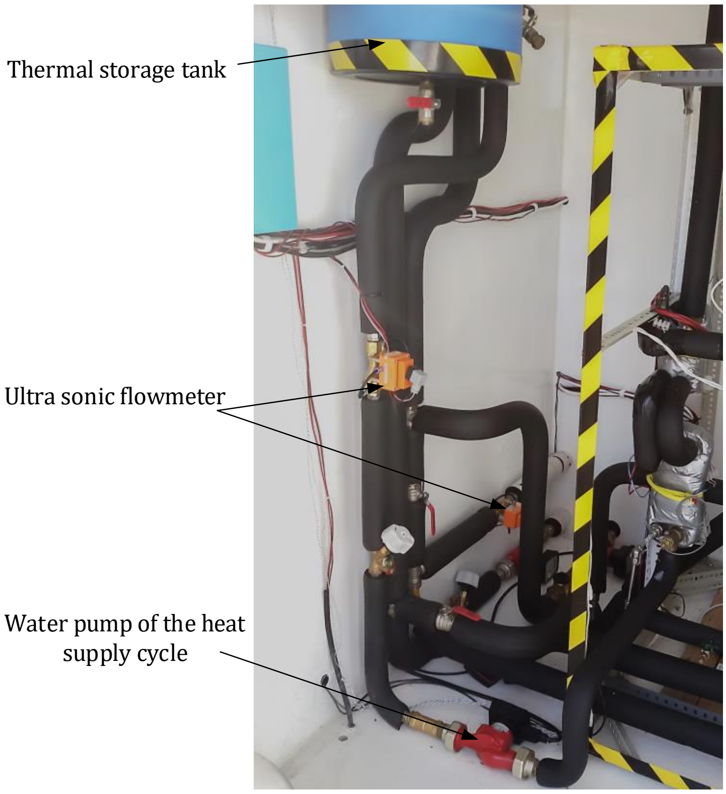

Figure 4.12 Side view of the ejector system.

Table 4.1: List of sensors installed in the ejector cooling cycle with their range and measurement error.

Sensor	**Technology**	**Range**	**Absolute error**	**Unit**
Primary inlet temperature	RTD	0-100	±0.8	°C
Secondary inlet temperature	RTD	0-100	±0.8	°C
Outlet temperature	RTD	0-100	±0.8	°C
Primary inlet pressure transducer	ID	0-25	±0.125	bar
Secondary inlet pressure transducer	ID	0-6	±0.03	bar
Outlet pressure transducer	ID	0-25	±0.125	bar
Outlet flowmeter	Variable area	2-20	±0.36	m^3/h
Secondary flowmeter	Variable area	1.5-15	±0.27	m^3/h

4.2.1.4 Pyranometer

A pyranometer (Kipp & Zonen) is used to monitor the global solar radiation and calculate the thermal coefficient as well as the heat rate of the solar collectors in real-time. The sensor is located with the same tilt angle as the collectors (about 35°). The sensor's maximum errors in the hourly radiation total and the daily radiation total are 8% and 5%, respectively [159]. It is because some response variations cancel out each other when the integration period is long.

Figure 4.13 Pyranometer used in the test rig.

4.2.2 Calibration of sensors

Calibrations were implemented for used sensors to improve the measuring accuracies. The area variable flowmeters were exclusively calibrated by the manufacturer for the refrigerant R600a. Pressure transducers were also calibrated by the manufacturer.

The thermocouples were calibrated by reference equipment Julabo F34-HE. The reference equipment is a high accuracy refrigerated/heating circulator with the working range from -30°C to 150°C. The thermocouples were calibrated in the temperature range of 0-90°C for every 10 K. The calibration function was recorded to LabVIEW program, for equalizing with the reference equipment. Similarly, the pyranometer was calibrated with a reference device, and the calibration function was added when the raw data were treated.

Schematic view of the cooling system with real-time data monitoring

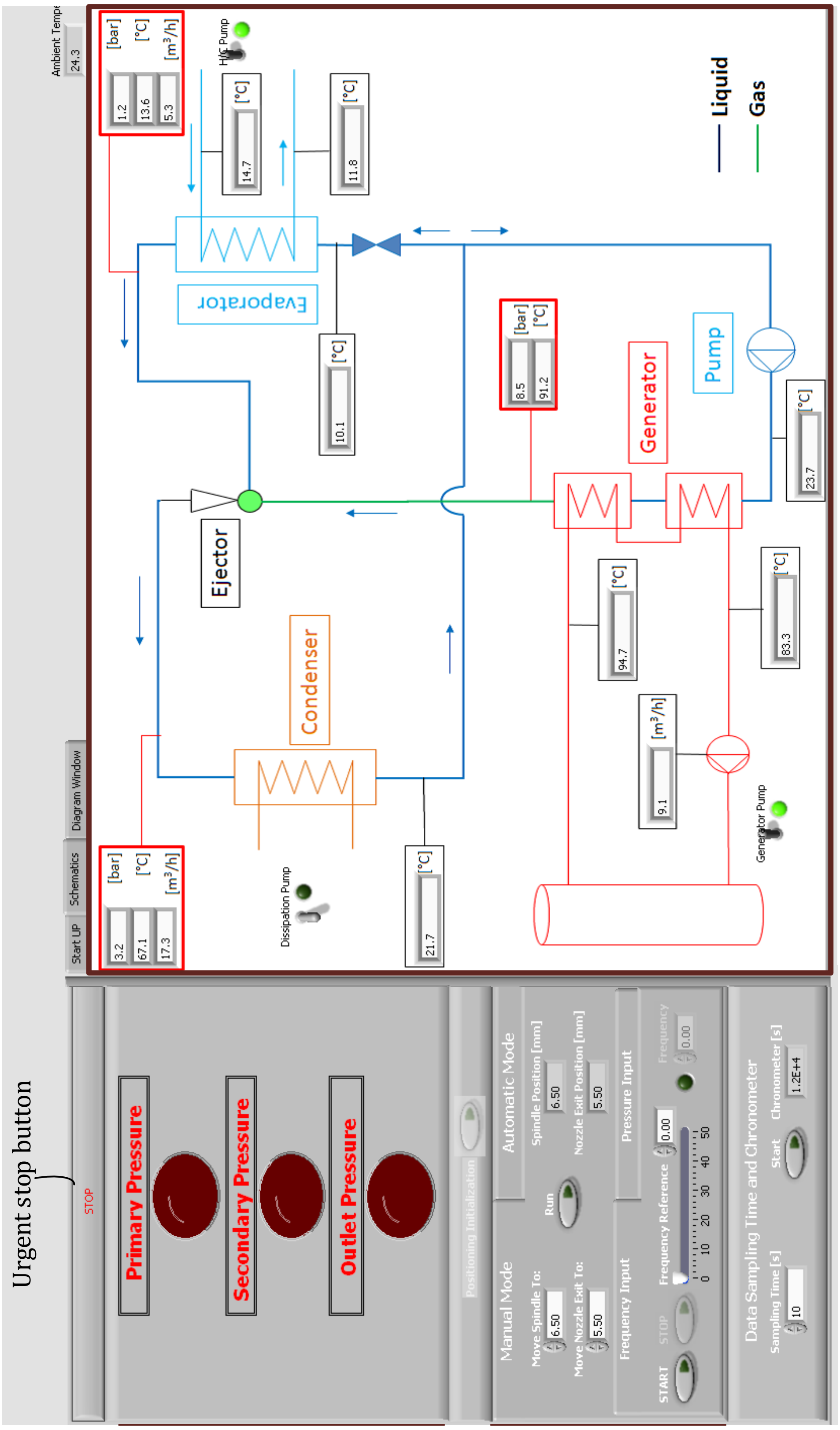

Urgent stop button

Pump On/Off switch

Pressure limit alerts

SP, NXP and pump frequency control

Figure 4.14 Controlling interface of the LabVIEW program.

4.2.3 Monitoring and data acquisition system

A monitoring and controlling system was designed to acquired measured data from the sensors and to control the operation of the ejector cooling system. Data from the sensors are logged by data acquisition unit HP Agilent 34970A, which is connected to a personal computer running a LabVIEW program. A monitoring and control application developed in program LabVIEW is based on a logical graphical interface. The diagram window of the application allows the most important measured data intuitively monitored on the PC display, as shown in Appendices. Figure 4.14 shows the control window of the application, where the important components, e.g., the spindle and nozzle exit positions, pump frequency, can be directly controlled. The stop button located at the top-left of the window is used to urgently stop the system if it exceeds pressure limits.

4.3 Experimental procedure

The experimental campaign was carried out on clear or partially clear days from May to the end of July 2018, which was about 30 hours in total under stable working conditions. During this period, a parametric study was carried out focusing on the system performance assessment under on-design and off-design conditions as a function of SP, NXP, and backpressure. In the present work, the system performance evaluation was carried out under a simple configuration; the variable geometry ejector cooling cycle was tested for fixed pump speeds.

Spindle and nozzle exit positions were calibrated at the beginning of each experimental run. Although the primary pressure changed during the experiments because of the constant pump speed and different SPs, the refrigerant temperature at the primary nozzle inlet was maintained with about 10 K superheating to ensure system stability. Each day of the experiment, the ejector cooling system was run for about 1 hour to get to a relatively steady state, after which data acquisition was started. After setting up a given experimental condition, the system was run at least for 10 min (mostly longer) using 10-second sampling intervals. When the spindle position or nozzle exit position was adjusted, the system needed only about one minute to respond due to the thermal inertia. The acquired data were treated in programs Microsoft Excel and Engineering Equation Solver.

4.4 Uncertainty analysis

Measurement accuracy is identified by considering both systematic and random errors. Random error (uncertainty type A) is caused by random fluctuations in the readings of measurement devices. The systematic error, also known as uncertainty type B or fixed error, is caused by imperfect calibration of the measurement devices, limitation of the measuring method used, and the interference of the environment to the measurement process. The influence of systematic error on an experiment is always in a predictable direction. Random error can be reduced by averaging multiple measurements for the same operating conditions.

Since the experimental works of this study were carried out in actual conditions, whereas the solar radiation flux fluctuated by time. Fluctuations caused by actual conditions were inevitable. Repeated measurement was applied for averaging multiple measurements. However, only the systematic error is presented in this uncertainty analysis.

Coefficient of Performance (COP) is the key performance indicator of the ejector refrigeration system. The experimental setup of the test rig allows the COP to be calculated in two ways: by the experimental data from the refrigerant flows in the ejector cooling cycle (COP_r), and from the water flows in the heat distribution and the solar heat supply cycle (COP_w).

4.4.1 Uncertainty of COP_r

Equation (2-3) is rewritten as follows

$$\mathrm{COP}_r \cong \frac{\dot{m}_e \cdot (h_e - h_v)}{\dot{m}_g \cdot (h_g - h_p)} = ER\frac{(h_e - h_v)}{(h_g - h_p)} \tag{4-2}$$

The mass flow rates at the ejector secondary inlet ($\dot{m}_e$) and the ejector outlet (diffusor) ($\dot{m}_d$) were calculated from directly measured quantities, including volumetric flow rates, pressures and temperatures, and calculated density, as seen in equation (4-1). The primary mass flow rate ($\dot{m}_g$) is the difference of $\dot{m}_d$ and $\dot{m}_e$.

The uncertainty associated with the determination of the ER (σ_{ER}) can be obtained by the following formula:

$$\sigma_{ER} = \sqrt{\left(\frac{\partial ER}{\partial \rho_e}\sigma_{\rho_e}\right)^2 + \left(\frac{\partial ER}{\partial \dot{V}_e}\sigma_{\dot{V}_e}\right)^2 + \left(\frac{\partial ER}{\partial \rho_d}\sigma_{\rho_d}\right)^2 + \left(\frac{\partial ER}{\partial \dot{V}_d}\sigma_{\dot{V}_d}\right)^2}\ . \tag{4-3}$$

The uncertainty associated with the determination of the working fluid density was obtained by:

$$\sigma_\rho = \sqrt{\left(\frac{\partial\rho}{\partial p}\sigma_p\right)^2 + \left(\frac{\partial\rho}{\partial T}\sigma_T\right)^2} \tag{4-4}$$

where σ_p and σ_T are the uncertainties of pressure and temperature sensors.

Uncertainty of enthalpy is defined as,

$$\sigma h = \sqrt{\left(\frac{\partial h}{\partial p}\sigma p\right)^2 + \left(\frac{\partial h}{\partial T}\sigma T\right)^2}\ . \tag{4-5}$$

In the same manner, uncertainties of all other variables were calculated by the directly measured data.

The uncertainty of the COP_r is then,

$$\sigma_{COP_r} = \sqrt{\left(\frac{\partial COP}{\partial ER}\sigma_{ER}\right)^2 + \left(\frac{\partial COP}{\partial h_e}\sigma_{h_e}\right)^2 + \left(\frac{\partial COP}{\partial h_v}\sigma_{h_v}\right)^2 + \left(\frac{\partial COP}{\partial h_g}\sigma_{h_g}\right)^2 + \left(\frac{\partial COP}{\partial h_p}\sigma_{h_p}\right)^2}\ . \tag{4-6}$$

4.4.2 Uncertainty of COP$_w$

The COP$_w$ (thermal COP) was acquired from water mass flow rates ($\dot{m}_{w,e}$ and $\dot{m}_{w,g}$) and the corresponding enthalpy differences between the inlet and outlet of evaporator and generator:

$$COP_w = \frac{\dot{m}_{w,e}\left(h_{w,e,in} - h_{w,e,out}\right)}{\dot{m}_{w,g}\left(h_{w,g,out} - h_{w,g,in}\right)} \tag{4-7}$$

A similar approach to determining σ_{ER} was applied to estimate the uncertainty in the COP$_w$.

4.4.3 Results from the uncertainty analysis

Data of a typical measurement was selected to analyze the uncertainty. The COP_r of this run is 0.27± 0.02 while the COP_w is 0.29± 0.03. The COP_r is smaller in most of the measurements.

As seen in the graph below, the factor that distributes the most to the uncertainty it the secondary flowmeter, 77%. Thus, in order to improve measuring uncertainty, we may want to substitute this flowmeter with others that have a more suitable range, or other technology such as Coriolis flowmeter. Overall, the uncertainty of COP in every run was within 10%, which is acceptable.

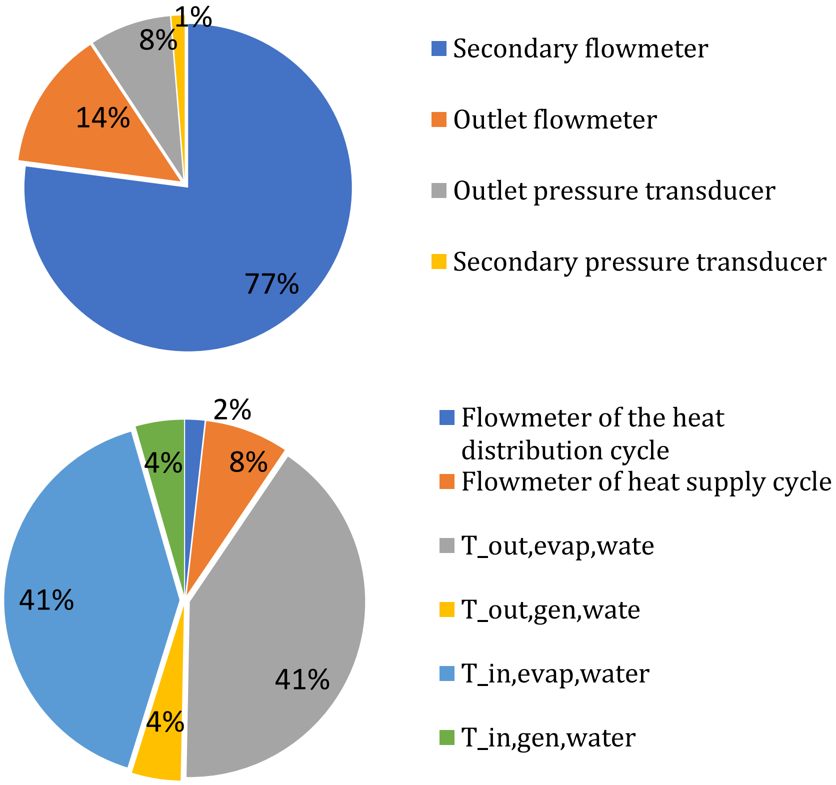

Figure 4.15: Distribution to measurement uncertainty – calculated from the refrigerant flows (upper) and from the water flows (lower).

The overall uncertainty of the ER and thermal COP during the experiments was estimated to be within ± 8% and ±12%, respectively.

5 EXPERIMENTAL RESULTS AND VALIDATION OF THE MATHEMATICAL MODEL

Figure 5.1 shows the operating pressures, the generator heat, and available solar radiation recorded on the 12th of July 2018. This experimental run was started up from 3:00 PM and had a duration of about 2 hours on a relatively sunny day. The primary inlet temperature (T_g) varied in the range of 84 ÷ 90°C with 16 ÷ 22°C of superheat. The speed of the pump was 2000 RPMs, and the spindle position was set to 5.75 mm. The figure shows considerably variation of solar radiation (green circles) due to the presence of cloud and the constant decay because of the trajectory of the sun in the afternoon. The longest cloudy period occurred during the first 15 minutes of the measurement, with some solar radiation values below 300 W/m^2. Despite the variability in the solar radiation, the operating pressures in the generator (primary), evaporator (secondary), and condenser (back) were rather stable (as indicated in Figure 5.1). The maximum variation was within 5% of the absolute pressure. The results, in general, showed that the system could operate about 20 min with no or reduced solar radiation using the accumulated heat in the 50 liters thermal storage tank. It is noted that a larger thermal tank could store a larger amount of heat to drive the ERS for longer periods, but it would also increase system thermal inertia and thus morning start-up time. As a consequence, the primary pressure was about 10.3 bar leading to a mass flow rate of about 18.5 g/s. The heat transfer rate from the hot water to the working fluid in the generator remained essentially constant, about 6 kW (dashed line). The secondary inlet pressure (1.1 bar) was also constant, corresponding to an evaporator temperature of 8.5ºC, indicating high system stability. The secondary mass flow was about 5.1 g/s resulting in cooling capacity of about 1.6 kW. The backpressure at the ejector outlet was 3.1 bar (dotted line in Figure 5.1), corresponding to a condenser temperature of 30.5ºC.

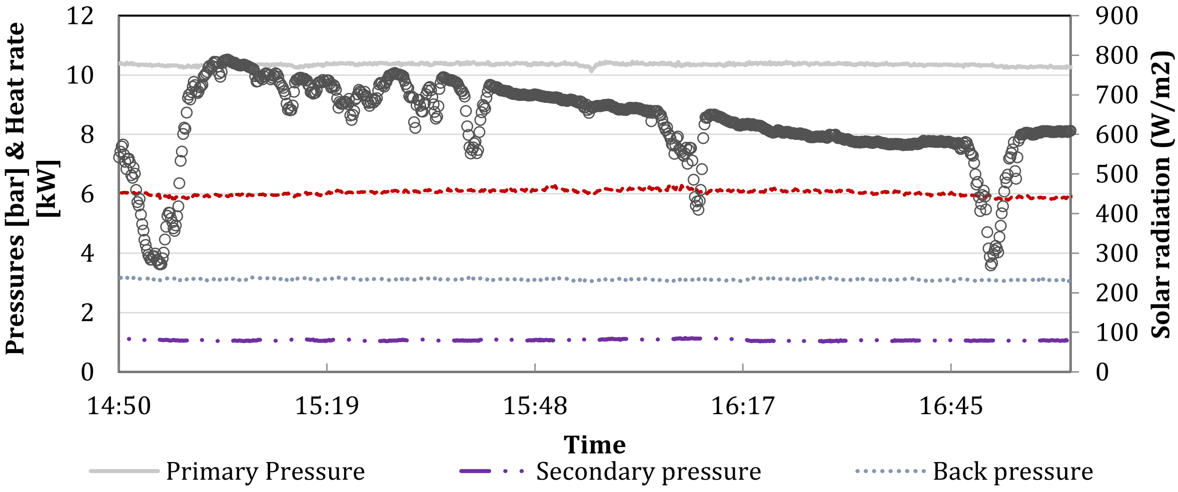

Figure 5.1: Operating system pressures, generator heat, and solar radiation on the 12th of July 2018.

5.1 Stability of the ejector cooling system

Figure 5.2 presents a data sample of selected variables on the 12th of July 2018. As can be seen, the system was extremely stable. The primary, secondary, outlet pressures were mostly constant even when the solar radiation fluctuated in a wide range (see Figure 5.1). Please note that the inlet temperature of the primary flow (T_g) reached a certain level of superheating, thus the small variation of generator temperature did not cause the change of primary pressure. Also, the hot water tank played a key role in stabilizing the generator temperature and primary pressure.

To demonstrate the cooling effect of the ERS, selected data of a measurement on the 17th of July, 2018 was presented in Figure 5.3. The whole measurement lasted roughly four and haft hours, from 12:30 PM to 5:00 PM. Profiles of room temperature of conditioned space and working pressures of the ejector cycle are shown. This measurement was aimed to study the impact of spindle position on system performance; the spindle position was adjusted in a wide range. Therefore, ERS did not work at its best performance. The refrigerant pump was stopped for one minute at 1:17 PM, as shown in the graph. The outlet and secondary pressure were stable when changing the primary flow rate.

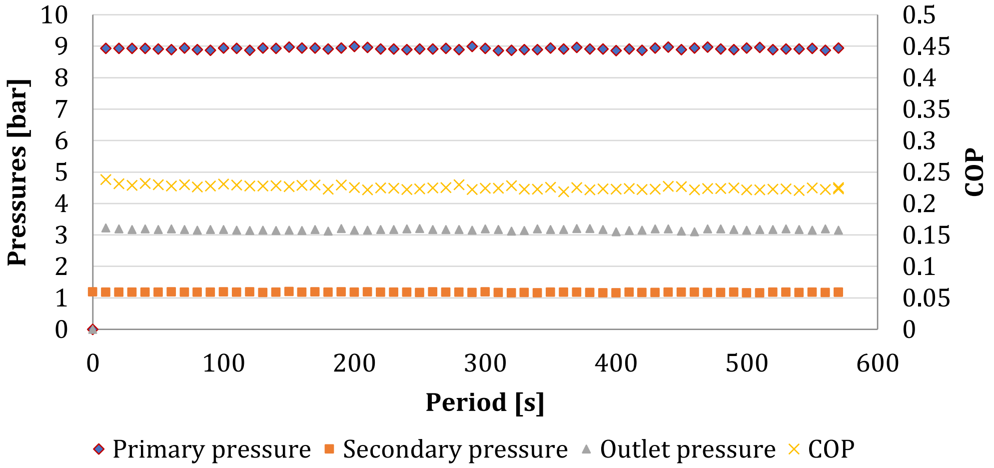

Figure 5.2: System stability of a measurement.

Located on the rooftop of a building, the conditioned room was under heavy heat loads on a clear day, even when it is well insulated. After having all the conditions ready for a run, the refrigerant pump was started. The ejector cycle got to a stable state within a few minutes, and after 14 minutes more, the cooling effect was noticeable by the room temperature logger, which was placed away from the fan coil. The delay of cooling effect was due to the thermal inertia of the auxiliary cycle and the air-conditioning cycle. Also, the temperature logger was placed away from the airflow of the fan coil. As we can see, the room temperature dropped quickly from 30^{o}C to 22^{o}C at 3:00 PM. After that, the spindle position (SP) was opened to the point where the primary flow rate was higher than the optimal value, which caused the reduction of secondary (evaporator) flow rate. Thus, the COP and the cooling capacity of the system decreased; accordingly, the decrease in room temperature was less intense. At 4:10 PM, SP was adjusted for reducing the primary flow rate. As a result, primary pressure and ER increased. At 5:00 PM, the system was stopped, resulting in the rapid increase of room temperature right after that. Heat loads of the conditioned room were not measured; however, we can have a sense of how they were when looking at the rise of room temperature in the late afternoon.

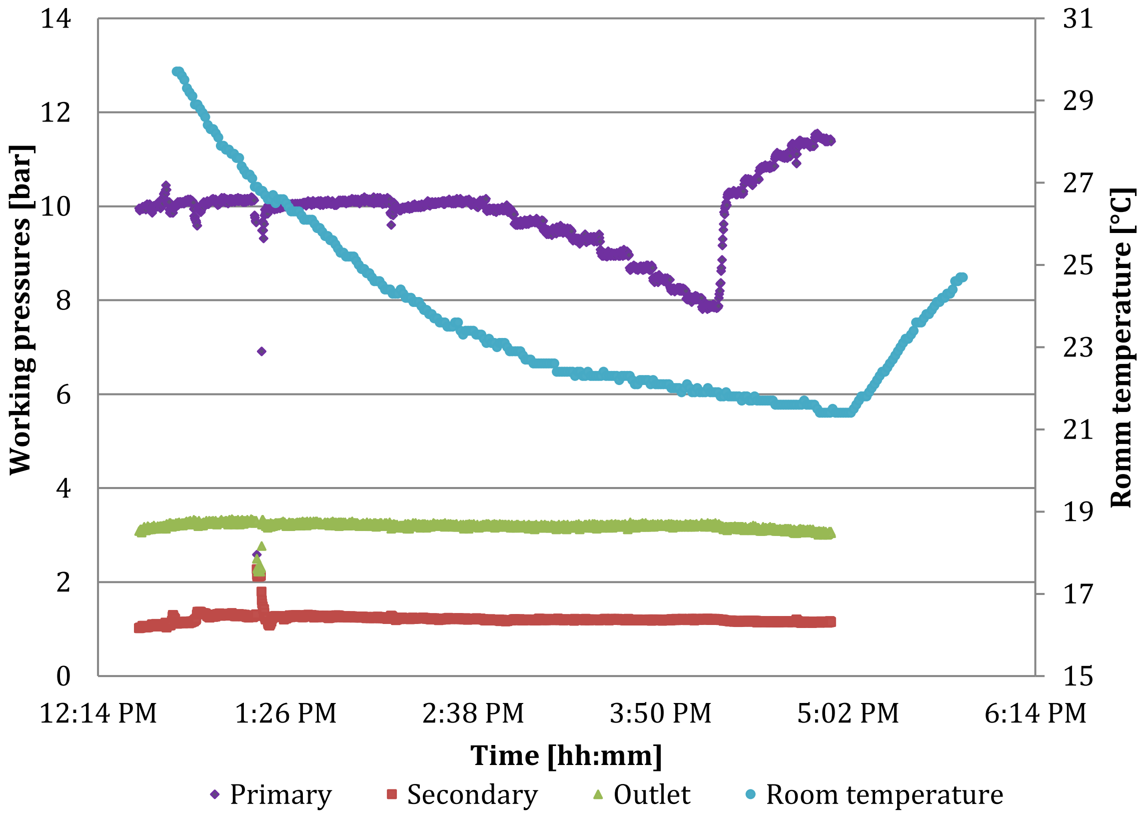

Figure 5.3 Conditioned space's temperature along an operating period of ERS.

5.2 COP as a function of the nozzle exit position

Three sets of experimental runs were performed to study the influence of NXP alone on the performance of the SERS. In the first set, NXP was gradually adjusted from 1.5 to 7.5 mm, resulting in 13 measurement points. Each point corresponds to the average values calculated over experiments that took approximately 10 min. Details of operating conditions and flow rates of the refrigerant are presented in Table 5.1

The spindle position was set to 5.75 mm and the pump speed to 2000 rpm. The setup resulted in a primary pressure and the primary mass flow rate of 10.2 bar and 16.4 g/s, respectively. The saturation temperature at the condenser remained about 30.5°C ($P_c \cong 3.1$ bar) during the tests. The refrigerant temperature at the evaporator outlet (T_e) varied somewhat because of the temperature variation inside the test room. However, the temperature difference ΔT_e of the water between evaporator inlet $\left(T_{e,in}\right)$ and outlet remained approximately constant, regardless of the variation of the room temperature. The enthalpy difference of refrigerant in the evaporator (Δh_e) did not vary considerably.

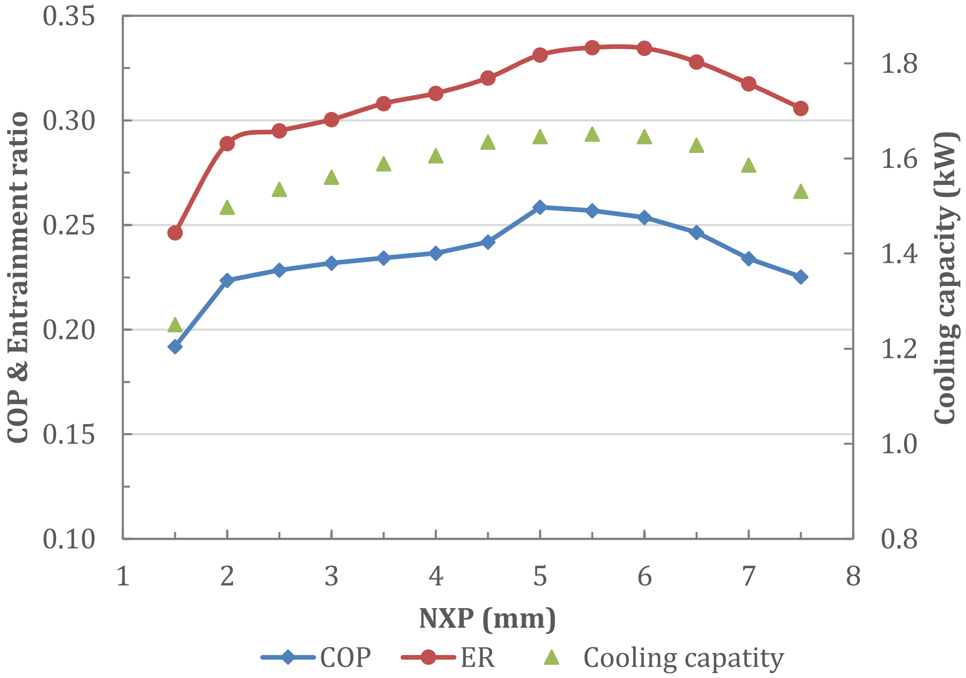

Figure 5.4 System performance as a function of nozzle exit position.

Table 5.1 Treated data of the first experimental set (12/7/2018)

NXP	P_g	T_g	P_e	T_e	P_c	$\dot{m}_g$	$\dot{m}_e$
mm	*bar*	*°C*	*bar*	*°C*	*bar*	*g/s*	*g/s*
1.5	10.0	80.19	1.14	11.62	3.02	16.08	3.96
2	10.2	82.34	1.08	11.62	3.07	16.52	4.77
2.5	10.3	82.80	1.06	12.12	3.09	16.66	4.91
3	10.3	83.48	1.05	11.96	3.09	16.68	5.01
3.5	10.3	85.95	1.06	11.56	3.10	16.63	5.12
4	10.4	87.42	1.06	11.86	3.12	16.63	5.20
4.5	10.4	88.59	1.04	12.63	3.13	16.60	5.32
5	10.3	84.23	1.06	14.63	3.13	16.52	5.47
5.5	10.4	86.58	1.07	13.89	3.13	16.43	5.50
6	10.4	88.23	1.06	13.24	3.12	16.41	5.49
6.5	10.4	88.92	1.07	12.21	3.11	16.43	5.39
7	10.4	89.74	1.10	9.55	3.10	16.44	5.22
7.5	10.4	89.48	1.12	9.21	3.10	16.48	5.04

Figure 5.4 represents cooling cycle performance as a function of the NXP, the corresponding operating data was shown in Table 5.1. It can be seen from the figure that the ejector resulted in the lowest ER and COP at NXP = 1.5 mm. The relatively deficient

performance was observed, most likely because of reduced effective area available for the secondary flow in the converging mixing chamber (see Figure 4.5). Consequently, ER increased from 0.25 to 0.34, as the nozzle exit position was moved upstream from 1.5 to 6 mm, due to the increase of the effective area and thus the secondary flow rate. After the optimal point (~ 6mm), the ER started to drop. This phenomenon could be a result of the formation of small recirculation zones in the convergent part of the mixing chamber, which again reduces the effective area for the secondary stream. This phenomenon was also observed by Han et al. [160] using CFD simulations. Experimental verification of this hypothesis would require a suitable flow visualization method. Since COP and the cooling capacity are both directly proportional to ER for a constant primary mass flow rate, their behavior was similar to the one observed for ER. The maximum cooling capacity was about 1.65 kW with a maximum COP of 0.26. Looking at Figure 5.4, one may also notice that nominal cooling capacity was reached in a relatively wide range of NXP (3 – 7 mm).

Figure 5.5 compares the COP results as a function of NXP obtained for two experimental sets. The first set was carried out with the conditions described in relation to Figure 5.4. The second set of experiments were carried out with a pump speed of 2500 rpm; an SP of 6.5 mm and a relative pressure at the primary inlet of 12.2 bar (T_g ~ 87°C). The secondary inlet pressure and backpressure remained in the same levels as they were in the first set of experiments. These conditions resulted in a primary mass flow rate of about 22.4 g/s. Because of the high primary inlet pressure, this set was carried out only for four NXP values (from 4.5 to 6 mm). The ERS was not tested for NXP < 4.5 mm in order to prevent any possible damage to the pump. The primary mass flow rates of the first and second experimental sets were 16.4 g/s and 22.4 g/s, respectively. As expected, for higher primary flow, when the ejector is operating in double-choking mode, higher P_g resulted in smaller COP and cooling capacity for all values of the NXP. This can be explained by the fact that during the second set of experiments, the primary jet leaves the nozzle exit section in a more under expanded state, which leads to smaller secondary mass flow rates (difference about 1 g/s). It can also be seen from Figure 5.5 that the optimal NXP value was the 5 mm for both sets of experiments, and the variation of COP with NXP is not very significant between 4 ÷ 6 mm. Further comparing the two curves, it seems that the influence of NXP before and after the optimal point is more relevant at the higher P_g one. This can also be explained the more under expanded primary jet for the higher P_g set, in which case any change in the cross section area in the mixing chamber has a higher impact on the effective area for the secondary stream (a similar argument can be found in [161]).

Figure 5.5 also presents the influence of NXP to the system performance at primary pressure of 8.6 bar (averaged T_g ~ 85°C with constant SP at 10 mm). Despite the low primary pressure inlet, the maximum open position of the spindle resulted in a high primary mass flow rate, of about 20.3 g/s. High $\dot{m}_g$ might be the reason of the low COP, backpressure was remained constant, as discussed previously. The COP of the experiment with P_g of 8.6 bar remained mostly constant, at about 0.21, in the entire NXP range. Discussion on the influence of NXP on the system performance is still opened. Some authors claimed that NXP plays an important role while others said differently. The results from these experiments seem to clarify one point that the influence of NXP strongly depends on the magnitude of p_g. Comparing all three experimental sets, it can be concluded that the higher P_g is, the influence of NXP to the COP is more significant NXP. It is also noticed that COP was highest in the first experimental set, in which the $\dot{m}_g$ was only 16.4 g/s, being the lowest in all three experiments.

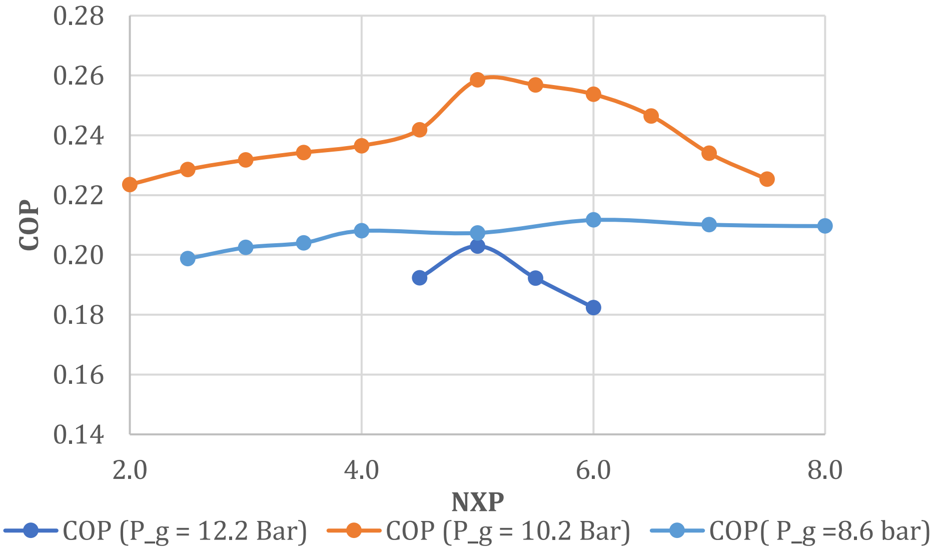

Figure 5.5 Comparison of COP as a function of NXP for three pressure levels of the primary flow.

5.3 System performance as a function of the spindle position

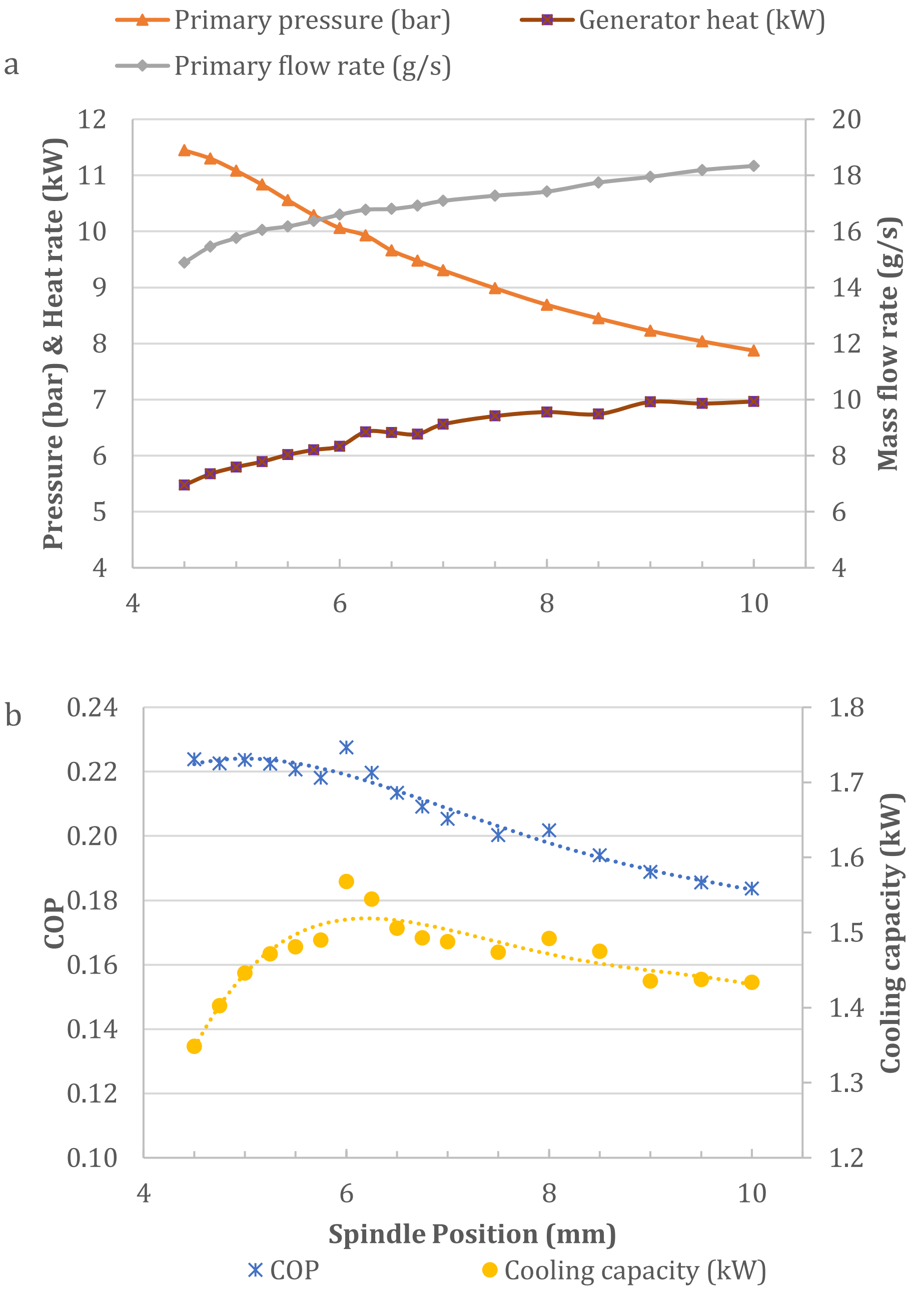

Figure 5.6 The influence of SP on (a) the primary inlet conditions and (b) system performance.

The ER and COP are complex functions of the inlet pressures/temperatures, back pressure, and flow path geometry. The individual impact of each of these variables is not easy to describe and quantify experimentally since they are strongly interconnected. In this section, the influence of SP is discussed. For a given ejector geometry, the system operates at the optimal performance (or at the critical point) when the primary inlet conditions are selected such that the primary jet is perfectly expanded as it leaves the nozzle or slightly over-expanded according to [162]. Nevertheless, the highest entrainment ratio is obtained when a parallel primary jet is formed downstream of the nozzle exit plain. Strong under expansion is not recommended because it may reduce the effective area for the secondary stream as it was mentioned in section 5.1. It has been observed by several authors (e.g., [161]) that a series of strong shockwaves may occur downstream the nozzle outlet resulting in unwanted losses of the kinetic energy and thus leading to the reduction of the entrainment ratio. Conversely, high overexpansion of the primary flow also causes a decline in the entrainment ratio. The primary mass flow rate should be just high enough in order to transfer sufficient momentum to the secondary stream to reach Ma = 1 in the mixing chamber [28, 34]. Further increase in $\dot{m}_g$ only increases generator heat consumption without further benefit regarding the cooling capacity.

Figure 5.6 shows the influence of the spindle position on the primary flow characteristics and system performance for a pump speed of 2000 rpm. In this experimental set, the spindle position was adjusted from 4.5 mm to 10 mm, while pump frequency was maintained constant. Accordingly, P_g decreased from 11.4 to 7.9 bar and $\dot{m}_g$ increased from 9 g/s to 18.3 g/s because of the larger primary nozzle throat area for the motive stream. Please note that the ejector outlet and the secondary inlet pressures remained nearly constant; 3.2 bar (saturation temperature ~31.4°C) and 1.1 bar (saturation temperature ~8.5°C), respectively. The results indicated that for an SP in the range of 4.5 to 6 mm, the increased primary flow enhanced the secondary flow entrainment and thus increased to cooling capacity from about 1.3 kW to 1.6 kW (see Figure 5.6b). For any SP > 6 mm, the cooling capacity started to decline. Mostly likely when the primary flow rate increased and primary pressure decrease, the flow at the downstream of the primary nozzle was over expanded, but the high flow rate occupied more space at the mixing chamber, resulted in a reduction of the effective area for the secondary stream. This phenomenon was accompanied by the reduction of the cooling capacity, as shown in Figure 5.6b. In contrast, the energy consumption in the generator monotonously increased with SP. Hence, the cooling cycle operated at nearly constant COP for SP < 6 mm because the energy consumption and the cooling capacity were nearly proportional. These performance characteristics could not be obtained with a constant geometry ejector. The optimal spindle position, under the tested operating conditions, was found to be between 5 to 6 mm yielding the highest cooling capacity as well as overall COP. A comparison to a fixed geometry ejector can be made by analyzing the improvement of the COP at the maximum point and the fully open SP (the case where the spindle does not influence the area ratio). In this case, a performance improvement of 24% was obtained.

Figure 5.7 visualizes the performance behavior of the SERS during a second experimental set, which was also carried out for a pump speed of 2000 rpm. In this case, however, a lower back pressure of about 2.88 bar (saturation temperature was about 29°C) and a higher evaporator pressure of about 1.2 bar ($T_e = 10$°C) were maintained. The primary inlet conditions were kept similar to the ones during the first experimental set. The spindle position was adjusted from 6 to 9 mm. The results indicated that the primary inlet pressure varied from 9 to 7.3 bar and the primary flow rate increased from 14.8 to 16.2 g/s, because of the same reasoning as before. Looking at the data in Figure 5.7, one may note that the ejector generally performed better in this second experimental set than during the first one, mostly because of the difference in the secondary inlet and condenser conditions. The secondary flow reached its peak value of 5.7 g/s at SP of 7.5 mm, while the highest COP (0.28) was obtained for an SP of 6.5 mm. For any SP > 7 mm, the COP considerably decreased, the lowest value was obtained for the most open spindle position tested. It is estimated that the performance improvement was about 20% compared to a fixed geometry ejector. Comparing the two data sets, one may note that the highest COPs were obtained for different spindle positions (5.5 mm for the first set versus 7.5 mm for the second set) due to the differences in the operating conditions. The incident clearly indicates the benefit of applying the variable geometry design over the fixed geometry solution. Nevertheless, it is believed by the authors that the ejector cycle performance can be further improved. Looking at the COP and secondary flow rate curves, one may note that the maximum values of these two variables did not occur for the same SP. It is because at SP = 6.5 mm, the primary stream, with a mass flow rate of about 15.2 g/s and the inlet pressure of 8.6 bar, did not transfer sufficient momentum to the secondary stream to entrain the maximum amount of refrigerant. The maximum value of $\dot{m}_e$ was observed for a primary fluid mass flow rate of 15.6 g/s with an inlet pressure of 8 bar (SP = 7.5 mm) due to better momentum exchange. The cooling cycle performance could be further improved by reducing the primary inlet pressure, without considerably changing its mass flow rate. This can only be done using a pump with continuous speed control and by simultaneously reducing the SP and the pump speed, which was not possible with the current experimental configuration. Although the benefit of the variable geometry ejector design was clearly demonstrated with the experimental data, the system can only be operated with optimal performance in a configuration where SP and the primary inlet pressure can be controlled independently.

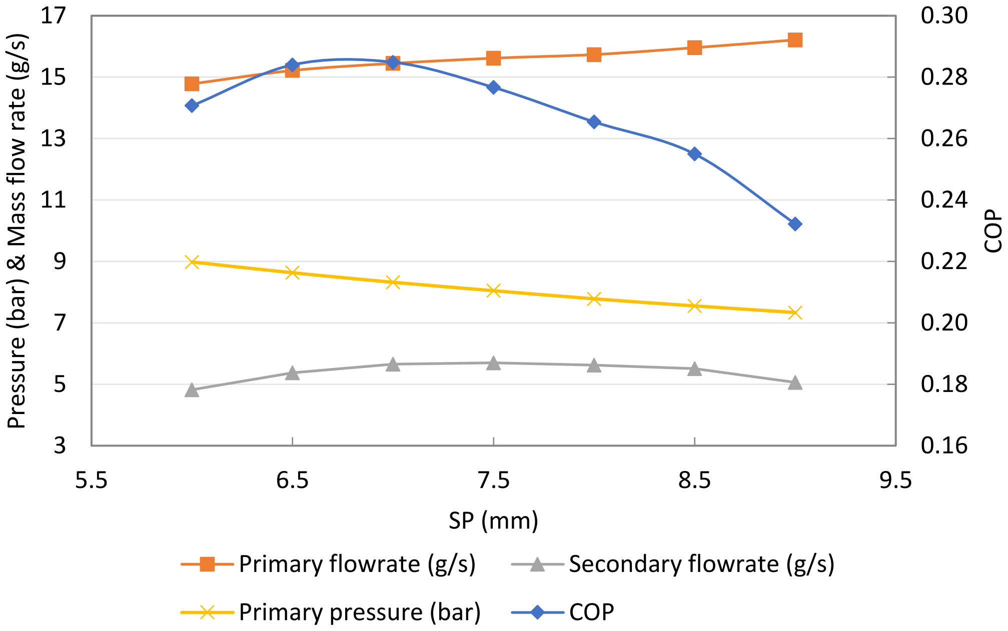

Figure 5.7: Ejector flow characteristics and COP as a function of the spindle position for the pump speed of 2000 rpm.

5.4 System behavior in off-design regime

Off-design operation of the solar heat driven ejector cooling cycle was tested by changing the ejector back pressure during the experiments. A flow control valve was installed to regulate the cooling water flow rate at the outlet of the condenser. Two sets of experiments were carried out for different values of spindle position but for a constant pump speed of 2000 rpm. For high cooling water flow rates, back pressure is determined by water temperature only. By reducing the cooling water flow rate, the refrigerant condenses at a higher temperature, which in turn increase P_c and the subcooled stated of the refrigerant liquid at the condenser outlet. Note that some degree of subcooling is always required to avoid refrigerant pump cavitation.

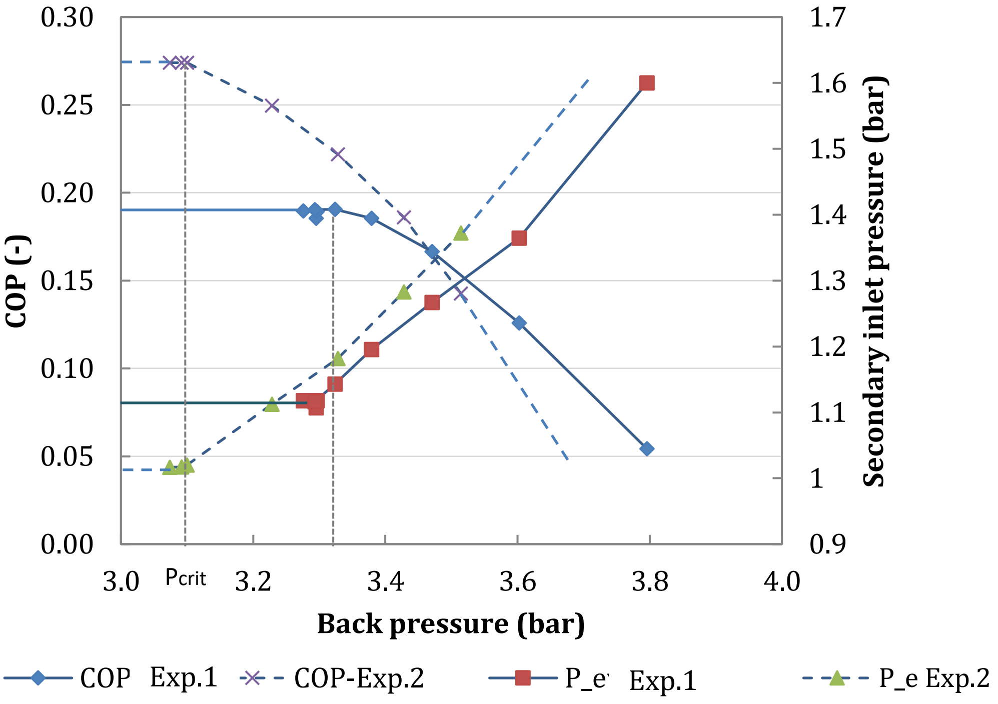

Figure 5.8: Behaviour of secondary inlet pressure and COP in variations of the backpressure.

Figure 5.8 shows the experimental data obtained for the COP and P_e with the backpressure. Two experimental sets, denoted by "Exp1" and "Exp2", were carried out on two distinct days. Exp1 was carried out for an SP of 9.5 mm and P_g = 8.0 bar, corresponding to a primary mass flow rate of about 18.6 g/s. This SP corresponds to a nearly fully open position so that the performance of the ejector is equivalent to a fixed geometry device. The secondary inlet pressure during this first set of experiments was about 1.1 bar (T_e = 8.5°C). The lower limit for the backpressure was 3.3 bar corresponding to a fully open cooling water valve. In this case, the SERS operated with its highest COP (~0.19), which remained nearly constant even by increasing P_c to about 3.4 bar (T_c = 33°C), indicating that the system operated within the on-design regime. Beyond this point, COP decreased rapidly up to a break pressure of about 3.9 bar (T_c = 37°C). The second experimental set (Exp2) was carried out for a more closed spindle position of 6 mm, resulting in a primary pressure of 10.2 bar and mass flow rate of 17.3 g/s, which are about 2.2 bar higher for P_g and 1.3 g/s lower for $\dot{m}_g$ when compared to Exp1. It is clear from Figure 5.8 that the system achieved a COP (0.27) that is about 42% higher than in Exp1, but with a somewhat lower of critical back pressure as the penalty. The reduction of both P_{crit} and P_{break} were about 0.2 bar. The fully open ejector (SP = 9.5 mm), equivalent to fixed geometry solution, only worked at better performance for condenser pressures above 3.5 bar, while for any P_c below this value, the variable geometry design is more beneficial. The evolution of P_e with the back pressure also reflects on the operating regime of the ejector. It can be seen in Figure 5.8 that the secondary inlet pressure remained essentially unchanged during on-design operation. The occurrence can be explained by the choking of the secondary stream below the critical backpressure. However, for any pressure beyond the critical value, the secondary flow was not chocked; thus, the pressure difference between inlet and outlet depends on the momentum exchange between the primary and secondary streams. In fact, the pressure lift ($P_c - P_e$) remained relatively constant 2.1 bar and 2.2 bar for Exp1 and Exp2 respectively. Similar observations were made by Falat et al. [163] in their experimental study using R134a. In conclusion, the variable geometry ejector was able to better respond to the off-design operating conditions than a fixed geometry unit.

5.5 Mathematical model validation

The experimental data were used for validating the mathematical model of the ejector. For the validating purpose, the spindle position was set to the maximum value, i.e., SP = 10 mm, at which the influence of the spindle to the primary flow is negligible [108]. Thus, the variable geometry ejector can now be considered as a fixed geometry ejector, which simplifies the mathematical modeling.

The experimental data were used as inputs to the mathematical model, i.e., the working temperatures, pressures at the ejector inlets and outlet, and the ejector geometry. The entrainment ratio and the COP from the mathematical model were compared with the results of experimental work.

As seen in Figure 5.9, the predicted values from the mathematical model well agreed with the experimental results, values of both entrainment ratio (ER) and the coefficient of performance (COP) were within ±15%.

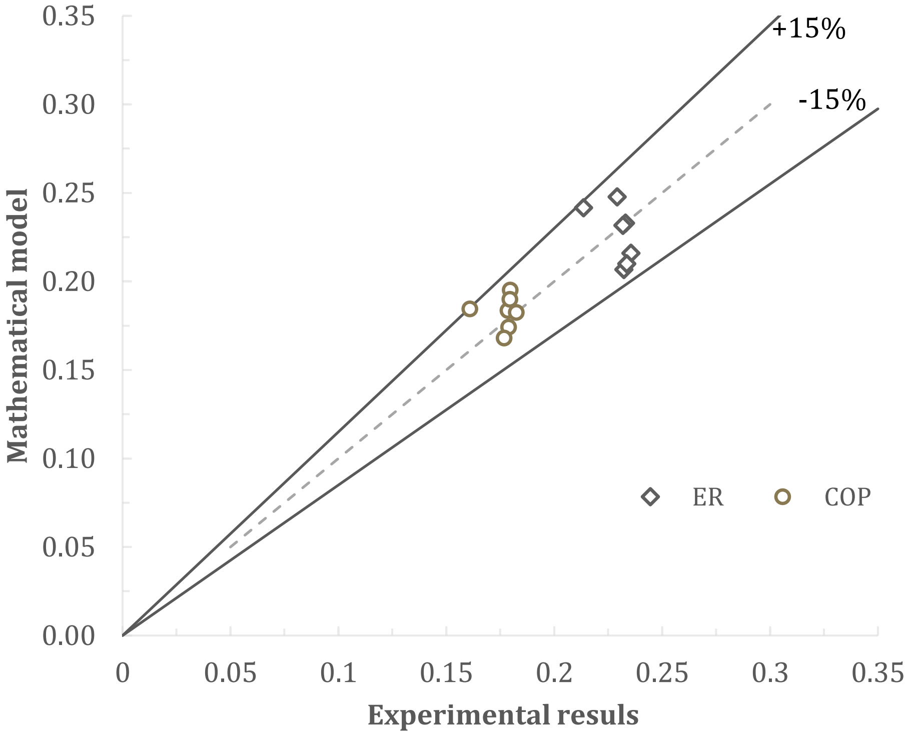

Figure 5.9: Comparison of experimental results with results from the mathematical model.

5.6 Conclusions

In the present study, the performance of a small capacity solar thermal energy driven variable geometry cooling system using R600a was experimentally assessed under various operating conditions. The objectives were to evaluate the influence of two geometric factors (NXP and SP) and the back pressure on the behavior of the system operating with constant circulator pump speed. In general terms, the results indicated a very stable operation of the cooling cycle on clear or partially cloudy days when the interruption of direct solar radiation was no longer than 30 minutes.

It was found that the nozzle exit position considerably influenced ejector performance for both levels of the vapor generator pressure tested (12.2 bar and 10.2 bar). The results indicated a stronger influence of NXP on the COP for the higher level of the primary nozzle inlet pressure. Nevertheless, in both cases, there was an optimum value of the COP obtained for the same NXP (5 mm from the fully closed position). It can be concluded that NXP should be optimized for each ejector design; however, its position does not need to be changed for variable primary nozzle inlet pressures.

The spindle position has a direct impact on the ejector area ratio. For constant pump speed, SP affected essentially all operating parameters, including generator pressure, mass flow rates, COP, generator heat, and cooling capacity. The results of the two sets of experiments that were carried out for different evaporator and back pressures indicated that there is an optimal SP, which results in the highest cooling cycle COP. However, this optimal SP depends on the operating conditions. This clearly shows the benefit of the variable geometry ejector design over the fixed geometry one. The improvement of the COP was up to 42% under the tested conditions. It is believed that the optimal COP can be further improved by independent control of the primary flow rate/spindle position and primary inlet pressure, which could be done using a variable speed pump with continuous control features. The present experimental test rig will be changed to verify this theory.

Finally, the solar driven cooling cycle performance was also tested for the off-design operation regime. Experiments were carried out for two different values of SP, one corresponding to the fully open position (fixed geometry ejector case), by varying the ejector backpressure. The operating curves were determined, and the results showed a clear benefit of the variable geometry solution for back pressure lower than the design values. The evolution of the evaporator pressure in the test unit, having a manual expansion vale, was found to be a function of the applied back pressure in the off-design regime, indicating the single chocking operation of the ejector.

6 WORKING FLUID ASSESSMENT

6.1 Working fluid selection

Chapter 2 comprehensively reviewed the refrigerants used in the ejector cooling technology. Generally, working fluids need to fulfill certain criteria on system performance, environmental safety, economics. Thermodynamic properties of refrigerants directly influence the performance of the refrigeration cycle; thus, they are the key factors in selecting working fluids. They must have low specific sensible heat capacity, high latent heat of vaporization [164], large generator temperature range, suitable critical temperature. The slope of the saturated-vapor line of the fluid in the Temperature-entropy diagram should be positive (dry fluid) to minimize the required superheating amount of the ejector inlet flows. They must be environmentally friendly, which means that GWP and ODP indexes of refrigerants must be within the limit values of the regulation 517/2014. They should be non-toxic, non-corrosive, chemically stable, and non-explosive. Also, a high molecular-mass refrigerant is preferable due to the compactness of the system.

For a particular set of operating temperatures at the ejector inlets and outlet, the following working pressures are preferable. The working pressure at the ejector primary inlet (generator) should not be too high to avoid a robust construction of the ejector refrigeration cycle. The working pressure at the ejector secondary inlet (evaporator) should be above atmospheric pressure to avoid the possible leakage from the ambiance. The working pressure at the ejector outlet (condenser) should not be too high compared with the secondary inlet pressure. Theoretically, an ejector could obtain a high entrainment ratio if the compression ratio (pressure ratio between the ejector outlet and secondary inlet) is low.

The current study presents assessments of seven working fluids that are potential for ejector cooling technology. They are two HFCs (R134a, R152a), one nature refrigerant (R600a), and four HFOs (R1234ze(e), R1234ze(z), R1234yf, R1233zd(e)).

As mentioned in chapter 2, R134a and R152a are the most favorable refrigerants in terms of performance. R152a and R134 are suitable for various refrigeration technologies, including ejector refrigeration technology. Probably R134a is currently the most common working fluid in the refrigeration industry. R152a has a fairly low GWP100 index (see Table

6.1); furthermore, it has exceptional performance as discussed in the literature review. R600a has a reasonable performance with promising working pressure levels. It is non-toxic and environmentally friendly with a negligible GWP100 index. However, its flammability could be a drawback. These working fluids were used in the current study as references.

Table 6.1 presents the key properties of the assessed refrigerants. Isomers, R1234ze(e), R1234ze(z) and R1234yf, have the same molecular weight but dissimilar in properties. For example, R1234ze(z) has a high boiling point (9.8°C), associating with a higher critical temperature (153.7°C) and a volumetric capacity of about 50% lower in comparison with R-1234ze(e). They are very environmental-friendly, but they are flammable at a low level (A2L). In contrary R1233zd(e) is nonflammable. It has a low working pressure level in the working range of a typical generator temperature working range for ejector cooling technology (< 100°C). Part of the study is to indicate which fluids among the HFOs are the most proper candidates for the ejector cooling system.

Table 6.1: Key properties of the selected working fluids.

	M_{mol} (g/mol)	T_{cri} (°C)	p_{cri} (bar)	**GWP100**	**Safety class**	**SSL**	L_{ratio}
R1233zd(e)	130.5	165.6	35.7	1	A1	Positive	1.29
R1234yf	114	94.7	33.8	4	A2L	Positive	2.35
R1234ze(e)	114	109.4	36.3	7	A2L	Positive	1.9
R1234ze(z)	114	150.1	35.3	≤ 6[165]	A2L	Positive	1.35
R134a	102	101	40.6	1430	A1	Negative	2.0
R152a	66.1	113.3	45.2	124	A2	Negative	1.67
R600a	58.1	134.7	36.4	3	A3	Positive	1.42

6.2 Working conditions of the assessment

The mathematical model was implemented in Engineer Equation Solver (EES) program. EES is a program that numerically solves a set of equations by an iterative method. EES provides high accuracy thermodynamic and transport property database of hundreds of substances which can be used with equation solving capability [137].

As mentioned in chapter 3, the mathematical model could propose a system that works at optimal performance for a random set of working conditions. As discussed in Chapter 2, the design point concept is used to describe the critical point of the ejector for particular working conditions. From which the ejector geometry is defined to obtain the optimal system performance.

The assessments study the behaviors of the refrigerants by analyzing the performance factors with variations of the operating temperatures. Due to the length limit of the thesis, only key performance factors are presented. By default, the degree of superheat at the generator was set to 7 K, and 2 K at the evaporator. The subcooling of refrigerant liquid at the condenser outlet is set to 2 K.

The design point is selected based on the required cooling capacity and the operating temperatures. The operating temperatures may depend on the actual situation where the ERS works. For example, the refrigerant temperature at the condenser (T_c) depends on the chilling (water) source and the refrigerant temperature of the evaporator (T_e) depends on the desired cooling temperature.

Based on the actual needs and requirements for space cooling purpose for a novel ejector refrigeration system, the default working temperatures of the of $T_{g,sat}$, $T_{c,sat}$, and $T_{e,sat}$ were set to 83°C, 34°C, and 10°C, respectively. The system nominal cooling capacity was set to 5 kW.

6.3 The influences of superheating of the inlet flows on the system performance

As mentioned in chapter 2, studies on the superheat of the primary flow and the secondary flow in the literature were not quite comprehensively presented. Besides, the behavior of working fluids on the superheating can be different from each other. In this section, the influences of the superheating of the ejector inlet flows are discussed.

The superheating range at the generator is 3÷23 K, and at the evaporator is 1÷11 K. Note that the subcooling degree at the condenser outlet is set to 2 K. The subcooled degree is necessary for the refrigerant pump, especially the centrifugal type, in order to avoid cavitation in the pump impeller. The cavitation may cause instability, even malfunction to the system. The cavitation also causes damage to the refrigerant pump. These observations were mentioned in the works of Yapici [121] and Grazzini [20]. The incidents were also observed in the present experimental work.

6.3.1 Superheat of the primary inlet flow

Figure 6.1 presents the behavior of the entrainment ratio on the variation of $\Delta T_{sh,g}$. As can be seen in in the figure, ERs of the selected refrigerants generally decrease as the superheating degree gets to higher values. Increasing only T_{sup} in the right hand side of equation (3-4) results in the raise of the primary flow rate; as consequently, entrainment ratio decreases. Assuming the ejector work at the critical condition, the critical velocity of the primary flow (v_{cr}) is limited by the speed of sound (a_{cr}), as shown in the following equation [166]:

$$v_{cr} = a_{cr} = \sqrt{2\frac{\kappa}{\kappa+1}r\left(T_{g,sat} + T_{sup}\right)} \quad , \qquad (6\text{-}1)$$

κ is the specific heat capacity ratio, and r is the specific gas constant of the working fluid. The equation indicates the direct influence of the superheating degree to the velocity of the flow. Besides, the values κ and r can be significantly varied by the variation of primary temperature. In general, the fluid velocity increase when the superheating amount increase.

The variations of these parameters result in a diversity of ERs of the selected working fluids. The less influenced fluid (by the superheat) were R600a and R1233zd(e). For example, ER_{R600a} at $\Delta T_{sh,g}$ of 3 K was 0.415 while ER_{R600a} at $\Delta T_{sh,g}$ of 23 K was 0.409. On the contrary, superheat has the most considerable influence on the entrainment ratio of working fluid R1234ze(e).

Interestingly, $ER_{R1234yf}$ and ER_{R134a} behaved dissimilarly in comparison with the others. The ERs of the two refrigerants slightly increase as the superheat was set to higher values (Figure 6.1). As $\Delta T_{sh,g}$ exceeded 9 K, $ER_{R1234yf}$ and ER_{R134a} behaved similar to the other refrigerants.

Figure 6.2 shows the impact of the superheat of the primary flow on the system coefficient of performance. The general trend that can be seen in the figure is that the COPs of the refrigerants decreased with the superheating amount. The variation of all the COPs with the superheat seemed to be linear. Unlike the variation of ERs in the previous discussion, COPs of the working fluids strongly decreased with the superheating amount. The COPs of high-performance refrigerants seemed to be more sensitive by the superheat than the COPs of other refrigerants. For example, COP_{R152a} at the $\Delta T_{sh,g}$ of 23 K was 13.4% lower in compared with COP_{R152a} at $\Delta T_{sh,g}$ of 3 K. In other words, between the two extremes of superheating range in this study, COP_{R152a} was 13.4% different. For R1234yf and R1234ze(e), this number is 17.9% and 15.9%, respectively. In contrast, the low-performance refrigerant R1233zd(e), the reduction of COP was only 8.9%.

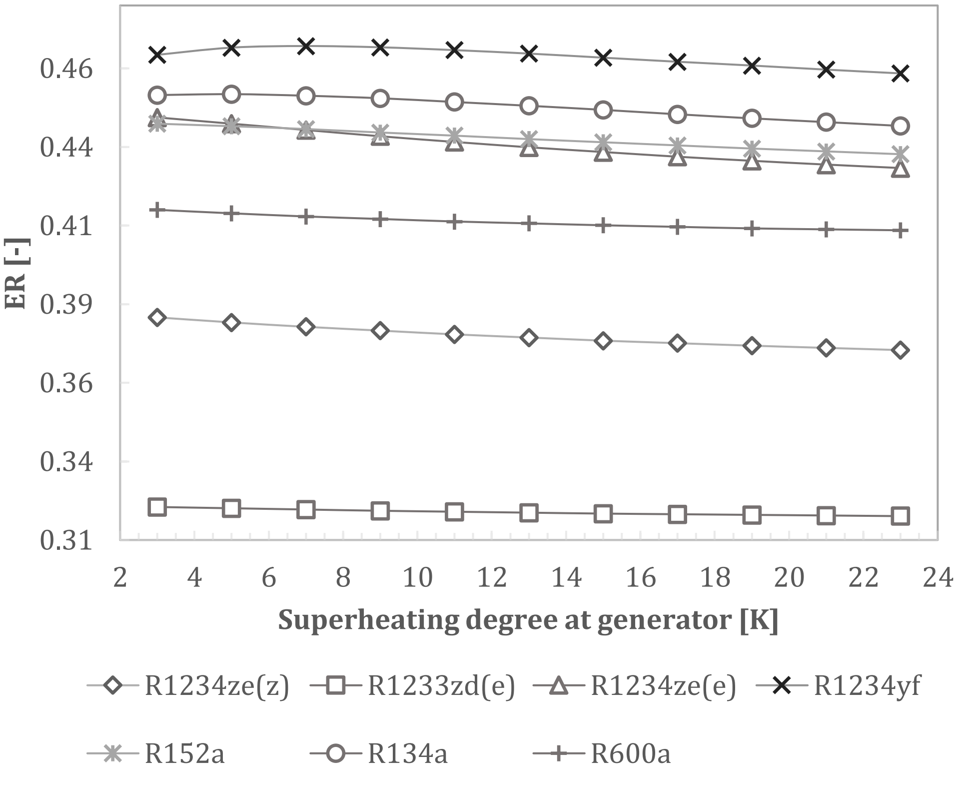

Figure 6.1 ER as a function of $\Delta T_{sh,g}$.

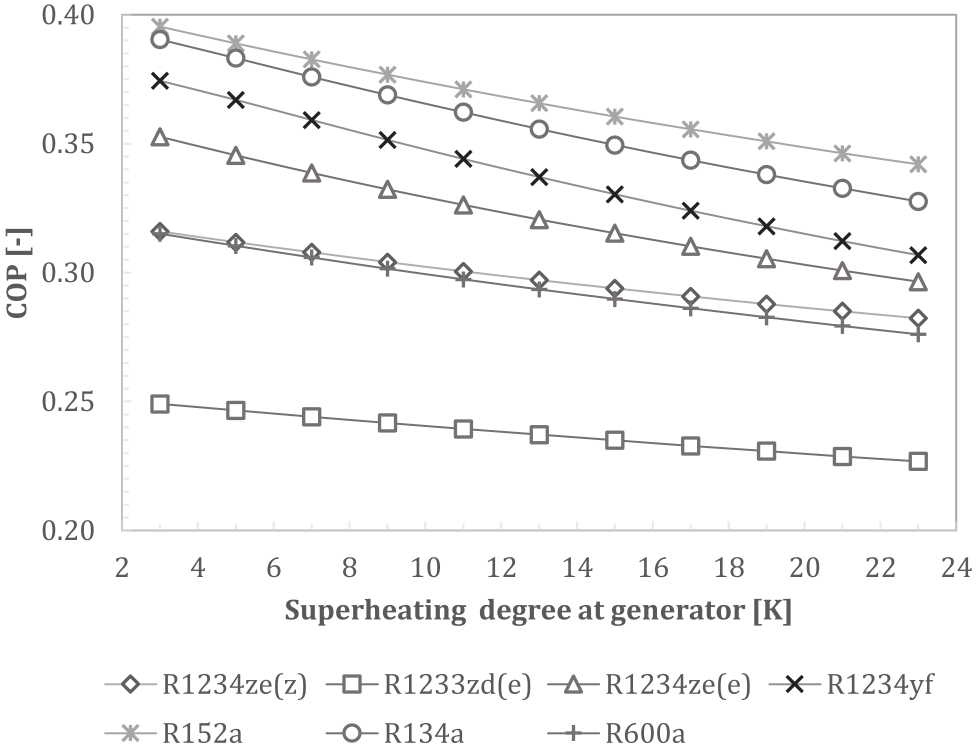

Figure 6.2 COP as a function of $\Delta T_{sh,g}$.

6.3.2 Superheat of the secondary inlet flow

Figure 6.3 shows the influence of the superheating of the secondary flow on the ejector entrainment ratio. During the variation of the superheating in the entire range (1÷11 K), ERs of the selected refrigerants were only slightly decreased. Similar to the previous case, the variation of ERs by $\Delta T_{sh,e}$ can be explained using equation (3-12). Comparing with ERs by $\Delta T_{sh,g}$ (see Figure 6.2), the variations of ERs by $\Delta T_{sh,e}$ of all the refrigerants is more uniform. The ER lines of the refrigerants were mostly parallel to each other; no irregular variation was noticed in the cases of $ER_{R1234yf}$ and ER_{R134a}, as previously discussed (see Figure 6.2).

It can be concluded that superheating in the inlet flows only causes a slight change of ERs. The behavior of the ER depends on the working fluid that is used and on the working temperature. For instance, ERs of the refrigerant more noticeably varied at the high working temperature (see Figure 6.2) in comparison with the low working temperature of the secondary inlet flow (Figure 6.3).

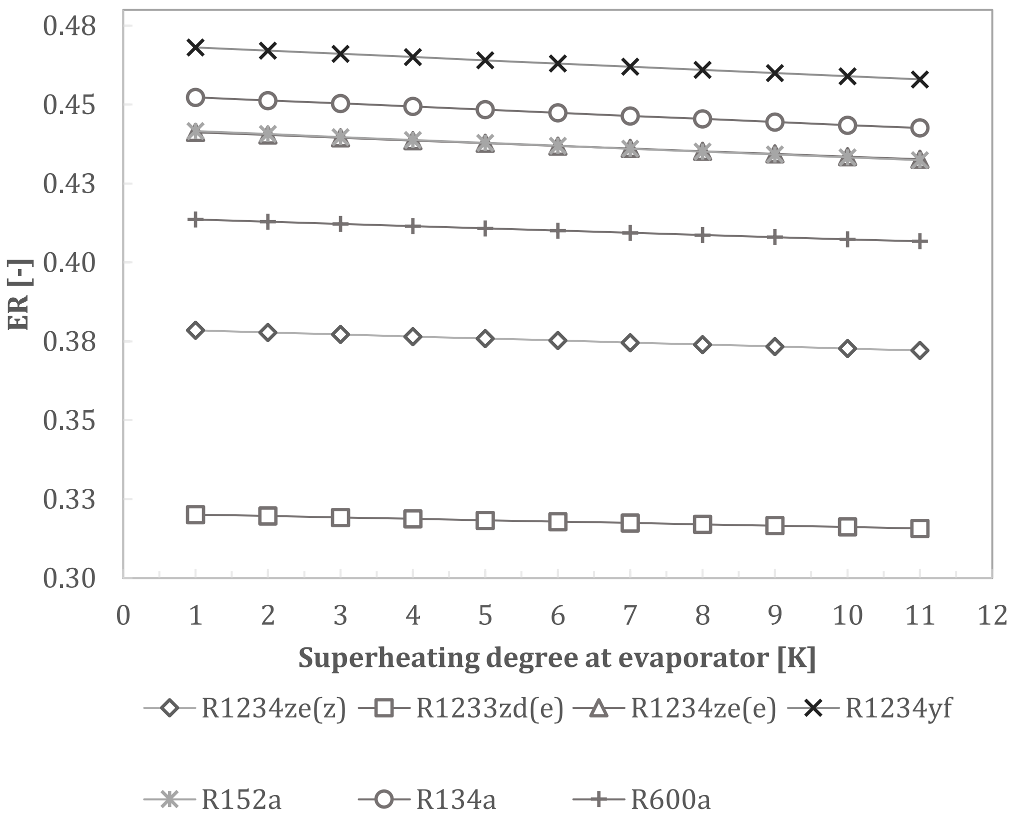

Figure 6.3 ER as a function of $\Delta T_{sh,e}$.

Figure 6.4 presents the influence of the superheating amount of the secondary inlet flow to the system performance. In contrary to the entrainment ratio, the COPs were considerably sensitive with the superheating variation. It can be seen in the figure that by increasing the superheating amount, the system performance got to more desired values. It can be explained by the formula of the system COP. The COP formula in equation 2.3 can be rewritten as:

$$COP \cong \frac{\dot{m}_e \, \Delta h_e}{\dot{m}_g \, \Delta h_g} \quad , \tag{6-2}$$

where, Δh_e is the enthalpy difference at the outlet and inlet of the evaporator and Δh_g is the enthalpy difference at the outlet and inlet of the generator.

As the superheating amount gets higher, the accumulated enthalpy into the secondary inlet flow becomes larger. Equation (6-2) indicates that Δh_e directly proportional to the COP. Thus, increasing the superheating amount yields an increment of the COP. As discussed before, the variation of the secondary flow rate by $\Delta T_{sh,e}$ is insignificant; the COP and $\Delta T_{sh,e}$

are directly proportional to each other. So, by increasing the superheating amount at the secondary inlet flow, the system performance is more favorable.

In the experimental work of the thesis, it was observed that the superheat in the secondary inlet flow seemed to always present. The refrigerant travels from the evaporator to the ejector secondary inlet by the sucking effect. It results in vacuum pressure in this area, thus there is some degree of superheating in the secondary inlet flow. The experimental work of the current thesis observed an amount of $\Delta T_{sh,e}$ of about 2÷7 K.

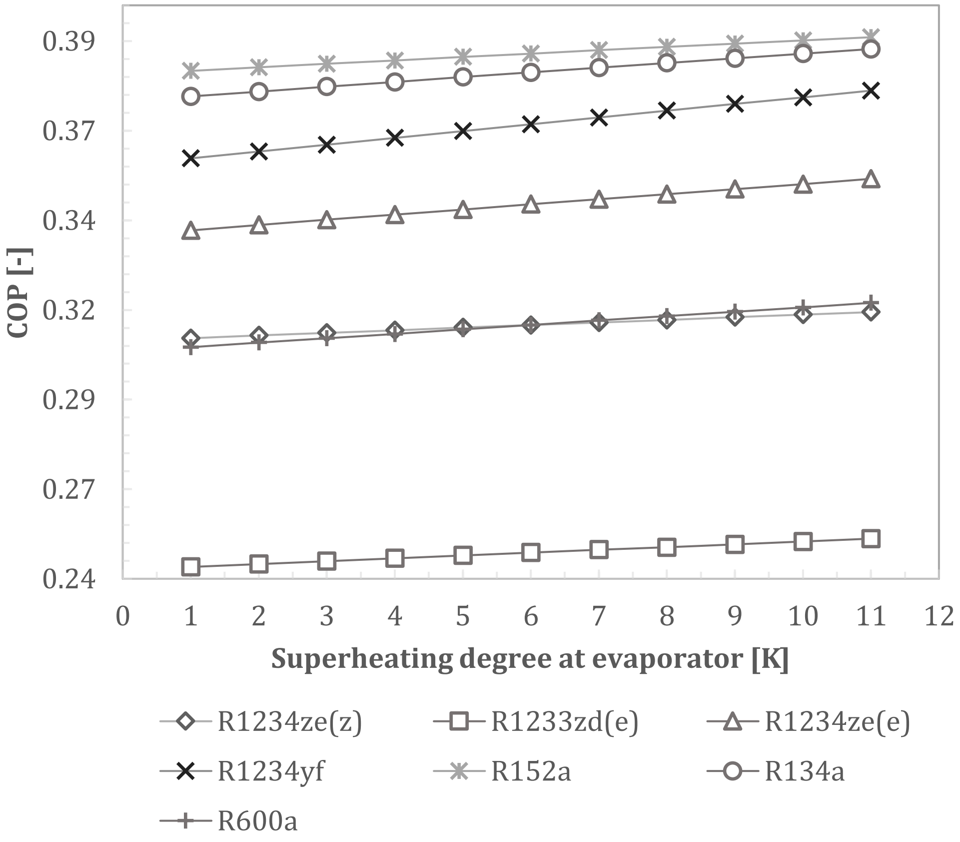

Figure 6.4 COP as a function of $\Delta T_{sh,e}$.

The COP variation by $\Delta T_{sh,e}$ of each refrigerant is dissimilar. It is mostly because the specific enthalpies of each refrigerant at the same amount of $\Delta T_{sh,e}$ are different. In the other words, the amount of specific enthalpy gain with a certain change of superheating is various for different refrigerants.

Comparing Figure 6.2 and Figure 6.4, it can be seen that the influence of the superheat in the primary inlet flow to the system performance seemed to be more significant than in the secondary inlet flow.

6.4 Influences of the working temperatures on system performance

Previously, the influences of superheating on system performance were discussed. In this section, saturation temperatures were used as reference for assessing the selected working fluids. By default, the superheating degrees were set to constant values to the rest of the working fluid assessments: $\Delta T_{sh,e}$ = 2 K and $\Delta T_{sh,g}$ = 7 K.

6.4.1 Entrainment ratio as a function of the saturation temperatures

Figure 6.5 shows the relationship between the entrainment ratio and the saturation temperature at the generator (or saturation temperature of the primary inlet flow) for the seven selected working fluids. The figure indicates a strong dependence of entrainment ratio on the saturation temperature at the generator ($T_{g,sat}$). The horizontal dashed line at ER of 0.25 (see Figure 6.5) presents the base value for the assessment. At $T_{g,sat}$ of ~ 67°C, ERs of all the refrigerants were significantly lower than the base value. At $T_{g,sat}$ of ~ 75°C, all the working fluids, excepts R1233zd(e), had ERs higher than 0.25. Correspondingly to these two values of $T_{g,sat}$, ER of R1234yf increased from 0.22 to ~0.35, i.e. about 60%. In fact, ERs of all working fluids were intensively influenced in the entire range of $T_{g,sat}$. ER of R1233zd(e), the poorest performance refrigerant, increased 280% as $T_{g,sat}$ varied from 70°C to 95°C.

R1234yf yielded the highest ER in its entire range of saturation temperature. Its ER reached 0.59 at $T_{g,sat}$ of about 94.7°C. As R1234yf approaches its critical temperature (94.7°C), increasing the generator temperature outlet can only increase the superheating amount of the primary inlet flow. Thus, the ER could slightly decrease, as discussed in the previous section. ER of the two HFCs were almost identical, following the most favorable working fluid, R1234yf. In contrast with R1234yf, ER of R1234ze(e) increased with higher intense when $T_{g,sat}$ increased. It surpassed ERs of R152a, R134a, and eventually R1234yf as $T_{g,sat}$ reached 98°C. R600a and R1234ze(z) offered average ERs compared to the others, being significantly higher than R1233zd(e). However, ER_{R600a} is visibly lower than ERs of the top four fluids, i.e., R1234yf, R152a, R134a, and R1234ze(e).

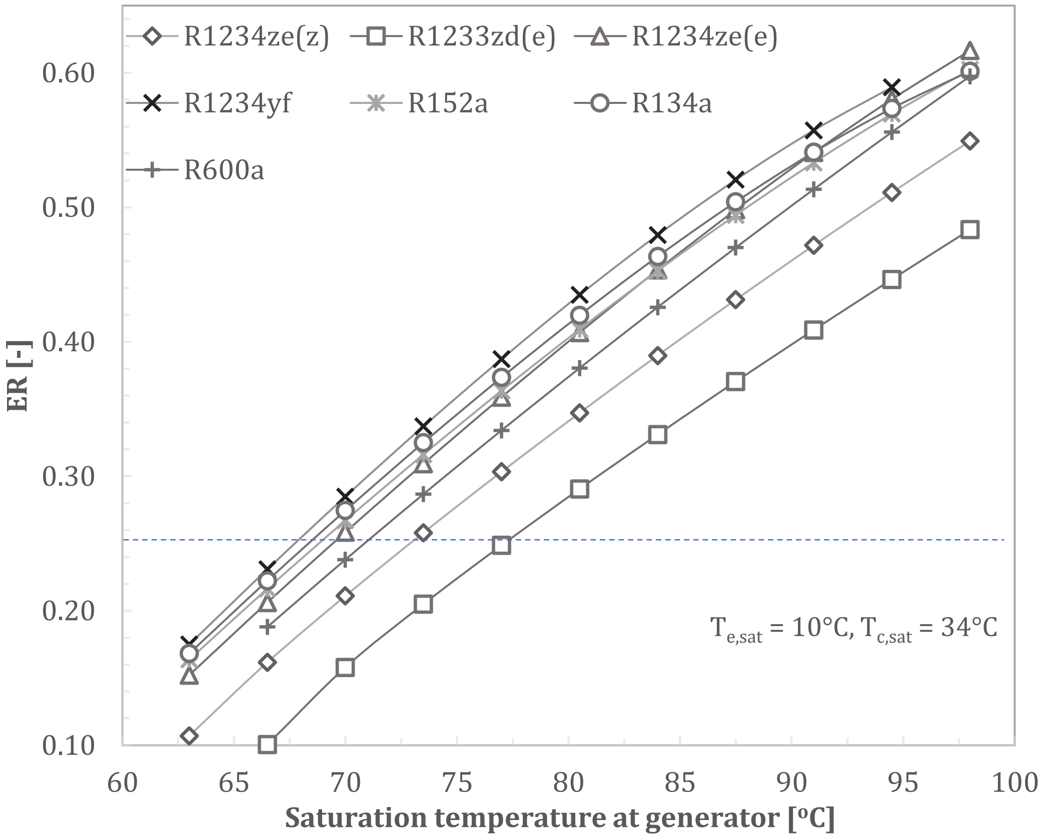

Figure 6.5 Entrainment ratio as a function of saturation temperature at generator ($T_{e,sat} = 10°C$ and $T_{c,sat} = 34°C$).

Figure 6.6 shows the influence of saturation temperature at the evaporator (in sort, evaporation temperature) on the ejector entrainment ratio of the selected working fluids. The saturation temperatures at the generator and condenser were set to 83°C and 34°C, respectively. As can be seen in Figure 6.6, ERs of the working fluids increased as $T_{e,sat}$ varied from 5 to 15°C. By increasing $T_{e,sat}$, the pressure at evaporator (p_e) intensifies, leading to the decline of pressure ratio p_c/p_e. Thus, ERs increase as $T_{e,sat}$ gets to higher value. The performance of the selected working fluids was significantly influenced by $T_{e,sat}$.

One might notice the similarity between Figure 6.5 and Figure 6.6 in terms of the placement of ER curves. That is to say, the refrigerants with the highest ERs were R1234yf, R152a, R134a, and R1234ze(e) followed by R600a, R1234ze(z), and R1233zd.

However, looking at Figure 6.6, it seemed like the ER of low-performance fluids, e.g., R1233zd(e), were more sensitive to the variation of $T_{e,sat}$ than the others. In the range $T_{e,sat}$ of 6-15°C, ER of R1233zd(e) gained 450% (from 0.1-0.45) while ER of R1234yf only gained 175% (0.32-0.56). Refrigerants reach a higher ER at a higher value of $T_{e,sat}$; and apparently, high evaporation temperature is even more preferred for the low-performance refrigerants like R1233zd(e) or R1234ze(z). ER of R1234ze(e) also seemed to be sensitive to the evaporation temperature than ERs of other top performance refrigerants. $ER_{R1234ze(e)}$ slowly surpassed ERs of R152a and R134a. A similar occurrence was observed in Figure 6.5.

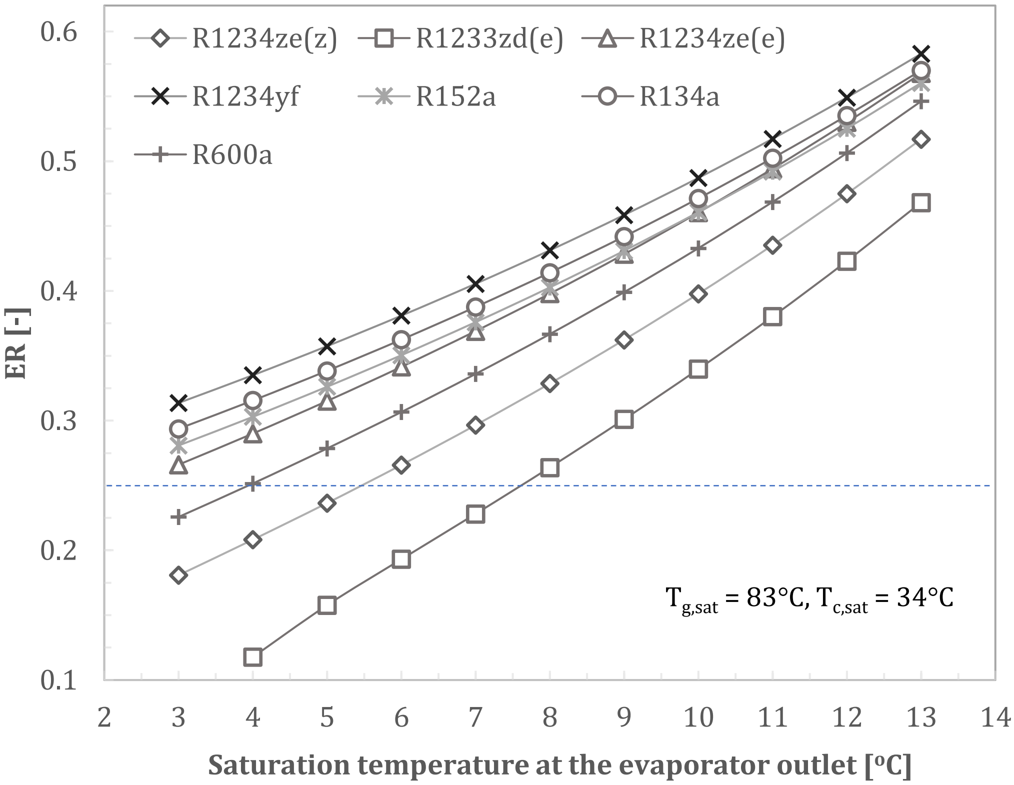

Figure 6.6 Entrainment ratio as a function of evaporator temperature for the seven selected working fluids (at constant $T_{g,sat} = 83°C$ and $T_{c,sat} = 34°C$).

Figure 6.7 presents the influences of saturation temperature at the condenser ($T_{c,sat}$) on the entrainment ratio. $T_{g,sat}$ and $T_{e,sat}$ were set to constants at 83°C and 10°C correspondingly. $T_{c,sat}$ range was 29÷39°C, the raise of $T_{c,sat}$ led to the increase of saturation pressure at the condenser (condensation pressure). This condensation pressure is approximately the pressure at ejector diffusor (the pressure drop of the refrigerant flow is usually negligible). Thus, the pressure ratio p_c/p_e (compression ratio) increased as the $T_{c,sat}$ was lifted higher. Consequently, ERs of the working fluids declined. Comparing to the influences of $T_{g,sat}$ and $T_{e,sat}$, the influence of $T_{c,sat}$ on ERs were more significant. Additionally, the variations of the ERs were mostly linear with the change of $T_{c,sat}$.

In the entire study range of condensation temperature, R1234yf always yielded the highest ER value, followed by R152a, R134a, and R1234ze(e); $ER_{\mathrm{R1233zd(e)}}$ was always the lowest. Interestingly, ER_{R600a} was comparable with the top performance refrigerants when $T_{c,sat}$ was low. For example at $T_{c,sat}$ of 29°C, ER_{R600a} was as high as ER_{R134a} and $ER_{\mathrm{R1234ze(e)}}$. ERs of these fluids diverged as the $T_{c,sat}$ approached to the high limit. At $T_{c,sat}$ of 39°C, ER_{R600a} was ~0.18, being considerably lower than ER_{134a} (~0.22).

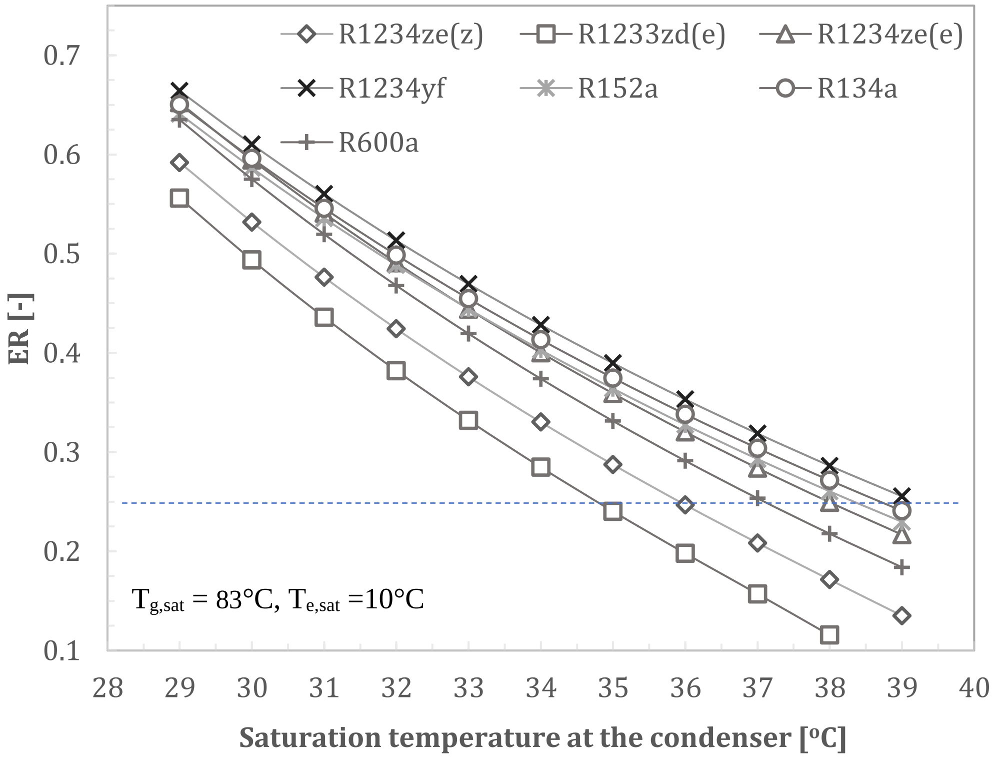

Figure 6.7 Entrainment ratio as a function of saturation temperature at condenser ($T_{g,sat} = 83°C$ and $T_{e,sat} = 10°C$).

6.4.2 Coefficient of performance as a function of the saturation temperatures

Figure 6.8 shows the variation of COP of the working fluids with $T_{g,sat}$. COP is directly proportional to ER, as indicated in equation(6-2). COPs generally increased with the generator temperature, regardless of the working fluid. However, the two HFCs (R152a and R134a offered the highest coefficient of performance despite having less desirable ER values compared to R1234yf. It could be because the enthalpy difference ratios ($\frac{\Delta h_e}{\Delta h_g}$) of the two HFCs are considerably greater than $\frac{\Delta h_e}{\Delta h_g}$ of R1234yf and R1234ze(e). Overall, R1234yf and R1234ze(e) offered favorable performances, while R1233zd(e) yielded a significantly poorer performance than the other working fluids. It is worthy of mentioning that the ratio $\frac{\Delta h_e}{\Delta h_g}$ increase with $T_{g,sat}$; and $\frac{\Delta h_e}{\Delta h_g}$ reaches the maximum as $T_{g,sat}$ is close to the critical temperature of the working fluid (as illustrated by the pressure-enthalpy diagram in Figure 0.4). This might be one reason for the performance improvement of R1234ze(z) or R152a. As shown in Figure 6.8, $COP_{R1234ze(z)}$ intensively increased with $T_{g,sat}$ and eventually surpassed COP_{R600a} at $T_{g,sat}$ of about 73°C.

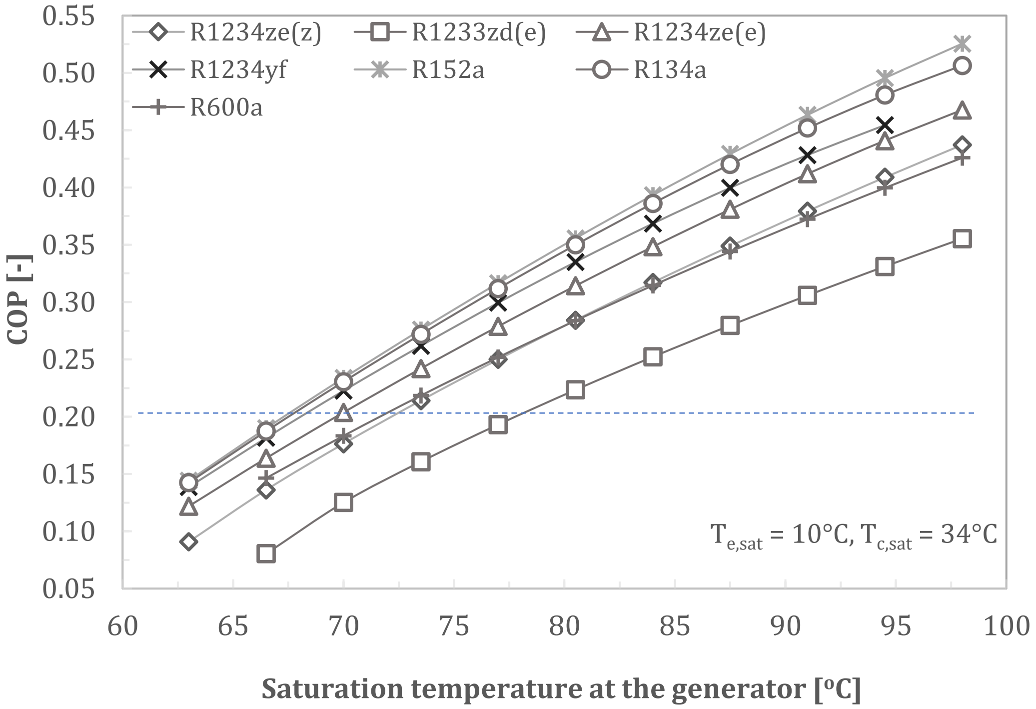

Figure 6.8 COP as a function of the saturation at the generator.

Figure 6.9, and Figure 6.10 present the relationships of the COPs and $T_{e,sat}$, $T_{c,sat}$, respectively. Figure 6.9 shows that the COPs increased sharply with the evaporation temperature. Apparently, it could be highly beneficial to employ an ejector refrigeration technology with a saturation temperature at the evaporator of 10÷15°C. It is especially suitable for residential cooling space, where the required room temperature is 25÷30°C.

R152a offered the highest performance among the compared refrigerants. The excellence of the refrigerant was acknowledged widely in the literature, e.g., [26, 167, 168], and it is confirmed in the current study. Comparing with R134a, probably being the most common refrigerant currently, R152a has higher COPs in all operating conditions (see Figure 6.8, Figure 6.9, and Figure 6.10). COP_{R152a} was about 1÷2% higher over COP_{R134a} in the assessed temperature ranges.

R1234yf showed its superior performance compared to the other HFOs in this study. At $T_{g,sat} \cong 90°\text{C}$, $COP_{R1234yf}$ was about 0.43, being higher than $COP_{\text{R1234ze(z)}}$ and $COP_{\text{R1233zd(e)}}$ by 23% and 59%, respectively (see Figure 6.8). At the lower ranges of $T_{g,sat}$ and $T_{e,sat}$, the performance of R1234yf mostly matched the performance of R152a and R134a (see Figure 6.8 and Figure 6.9). R1234ze(e) offered visible lower COP than R1234yf in the entire ranges of the working temperatures. Still, R1234ze(e) can be considered as an excellent performance refrigerant in comparison with the others.

Please note that the critical temperature R1234yf is 94.7°C. Further increasing generator temperature does not increase the system performance. Rather it increases the system stability as the degree of superheating increases, as discussed in the previous section.

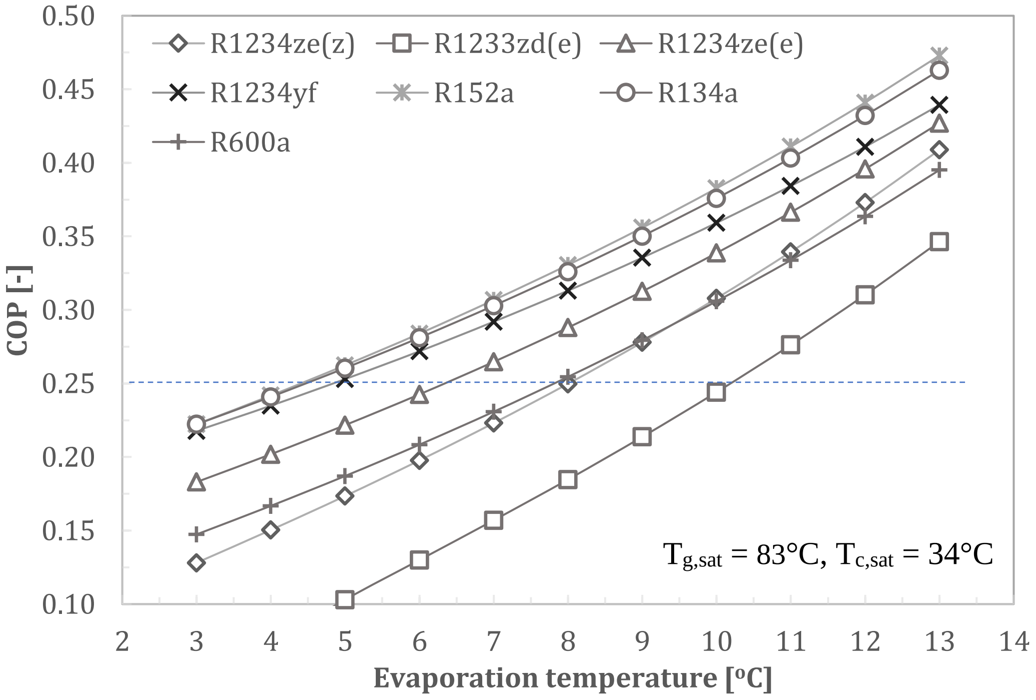

Figure 6.9 COP as a function of the evaporation temperature.

Comparing all three figures (Figure 6.8 to Figure 6.10) of this section, it is found that the condensation temperature has the most impact on the performance of the ERS. For example, as $T_{c,sat}$ varied from 29÷39°C, the $COP_{R1234ze(e)}$ dropped from 0.52 to 0.17, about

70% off compared with the initial value. In hot areas where space cooling is commonly needed, the outdoor temperature can be as high as 40°C. That being said, the selected range of $T_{c,sat}$ in this study is logical; however, high condenser temperatures cause an undesirable performance of the ejector cooling cycle.

It is believed that the performance sensitivity of the ERS on the condenser temperature is one of the major barriers that prevent applying ejector cooling technology to life. This issue could be solved using the water from sea, lake, etc. for chilling the condenser. However, this solution may limit the usage possibility of the ejector cooling technology due to the limited resources (water is less available than air).

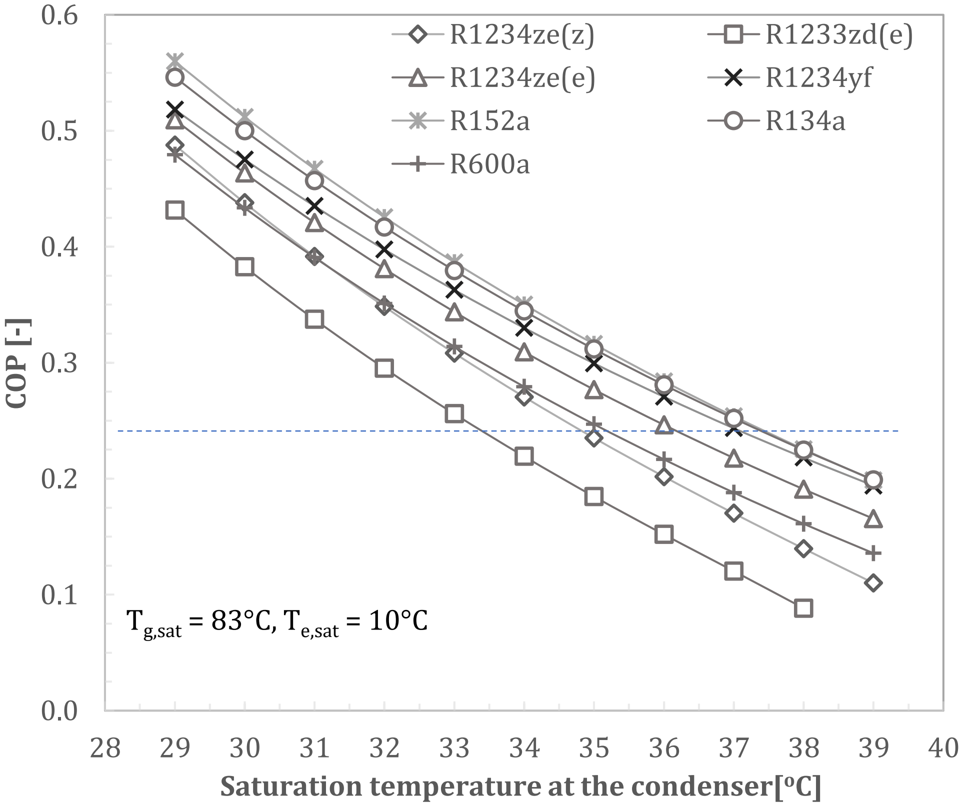

Figure 6.10 COP as a function of the condensation temperature.

6.4.3 Required heat flow rate at generator

The required heat rate for the generator $\dot{Q}_g$ is also a factor for evaluating the refrigerants. This section presents an assessment of the working fluids based on heat power used by the generator to produce 5 kW of cooling at various working temperatures. Basically, a low-performance refrigerant (low COP) requires a higher amount of heat power to produce the same cooling capacity. Accessing the refrigerants based on how much the heat rate at the generator is required is similar to the question "how well the refrigerants perform?". They are mostly the same but are viewed from a different angle.

The previous section showed that a low generator temperature results in a low COP. Equation (6-3) indicates that in order to maintain a constant cooling capacity ($\dot{Q}_e$), the generator heat rate needs to be high to compensate for the low COP. In other words, to conduct a constant $\dot{Q}_e$ (in this case, a constant entrained flow $\dot{m}_e$), higher primary flow $\dot{m}_g$ is required when the primary temperature decrease.

$$\dot{Q}_e \cong COP \cdot \dot{Q}_g \tag{6-3}$$

Figure 6.11 shows the association between the required $\dot{Q}_g$ and $T_{g,sat}$. Generally, the generator heat flow rates of the selected refrigerants were when $T_{g,sat}$ was low; the required $\dot{Q}_g$ intensively decreased with the increase of $T_{g,sat}$. For example, a 5 kW cooling capacity system with R1234ze(z) as the working fluid required 50 kW generator heat rate when $T_{g,sat}$ was 63^{o}C; the corresponding value when $T_{g,sat}$ of 98^{o}C was 11.4 kW. That was about 4 times the difference of required $\dot{Q}_g$.

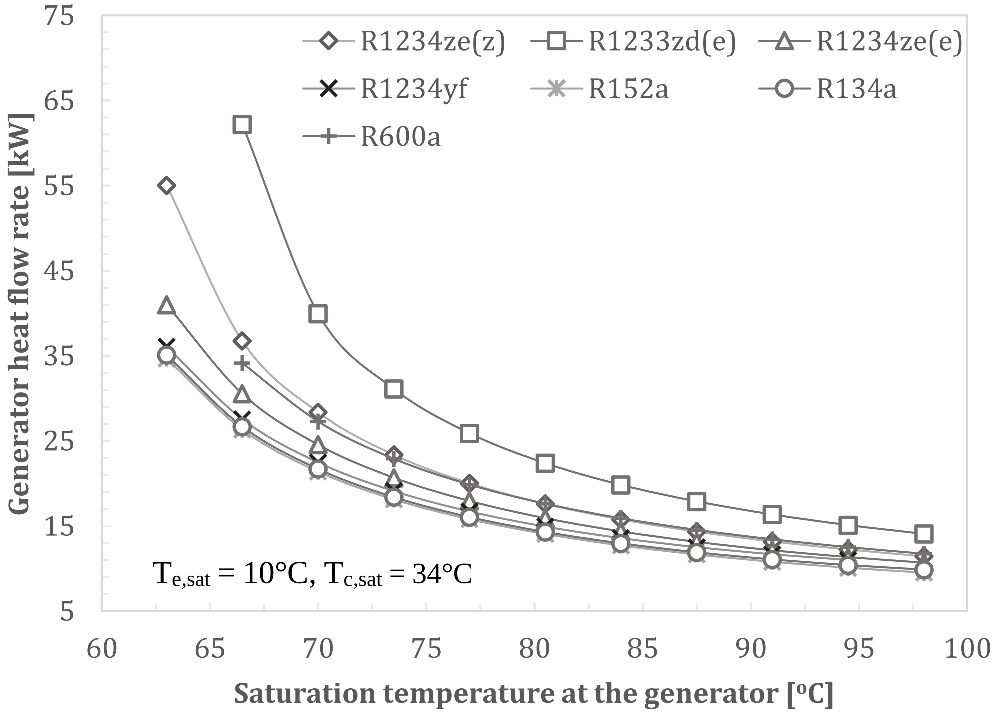

Figure 6.11 Required generator heat flow rate for producing 5 kW of cooling capacity.

The worst performance working fluid, R1233zd(e), required the highest $\dot{Q}_g$. At $T_{g,sat}$ of 66.5°C, R1233zd(e) required 62.2 kW of $\dot{Q}_g$ to produce 5 kW of $\dot{Q}_e$. That was more than double the amount of $\dot{Q}_g$ that R1234ze(e) was required at the same conditions. R134a and R152a required the least amount of the generator heat rate. R1234yf was the most favorable HFOs in this aspect as it was comparable with the two HFCs in the entire generator working range.

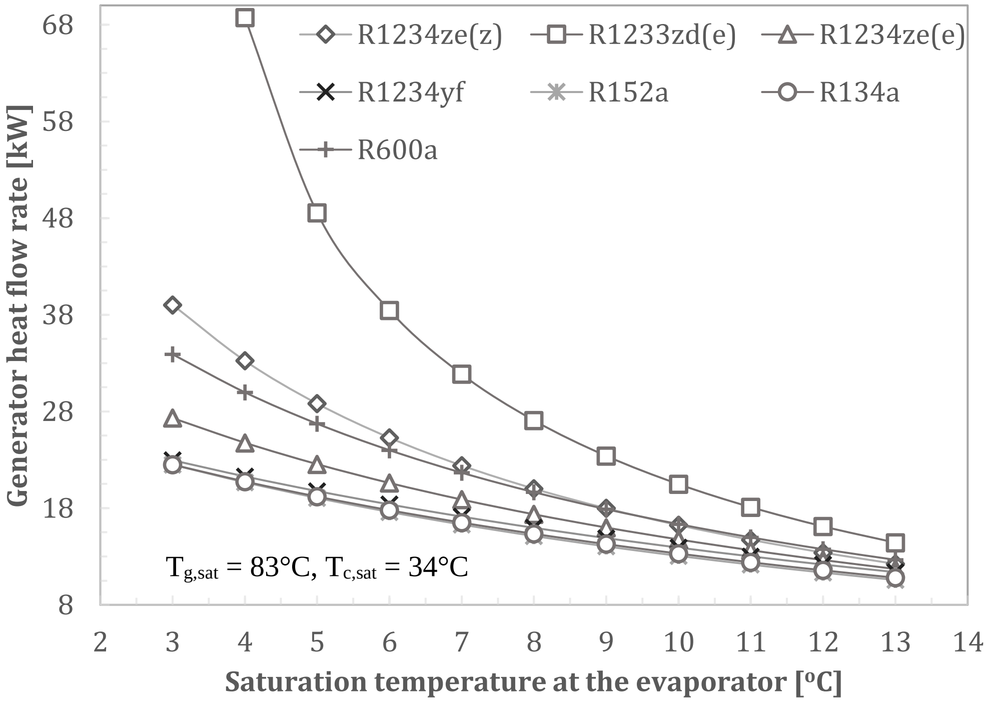

Figure 6.12 Relationship of the evaporation temperature and generation heat flow rate.

Figure 6.12 presents the relationship between $T_{e,sat}$ and $\dot{Q}_g$. Similar to what is shown in Figure 6.11, the required generator heat rate increased with the saturation temperature at the evaporator. The influence of $T_{e,sat}$ on $\dot{Q}_g$ was quite intensive. HFCs required the lowest generator heat flow rate in the entire temperature working range. The two HFCs visibly outperformed R1234yf; still, R1234yf yielded a better result than the other HFOs. As usual, R1233zd(e) offered the worst performance among the selected refrigerants.

Interestingly, the $\dot{Q}_g$ curves (of the refrigerants) seemed to converge at a certain point (as $T_{e,sat}$ exceeds 15°C). Consideration on which working fluid to use does not seem to be crucial when the evaporation temperature is high enough.

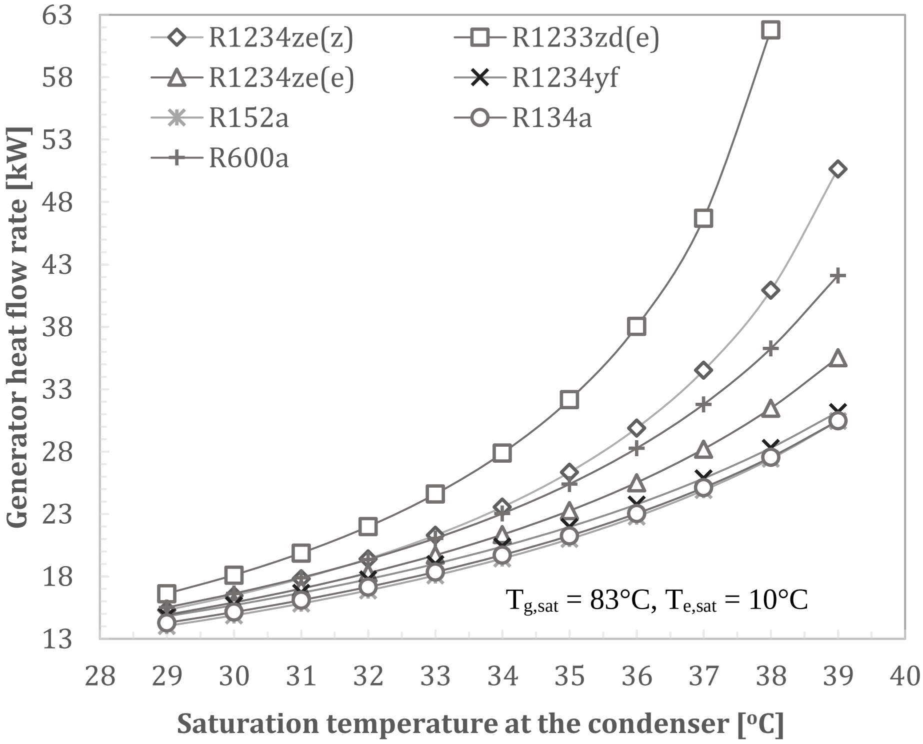

Figure 6.13 Association between the saturation temperature at the condenser and the generator heat flow rate.

Figure 6.13 shows the variation of the generator heat flow rate concerning $T_{c,sat}$. As seen, the best performance refrigerants were the two HFCs, followed by the two HFOs: R1234yf and R1234ze(e). The worst performance refrigerant, R1233zd(e), required an extreme amount of generator heat flow rate when the ERS worked at $T_{c,sat}$ of 37÷39°C. The favorable performance refrigerants like R134a, R1234yf also needed a considerable amount of $\dot{Q}_g$ at high values of $T_{c,sat}$; nevertheless, it was usually less than haft the amount of $\dot{Q}_g$ in comparison with R1233zd(e).

The above discussion leads to some thoughts. Firstly, the high-performance refrigerants reveal their advantages at extreme working temperatures: low generator temperatures, low evaporator temperature, or high condenser temperature. Secondly, the concept of ERS using a “low-grade driven heat source” does not seem to be very practical. COP is inversely proportional to $\dot{Q}_g$. When using a low-grade driven heat source, the high amount of $\dot{Q}_g$ would require an extra-large generator for heat transferring between the heat supplying source and the ejector cooling cycle. Also, a high generator heat rate causes stress on the chilling cycle. So, low-grade driven heat source requires a larger system, and thus a higher initial cost in comparison with a "proper-grade" heat source ERS.

6.4.4 Area ratio as functions of the working temperatures

The area ratio (AR) is the ratio of the mixing area A_2 to the throat area of the primary nozzle A_t (as was defined in chapter 2).

$$AR = \frac{A_2}{A_t} \tag{6-4}$$

The ejector geometry was proposed to obtain the optimal system performance for the given set of working conditions. That ejector geometry is called optimal geometry, and its AR is called the optimal AR. The optimal AR varies with the operational conditions. This variation of the optimal AR indicates the sensitivity of the ejector geometry on the working conditions. The sensitivity of the AR connects with the performance stability of the ejector as the working conditions vary. This section accesses the working fluids based on the variation of the optimal AR.

The variation of optimal AR, or optimal ejector geometry, apparently because of the compressibility and thermal expansion of the working fluids vary with the operating conditions. As known, coefficients of the compressibility and thermal expansion of gases are high and complex. Fortunately, applying real-gas data in the program Engineering Equation Solver could offer reasonable results.

Figure 6.14 presents the AR profiles of the selected working fluids concerning the saturation temperature at the generator. It seemed like the ARs strongly increased with the $T_{g,sat}$. Partially because the range of $T_{g,sat}$ is wide in comparison with others, e.g., with the range of $T_{e,sat}$ (see Figure 6.15). The unfavorable-performance refrigerants, like R1233zd(e) and R1234ze(z), had the most AR increment per temperature unit. In the entire study range of $T_{g,sat}$, AR of these refrigerants increased from 2.2 to $\sim$ 9. In contrast, $AR_{R1234yf}$ was 2.1÷5.4 in the entire $T_{g,sat}$ range, being the most favorable refrigerant in terms of performance stability. The two HFCs also indicated reasonable performance stability from the variation of the generator temperature.

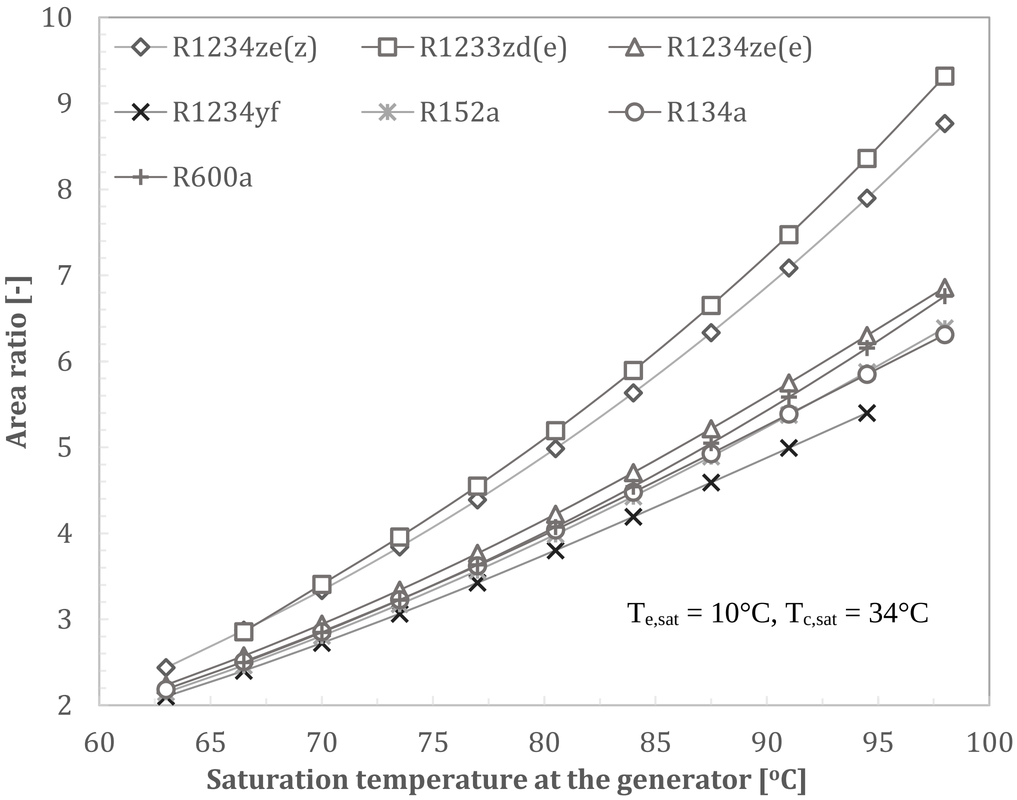

Figure 6.14 Area ratio as a function of saturation temperature at the generator.

Figure 6.15 shows the variation of AR with the saturation temperature at the evaporator. Generally, the order of AR variations with the saturation temperatures was similar to each other. The AR variations of the selected working fluids seemed to be less in comparison with corresponding values at the generator and at the condenser (see Figure 6.16). Still, the AR variations by $T_{e,sat}$ were significant.

To reduce the influence of the AR variations certainly influence the ejector performance. This fact is considered one of the most challenges of ejector cooling technology. In order to reduce the influences, the concept of variable geometry ejector was proposed. The variable geometry ejector helps retain the AR as close to the ideal value as possible when the working temperatures vary.

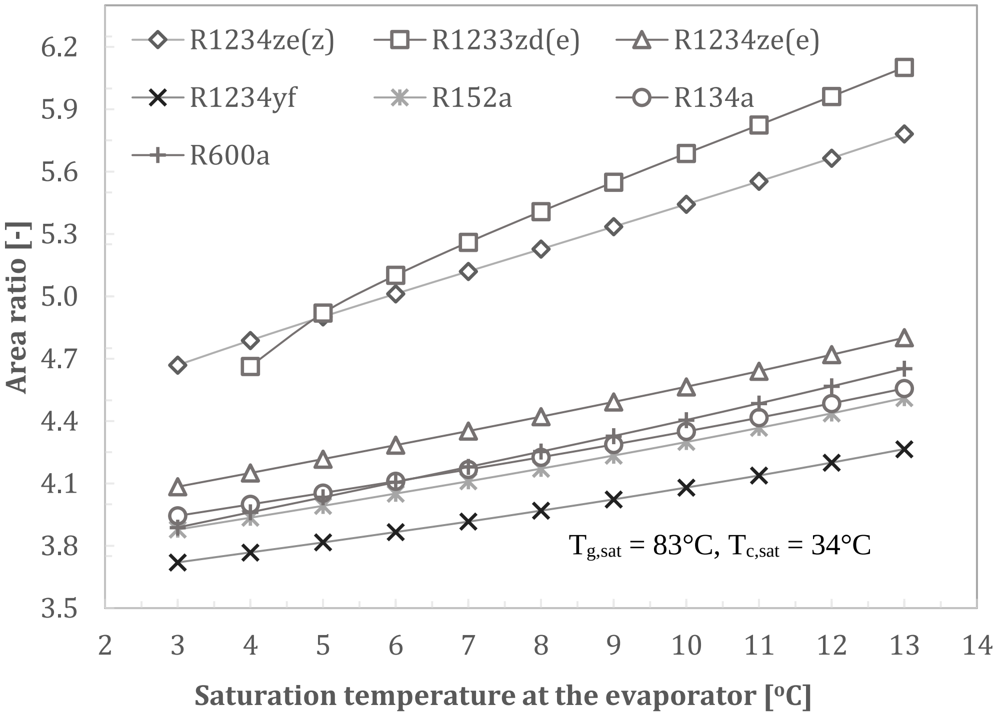

Figure 6.15 Area ratio as a function of the saturation temperature at the evaporator.

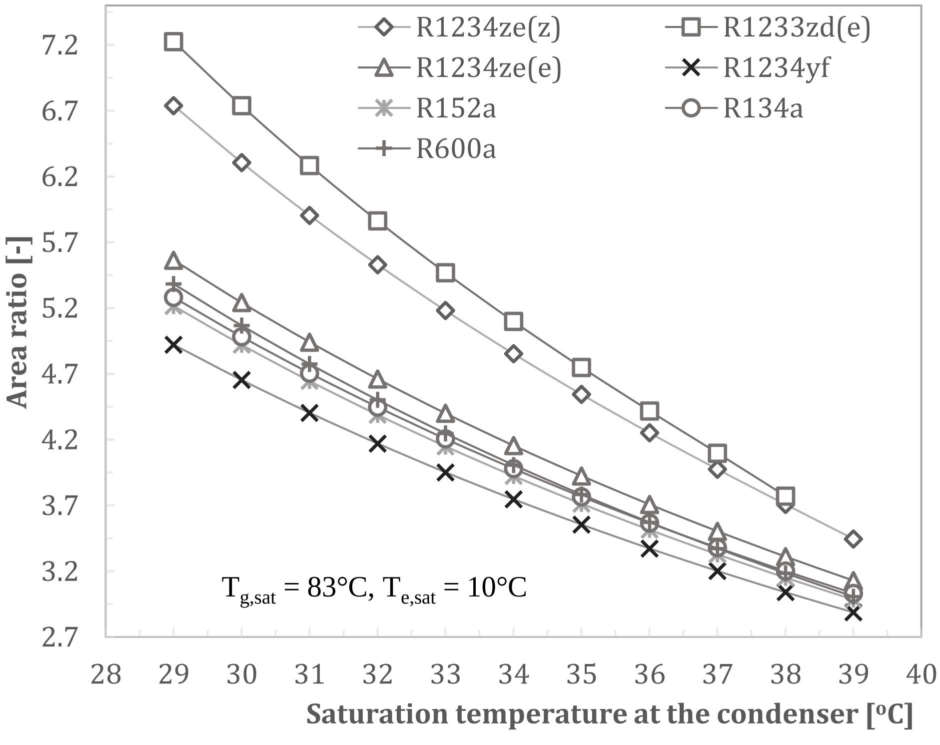

Figure 6.16 Area ratio in the correlation with the condensation temperature

Looking at the figures of area ratio profiles, one can see that R1233zd(e) and R1234ze(z) are the most beneficial refrigerants with the use of a variable geometry ejector. Nevertheless, applying VGE in an ERS is recommended for all seven working fluids.

6.4.5 Working pressures as the functions of the working temperatures

Working pressures of different working fluids at a particular working temperature are usually dissimilar. The working pressures mentioned here are the pressures at the primary and secondary inlets and outlet of the ejector, corresponding to the pressures at the generator, evaporator, and condenser, respectively.

As discussed in section 6.1, the generator pressure has the highest-pressure level in the ejector cooling cycle. Thus, the generator pressure determines the robustness of the system. Most importantly, the durability of the generator and the piping system under extreme pressure. Also, a high operating pressure level at the generator could lead to difficulty in selecting the refrigerant pump. The condensation pressure (backpressure) and the evaporation (secondary) pressure directly influence the ejector performance. Therefore, operating pressures are decisive factors in the refrigerant assessment.

Figure 6.17 presents the relation of the saturation temperature and the pressure in the generator. The generator pressures of the selected refrigerants mostly linearly increased with the operating temperature. In the range $T_{g,sat}$ of 63÷98°C, the generator pressures of the selected refrigerants increased by roughly double. For instance, P_{R134a} increased from 18.1 to 38.2 bara, $P_{R1234yf}$ from 16.1 to 33.7 bara, $P_{R1234ze(z)}$ from 5.6 to 12.9.

The profile orders of Figure 6.5 and Figure 6.17 are fairly similar. The generator pressure significantly influenced the refrigerant performance. The pressures of the top performance refrigerants, i.e., R134a, R1234yf, and R152a, were the highest among the selected working fluids. Conversely, R1233zd(e) and R1234ze(z) had the lowest operating pressure in the entire temperature range. Needless to say, they yielded the least favorable performances.

As seen, the change of pressure level on the variation of $T_{g,sat}$ were significant. One of the major concerns of designing the ejector refrigeration cycle is the system's upper working pressure limit, generator pressure. Currently, there are only a few companies that could build commercial plate heat exchangers (e.g., SWEP and Alfa Lava) that can withstand the operating pressure above 30 bar. Moreover, these heat exchangers are costly. The refrigerant pump could be another technical barrier if the required pressure level is high. Centrifugal pump technology is commonly used since it is affordable. However, the centrifugal technology typically generates pressure head up to about 20 bar. At the present, diaphragm pump technology (e.g., Hydra-cell pump of Wanner Engineering) could produce pressure heads. Overall, having an ejector cooling cycle that works at a high-pressure level (above 20 bar) would be challenging: it needs a significantly high initial investment compared to a low-pressure cycle. In addition, safety and maintenance could be the concerns.

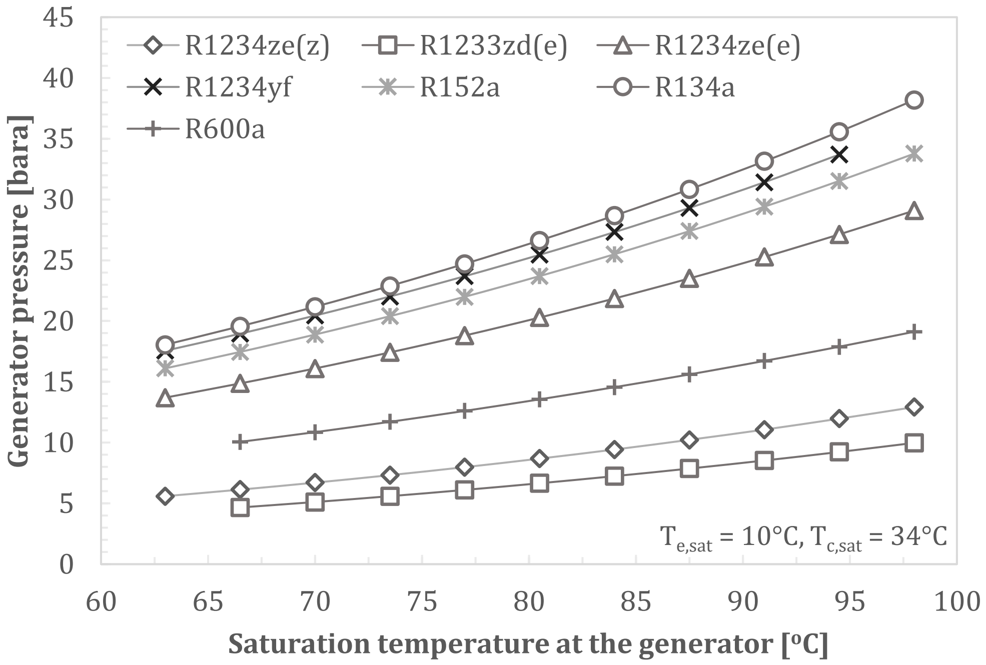

Figure 6.17 Generator pressure as a function of saturation temperature at the generator.

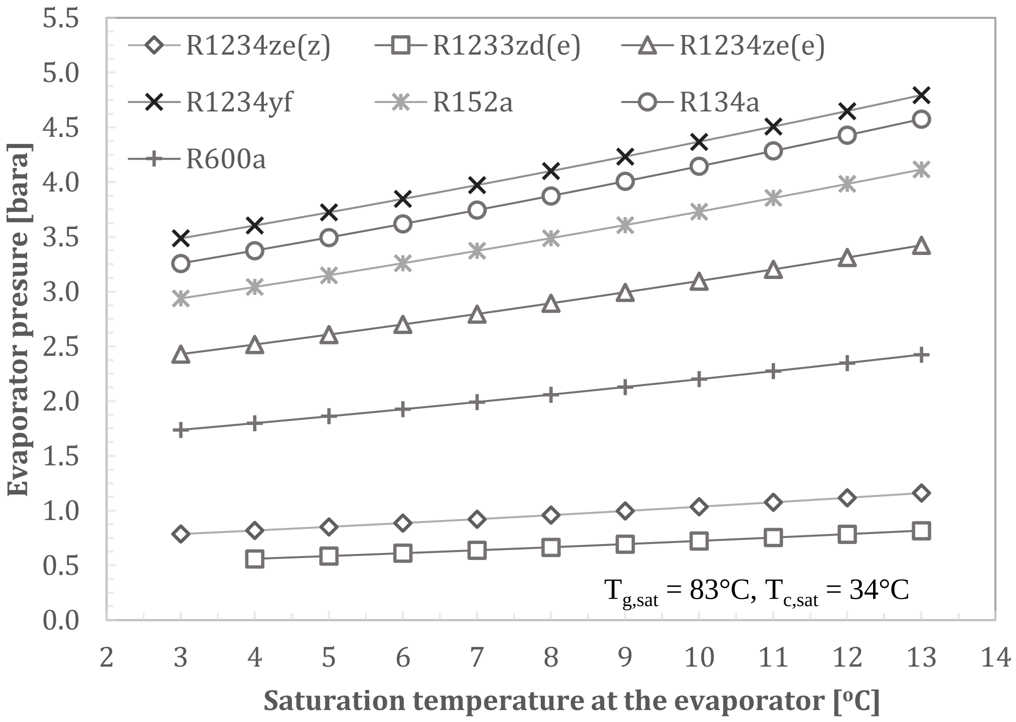

Figure 6.18 Relation between temperature and pressure at the evaporator.

Table 6.2 Pressure gain between the two extremes of $\boldsymbol{T_{e,sat}}$ range.

	R1234ze(z)	R1233zd(e)	R1234ze(e)	R1234yf	R152a	R134a	R600a
Pressure gain	48%	51%	41%	38%	40%	40%	40%

The evaporator pressures of the refrigerants as a function of saturation pressure at the evaporator are shown in Figure 6.18. The two lowest performance refrigerants, R1233zd(e) and R1234ze(z) gained about 50% pressure level as the saturation temperature varied from 3 to 13°C, while the other working fluid gained about 40%. The pressure of the working fluids fairly linearly increased.

The two lowest performance refrigerants worked at vacuum pressure in the entire $T_{e,sat}$ range. As discussed in chapter 2, the vacuum pressure in the evaporator could cause some issues related to the impurity of the working fluid in the ejector cooling cycle. The system, thus, may not properly work after an operational period. In terms of operating pressures, R600a could be the best candidate as the working fluid for ejector refrigeration technology. Its operating pressure at the evaporator is above the atmospheric level. Its operating pressure level at the generator is only less than 20 bar. Therefore, ERS using R600a as the working fluid would not confront with robustness related issues as discussed above.

Theoretically, a high value of operating pressure at the evaporator is favorable since the flow from the evaporator outlet could be more easily entrained to the ejector. As seen in Figure 6.18, the highest saturation pressure refrigerants were R1234yf, R134a, R152a, and R1234ze(e), respectively. As expected, these refrigerants yielded the highest ER, as shown in Figure 6.5.

However, the saturation pressure at the condenser also plays a key role in the performance of the ejector. As known, the ejector performance is highly influenced by the ejector backpressure (the condenser pressure), along with the evaporator pressure. Figure 6.19 presents pressure profiles of the refrigerants by the variation of $T_{c,sat}$. Looking at Figure 6.17, Figure 6.18 and Figure 6.19, one may notice that the pressure variations of the assessed refrigerants were relatively linear with the operating temperatures. The order of pressure levels of the refrigerants maintained mostly the same in temperature range 3÷98°C. The pressure levels at the heat exchangers have crucial influence on the ejector performance.

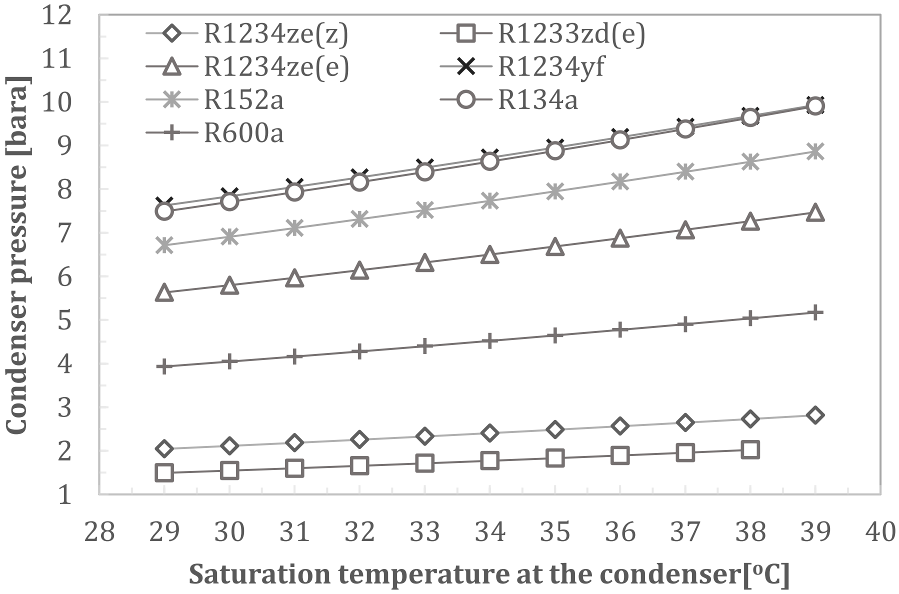

Figure 6.19 Relationship of temperature and pressure at the condenser.

6.5 The influences of the heat exchangers size on the system performance

Two plate sizes are used in the modeling. Plate size B03 was used for the evaporator, B12 for the generator, and condenser. Dimensions of the plates are presented in Table 6.3. The plates were made from stainless steel, which has a conductivity of 16.27 (W m^{-1} K^{-1}).

Table 6.3 Dimensions of the plate of the heat exchangers.

Parameter	**Plate size B12**	**Plate size B03**
Inclination (chevron) angle (θ)	60°	60°
Thickness of the plate (t)	0.0006 m	0.0006 m
Size of corrugation pitch (λ)	0.0068 m	0.0068 m
Corrugation pitch (pit)	0.0028 m	0.0025 m
Port diameter (D_p)	0.055 m	0.03 m
Effective flow length between the vertical ports (L_v)	0.485 m	0.25 m
Plate width (L_w)	0.245 m	0.095 m

The number of plates of the heat exchangers was selected as the reference (x-axis) to evaluate the refrigerants. The range of the generator's plates was 7÷167 units, evaporator and condenser were 7÷207 units.

Besides the geometry, the performance of the heat exchangers obviously depends on the temperature gradients between the two flows. The working temperatures of the refrigerant at the heat exchanger inlet and outlet were determined by the in working conditions of the ejector cooling cycle. In this section, the working temperatures of the water were set as follows: $T_{w,g,in}= T_g + 4$ (°C); $T_{w,g,out}= T_g + 1$ (°C); $T_{w,e,in}= T_e + 2$ (°C); $T_{w,e,out}= T_e + 1$ (°C); $T_{w,c,in}= T_c - 2$ (°C); $T_{w,c,out}= T_c - 1$ (°C). The left-hand side of these equations are the temperatures of the water side, and the right-hand sides are the working temperature of the refrigerant flows.

6.5.1 Overall heat transfer coefficient of a heat exchanger

The overall heat transfer coefficient is a function of specific convective heat transfer coefficients, conductive heat transfer coefficient, fouling factors, as shown in equation (3-55). The heat transfer coefficient is a function of Nusselt number (Nu), and Nu is the function of Re. As the number of plate increase, the mass velocity of the flow decreased, and so does the Re.

As an example, Figure 6.20 presents the Reynolds and Nusselt numbers of the two-phase flow in the evaporator as a function of the number of plates. As seen, the Re value aggressively decreased as the increase in the number of the plate. Nusselt curve had a similar trend as the Reynolds.

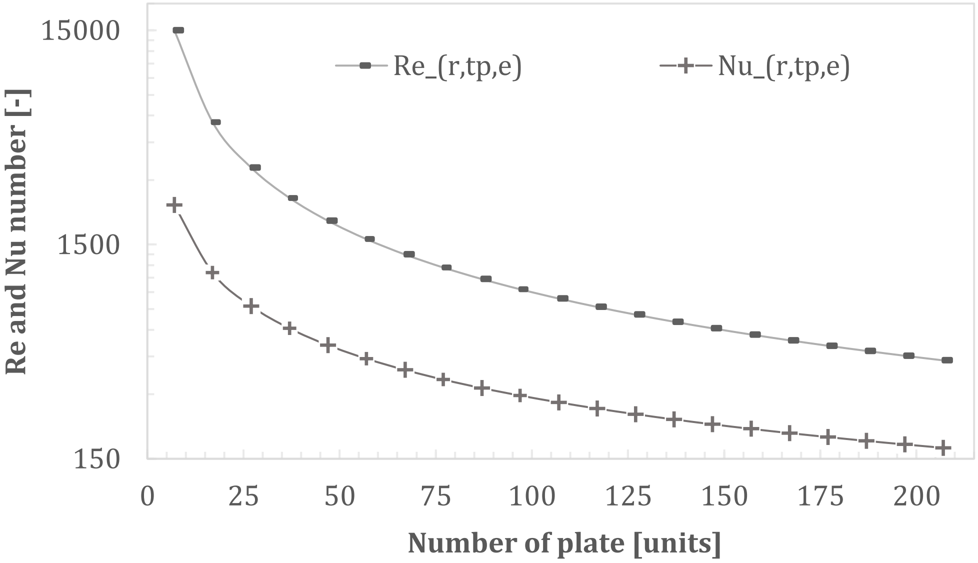

Figure 6.20 The Reynolds number and Nusselt number of the two-phase section of the evaporator as functions of the number of plates (R600a as the working fluid).

Figure 6.21 shows the average convective heat transfer coefficient on the refrigerant side of the generator of the selected working fluids. Similar to the above-mentioned parameters, he values of the working fluids decreased significantly as the number of plates increased from 7 to about 70. The number of plates then seemed to have less impact on the he values. The behavior of he parameter in the two other heat exchangers was similar to the one presented here.

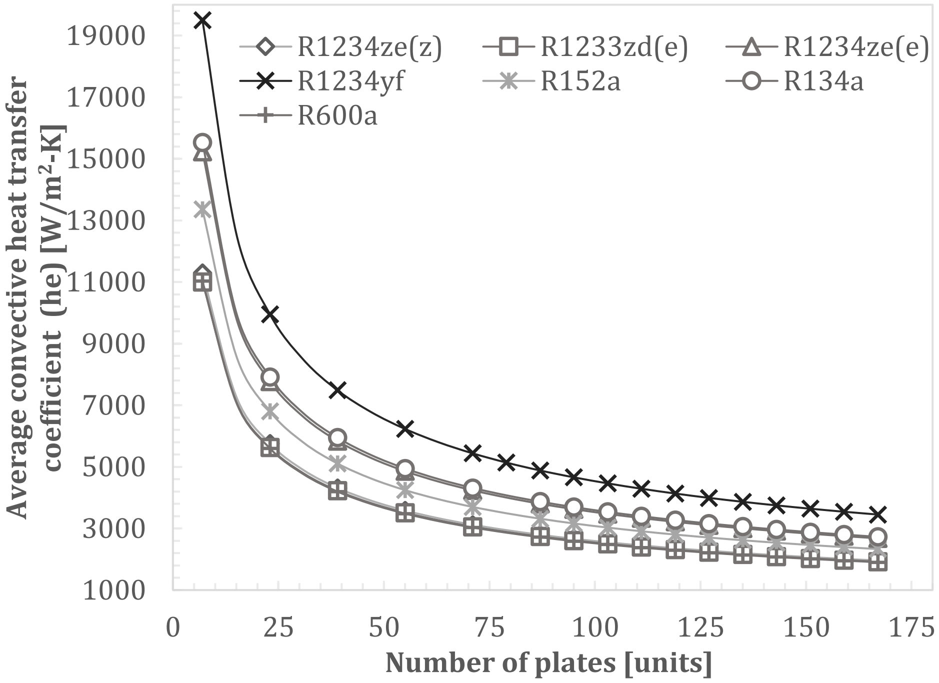

Figure 6.21 Average convective heat transfer coefficient in the refrigerant side of the generator.

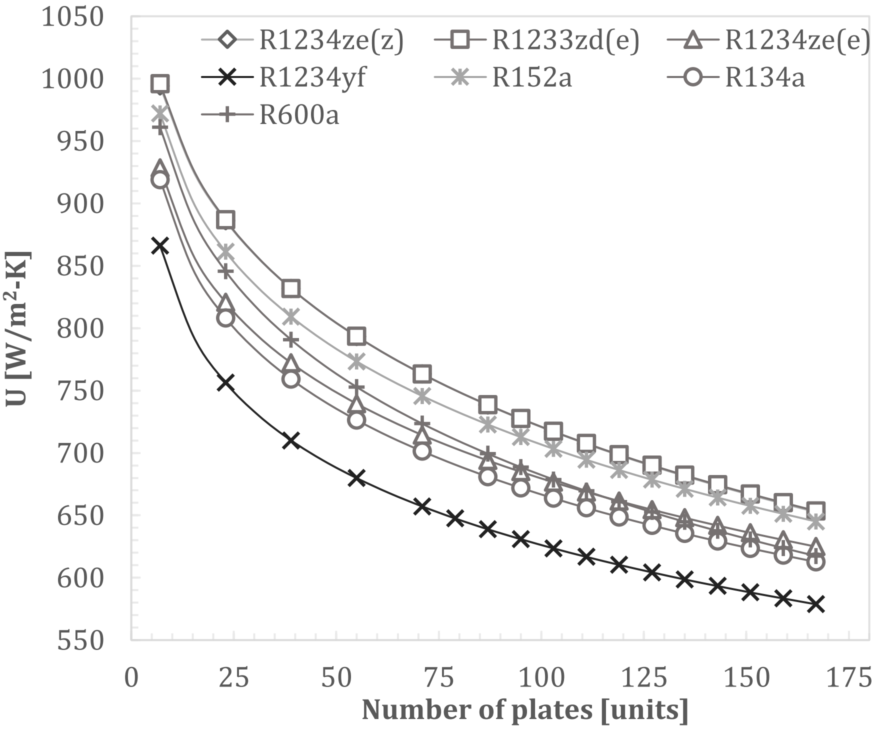

Figure 6.22 Average overall heat transfer coefficient of the generator.

Figure 6.22 compares the average overall heat transfer coefficient of the selected refrigerants with a variation of plate quantity of the generator. Generally, increasing the number of the plate resulted in an aggressively decrease in the U-values. It is because as the number of plates increased, the flow rate of the working fluid decreased and so did the overall conduction (U), as explained above. Interestingly, the high-performance refrigerants at the ejector like R1234yf or R134a had the lowest U values. While the lowest performance refrigerant like R1233zd(e) obtained the highest U value in the entire generator temperature range.

Comparing Figure 6.22, Figure 6.23, and Figure 6.24, it can be seen that the order of the U curves of the refrigerants was dissimilar to each other. The reason could be from the flow rates were different (both flowrates in the water side and the refrigerant side of the heat exchangers), thus the characteristics of the flow and the heat transfer processes could be extremely diverse. Please note that at the generator, the heat transfer areas of the liquid section and the two-phase section were usually much large than the superheat section. While in the evaporator, the heat transfer area of the liquid section was considered as zero, most of the heat transfer area was the two-phase section. All the flow characteristics resulted in variations of Nusselt numbers, and so do the he values and others.

The temperatures and pressures in the water side of the heat exchangers can significantly impact the he values in the water side; thus, influence the overall heat transfer coefficient (as was explained in chapter 3). For example, selecting the temperature inlet and outlet of water at the condenser determines the flow rate of the chilling water going through the condenser. Then, again the flow rate determines the Re, Nu, he of the flow.

Figure 6.22, Figure 6.23, and Figure 6.24 indicate that depending on the working conditions, like temperature, type of flows, the overall heat transfer coefficients of the selected refrigerants can vary quite significantly. The current set of the working conditions at the condenser resulted in the U values from about 650 to 1220 (W/m^2K). The U value of R1234yf in was the most desirable.

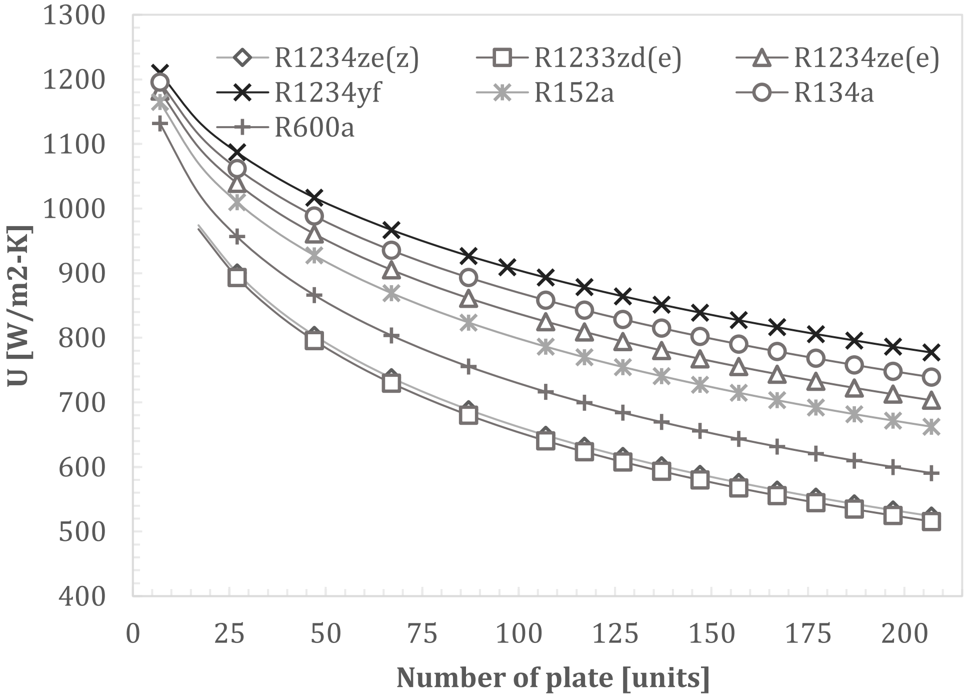

Figure 6.23 Average overall heat transfer coefficient of the evaporator.

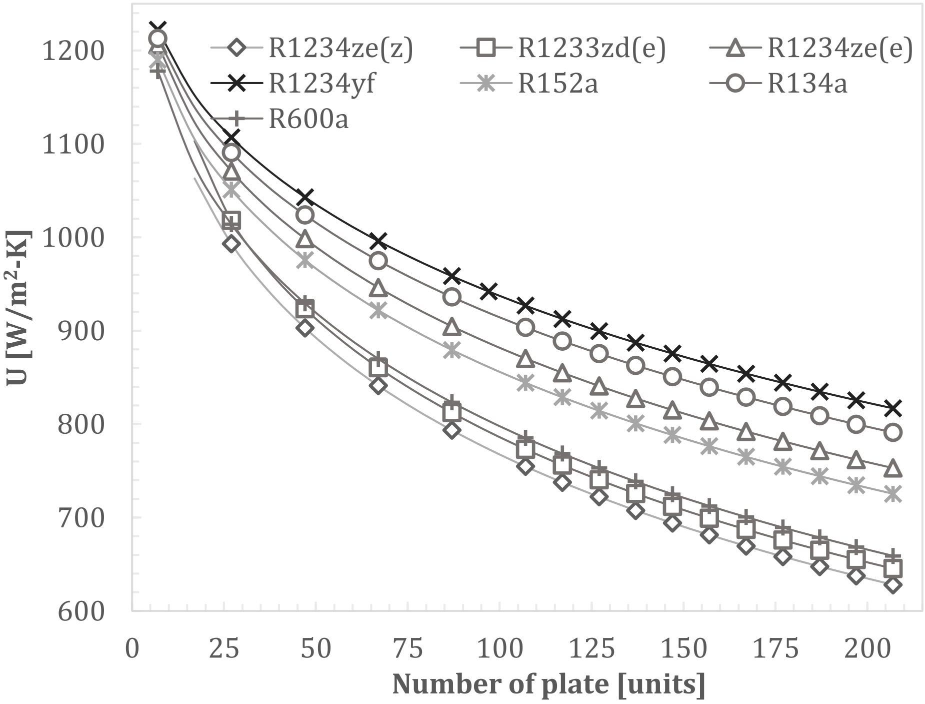

Figure 6.24 Average overall heat transfer coefficient of the condenser.

6.5.2 Heat exchanger effectiveness

The effectiveness of a heat exchanger represents the possible heat transfer rate at specific operating conditions and structural configuration of the heat exchanger (see equation (2-8). The following text discusses the performance of the selected working fluids based on their effectiveness when the number of the plates varies.

Figure 6.25 presents evolutions of effectiveness with the generator's number of the plates. Generally, the generator could obtain high effectiveness when the number of the plates is high. It can be seen that the high COP group (R1234yf, R1234ze(e), R152a, R134a) also showed their superior in terms of heat transfer effectiveness. The two HFCs overperformed R1234yf as the number of the plates exceeded 75. R1234yf likely performed better when the flow was highly turbulent. The ϵ values of R600a and R1234ze(z) at the generator were very reasonable. Heat transferring did not seem to be an issue of the selected working fluids, excepts R1233zd(e). The effectiveness of R1233zd(e) was quite low, and its increase with the number of plates was less significant than the others.

Overall, the change of effectiveness at the generator became less intensive after the plates reached ∼50 units. As was found in the previous section, the overall heat transfer coefficient logarithmically decreased as the plates were added. The heat transfer coefficient of the heat exchanger significantly decreased with the flow rate. There is a compromise between the initial investment and the operating cost. In this instance, it is the number of the plates and the heat transfer effectiveness. The reasonable N_{pl} at the generator of the selected refrigerants, excepts R1233zd(e), could be between 55 and 75 units.

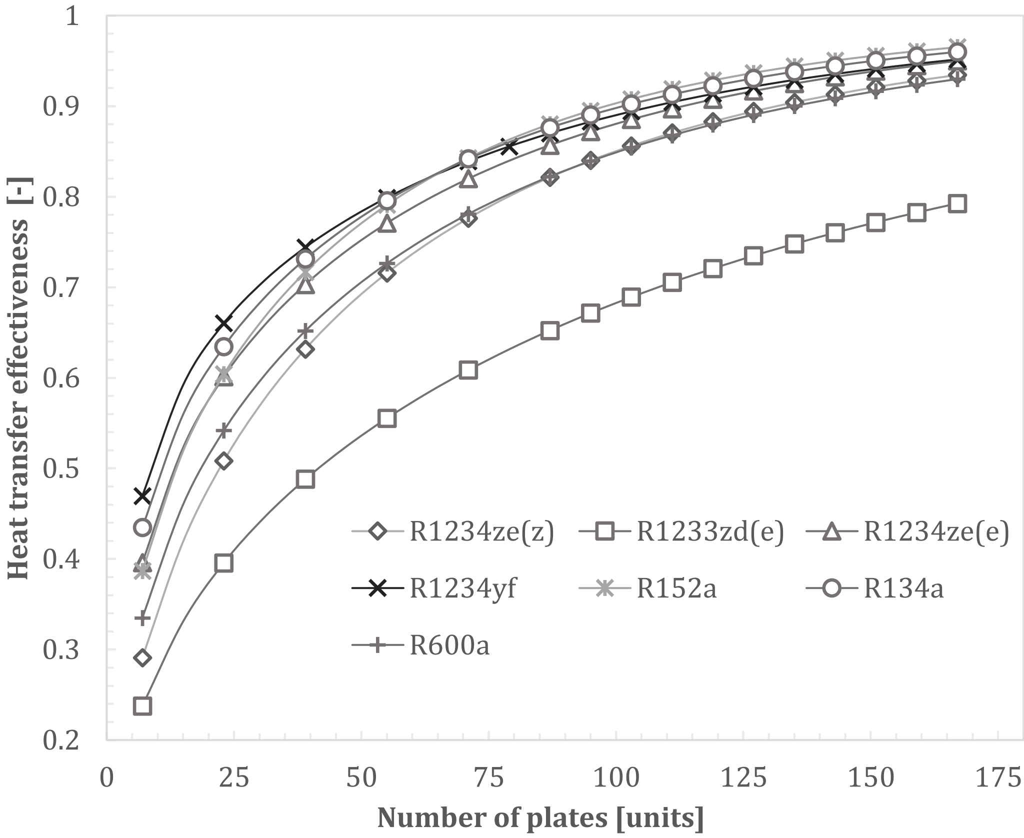

Figure 6.25 Heat transfer effectiveness of the generator.

Figure 6.26 shows the variation of the heat transfer effectiveness with the number of plates of the evaporator. N_{pl} of the evaporator varied from 7 to 207 units. The effectiveness of the working fluids increased, but not as significant as what was seen in the generator. It might be because of the low-temperature difference between two working media (the refrigerant flow and the water flow). More importantly, there was no sensitive heat transfer process between the refrigerant in the liquid state and the other working medium. As know, heat transfer coefficient between gas and liquid is low compared with liquid and liquid. Therefore, the overall heat transfer of the refrigerants at the evaporator was generally lower than at the generator.

Based on the ratio of the actual heat transfer area to the required heat transfer area that is shown in Figure 6.27, the recommended N_{pl} value for the current working conditions at the evaporator (cooling capacity, temperature gradient, etc.) was from 125 to 165.

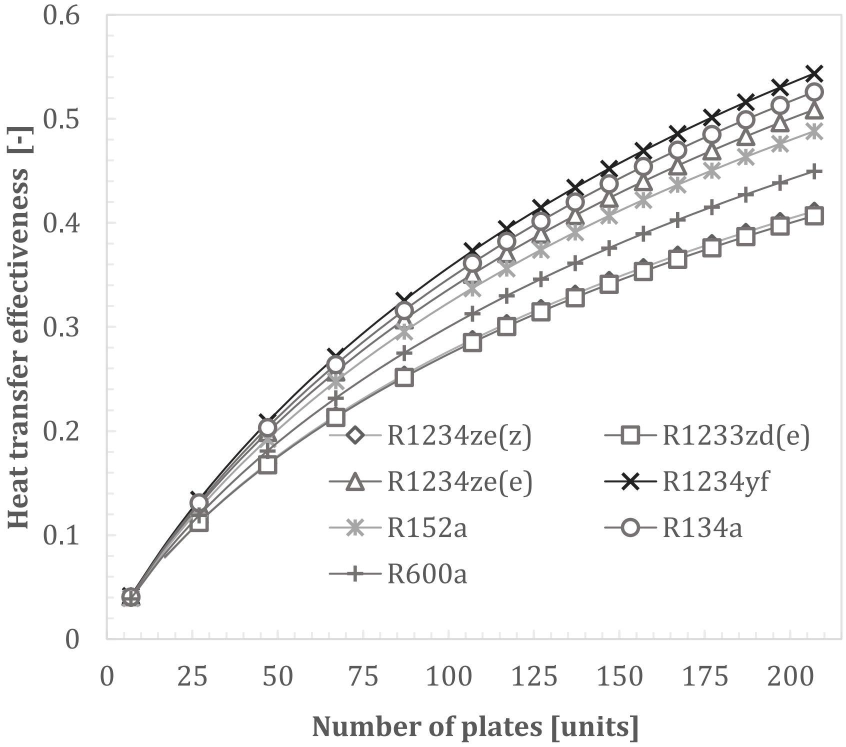

Figure 6.26 Heat transfer effectiveness of the evaporator.

Figure 6.28 presents the heat transfer effectiveness of the refrigerants as a function of the condenser's number of plates. Note that the generator and condenser consisted of the same plate size. The plate size somewhat has an impact on the heat transfer effectiveness. In the condenser, the heat was transferred from the refrigerant to the chilling water at three "parts" of the condenser: superheat, two-phase, and liquid. In the current study, the liquid part brings the refrigerant in the liquid state to 2 K of the subcooling degree. The subcooled liquid of the refrigerant at the condenser outlet was believed to ensure the refrigerant remains in the liquid state (to minimize the possible cavitation may occur in the pump) as it goes through the refrigerant pump. As expected, the liquid part is insignificant compared with the two other parts. The average heat transfer effectiveness of the condenser is generally lower than the generator but higher than the evaporator. Based on the heat transfer area ratio, the recommended value of N_{pl} of the condenser was 100 to 150 units.

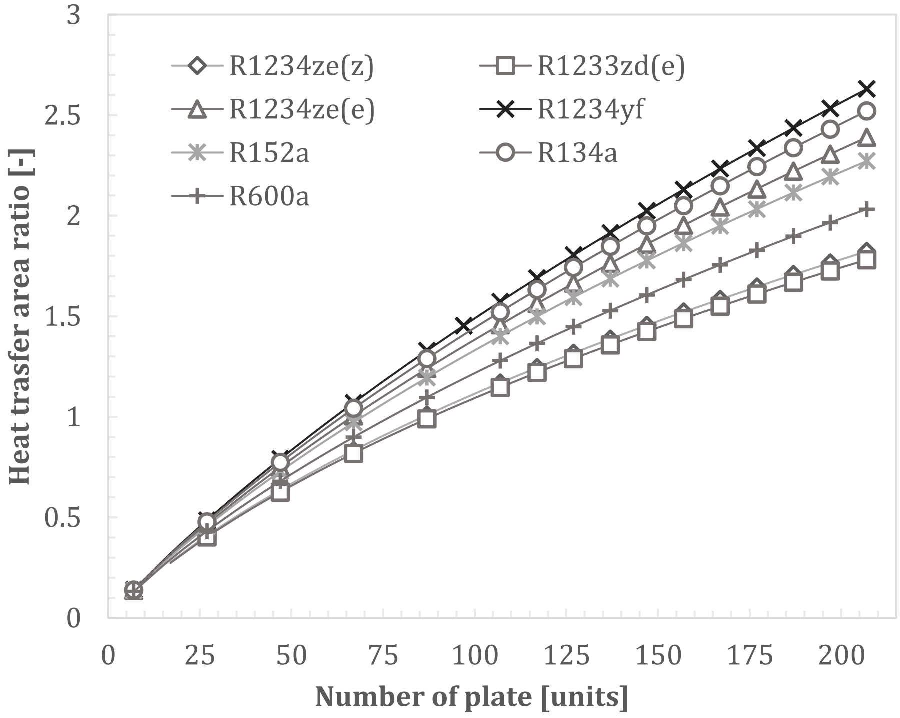

Figure 6.27 Heat transfer area ratio at the evaporator.

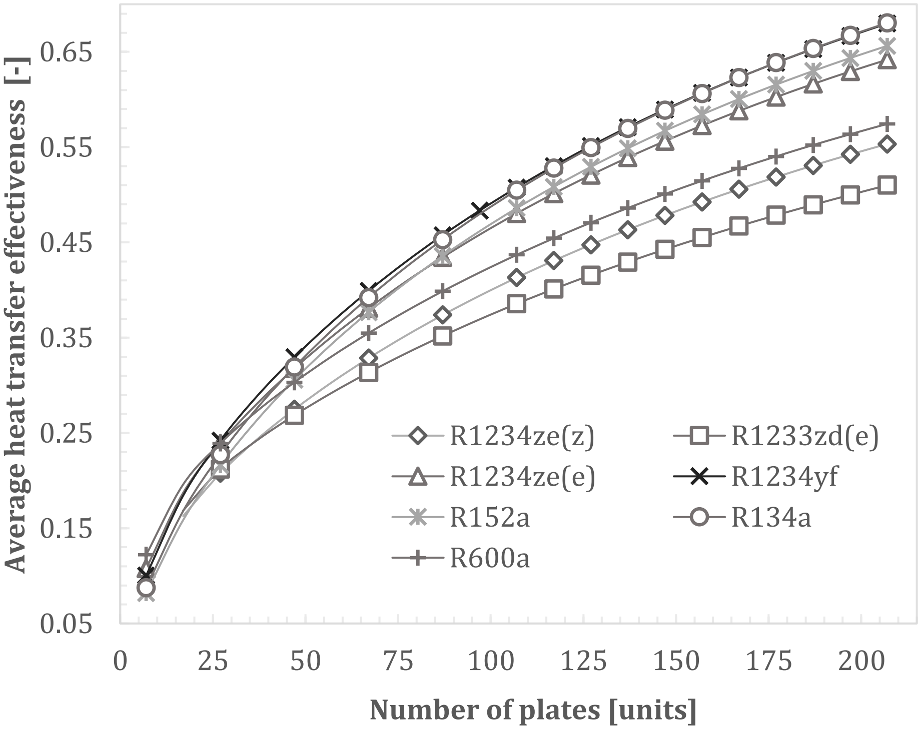

Figure 6.28 Average heat transfer effectiveness at the condenser.

6.5.3 Pressure drops of the working fluids through the heat exchangers

As presented in section 6.4, the system performance was sensitive to the saturation temperatures (or the working pressures), especially the working pressures at the evaporator outlet and condenser inlet. The pressure drop of the refrigerant flow through the heat exchangers could significantly influence the performance of the ejector. In this section, the pressure drops through the heat exchanger are discussed. The pressure drop was generalized by using a pressure drop per length unit. It is called specific pressure drop (Pa/m).

Figure 6.29 presents the specific pressure drop of the generator as a function of the number of the plates. As seen, the specific pressure drops (ΔP_{sp}) of the working fluids were as high as 50 kPa when the N_{pl} was 7 units. The ΔP_{sp} were quickly drop to 5÷6 kPa as N_{pl} was 25. ΔP_{sp} were then about 0.6÷0.7 kPa as N_{pl} was 125. Note that the pressure drop of the refrigerant flow caused by the heat exchanger's ports is insignificant. For instance, this value for R1234yf was 3.2 Pa for the default operating conditions.

The pressure drop through the generator does not have too much meaning to the performance of the system. The pressure drops of the working fluids were trivial as N_{pl} exceeded 125 units, especially in comparison with the generator pressure. The refrigerant pump located next to the generator can easily compensate for the pressure drop caused by the generator.

It is seen that among the refrigerants, R152a, and R600a offered the lowest pressure drop at the working conditions of the generator. The two high-performance HFOs (R1234yf, R1234ze(e)) also had favorable pressure drop.

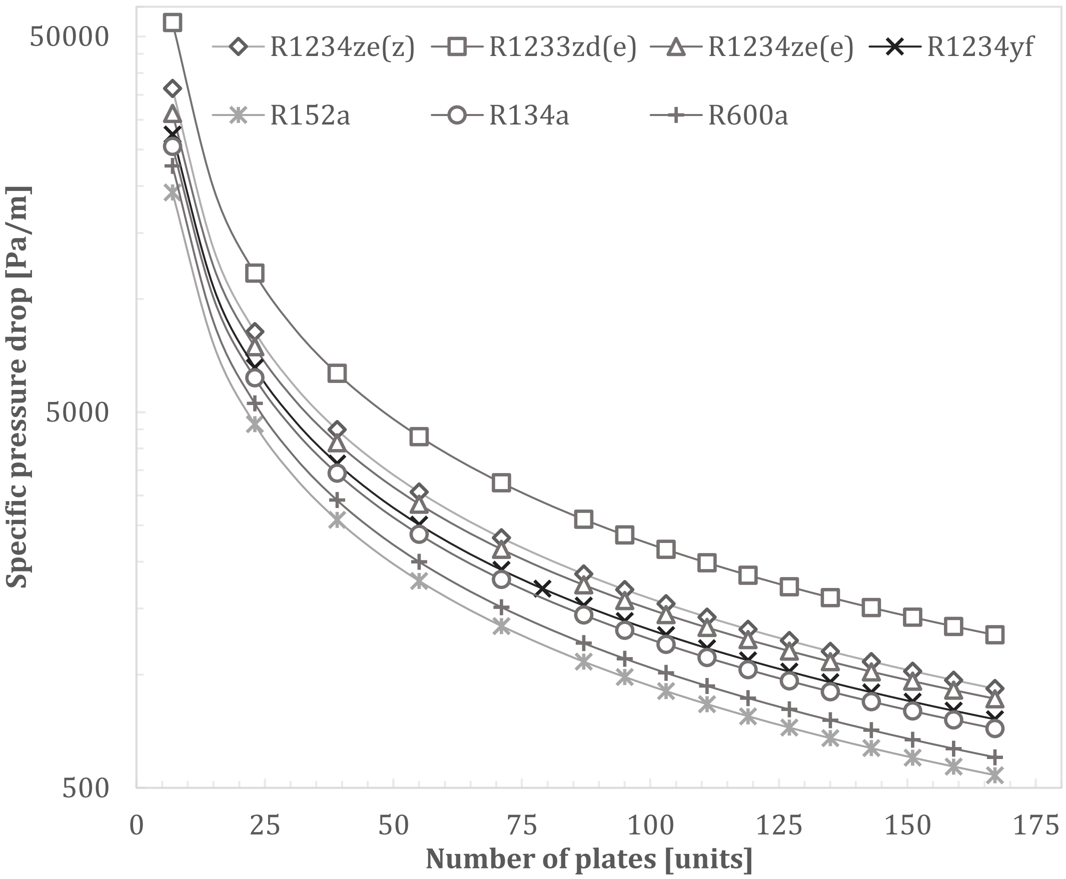

Figure 6.29 Specific pressure drop at the generator as a function of the number of plates.

Figure 6.30 shows the specific pressure drop at the evaporator as a function of the number of the plates. The pressure drops decreased with the number of plates, probably with less intensity compared with the case at the generator. The specific pressure loses of the working fluids remained high when the N_{pl} was increased to 125 units, about 400 to 800 Pa/m. As can be observed in the figure, the pressure drop of R1234yf was the highest among the refrigerants. This is one of the most significant disadvantages of R1234yf, since the ejector performance is sensitive to the evaporator outlet pressure, as was discussed in section 6.4.

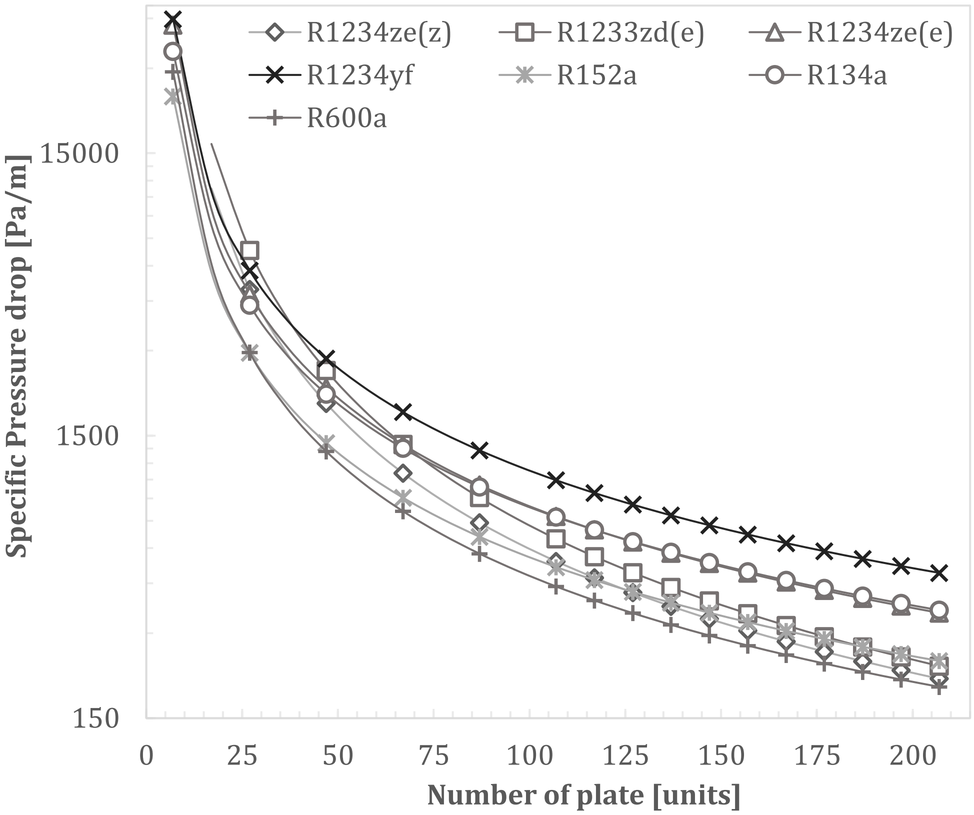

Figure 6.30 Specific pressure drop at the evaporator as a function of the number of plates.

As indicated in equations (3-60) to (3-62), besides the flow rate, plate dimensions of the channel pressure drops are influenced by the mass velocity of the flow and Fanning friction factors. The Fanning friction factors are determined by Re, We numbers, etc., as shown in chapter 3. Figure 6.31 presents the variations of the fluid mass velocity in the evaporator channel ($G_{r,ch,e}$) and the average Fanning friction factor ($f_{r,e,ave}$). The impact of the Fanning friction factors to the pressure drop in the evaporator seemed to be predominant. As seen, the variation of $G_{r,ch,e}$ intensively dropped with N_{pl}; when N_{pl} exceeded 100, the change became insignificant. While the average Fanning friction factor increased with the number of the plates in mostly a constant rate.

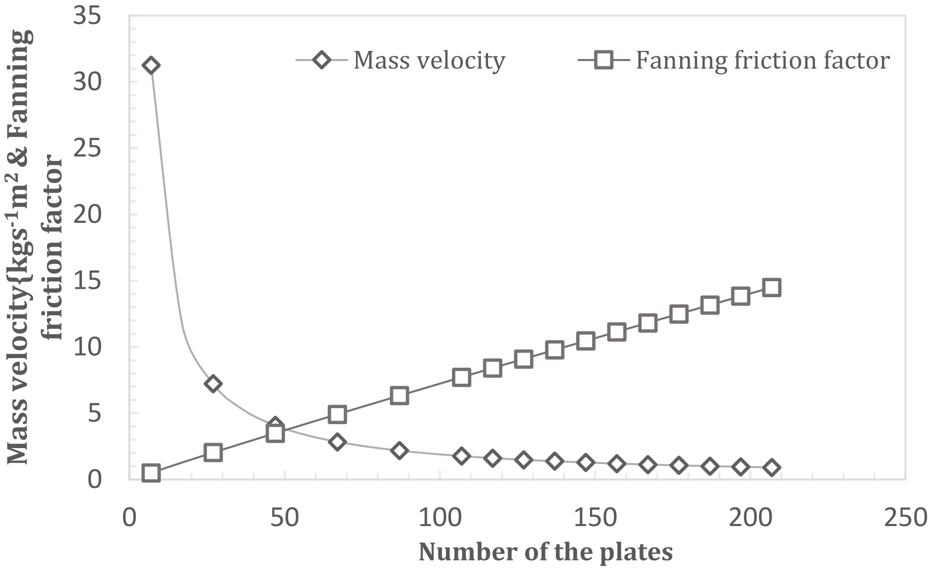

Figure 6.31 Mass velocity and Fanning friction factor as a function of the evaporator's number of the plates.

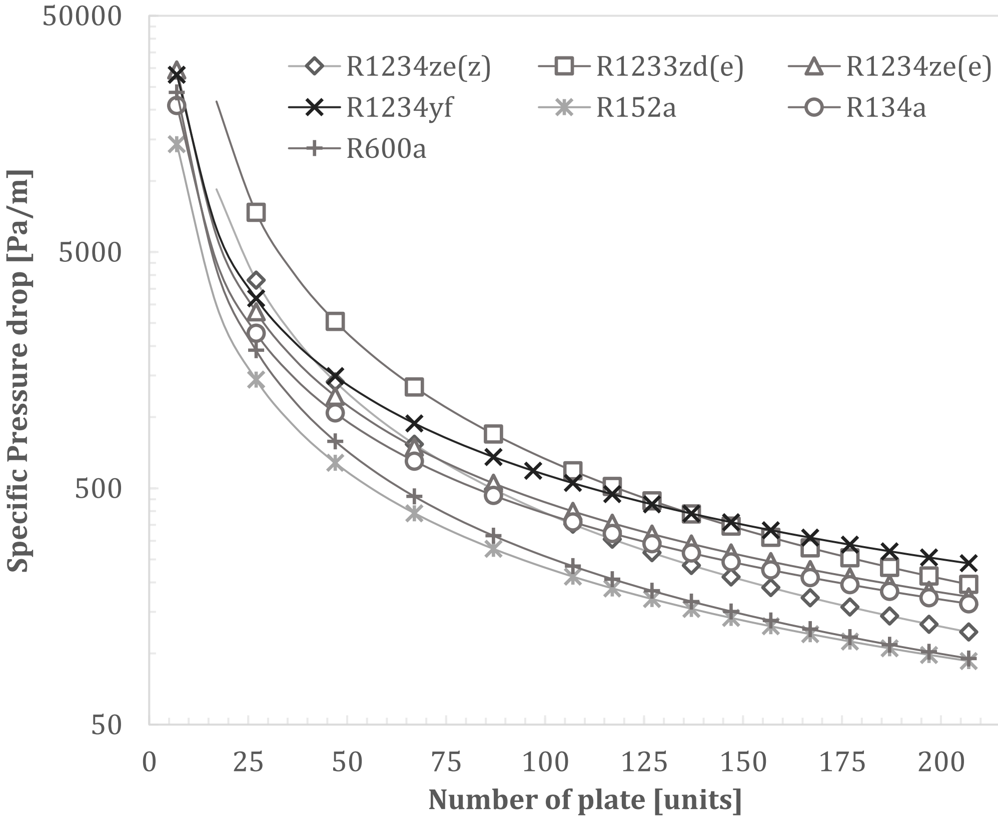

Figure 6.32 Specific pressure drop at the condenser as a function of the number of plates.

Figure 6.32 presents the relation of the specific pressure drop with the number of plates at the condenser. As expected, the channel pressure drops of the working fluids hugely decreased with the number of the plates. When N_{pl} reached 125 plates, the specific pressure drops of all the refrigerants were below 500 Pa/m. R1234yf again showed its disadvantage in this aspect. The ejector is sensitive to the condenser pressure inlet (ejector backpressure). However, the pressure drop caused by the condenser is quite trivial when the fluid mass velocity is small, or when the number of the plates is sufficient.

6.5.4 The influence of the heat exchangers' size on the system performance

The size of the heat exchangers (or the number of plates in this study) determines the heat transfer capability and the pressure drops. Based on the heat transfer area ratio (see the Appendices), the numbers of plates of the heat exchangers were recommended in Appendix 3.

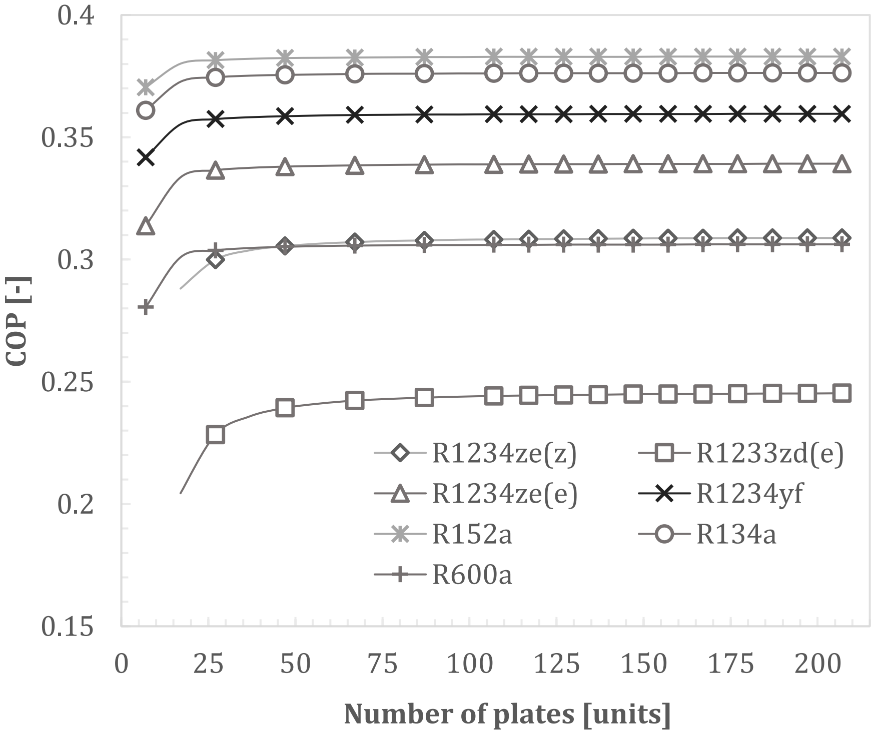

Figure 6.33 The influence of the evaporator size on the system performance.

As stated earlier, the pressure drop of the primary flow through the generator can be ignored since it can be easily compensated by the refrigerant pump at the upstream. The following text discusses the influence of the evaporator and condenser's size on the system performance.

Figure 6.33 shows the association between the COP and the number of plates of the evaporator. As can be seen, the system COPs rapidly increased with the $N_{pl,eva}$. It was because the pressure drops of the working fluids through the evaporator were considerably large since the mass rates per channel were high. As $N_{pl,eva}$ exceeded about 30 units, the COPs of most of the selected working fluids did not noticeably vary. COPs of R1233zd(e) and R1234ze(z) still slightly improved as $N_{pl,eva}$ went up to about 100 units. Note that, evaporation pressure of R1233zd(e) is low so a small amount of the pressure loss could be significant.

Generally, the pressure loss through the evaporator was not an issue. Because the evaporator has to satisfy the heat transfer rate. The recommended $N_{pl,eva}$ for it was 125 to 165 units (as discussed in section 0). With this value, the pressure drop is not a concern with any selected working fluid.

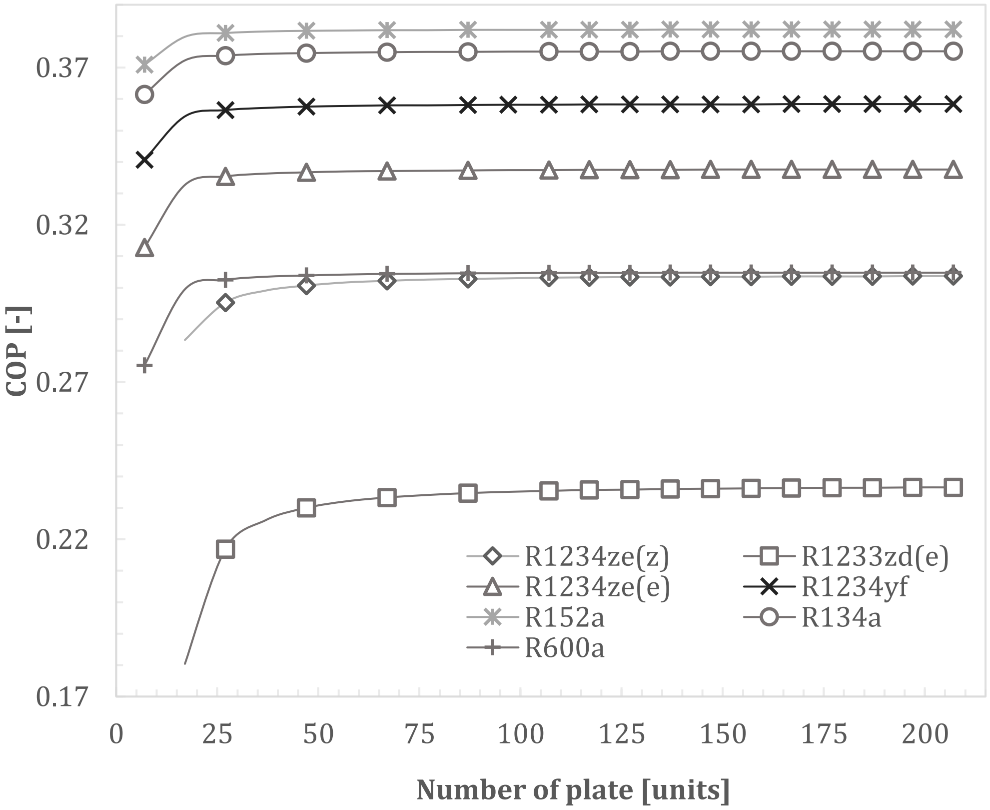

Figure 6.34 The influence of the condenser size on the system performance.

Figure 6.34 shows the influence of the condenser size on the system performance. A very similar manner of the COPs of the selected refrigerants was found. The two lowest performance fluids showed the impact of the condenser's size until about 90 plates; while with other working fluids was only about 30 plates, there was no noticeable change. It can be concluded that the influence of the pressure loss through the heat exchangers should not be an issue.

6.6 Conclusions

The chapter assessed the selected fluids at several aspects. The behaviors of the system performance on the superheating amounts in the inlet flows were discussed. The influence of the heat exchangers' size on the system performance was generally studied.

From the experimental and mathematical work, it was found that the superheating in the primary and secondary flows was necessary and, inevitable. Superheating inlet flows help eliminating the phase change that possibly occurs as the flows go through complex expansions and shockwave inside the ejector. It is inevitable because of the suction effect at the secondary inlet, as explained in section 6.3. The superheating of the secondary flow resulted in a better COP, while the superheating of the primary flow caused a negative effect on COP since more heat was needed for driving the system.

The operating temperatures tremendously affected the system performance. The COPs of all working fluids significantly increased with the saturation temperatures (or the working pressures) of the two inlet flows and decreased with the saturation temperature of the outlet flow at the condenser.

The area ratios suggested that the use of a variable geometry ejector is necessary for maintaining favorable system performance at various operating conditions, especially with the low-performance working fluids R1233zd(e) and R1234ze(z).

The size of the heat exchangers clearly influenced the heat transfer coefficient and the pressure loss of the refrigerant flows, in which the heat transfer coefficient was more important parameter. It was because the required number of plates in order to reach to ignorable pressure drop level were much less than the required plate number for the heat transfer rates. Of course, it depends on the working temperatures at the inlets and outlets of the heat exchangers.

Though the pressure drops thought heat exchangers could be significant, their impact on the ejector performance is quite trivial, especially when the numbers of plates were sufficient for the heat transfer tasks.

It is found that R1234yf and R1234ze(e) were the qualified working fluids of the study. R1234yf had better overall performance than the other. However, its working pressures could be challenging as a much more robust system is required. R1234ze(e) is a reasonable choice in terms of performance and initial investment.

7 COMPARISON OF RESULTS BY THE MATHEMATICAL MODEL AND CFD

Computational fluid dynamics enables the designer to simulate different working conditions in a short period of time. It obtains comprehensive information of the model with a relatively low cost compared with the experimental method. Along with the other two methods, CFD was used frequently in studying ejector thanks to its advantages. For instance, the work of Pianthong et al. [25] on the impact of ejector geometry on the performance of ERS or Sriveerakul et al. [169] for predicting the performance of steam ejector.

The results of the assessments in the previous chapter showed that R1234ze(e) was the most reasonable working fluid. Thus, R1234ze(e) was used in a further study using CFD. Applying recommendations for steam-jet refrigeration equipment (Chapter 13 -ASHRAE guide and data book [170]), the mathematical model could generate the optimal geometry for a specific set of operating conditions.

Chapter 7 presents a quick look at using CFD tool for validating the ejector geometry generated by the mathematical model. The program Ansys Fluent is the industry-leading fluid simulation software [171]. It is integrated real gas based data (NIST real gas models) of many working fluids. Simulation using real gas based data could be highly beneficial with the complex flows, including shockwaves, highly turbulent, in the ejectors.

7.1 Methodology for the ejector simulating

Several turbulent models were found to be suitable for the compressible flow model. RNG (Renormalization-group) k-epsilon and k-omega-SST (shear-stress transport) are the best for simulating high-velocity flow in the ejector [167]; RNG-k-epsilon model was believed to better predict ejector entrainment ratio and shockwave structure compared with the other turbulent model [61, 67, 172]. Zhu et al. [67] found that RNG-k-epsilon model agreed best with the experiments. Furthermore, RNG-k-epsilon model does not require a very fine mesh, its recommended y^+ are 30÷200. As consequence, it needs less calculating time (computing resource) compared with k-omega-SST. Thus RNG-k-epsilon model was selected in the current work.

The enhanced wall treatment was applied to obtain a more accurate representation of the flow in the near-wall regions. The enhanced wall functions can be used with coasted meshes as well as fine meshes without causing an excessive error [173]. The enhanced wall functions were proved to be suitable for the near-wall treatment of the supersonic ejectors [160, 174]. When wall functions are used, it is recommended to have the meshes with the non-dimensional distance (y^+) in the range 30÷200 at near-wall grid [173]. When an omega-based turbulent model is selected, near-wall meshes with $y^+ \sim 1$ is recommended [173]. That results in excessively fine meshes and thus, much more computing resource is required.

Table 7.1 Details of the model setup.

Domain	**2-D axisymmetric**
Turbulent viscosity model	RNG k-epsilon
Near-wall function	Enhanced wall functions
Working fluid	R1234ze(e) – Real gas NIST model
Boundary conditions	- Pressure inlet at the two inlets - Pressure outlet at the outlet

The pressure-based coupled solver was used in the current study since it showed great stability and computing-resource saving compared with the density-based solver [41]. The ejector was modeled as a two-dimensional problem, with the domain is axisymmetric about the horizontal axis. Pressure boundary conditions were applied at the two ejector inlets and the outlet. The NIST database was used to improve the result accuracy. Table 7.1 and Table 7.2 present the more detailed setups and solutions for the ejector model.

Table 7.2 Details of the model solutions.

Solution methods	
- Pressure-velocity coupling	Coupled
- Spatial discretization	Second order Upwind
Solution controls	Under-relaxation factors were adjusted during the simulations
Convergent criteria	Residuals < 10^{-6}

7.2 Comparison of viscous turbulence models

As discussed above, RNG k-epsilon and SST k-omega were considered as the most suitable for simulating high compressible flow. This section gives a quick comparison between these two turbulence models. Excepts for the selected turbulence models, the setups for the two simulations were identical. Table 7.3 shows that the two turbulence models predicted the mostly the same value of the primary mass flow rate, the difference between them was 0.2 g/s. The difference between the secondary mass flow rates between the two turbulence models was more considerable. Please note that the simulations were executed with a mesh size of about 60 thousand cells. The mesh density was certainly insufficient for the SST k-omega model. A primary requirement of this model is that the non-dimensional wall distance should be around 1 since no near-wall treatment function is available for this turbulence model.

Table 7.3 The inlet mass flow rates of the two turbulence models.

	RNG k-epsilon	**SST k-omega**
$\dot{m}_g$ (g/s)	68.6	68.4
$\dot{m}_e$ (g/s)	33.1	31.3

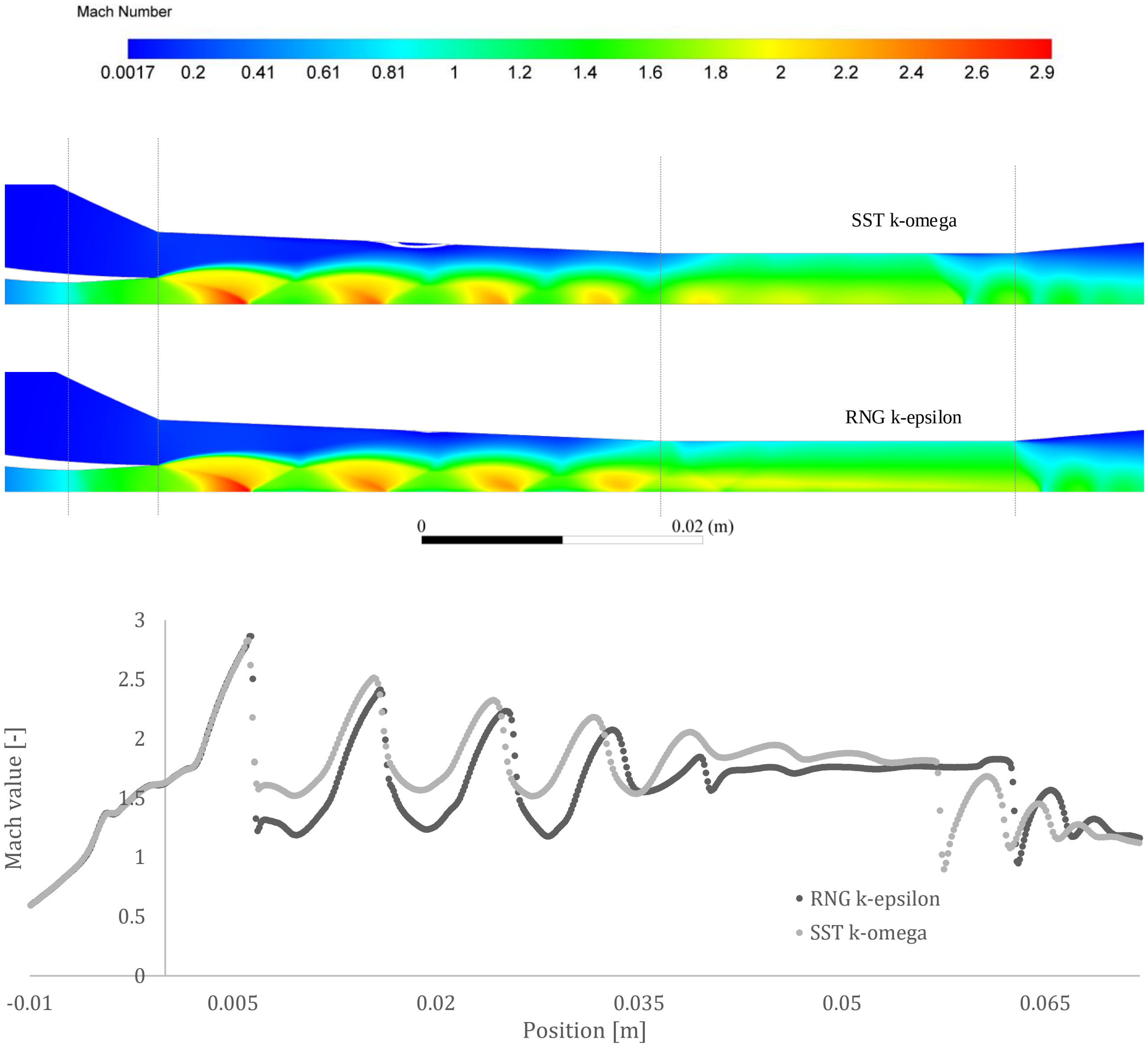

Figure 7.1 Mach contour comparison between SST k-omega and RNG k-epsilon model.

Figure 7.1 presents the Mach contours of the two turbulence models. It is difficult to pinpoint the differences between the two contours. Both show a series of four shockwaves of the primary flow at the primary nozzle downstream. The location of the shockwaves between the two models were, however, shifted by a little. It can be observed in the chart of Mach value on the x-axis. Besides, their shocks' intensities were slightly different from each other. The shockwaves of RNG k-epsilon seemed to be more intense compared with the other model. Therefore, the Mach differences between the two models became more significant after every shock.

The most noticeable difference between the two models was in the constant area section of the ejector. The shockwave of the mixed flow at the end of the constant area section of the two models was also considerably dissimilar. In the RNG k-epsilon model, the shock occurred at the very end of the constant area section; while in the other model, the major shock took place somewhere within the constant area section, then another less-intensive shock right at the end of the section. The intensity of the shockwaves was clearly illustrated in the chart.

Based on the analyses above and the results from the literature (presented in section 7.1), the RNG k-epsilon model was selected to carry on the next steps of this study.

7.3 Mesh and mesh independence study for the simulation

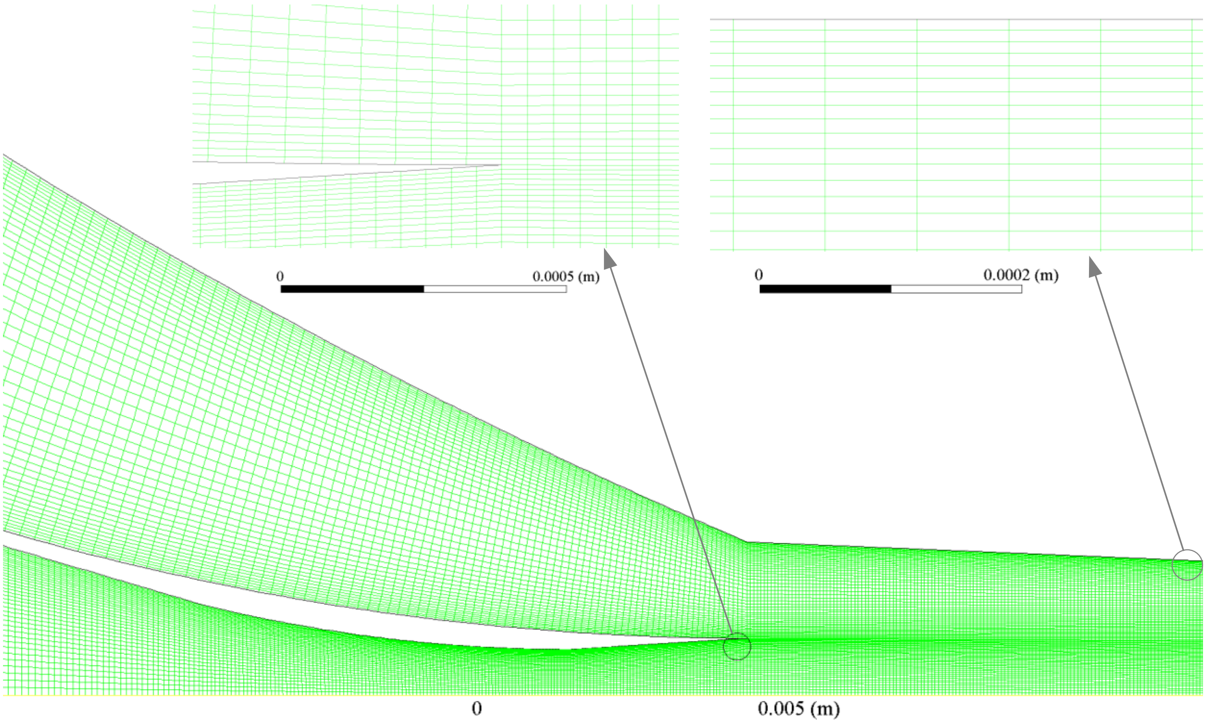

Figure 7.2 The generated mesh by Ansys Mesher.

Figure 7.2 shows part of the computational grid, which was generated in Ansys Mesher. The Ansys Mesher is a sufficient tool for simple geometry like the two-dimensional ejector model. The mesh was made of structured quadrilateral elements. The grid density at the ejector walls was high to ensure the non-dimensional distance remain at ~30÷50.

Besides, other quality indicators showed that the generated mesh was adequate for acquiring high accurate simulations. For example, the aspect ratio of the mesh was mostly less than 3 and did not exceed 10, the mesh skewness was typically 10^{-9}. It was observed in this work, aspect ratio/mesh quality affect greatly to the computational convergence (and also to the accuracy).

The mesh independence study was conducted with nine different mesh sizes of the 2D ejector model. The size varied from $15\times10^3\div90\times10^3$ cells. Figure 7.3 shows the impact of the grid size on the inlet flow rates ($\dot{m}_g$ and $\dot{m}_e$). As can be seen, the secondary mass flow rate varied more significantly in comparison with the other mass flow rate. $\dot{m}_g$ remained at ~68.6g in this particular working conditions. The model could well predict the primary flow rate already with a coast mesh (15×10^3 cells). However, $\dot{m}_e$ varied from 31.49g to 33.34g, or about 5.9% difference in the entire mesh size range. The change of $\dot{m}_e$ was quite trivial when the mesh exceeded 60×10^3 cells.

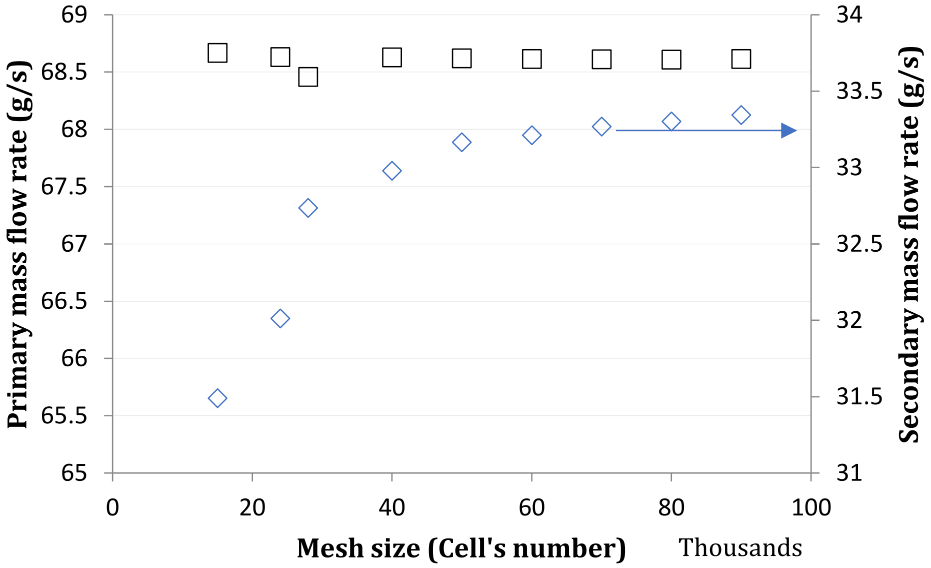

Figure 7.3 Impact of the grid size on the mass flow rates.

Figure 7.4 shows the variation of the ejector entrainment ratio with the mesh size. The ER was fairly consistent at different grid sizes of the ejector model. The ER insignificantly varied the mesh size range of $60\times10^3\div90\times10^3$. In this size range, the difference of ER values between two adjacent mesh sizes was only 0.1÷0.2%.

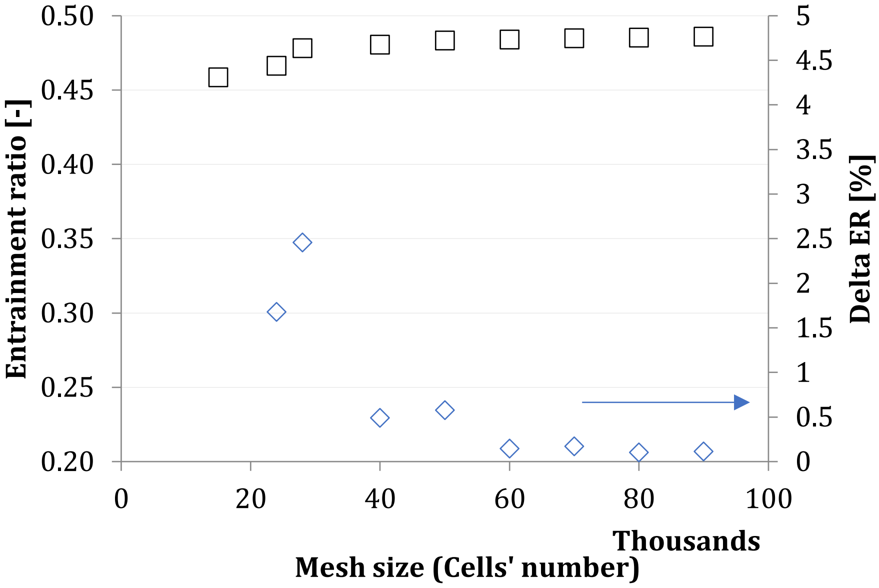

Figure 7.4 Variation of the entrainment ratio with the mesh size.

The mesh independence study proposed that $60\times10^3 \div 70\times10^3$ cells should be the reasonable size of the mesh sizes for the current ejector model. Finer mesh could not offer any noticeable benefit; while it requires considerable computing resources, especially with simulations using the real gas database.

7.4 Comparing of the mathematical model and CFD simulation

The working conditions and the desired cooling capacity were used as the input parameters of the mathematical model. The obtained ejector geometry and operating conditions from the mathematical model were used to generate the corresponding ejector model in Ansys Fluent. The mass flow rates from the CFD simulation was then compared with the results of the mathematical work.

Table 7.4 Working conditions of ERS for the comparison.

	$T_{g,sat}$ / P_g	$T_{e,sat}$ / P_e	$T_{c,sat}$ / P_c	$\Delta T_{g,sh}$	$\Delta T_{e,sh}$
Set 1	83 °C / 21.4 bara	10 °C / 3.09 bara	34 °C / 6.5 bara	7 K	2 K
Set 2	85 °C / 22.1 bara	10 °C / 3.09 bara	30.2°C / 5.81 bara	5.1 K	1 K

Two sets of the working conditions were selected for the study, as showed in Table 7.4. The designed cooling capacity of the ejector cooling system of both sets was 5 kW and R1234ze(e) was used as the working fluid. Figure 7.5 presents the dimensions of the ejector for the first set of working conditions.

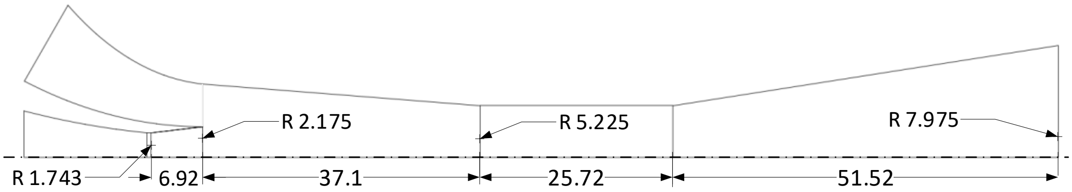

Figure 7.5 Dimensions of the ejector (mm).

Figure 7.6 compares the results from the two methods. It shows that the secondary flow rates of the two methods well agreed with each other. Since the cooling capacity was set at 5 kW and the operating conditions at the evaporator were similar for both sets, the secondary flow rates of both cases were similar. However, it not the case for the primary flow rates. That was the major reason for the entrainment ratio differences between the two methods. Nevertheless, the deviations of these parameters were within 10%

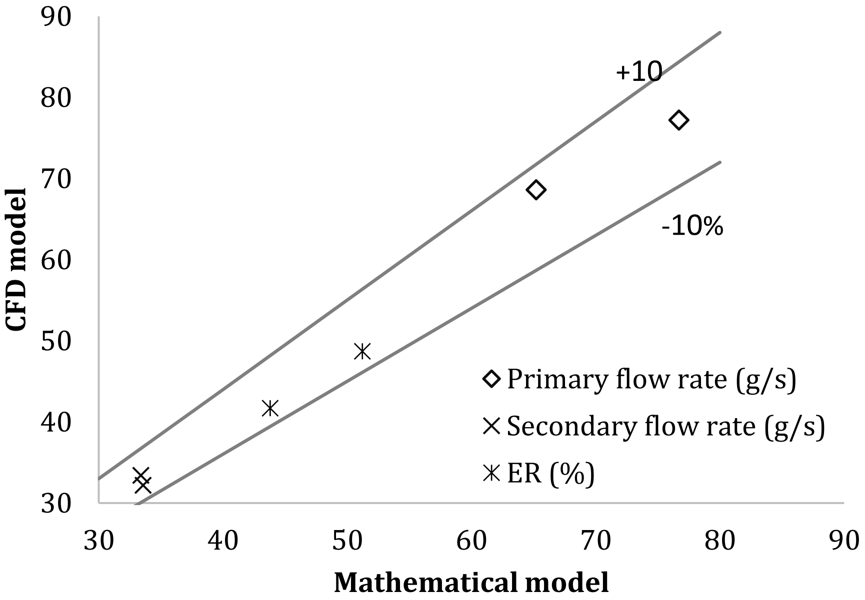

Figure 7.6 Comparison between the mathematical and CFD model.

These brief comparisons were aimed for quick validation of the mathematical model, specified on the ejector performance. Certainly, further investigations, including experimental work, are needed to confirm the validity of the results.

8 CONCLUSIONS AND FUTURE WORKS

8.1 Conclusions

The largest share of electricity consumption in buildings is the consumption of space cooling; and space cooling is a major source of carbon dioxide emissions. Reducing the emission of CO_2 and greenhouse gases could slow down the climate change. Ejector cooling technology using low GWP100 index refrigerant could perfectly fit in to the efforts for inverse the current climate trend.

The final goal of current research using various methods was thermal design of an ejector cooling system with a novel refrigerant as the working fluid. An experimental method was implemented to study the influence of key factors on the system performance. The experimental results were used as references for the mathematical model. In the numerical works, a detailed model of the ejector cooling cycle, including the phase change processes in the heat exchangers, was built. The mathematical model was employed to access the selected working. Afterwards, an ejector model in Ansys Fluent with the qualified refrigerant as the working fluid was built to validate the mathematical model.

8.1.1 The experimental work

The thermocouples and pyranometer of the test rig were carefully calibrated. The uncertainty analyses were performed to ensure the validity of experimental results. Looking at the results obtained, it is clear that the system was extremely stable during the tests.

The study investigated the effect of the nozzle exit position and spindle position on the performance of the solar thermal energy driven ERS. It was found that the influence of the NXP strongly depends on the primary inlet pressure. At the highest-pressure level tested (12.2 bar), the COP was significantly varied with the NXP; while at the low-pressure level (8.6 bar), the influence of the NXP was mostly unnoticeable. The spindle position affected all operating parameters, including the generator pressure, mass flow rates, system performance and cooling capacity. The SP can be adjusted to obtain an optimal performance in various operating conditions. The improvement of the COP was up to 42% compared to a similar system using a fixed geometry ejector. It has been found that the COP can be further improved by independent control of the primary flow rate/spindle position and the primary inlet pressure. Experimental results also showed great stability of the system, although it operated under partially cloudy days with interruption of sunlight for up to about 30 minutes.

The results revealed the possibility of improving the design of the variable geometry ejector in terms of simplicity and cost efficiency. The optimal nozzle exit position of the current ejector was 5 mm. The observations during the experiments suggested that there is an optimal value of the NXP for each ejector design regardless of the primary pressure variation. Therefore, using an ejector with variable spindle position (with fixed NXP) could simplify the design without significantly compromising on system performance.

The experiments also revealed interesting behavior of the secondary pressure inlet in off-design mode of operation. When the backpressure was increased in the off-design regime, the secondary pressure had the exactly opposite trend. It is very interesting phenomenon and the author would expect to see further studies on it.

8.1.2 The numerical works

The mathematical model was built in the EES program. It was modeled in detail using the real gas database to achieve high accuracy. This model allows a comprehensive study, including a study of the effects of the superheat on the primary and secondary flows on the system performance, a study of the heat transfer efficiency at different operation temperatures and pressures of the heat exchangers, the chevron angle of the plates for pressure drop and heat transfer coefficient and much more.

Seven working fluids were assessed by a series of parameter study. The common HFC-152a and HFC-134a, HC-600a were used as references to compare with four HFOs: R1234yf, R1234ze(e), R1234ze(z), and R1233zd(e).

The results showed that the performance of the fluids somewhat influenced by the amount of superheating in the inlet flows. The present of superheat in the inlet flows is necessary for the ejector operating stability.

Overall, the operating temperatures extremely influenced the system performance, especially condenser temperature. For example, as $T_{c,sat}$ ranged from 29÷39°C, the

$COP_{R1234ze(e)}$ dropped from 0.52 to 0.17. Or when $T_{g,sat}$ went from 63 to 94.5°C, the $COP_{R1234yf}$ increased threefold, from 0.143 to 0.454.

R1234yf and R1234ze(e) were qualified as the most suitable working fluids in this study. R1234yf was the most promising HFO working fluid in the terms of performance. However, the high working pressure in the generator can be a disadvantage because it requires a robust system. R1234ze(e) is a more suitable choice in terms of the system performance and robustness. R1234ze(z) and R1233zd(e) in many respects were not decent candidates for ejector cooling technology.

The study also indicated that sufficient generator temperatures ($T_{g,sat} > 80°C$) is better compared with a low-grade driven heat source since it requires a significantly lower heat input.

According to the current study, the size of the heat exchangers clearly affected the heat transfer coefficient and the pressure loss of the refrigerant flows. However, the pressure drops though the heat exchanger became insignificant when the heat exchanger sizes were increased to meet the requirements for the heat transfer capacity. The heat transfer capacity was the decisive factor in selecting heat exchangers for ejector cooling cycle. In future work, detailed studies of the plate geometry and operating temperatures of hot and cold fluids should be carried out in order to better understand this issue.

8.2 Future works

During the experimental work, it was noticed that the test rig can be improved by improving three components: the circulating pump, the expansion valve, and the flowmeters.

Although the proposed pressure head of the circulating pump of the experimental rig is 16 bar, it could only work properly with a pressure of up to about 13 bar. As the pump speed was increased to obtain a higher-pressure head, the pressure head dropped, and cavitation occurred in the pump. Using a seal-less diaphragm pump could generate much higher-pressure head (hundreds of bar) compared with a centrifugal pump. Also, the use of a seal-less pump does not create impurities for the working fluid, which leads to another problem as discussed below.

The worn-out graphite in the centrifugal pump could cause the expansion valve to block. Most likely, fraction of worn-out graphite became the impurity in the working fluid, which was trapped in the needle of the expansion valve. Consequently, the expansion valve sometimes did not work properly. The flowrate to the evaporator was not sufficient, and its pressure was only 0.3 to 0.7 bar, instead of 1.1 to 1.2 bar. The cooling capacity was lower than usual. Therefore, it is recommended to use a filter in front of the expansion valve.

The measurement of the gas flow in the ejector cooling cycle could be improved. Variable area flowmeters could achieve high accuracy in most of operating conditions. However, when they work in a lower working range, the measured value significantly fluctuated. This could lead to high measurement uncertainty. With the setting of the test rig, it is assumed that the COP can be calculated more accurately using data from water cycles. Therefore, it is no necessary to use gas flowmeters in the ejector cooling cycle. It helps reduce costs and pressure drops caused by gas flowmeters.

The mathematical model should be more carefully verified with experimental study as a whole unit (entire cycle). The mathematical model of the ejector has been verified by experimental work, but it is not sufficient to ensure the validity of the entire ejector cooling cycle. The experimental test rig of the future work should be designed to allow validation of the mathematical model of heat exchangers.

There are some more parameters that need to be explored to improve the heat exchangers used in ejector cooling technology, e.g., the chevron corrugation angle, plate thermal conductivity, plate thickness. It would be interesting to observe how these parameters affect the pressure drop and heat transfer coefficient of the heat exchangers and the performance of the cooling cycle.

The computational fluid dynamics can be used to optimize the ejector geometry. For example, Ansys DesignXplorer is a powerful tool for design optimization using automatic parametric analysis.

REFERENCES

[1] Yew LK. From Third World to First : The Singapore Story, 1965-2000. 2000.

[2] Happle G, Wilhelm E, Fonseca JA, Schlueter A. Determining air-conditioning usage patterns in Singapore from distributed, portable sensors. Energy Procedia 2017;122:313–8. https://doi.org/10.1016/J.EGYPRO.2017.07.328.

[3] OECD/IEA. The Future of Cooling Opportunities for energy-efficient air conditioning Together Secure Sustainable 2018:92.

[4] Mohan V. India's share in global air conditioning units to jump from 2.2% to almost 25% by 2050 2018:Read more at: //economictimes.indiatimes.com/artic. https://economictimes.indiatimes.com/news/environment/global-warming/indias-share-in-global-air-conditioning-units-to-jump-from-2-2-to-almost-25-by-2050/articleshow/66595350.cms.

[5] International Agency Energy. Key World Energy Statistics 2018. n.d.

[6] IEA Statistics. Electricity production from oil, gas and coal sources (% of total) | Data. World Bank Gr 2015. https://data.worldbank.org/indicator/EG.ELC.FOSL.ZS (accessed August 9, 2019).

[7] International Energy Agency. World Energy Outlook 2014. 2040.

[8] EEA. Annual European Union greenhouse gas inventory 1990–2017 and inventory report 2019. Off Off Publ Eur Communities 2019:962. https://doi.org/10.2800/41819.

[9] U.N. Global temperatures on track for 3-5 degree rise by 2100: U.N. - Reuters. Reuters 2018. https://www.reuters.com/article/us-climate-change-un/global-temperatures-on-track-for-3-5-degree-rise-by-2100-u-n-idUSKCN1NY186 (accessed August 10, 2019).

[10] WEF. The Global Risks Report 2019 14th Edition Insight Report. 2019.

[11] THE EUROPEAN PARLIAMENT. Regulation (EU) no 517/2014 of the European parliament and of the council. 2014.

[12] Guo J, Shen HG. Modeling solar-driven ejector refrigeration system offering air

conditioning for office buildings. Energy Build 2009;41:175–81. https://doi.org/10.1016/j.enbuild.2008.07.016.

[13] De Laval CGP. Steam turbine. 522,066., 1889.

[14] Leblanc M. THE LEBLANC EJECTOR CONDENSER. J Am Soc Nav Eng 1909;21:1338–43. https://doi.org/10.1111/j.1559-3584.1909.tb02179.x.

[15] Stoecker WF. Steam-jet refrigeration. New York, Toronto, London: Boston: McGraw-Hill; 1958.

[16] Thulukkanam K. Heat Exchanger Design Handbook, Second Edition. 2013. https://doi.org/10.1201/b14877.

[17] Hesselgreaves JE. Compact Heat Exchangers Selection, Design and Operation. 2001.

[18] Riffat SB, Holt A. A novel heat pipe/ejector cooler. Appl Therm Eng 1998;18:93–101. https://doi.org/10.1016/S1359-4311(97)00053-7.

[19] Sadik, Kakac, Hongtan L. Heat exchangers, Selection, Rating, and Thermal Design, Third Edition. n.d.

[20] Grazzini G, Milazzo A, Mazzelli F. Ejectors for efficient refrigeration: Design, applications and computational fluid dynamics. 2018. https://doi.org/10.1007/978-3-319-75244-0.

[21] Al-Khalidy N. An experimental study of an ejector cycle refrigeration machine operating on R113. Int J Refrig 1998;21:617–25. https://doi.org/10.1016/S0140-7007(98)00030-9.

[22] Sumeru K, Nasution H, Ani FN. A review on two-phase ejector as an expansion device in vapor compression refrigeration cycle. Renew Sustain Energy Rev 2012;16:4927–37. https://doi.org/10.1016/j.rser.2012.04.058.

[23] Tashtoush B, Alshare A, Al-Rifai S. Performance study of ejector cooling cycle at critical mode under superheated primary flow. Energy Convers Manag 2015;94:300–10. https://doi.org/10.1016/j.enconman.2015.01.039.

[24] KEENAN, H. J. An Investigation of Ejector Design by Analysis and Experiment. J Appl Mech 1950;17:299.

[25] Pianthong K, Seehanam W, Behnia M, Sriveerakul T, Aphornratana S. Investigation and improvement of ejector refrigeration system using computational fluid dynamics

technique. Energy Convers Manag 2007;48:2556–64. https://doi.org/10.1016/j.enconman.2007.03.021.

[26] Tashtoush B, Alshare A, Al-Rifai S. Hourly dynamic simulation of solar ejector cooling system using TRNSYS for Jordanian climate. Energy Convers Manag 2015;100:288–99. https://doi.org/10.1016/j.enconman.2015.05.010.

[27] Chen S, Chen G, Fang L. An experimental study and 1-D analysis of an ejector with a movable primary nozzle that operates with R236fa. Int J Refrig 2015;60:19–25. https://doi.org/10.1016/j.ijrefrig.2015.08.011.

[28] Munday JT, Bagster DF. A New Ejector Theory Applied to Steam Jet Refrigeration. Ind Eng Chem Process Des Dev 1977;16:442–9. https://doi.org/10.1021/i260064a003.

[29] Fabri J, Siestrunck R. Supersonic Air Ejectors. Adv Appl Mech 1958;5:1–34. https://doi.org/10.1016/S0065-2156(08)70016-4.

[30] Li A, Yuen ACY, Chen TBY, Wang C, Liu H, Cao R, et al. Computational study of wet steam flow to optimize steam ejector efficiency for potential fire suppression application. Appl Sci 2019;9. https://doi.org/10.3390/app9071486.

[31] James R. Understanding ejector systems necessary to troubleshoot vacuum distillation. n.d.

[32] Aidoun Z, Ameur K, Falsafioon M, Badache M. Current Advances in Ejector Modeling, Experimentation and Applications for Refrigeration and Heat Pumps. Part 1: Single-Phase Ejectors. Inventions 2019;4:15. https://doi.org/10.3390/inventions4010015.

[33] Huang BJ, Chang JM, Petrenko VA, Zhuk KB. A solar ejector cooling system using refrigerant R141b. Sol Energy 1998;64:223–6. https://doi.org/10.1016/S0038-092X(98)00082-6.

[34] Huang BJ, Chang JM, Wang CP, Petrenko VA. A 1-D analysis of ejector performance. Int J Refrig 1999;22:354–64. https://doi.org/10.1016/S0140-7007(99)00004-3.

[35] Huang B., Chang J. Empirical correlation for ejector design. Int J Refrig 1999;22:379–88. https://doi.org/10.1016/S0140-7007(99)00002-X.

[36] Varga S, Oliveira AC, Diaconu B. Numerical assessment of steam ejector efficiencies using CFD. Int J Refrig 2009;32:1203–11. https://doi.org/10.1016/j.ijrefrig.2009.01.007.

[37] Liu F, Groll EA. Study of ejector efficiencies in refrigeration cycles. Appl Therm Eng 2013;52:360–70. https://doi.org/10.1016/j.applthermaleng.2012.12.001.

[38] Chen J, Havtun H, Palm B. Investigation of ejectors in refrigeration system: Optimum performance evaluation and ejector area ratios perspectives. Appl Therm Eng 2014;64:182–91. https://doi.org/10.1016/j.applthermaleng.2013.12.034.

[39] Chen W, Shi C, Zhang S, Chen H, Chong D, Yan J. Theoretical analysis of ejector refrigeration system performance under overall modes. Appl Energy 2017;185:2074–84. https://doi.org/10.1016/j.apenergy.2016.01.103.

[40] Chunnanond K, Aphornratana S. Ejectors: applications in refrigeration technology. Renew Sustain Energy Rev 2004;8:129–55.

[41] Vu N Van, Kracik J. CFD simulation of ejector : is it worth to use real gas models. EPJ Web Conf 2018;02075:7. https://doi.org/10.1051/epjconf/201818002075.

[42] Allouche Y, Bouden C, Varga S. A CFD analysis of the flow structure inside a steam ejector to identify the suitable experimental operating conditions for a solar-driven refrigeration system. Int J Refrig 2014;39:186–95. https://doi.org/10.1016/j.ijrefrig.2013.07.027.

[43] Giuseppe Tommasone. Food & Dairy: Different type of Heat Exchangers n.d. http://heatexchan.blogspot.com/2017/04/food-dairy-different-type-of-heat.html (accessed August 15, 2019).

[44] Laval A. Alfa Laval CB11 / CBH11. n.d.

[45] Shah R, Sekulic D. Fundamentals of Heat Exchangers Design. 2003.

[46] Haskell - Wikibooks, open books for an open world n.d. https://en.wikibooks.org/wiki/Heat_Transfer/Heat_Exchangers (accessed October 19, 2019).

[47] Magadum A, Pawar A, Patil R, Phadtare R. Experimental Investigation of Parallel and Counter flow Heat Exchanger. Int J Adv Res Sci Eng Technol 2016;3.

[48] Natural Refrigerants | Linde Gas n.d. https://www.linde-

gas.com/en/products_and_supply/refrigerants/natural_refrigerants/index.html (accessed August 7, 2020).

[49] Barrett S, Barrett S. The Montreal Protocol. Environ Statecr 2005:221–40. https://doi.org/10.1093/0199286094.003.0008.

[50] EUROPEAN PARLIAMENT. REGULATION (EC) No 2037/2000 OF THE EUROPEAN PARLIAMENT AND OF THE COUNCIL 2000:1–31.

[51] Kim M-H, Lim B-H, Chu E-S. The performance analysis of a hydrocarbon refrigerant R-600a in a household refrigerator/freezer. KSME Int J 1998;12:753–60. https://doi.org/10.1007/BF02945737.

[52] Chen J, Havtun H, Palm B. Screening of working fluids for the ejector refrigeration system. Int J Refrig 2014;47:1–14. https://doi.org/10.1016/j.ijrefrig.2014.07.016.

[53] Choudhari CS, Sapali SN. Performance Investigation of Natural Refrigerant R290 as a Substitute to R22 in Refrigeration Systems. Energy Procedia 2017;109:346–52. https://doi.org/10.1016/J.EGYPRO.2017.03.084.

[54] Ip YK, Chew SF, Randall DJ. Ammonia toxicity, tolerance, and excretion. Nitrogen Excretion, vol. 20, Academic Press; 2001, p. 109–48. https://doi.org/https://doi.org/10.1016/S1546-5098(01)20005-3.

[55] S PA, D KA. Carbon Dioxide as Natural Refrigerant. Int J Appl Eng Res DINDIGUL 2010;1.

[56] Water as a refrigerant - Efficient Energy n.d. https://efficient-energy.de/en/the-most-efficient-chiller/water-as-a-refrigerant/ (accessed August 7, 2020).

[57] Fisher DA, Hales CH, Filkin DL, Ko MKW, Dak Sze N, Connell PS, et al. VIII. OZONE DEPLETION POTENTIALS Relative Effects on Stratospheric Ozone of Halogenated Methanes and Ethanes of Social and Indtc_trial Interest. n.d.

[58] Greenhouse gas protocol. Global Warming Potential Values. 2014.

[59] ASHRAE. Safety Standard for Refrigeration Systems and Designation and Classification of Refrigerants (ANSI Approved). 2016.

[60] Jia L, Jin W, Zhang Y. Analysis of Indoor Environment Safety with R32 Leaking from a Running Air Conditioner. Procedia Eng 2015;121:1605–12. https://doi.org/10.1016/j.proeng.2015.09.190.

[61] Wang C, Wang L, Gao R. The effects of superheated refrigerant on ejector performances. 2015 IEEE 10th Conf. Ind. Electron. Appl., IEEE; 2015, p. 2055–60. https://doi.org/10.1109/ICIEA.2015.7334453.

[62] Elbarghthi AFA, Mohamed S, Nguyen VV, Dvorak V. CFD Based Design for Ejector Cooling System Using HFOS (1234ze(E) and 1234yf). Energies 2020;13:1408. https://doi.org/10.3390/en13061408.

[63] Varga S, Oliveira AC, Palmero-Marrero A, Vrba J. Preliminary experimental results with a solar driven ejector air conditioner in Portugal. Renew Energy 2017;109:83–92. https://doi.org/10.1016/j.renene.2017.03.016.

[64] Pereira PR, Varga S, Oliveira AC, Soares J. Development and Performance of an Advanced Ejector Cooling System for a Sustainable Built Environment. Front Mech Eng 2015;1:1–12. https://doi.org/10.3389/fmech.2015.00007.

[65] Pridasawas W. Solar-driven refrigeration systems with focus on the ejector cycle. 2006.

[66] He S, Li Y, Wang RZ. A new approach to performance analysis of ejector refrigeration system using grey system theory. Appl Therm Eng 2009;29:1592–7. https://doi.org/10.1016/j.applthermaleng.2008.07.016.

[67] Zhu Y, Cai W, Wen C, Li Y. Numerical investigation of geometry parameters for design of high performance ejectors. Appl Therm Eng 2009;29:898–905. https://doi.org/10.1016/j.applthermaleng.2008.04.025.

[68] Jia Y, Wenjian C. Area ratio effects to the performance of air-cooled ejector refrigeration cycle with R134a refrigerant. Energy Convers Manag 2012;53:240–6. https://doi.org/10.1016/j.enconman.2011.09.002.

[69] Yan J, Cai W, Li Y. Geometry parameters effect for air-cooled ejector cooling systems with R134a refrigerant. Renew Energy 2012;46:155–63. https://doi.org/10.1016/j.renene.2012.03.031.

[70] Varga S, Lebre PS, Oliveira AC. Readdressing working fluid selection with a view to designing a variable geometry ejector. Int J Low-Carbon Technol 2013;10:205–15. https://doi.org/10.1093/ijlct/ctt026.

[71] Sankarlal T, Mani A. Experimental investigations on ejector refrigeration system with ammonia. Renew Energy 2007;32:1403–13.

https://doi.org/10.1016/j.renene.2006.05.008.

[72] Yapıcı R, Ersoy HK, Aktoprakoğlu A, Halkacı HS, Yiğit O. Experimental determination of the optimum performance of ejector refrigeration system depending on ejector area ratio. Int J Refrig 2008;31:1183–9. https://doi.org/10.1016/j.ijrefrig.2008.02.010.

[73] Hewedy NII, Hamed MH, Abou-Taleb FS, Ghonim T a. Optimal Performance and Geometry of Supersonic Ejector. J Fluids Eng 2008;130:041204. https://doi.org/10.1115/1.2903742.

[74] Sun D-W. Variable geometry ejectors and their applications in ejector refrigeration systems. Energy 1996;21:919–29. https://doi.org/10.1016/0360-5442(96)00038-2.

[75] Besagni G, Mereu R, Inzoli F. Ejector refrigeration: A comprehensive review. Renew Sustain Energy Rev 2016;53:373–407. https://doi.org/10.1016/j.rser.2015.08.059.

[76] Yapıcı R, Yetişen CC. Experimental study on ejector refrigeration system powered by low grade heat. Energy Convers Manag 2007;48:1560–8. https://doi.org/10.1016/j.enconman.2006.11.015.

[77] Allouche Y, Bouden C, Riffat S. A solar-driven ejector refrigeration system for Mediterranean climate: Experience improvement and new results performed. Energy Procedia, vol. 18, Elsevier BV; 2012, p. 1115–24. https://doi.org/10.1016/j.egypro.2012.05.126.

[78] Chen X, Worall M, Omer S, Su Y, Riffat S. Experimental investigation on PCM cold storage integrated with ejector cooling system. Appl Therm Eng 2014;63:419–27. https://doi.org/10.1016/j.applthermaleng.2013.11.029.

[79] Nguyen V., Riffat S., Doherty P. Development of a solar-powered passive ejector cooling system. Appl Therm Eng 2001;21:157–68. https://doi.org/10.1016/S1359-4311(00)00032-6.

[80] Wang F, Shen S. A novel solar bi-ejector refrigeration system and the performance of the added injector with different structures and operation parameters. Sol Energy 2009;83:2186–94. https://doi.org/10.1016/j.solener.2009.08.012.

[81] Zhang S, Cheng Y. Performance improvement of an ejector cooling system with thermal pumping effect (ECSTPE) by doubling evacuation chambers in parallel. Appl Energy 2017;187:675–88. https://doi.org/10.1016/j.apenergy.2016.11.080.

[82] Huang BJ, Hu SS, Lee SH. Development of an ejector cooling system with thermal pumping effect. Int J Refrig 2006;29:476–84. https://doi.org/10.1016/j.ijrefrig.2005.08.004.

[83] Wang JH, Wu JH, Hu SS, Huang BJ. Performance of ejector cooling system with thermal pumping effect using R141b and R365mfc. Appl Therm Eng 2009;29:1904–12. https://doi.org/10.1016/j.applthermaleng.2008.08.015.

[84] Selvaraju A, Mani A. Experimental investigation on R134a vapour ejector refrigeration system. Int J Refrig 2006;29:1160–6. https://doi.org/10.1016/J.IJREFRIG.2006.01.004.

[85] Chen LT. A new ejector-absorber cycle to improve the COP of an absorption refrigeration system. Appl Energy 1988;30:37–51. https://doi.org/10.1016/0306-2619(88)90053-0.

[86] Majdi HS. Performance evaluation of combined ejector LiBr/H2O absorption cooling cycle. vol. 7. 2016. https://doi.org/10.1016/j.csite.2016.01.003.

[87] Angelino G, Invernizzi C. Thermodynamic optimization of ejector actuated refrigerating cycles. Int J Refrig 2008;31:453–63. https://doi.org/10.1016/j.ijrefrig.2007.07.014.

[88] Yari M, Mehr AS, Mahmoudi SMS. Simulation study of the combination of absorption refrigeration and ejector-expansion systems. Renew Energy 2013;60:370–81. https://doi.org/10.1016/j.renene.2013.05.039.

[89] Sokolov M, Hershgal D. Enhanced ejector refrigeration cycles powered by low grade heat. Part 1. Systems characterization. Int J Refrig 1990;13:351–6. https://doi.org/10.1016/0140-7007(90)90023-P.

[90] Sokolov M, Hershgal D. Enhanced ejector refrigeration cycles powered by low grade heat. Part 2. Design procedures. Int J Refrig 1990;13:357–63. https://doi.org/10.1016/0140-7007(90)90024-Q.

[91] Sokolov M, Hershgal D. Enhanced ejector refrigeration cycles powered by low grade heat. Part 3. Experimental results. Int J Refrig 1991;14:24–31. https://doi.org/10.1016/0140-7007(91)90018-C.

[92] Dorantes R, Estrada CA, Pilatowsky I. Mathematical simulation of a solar ejector-compression refrigeration system. Appl Therm Eng 1996;16:669–75.

[93] Yu J, Chen H, Ren Y, Li Y. A new ejector refrigeration system with an additional jet pump. Appl Therm Eng 2005;26:312–9. https://doi.org/10.1016/j.applthermaleng.2005.04.018.

[94] Zhu Y, Jiang P. Hybrid vapor compression refrigeration system with an integrated ejector cooling cycle. Int J Refrig 2012;35:68–78. https://doi.org/10.1016/j.ijrefrig.2011.09.003.

[95] Wang H, Cai W, Wang Y. Optimization of a hybrid ejector air conditioning system with PSOGA. Appl Therm Eng 2017;112:1474–86. https://doi.org/10.1016/j.applthermaleng.2016.10.192.

[96] Lin C, Li Y, Cai W, Yan J, Hu Y. Experimental investigation of the adjustable ejector in a multi-evaporator refrigeration system. Appl Therm Eng 2013;61:2–10. https://doi.org/10.1016/j.applthermaleng.2013.07.045.

[97] Elbel S, Hrnjak P. Experimental validation of a prototype ejector designed to reduce throttling losses encountered in transcritical R744 system operation. Int J Refrig 2008;31:411–22. https://doi.org/10.1016/j.ijrefrig.2007.07.013.

[98] Li D, Groll EA. Transcritical CO2 refrigeration cycle with ejector-expansion device. Int J Refrig 2005;28:766–73. https://doi.org/10.1016/j.ijrefrig.2004.10.008.

[99] Wang F, Li DY, Zhou Y. Theoretical research on the performance of the transcritical ejector refrigeration cycle with various refrigerants. Appl Therm Eng 2015;91:363–9. https://doi.org/10.1016/j.applthermaleng.2015.08.036.

[100] Yu J, Du Z. Theoretical study of a transcritical ejector refrigeration cycle with refrigerant R143a. Renew Energy 2010;35:2034–9. https://doi.org/10.1016/j.renene.2010.02.004.

[101] Bodys J, Palacz M, Haida M, Smolka J, Nowak AJ, Banasiak K, et al. Full-scale multi-ejector module for a carbon dioxide supermarket refrigeration system: Numerical study of performance evaluation. Energy Convers Manag 2017;138:312–26. https://doi.org/10.1016/j.enconman.2017.02.007.

[102] Danfoss. Transcritical CO 2 system in a small supermarket Article Transcritical CO 2 system in a small supermaket. 2008.

[103] Saleh B. Performance analysis and working fluid selection for ejector refrigeration cycle. Appl Therm Eng 2016;107:114–24.

https://doi.org/10.1016/j.applthermaleng.2016.06.147.

[104] Shen S, Qu X, Zhang B, Riffat S, Gillott M. Study of a gas–liquid ejector and its application to a solar-powered bi-ejector refrigeration system. Appl Therm Eng 2005;25:2891–902. https://doi.org/10.1016/J.APPLTHERMALENG.2005.02.012.

[105] Sankarlal T, Mani A. Experimental studies on an ammonia ejector refrigeration system. Int Commun Heat Mass Transf 2006;33:224–30. https://doi.org/10.1016/j.icheatmasstransfer.2005.08.002.

[106] Grazzini G, Milazzo A, Piazzini S. Prediction of condensation in steam ejector for a refrigeration system. Int J Refrig 2011;34:1641–8. https://doi.org/10.1016/J.IJREFRIG.2010.09.018.

[107] Chandra V V., Ahmed MR. Experimental and computational studies on a steam jet refrigeration system with constant area and variable area ejectors. Energy Convers Manag 2014;79:377–86. https://doi.org/10.1016/j.enconman.2013.12.035.

[108] Varga S, Oliveira AC, Ma X, Omer SA, Zhang W, Riffat SB. Experimental and numerical analysis of a variable area ratio steam ejector. Int J Refrig 2011;34:1668–75. https://doi.org/10.1016/J.IJREFRIG.2010.12.020.

[109] Yari M. Performance analysis and optimization of a new two-stage ejector-expansion transcritical CO2 refrigeration cycle. Int J Therm Sci 2009;48:1997–2005. https://doi.org/10.1016/J.IJTHERMALSCI.2009.01.013.

[110] Fangtian S, Yitai M. Thermodynamic analysis of transcritical CO2 refrigeration cycle with an ejector. Appl Therm Eng 2011;31:1184–9. https://doi.org/10.1016/J.APPLTHERMALENG.2010.12.018.

[111] Pounds DA, Dong JM, Cheng P, Ma HB. Experimental investigation and theoretical analysis of an ejector refrigeration system. Int J Therm Sci 2013;67:200–9. https://doi.org/10.1016/j.ijthermalsci.2012.11.001.

[112] Veser G, Schmidt LD. Ignition and Extinction in the Catalytic Oxidation of Hydrocarbons over Platinum. AIChE J 1996;42:1077–87. https://doi.org/10.1002/aic.690420418.

[113] Pridasawas W, Lundqvist P. A year-round dynamic simulation of a solar-driven ejector refrigeration system with iso-butane as a refrigerant. Int J Refrig 2007;30:840–50. https://doi.org/10.1016/j.ijrefrig.2006.11.012.

[114] Petrenko VO, Volovyk OS. Theoretical study and design of a low-grade heat-driven pilot ejector refrigeration machine operating with butane and isobutane and intended for cooling of gas transported in a gas-main pipeline. Int J Refrig 2011;34:1699–706. https://doi.org/10.1016/j.ijrefrig.2011.01.016.

[115] Roman R, Hernandez JI. Performance of ejector cooling systems using low ecological impact refrigerants. Int J Refrig 2011;34:1707–16. https://doi.org/10.1016/j.ijrefrig.2011.03.006.

[116] Śmierciew K, Gagan J, Butrymowicz D, Karwacki J. Experimental investigations of solar driven ejector air-conditioning system. Energy Build 2014;80:260–7. https://doi.org/10.1016/j.enbuild.2014.05.033.

[117] Pereira PR, Varga S, Soares J, Oliveira AC, Lopes AM, de Almeida FG, et al. Experimental results with a variable geometry ejector using R600a as working fluid. Int J Refrig 2014;46:77–85. https://doi.org/10.1016/J.IJREFRIG.2014.06.016.

[118] Suna D-W, Sun DW. Comparative study of the performance of an ejector refrigeration cycle operating with various refrigerants. Energy Convers Manag 1999;40:873–84. https://doi.org/10.1016/S0196-8904(98)00151-4.

[119] Khalil A, Fatouh M, Elgendy E. Ejector design and theoretical study of R134a ejector refrigeration cycle. Int J Refrig 2011;34:1684–98. https://doi.org/10.1016/j.ijrefrig.2011.01.005.

[120] Huang B-J, Ton W-Z, Wu C-C, Ko H-W, Chang H-S, Hsu H-Y, et al. Performance test of solar-assisted ejector cooling system. Int J Refrig 2014;39:172–85. https://doi.org/10.1016/j.ijrefrig.2013.06.009.

[121] Yapıcı R. Experimental investigation of performance of vapor ejector refrigeration system using refrigerant R123. Energy Convers Manag 2008;49:953–61. https://doi.org/10.1016/j.enconman.2007.10.006.

[122] Besagni G, Mereu R, Di Leo G, Inzoli F. A study of working fluids for heat driven ejector refrigeration using lumped parameter models. Int J Refrig 2015;58:154–71. https://doi.org/10.1016/j.ijrefrig.2015.06.015.

[123] Li YL, Wang K, Wu W, Xia XY, Niu BL, Zhang Z Bin. Investigation on the effect of ejector liquid recirculation system on the performance of falling-film water chiller with R134a. Int J Refrig 2017;74:333–44.

https://doi.org/10.1016/j.ijrefrig.2016.11.009.

[124] Yan J, Lin C, Cai W, Chen H, Wang H. Experimental study on key geometric parameters of an R134A ejector cooling system. Int J Refrig 2016;67:102–8. https://doi.org/10.1016/j.ijrefrig.2016.04.001.

[125] Yu J, Ren Y, Chen H, Li Y. Applying mechanical subcooling to ejector refrigeration cycle for improving the coefficient of performance. Energy Convers Manag 2007;48:1193–9. https://doi.org/10.1016/j.enconman.2006.10.009.

[126] Dahmani A, Aidoun Z, Galanis N. Optimum design of ejector refrigeration systems with environmentally benign fluids. Int J Therm Sci 2011;50:1562–72. https://doi.org/10.1016/j.ijthermalsci.2011.02.021.

[127] Fang Y, Croquer S, Poncet S, Aidoun Z, Bartosiewicz Y. Drop-in replacement in a R134 ejector refrigeration cycle by HFO refrigerants. Int J Refrig 2017;77:87–98. https://doi.org/10.1016/j.ijrefrig.2017.02.028.

[128] Dong J, Chen X, Wang W, Kang C, Ma H. An experimental investigation of steam ejector refrigeration system powered by extra low temperature heat source. Int Commun Heat Mass Transf 2017;81:250–6. https://doi.org/10.1016/j.icheatmasstransfer.2016.12.022.

[129] Kasperski J, Gil B. Performance estimation of ejector cycles using heavier hydrocarbon refrigerants. Appl Therm Eng 2014;71:197–203. https://doi.org/10.1016/j.applthermaleng.2014.06.057.

[130] Cizungu K, Mani A, Groll M. Performance comparison of vapour jet refrigeration system with environment friendly working fluids. Appl Therm Eng 2001;21:585–98. https://doi.org/10.1016/S1359-4311(00)00070-3.

[131] Shestopalov KO, Huang BJ, Petrenko VO, Volovyk OS. Investigation of an experimental ejector refrigeration machine operating with refrigerant R245fa at design and off-design working conditions. Part 2. Theoretical and experimental results. Int J Refrig 2015;55:212–23. https://doi.org/10.1016/j.ijrefrig.2015.02.004.

[132] Chen J, Zhu K, Huang Y, Chen Y, Luo X. Evaluation of the ejector refrigeration system with environmentally friendly working fluids from energy, conventional exergy and advanced exergy perspectives. Energy Convers Manag 2017;148:1208–24. https://doi.org/10.1016/J.ENCONMAN.2017.06.051.

[133] Chen J, Havtun H, Palm B. Parametric analysis of ejector working characteristics in the refrigeration system. Appl Therm Eng 2014;69:130–42. https://doi.org/10.1016/j.applthermaleng.2014.04.047.

[134] Zegenhagen MT, Ziegler F. Experimental investigation of the characteristics of a jet-ejector and a jet-ejector cooling system operating with R134a as a refrigerant. Int J Refrig 2015;56:173–85. https://doi.org/10.1016/J.IJREFRIG.2015.01.001.

[135] Thompson PA, Carofano GC, Kim Y-G. Shock waves and phase changes in a large-heat-capacity fluid emerging from a tube. J Fluid Mech 1986;166:57. https://doi.org/10.1017/S0022112086000046.

[136] Wang X, Dong J, Li A, Lei H, Tu J. Numerical study of primary steam superheating effects on steam ejector flow and its pumping performance. Energy 2014;78:205–11. https://doi.org/10.1016/J.ENERGY.2014.10.004.

[137] Klein Sanford and Gregory Nellis. Mastering EES 2018.

[138] Liu F. Purdue e-Pubs Review on Ejector Efficiencies in Various Ejector Systems Review on Ejector Efficiencies in Various Ejector Systems. n.d.

[139] Yu J, Zhao H, Li Y. Application of an ejector in autocascade refrigeration cycle for the performance improvement. Int J Refrig 2008;31:279–86. https://doi.org/10.1016/J.IJREFRIG.2007.05.008.

[140] Salih A. Dimensionless Numbers. n.d.

[141] Fatoyinbo HO. Microfluidic devices for cell manipulation. Microfluid. Devices Biomed. Appl., Elsevier Inc.; 2013, p. 283–350. https://doi.org/10.1533/9780857097040.3.283.

[142] Maliska CR. ON THE PHYSICAL SIGNIFICANCE OF SOME DIMENSIONLESS NUMBERS USED IN HEAT TRANSFER AND FLUID FLOW. n.d.

[143] Kew PA, Cornwell K. Correlations for the prediction of boiling heat transfer in small-diameter channels. Appl Therm Eng 1997;17:705–15. https://doi.org/10.1016/s1359-4311(96)00071-3.

[144] AMALFI RL. Two-Phase Heat Transfer Mechanisms Within Plate Heat Exchangers: Experiments, Modeling and Simulations. 2016;6856. https://doi.org/10.5075/EPFL-THESIS-6856.

[145] Kumar H. THE PLATE HEAT EXCHANGER: CONSTRUCTION AND DESIGN. First U.K. Natl. Conf. Heat Transf., Elsevier; 1984, p. 1275–88. https://doi.org/10.1016/B978-0-85295-175-0.50054-0.

[146] Martin H. A theoretical approach to predict the performance of chevron-type plate heat exchangers. Chem Eng Process Process Intensif 1996;35:301–10. https://doi.org/10.1016/0255-2701(95)04129-X.

[147] Muley A, Manglik RM. Experimental Study of Turbulent Flow Heat Transfer and Pressure Drop in a Plate Heat Exchanger With Chevron Plates. J Heat Transfer 1999;121:110. https://doi.org/10.1115/1.2825923.

[148] Neagu AA, Koncsag CI, Barbulescu A, Botez E. Estimation of pressure drop in gasket plate heat exchangers. Ovidius Univ Ann Chem 2016;27:62–72. https://doi.org/10.1515/auoc-2016-0011.

[149] Akturk F, Sezer Uzol N, Aradag S, Kakaç S. Experimental investigation and performance analysis of gasketed plate heat exchangers. 0 Isı Bilim ve Tek Derg = J Therm Sci Technol 2015;35:43–52.

[150] Yang J, Jacobi A, Liu W. Heat transfer correlations for single-phase flow in plate heat exchangers based on experimental data. Appl Therm Eng 2017;113:1547–57. https://doi.org/10.1016/J.APPLTHERMALENG.2016.10.147.

[151] Amalfi RL, Thome JR. High resolution infrared measurements of single-phase flow of R245fa and R236fa within a compact plate heat exchanger, Part 2: Heat transfer results. Appl Therm Eng 2016;101:555–63. https://doi.org/10.1016/j.applthermaleng.2015.11.010.

[152] Tao X, Infante Ferreira CA. Heat transfer and frictional pressure drop during condensation in plate heat exchangers: Assessment of correlations and a new method. Int J Heat Mass Transf 2019;135:996–1012. https://doi.org/10.1016/J.IJHEATMASSTRANSFER.2019.01.132.

[153] Genić SB, Jaćimović BM, Mandić D, Petrović D. Experimental determination of fouling factor on plate heat exchangers in district heating system. Energy Build 2012;50:204–11. https://doi.org/10.1016/J.ENBUILD.2012.03.039.

[154] Porkhial S, Moghaddam EA, Yousefi P, Sheydae H. Using Two Phase Heat Exchanger in Replacement of Separator for Sabalan Field. 2015.

[155] Rotary vane pumps: TMFR 30-200 SERIES VANE PUMPS - Fluidotech - Fluid-o-Tech n.d. https://www.fluidotech.it/en/products/technologies/rotary-vane-pumps/tmfr-30-200-series/ (accessed November 14, 2019).

[156] KCP1ERB2A2P60000 | Swagelok n.d. https://www.swagelok.com/en/catalog/Product/Detail?part=KCP1ERB2A2P60000 (accessed November 14, 2019).

[157] Pressure Sensors with Ceramic Element SEN-86 / -87 with AUF - Pressure gauges and pressure switches for different media from Kobold n.d. https://www.kobold.com/en/product/detail/~nm.61~nc.18~id.180/Pressure-Sensors-with-Ceramic-Element-SEN-86-87-with-AUF.html (accessed November 14, 2019).

[158] Advantages Small pressure loss O O High repeat accuracy ± 0.1 % of full scale O O Independent from density and temperature Areas of Application Machine building. n.d.

[159] Albedometer P. PYRANOMETER / ALBEDOMETER INSTRUCTION MANUAL. 2003.

[160] Han Y, Wang X, Sun H, Zhang G, Guo L, Tu J. CFD simulation on the boundary layer separation in the steam ejector and its influence on the pumping performance. Energy 2019;167:469–83. https://doi.org/10.1016/J.ENERGY.2018.10.195.

[161] Ruangtrakoon N, Thongtip T, Aphornratana S, Sriveerakul T. CFD simulation on the effect of primary nozzle geometries for a steam ejector in refrigeration cycle. Int J Therm Sci 2013;63:133–45. https://doi.org/10.1016/j.ijthermalsci.2012.07.009.

[162] Hakkaki-Fard A, Aidoun Z, Ouzzane M. A computational methodology for ejector design and performance maximisation. Energy Convers Manag 2015;105:1291–302. https://doi.org/10.1016/j.enconman.2015.08.070.

[163] Falat A, Poirier M, Sorin M, Teyssedou A. Experimental study of the performance of an ejector system using Freon 134a. Exp Therm Fluid Sci 2019;105:165–80. https://doi.org/10.1016/j.expthermflusci.2019.03.022.

[164] Gil B, Kasperski J. Efficiency analysis of alternative refrigerants for ejector cooling cycles. Energy Convers Manag 2015;94:12–8. https://doi.org/10.1016/j.enconman.2015.01.056.

[165] Akasaka R, Higashi Y, Miyara A, Koyama S. A fundamental equation of state for cis-

1,3,3,3-tetrafluoropropene (R-1234ze(Z)). Int J Refrig 2014;44:168–76. https://doi.org/10.1016/J.IJREFRIG.2013.12.018.

[166] Dvorak V. Introduction to flow of compressible fluids. Liberec: 2015.

[167] He S, Li Y, Wang RZ. Progress of mathematical modeling on ejectors. Renew Sustain Energy Rev 2009;13:1760–80. https://doi.org/10.1016/j.rser.2008.09.032.

[168] Sarkar J. Performance analyses of novel two-phase ejector enhanced multi-evaporator refrigeration systems. Appl Therm Eng 2017;110:1635–42. https://doi.org/10.1016/j.applthermaleng.2016.08.163.

[169] Sriveerakul T, Aphornratana S, Chunnanond K. Performance prediction of steam ejector using computational fluid dynamics: Part 2. Flow structure of a steam ejector influenced by operating pressures and geometries. Int J Therm Sci 2007;46:823–33. https://doi.org/10.1016/j.ijthermalsci.2006.10.012.

[170] ASHRAE. Steam-jet refrigeration equipment. ASHRAE Guid. Data B., 1969, p. 655–60.

[171] ANSYS. ANSYS FLUENT User’s Guide 2011;15317:2498.

[172] Chong D, Hu M, Chen W, Wang J, Liu J, Yan J. Experimental and numerical analysis of supersonic air ejector. Appl Energy 2014;130:679–84. https://doi.org/10.1016/j.apenergy.2014.02.023.

[173] Ansys I. ANSYS Fluent Theory Guide 2013;15317:514.

[174] Besagni G, Inzoli F. Computational fluid-dynamics modeling of supersonic ejectors: Screening of turbulence modeling approaches. Appl Therm Eng 2017;117:122–44. https://doi.org/10.1016/j.applthermaleng.2017.02.011.

[175] Güner M, Özbayer MM. Wear and its effects in centrifugal pumps. Yuz Yil Univ J Agric Sci 2019;29:569–82. https://doi.org/10.29133/yyutbd.518139.

APPENDICES

APPENDIX 1 THE MATHEMATICAL MODEL OF THE EJECTOR COOLING CYCLE IN EES PROGRAM

The mathematical model of the ejector cooling cycle with R1234yf as the working fluid, with the standard operating condition of the current study.

```
"===========The working fluid============="

Fluid$=   'R1234yf'                              " working refrigerant"


"===========INPUT HEXs GEOMETRY============="
 "============Chevron corrugation==============="


 "GENERATOR"
   "-----Plate geometry: ST12(Schmith) ------------"
 theta = 60 [Deg]                                "inclination angle - Note: the work follows
the geometry of Muley et. at paper,  "
 t = 0.0006 [m]                                  "thickness of the plate"
lambda_g = 0.0068 [m]                            "size of corrugation pitch"
pit_g = 0.0028 [m]                               " currugation pitch"
b_g  = (pit_g-t)                                 "mean channel spacing"
D_p_g = 0.055 [m]                                "Port diameter"
L_v_g = 0.485 [m]                                "effective flow length between the vertical
ports"
L_w_g = 0.245 [m]                                "plate width"
N_pl_g = 37                                      "Usable number of plates - usually is odd
number"
A_pl_g = phi_pl_g*L_w_g*(L_v_g - D_p_g)          "area of one plate"
A_tot_g = A_pl_g*N_pl_g                          "Total area of hx - generator"
A_ch_g = b_g*L_w_g                               "One channel flow area"

k_pl_g = 16.27 [W/m-K]                           "the conductivity value of stainless plate"
 fou_tot_g = (0.00053+0.00018) [m^2*K/W]         "fouling factor,  River water = 0.00053
m^2*K/W (Average of river water) and assume refrigerant side averaged at 0.00018 [m^2*K/W]
nature gas  (Marner and Suitor 1987)"

 "EVAPORATOR "
   "-----Plate geometry: ST03 (Schmith) ------------"
lambda_e = 0.0068 [m]                            "size of corrugation pitch"
pit_e = 0.0025 [m]                               " currugation pitch"
b_e  = (pit_e-t)                                 "mean channel spacing"
D_p_e = 0.03 [m]                                 "Port diameter"
 L_v_e = 0.25 [m]                                "effective flow length between the vertical
ports"
```

```
 L_w_e = 0.095 [m]                                "plate width"
N_pl_e = 29                                       "number of plates - usually is odd number"
A_pl_e = phi_pl_e*L_w_e*(L_v_e - D_p_e)           "area of one plate"
A_tot_e = A_pl_e*N_pl_e                           "Total area of hx - evaporator"
A_ch_e = b_e*L_w_e                                "One channel flow area"
k_pl_e = 16.27 [W/m-K]                            "the conductivity value of stainless plate"
fou_tot_e =  (0.00053+0.00018)  [m^2*K/W]

 "CONDENSER"
  "-----Plate geometry: ST12 (Schmith) ------------"
lambda_c = 0.0068 [m]                             "size of corrugation pitch"
pit_c = 0.0028 [m]                                " currugation pitch"
b_c  = (pit_c-t)                                  "mean channel spacing"
D_p_c = 0.055 [m]                                 "Port diameter"
 L_v_c = 0.485 [m]                                "effective flow length between the vertical
ports"
 L_w_c = 0.245 [m]                                "plate width"
N_pl_c = 49                                       "number of useful plates - usually is odd
number"
A_pl_c = phi_pl_c*L_w_c*(L_v_c - D_p_c)           "area of one plate"
A_tot_c = A_pl_c*N_pl_c                           "Total area of hx"
A_ch_c = b_c*L_w_c                                "One channel flow area"
k_pl_c = 16.27 [W/m-K]                            "the conductivity value of stainless plate"
fou_tot_c =  ( 0.00053+0.00018) [m^2*K/W]

"===========Operating condition============="

Q_dot_e_tot=5000 [W]                              " desired cooling power"

"Working conditions Input parameters"
T_g_tp = 83  [C]                                  "saturated vapor temp. at the outlet
generator"
DeltaT_sh_g = 7 [C]                               "degree of Superheat  "
T_g = T_g_tp + DeltaT_sh_g                        "generator temperature"

T_g_K=converttemp('C', 'K', T_g)

T_c_tp = 34  [c]                                  "condensation temp "
T_c= T_c_tp- DeltaT_sc_c                          "condenser temperature outlet - "
T_c_K=converttemp('C', 'K', T_c)
DeltaT_sc_c = 2 [C]                               "subcooled degree of refri. at condenser
outlet"

T_e_tp= 10 [c]
T_e_tp_K=converttemp('C', 'K', T_e_tp)
DeltaT_sh_e = 2 [C]                               "degree of Superheat"
T_e = T_e_tp + DeltaT_sh_e
 T_e_K=converttemp('C', 'K', T_e)

  "===========ejector efficiencies============="
"The ejector efficiencies were selected based on references in the literature and the results from the
current experimental work"
eta_t=0.8                                         "nozzle eficiency"
eta_s=0.85                                        "entrainment efficiency"
eta_dif=0.8                                       "diffuser efficiency"
phi_p=0.88                                        " viscosity effect at the boundary "
phi_m= 0.84                                       "mixing coefficient"
```

```
 "===========EJECTOR============="
"Pressure  outlets at the heat exchangers"
p_g=pressure(Fluid$,T=T_g_tp,x=1)
p_c = pressure(Fluid$, T = T_c_tp, x = 0)              " pressure at condenser outlet "
p_e= pressure(Fluid$,T=T_e_tp,x=1) -  DeltaP_e_cal

"Pressure Inlets at the heat exchangers"
 P_p =   P_g + DeltaP_g_cal                             "Required pressure outlet of Pump"
P_v = pressure(Fluid$,T=T_e_tp,x=1)                     "Pressure outlet of expansion valve"
  p_d = p_c + DeltaP_c_cal                              " pressure at diffuser, including the
pressure drop through condenser "

T_d_tp = temperature(Fluid$, P = P_d, x =1)             "saturated  temp. at the diffusor outlet-
ejector "
DeltaT_d_sh  = T_d - T_d_tp                             "degree of Superheat, should not be a input
parameter "

A_t=pi*(d_t^2)/4                                        "cross section at the nozzle"
A_noz_ex=A_ratio*A_t                                    "Nozzle exit area"
d_noz_ex=sqrt(4*A_noz_ex/pi)

 R_univ= 8314.472  [J/kmol-K]                           "universal gas constant KJ/MolK"

 h_g=enthalpy(Fluid$,T=T_g,P=p_g)                       "enthalpy in the generator"

h_e=enthalpy(Fluid$,T=T_e,P=p_e)                        "enthalpy at evaporator outlet"
rho_r_g_sh=density(Fluid$,T=T_g,P=p_g)                  "fluid density leaving the generator"

cp_t=cp(Fluid$,T=T_g,P=p_g)                             "specific heat at constant pressure"
cv_t=cv(Fluid$,T=T_g,P=p_g)                             "specific heat at constant volume"
kappa=cp_t/cv_t                                         "specific heat ratio"
R_fluid=R_univ/mass                                     "gas constant of the fluid, kJ/kgK"
mass = molarmass(Fluid$)

"Primary nozzle equations"
m_dot_g_R=(A_t*p_g/sqrt(T_g_K))*sqrt(eta_t*((kappa/R_fluid)*((2/(kappa+1))^((kappa+1)/(kappa-
1)))))  "mass flow rate in the nozzle according to Huang et al. , eq.(1)"
A_noz_ex=(A_t/Ma_noz_ex)*((2/(kappa+1))*(1+((kappa-1)/2)*(Ma_noz_ex^2)))^(((kappa+1)/(kappa-
1))/2)                                                  "eq.(2)"
p_noz_ex=p_g/(1+((kappa-1)/2)*(Ma_noz_ex^2))^(kappa/(kappa-1))  "pressure at nozzle exit, eq (3)"
 p_noz_ex=p_e                                           "optimal working conditions - primary
works at critical point/ the column shaped hypothesis "

"Mixing section"

Ma_s2=1
p_s2=p_e*(1+((kappa-1)/2)*(Ma_s2^2))^(-kappa/(kappa-1))    "pressure os secondary flow at section
y - y, eq.6"
p_p2=p_s2
p_p2= p_g*(1+((kappa-1)/2)*(Ma_p2^2))^((-kappa)/(kappa-1))         "pressure of primary flow at
section 2, eq.4"
A_p2=phi_p*A_t/Ma_p2*((2/(kappa+1))*(1+((kappa-1)/2)*(Ma_p2^2)))^(((kappa+1)/(kappa-1))/2)
"primary flow area at section 2, eq.5 "
d_p2=sqrt(4*A_p2/pi)
A_2=A_p2+A_s2                                           "Total area  at section 2, eq.8"
A_2=pi*d_2^2/4
d_ratio=d_2/d_t
A_ratio_t=A_2/A_t
```

```
m_dot_e_R=(A_s2*p_e/sqrt(T_e_K))*sqrt(eta_s*((kappa/R_fluid)*((2/(kappa+1))^((kappa+1)/(kappa
-1)))))                                          "mass flow rate in the nozzle according to
Huang et al.1998, eq. 7"


T_p2_K=(T_g_K)/(1+((kappa-1)/2)*(Ma_p2^2))       "temperature of primary flow at 2 in K, eq.
9."

T_p2=converttemp('K', 'C', T_p2_K)               "temperature of primary flow at 2 in ºC, eq.
9."
T_s2_K=T_e_K/(1+((kappa-1)/2)*(Ma_s2^2))         "temperature of secondary flow at 2 in K,
eq. 10"
T_s2=converttemp('K', 'C', T_s2_K)               "temperature of secondary flow at 2 in ºC,
eq. 10"

Mom_p2=m_dot_g_R*v_p2
Mom_s2=m_dot_e_R*v_s2
Mom_m=(m_dot_g_R+m_dot_e_R)*v_m
v_m=(v_p2+ER*v_s2)*sqrt(phi_m)/(1+ER)            "eq 5 Yu - Paper: Application of an ejector in
autocascade refrigeration cycle for the performance improvement"
v_p2=Ma_p2*sqrt(kappa*R_fluid*T_p2_K)            "eq. 13"
v_s2=Ma_s2*sqrt(kappa*R_fluid*T_s2_K)            "eq. 14"
cp_mix=cp_t

(m_dot_g_R+m_dot_e_R)*(T_m_K*cp_mix+0.5*(v_m)^2)=m_dot_g_R*(T_p2_K*cp_mix+0.5*(v_p2)^2)+m
_dot_e_R*(T_s2_K*cp_mix+0.5*(v_s2)^2)  "energy balance in the mixing section, eq. 12"
T_m_K=converttemp('C', 'K', T_m)
Ma_m=v_m/sqrt(kappa*R_fluid*T_m_k)               "eq. 15"

"Shock wave"

p_sh=p_p2*(1+(2/(kappa+1))*kappa*((Ma_m^2)-1))   "Pressure after the shock wave, eq. 16"
Ma_sh^2=(1+((kappa-1)/2)*(Ma_m^2))/(kappa*(Ma_m^2)-((kappa-1)/2))  "eq. 17 "

"Diffuser"

p_d=p_sh*(1+eta_dif*((kappa-1)/2)*(Ma_sh^2))^(kappa/(kappa-1)) " ejector exit pressure, eq. 18"


h_d=(m_dot_g_R*h_g+m_dot_e_R*h_e)/(m_dot_g_R+m_dot_e_R)

T_d = temperature(Fluid$,P=p_d,h=h_d)            "temp. at diffusor outlet"


h_c=enthalpy(Fluid$,T=T_c,x=0)                   "enthalpy at condeser outlet - replaced with
other equ. "
Q_dot_c_tot=(m_dot_g_R+m_dot_e_R)*(h_d-h_c)      "condenser power output"

"Pump power"

W_pump=(P_p - p_c)*m_dot_g_R/(0.5*(density(Fluid$,T=T_c, P=p_c) +density(Fluid$,T=T_g, P=p_g)))
"required pump power, P_g is replaced by P_p"

 "Generator equations"
Q_vol_g=m_dot_g_R/rho_r_g_sh                     "volumetric flow rate from generator"
h_p=h_c+W_pump/m_dot_g_R                         "generator inlet enthalpy"
Q_dot_g_tot=m_dot_g_R*(h_g-h_p)                  "generator power"

"Evaporator equations"
```

```
h_v=h_c                                           "assumed: enthalpy conservation before
and after the valve - enthalpy at expansion outlet"
m_dot_e_R=Q_dot_e_tot/(h_e-h_v)                   "secondary mass flow rate -  the energy
conservation assumtion may cause the inconsistency"
rho_e=density(Fluid$,T=T_e,P = P_e)               " evaporator pressure outlet = rho_r_e_sh"
Q_vol_e=m_dot_e_R/rho_e                           "volumetric flow rate"

"Entrainment ratio and COP"
ER=m_dot_e_R/m_dot_g_R
COP=Q_dot_e_tot/Q_dot_g_tot                       "cooling cycle COP"


"Other ejectors' dimensions - from ASHRAE Handbook - Chapter 13, “Steam-Jet Refrigeration
Equipment”, American Society of Heating, Refrigerating and Air-Conditioning Engineers,"
 alfa_diff=10 [deg]                               "diffuser angle in degrees"
alfa_conv=7 [deg]                                 "suction side convergence angle"

L_t=8*(d_noz_ex-d_t)                              "primary nozzle tapper length"

L_diff=7*d_2                                      "diffuser length"
d_diff=d_2+L_diff/6                               "diffuser diameter"

d_conv=1.42*d_2
L_x=12*(d_conv-d_2)                               "length from primary nozzle exit to
constant area section"

L_m_min=3*d_2                                     "minimum length of the constant area
section"
L_m_max=4*d_2                                     "maximum length of the constant area
section"

d_sec_inlet=d_conv+2*L_t*tan(alfa_conv)           "suction inlet diameter"

L_tale_min=L_x+L_m_min+L_diff                     "tail length"
L_tale_max=L_x+L_m_max+L_diff                     "tail length"

 "====================GENERATOR - counterflow======================="
N_cp_g = (N_pl_g - 1)/(2*N_p)                     "Number of channel per pass ( for each
working fluid)"
 N_p =1 [-]                                       "Number of pass"
x_g = pi*b_g/lambda_g
 phi_pl_g = (1+(1+x_g^2)^0.5+4*(1+(x_g^2)/2)^0.5)/6     " enlargement factor of plate"

 "Define the D_h_g"
D_h_g = (4*b_g*L_w_g)/(2*(b_g+L_w_g*phi_pl_g))
rho_r_g_l = density(Fluid$, T = T_c, P = P_p)     "density at the pump outlet - Assume that
there is no heat gain by the pump"

 "in Water side"

F2$='Water'                                       "usually is water"
T_w_g_in = T_g+4

T_w_g_out =T_g+1
 P_w_g = 320000 [Pa]                              "absolute pressure in the heat supply cycle,
~ 3.2 Bara"
 h_w_g_in = enthalpy(F2$, P= P_w_g, T=T_w_g_in)   "w stand for water"
 h_w_g_out = enthalpy(F2$, P= P_w_g, T=T_w_g_out)
```

```
 mu_w_g = viscosity(F2$,P= P_w_g, T= (T_w_g_in+T_w_g_out)/2) "dyna. viscosity of water, average
value is used"

Pr_w_g = prandtl(F2$, T = (T_w_g_in+T_w_g_out)/2, P = P_w_g)

"Enthalpies of the fluids"
 h_g_tpv = enthalpy(Fluid$, P= P_g, x=1)
h_g_tpL =  enthalpy(Fluid$, P= P_p, x= 0)                    "enthalpy of saturated liquid - at the
beginning of phase-change process"

Q_dot_g_tot = m_dot_w_g*(h_w_g_in - h_w_g_out)

"Heat capacity rates"
Q_dot_g_sh = m_dot_g_R*(h_g - h_g_tpv)                       "heat transfer rate of superheat section"

 Q_dot_g_sh = m_dot_w_g*C_w_g_sh*(converttemp('C', 'K', T_w_g_in) - converttemp('C', 'K',
T_w_g_in_tp)) "T_w_g_in_tp is the water temp when refri reaches saturatured temperature"

Q_dot_g_tp = m_dot_g_R*( h_g_tpv - h_g_tpL)                  "heat flow rate of phase-change process"
Q_dot_g_tp = m_dot_w_g*Cp_w_g_tp*(T_w_g_in_tp - T_w_g_out_tp) "T_w_g_out_tp is the water temp at
refri. Liquid saturatured temperature"

Q_dot_g_L = m_dot_g_R*(h_g_tpL - h_p)                        "heat flow rate at the section where the
coolant gains tempurature to saturated T_g_tpL: process"
Q_dot_g_L = m_dot_w_g*C_w_g_L*( T_w_g_out_tp - T_w_g_out)

Cp_w_g_tp = cp(F2$, T = (T_w_g_in_tp + T_w_g_out_tp)/2,P = P_w_g)
C_w_g_L = cp(F2$, T = (T_w_g_out_tp + T_w_g_out)/2,P = P_w_g)

      "The heat flow rate ratio"
R_Q_g_sh = Q_dot_g_sh/Q_dot_g_tot                            "Ratio of heat flow rate at super heat
section"
R_Q_g_tp = Q_dot_g_tp/Q_dot_g_tot                            "Ratio of heat flow rate at phase change
section"
R_Q_g_L = Q_dot_g_L/Q_dot_g_tot                              "Ratio of heat flow rate at senitive heat
(temperature gain at liquid state) section"


  "============Pressure drop and heat transfer - Water side==========="

"Applying the Muley correlation for Re > 1000"
Nu_w_g = (2.668-0.006967*theta+7.244*10^(-5)*theta^2 )*(20.78-50.94*phi_pl_g+41.16*phi_pl_g^2-
10.51*phi_pl_g^3 )*Re_w_g^((0.728+0.0543*sin((pi*theta/45)+3.7)) ) *Pr_w_g^(1/3)

f_w_g =   (2.917-0.1277*theta+2.016*10^(-3)*theta^2 )*(5.474-19.02*phi_pl_g+18.93*phi_pl_g^2-
5.341*phi_pl_g^3)*Re_w_g^(-(0.2+0.0577*sin((pi*theta/45)+2.1))) "Muley colleration for Re > 1000,
turbulent flow"

      "Frictional channel Pressure drops"
DeltaP_w_g = 4*f_w_g*L_v_g*N_p*G_w_ch_g^2/(2*rho_w_g*D_h_g)"equ. 11.20 in heat exchanger"
rho_w_g = density(F2$, T = T_w_g_in/2+T_w_g_out/2, P = (P_w_g ))

DeltaP_w_g_sh = DeltaP_w_g*R_Q_g_sh
 DeltaP_w_g_tp = DeltaP_w_g*R_Q_g_tp

      "Port pressure drop"
DeltaP_w_g_p = 1.5*N_p*G_P_w_g^2/(2*density(F2$, T = (T_w_g_in+ T_w_g_out)/2, P = P_w_g))

G_P_w_g = m_dot_w_g/(pi*D_p_g^2/4)
```

```
    "Total pressure drop in water side is sum of channel and port pressure, others can be ignored "
DeltaP_w_g_tot = DeltaP_w_g + DeltaP_w_g_p

 "HEAT TRANSFER ANALYSIS"

"Mass flow rate per channel"
m_dot_w_g_ch = m_dot_w_g/N_cp_g                  "mass flow rate per channel"
G_w_ch_g = m_dot_w_g_ch/A_ch_g                   "The mass velocity"

Re_w_g = G_w_ch_g*D_h_g/mu_w_g                   "Reynold number (Assumed that Re_w_g
does not vary much)"


k_w_g = conductivity(F2$, P= P_w_g, T= (T_w_g_in+T_w_g_out)/2) "Thermal conductivity of water"

he_w_g = Nu_w_g*k_w_g/D_h_g                      "Heat transfer convection coefficient in
water side"

 "============Pressure drop and heat transfer - refrigerant side==========="

m_dot_g_R_ch = m_dot_g_R/N_cp_g                  "flow rate per channel (refrigerant)"
G_r_ch_g = m_dot_g_R_ch/ A_ch_g                  " Mass velocity of refrigerant, superheat
section"


 "Liquid state - Refrigerant reaches to saturated liquid point - The pressure is the pump outlet
pressure"
 Re_r_l_g = G_r_ch_g*D_h_g/mu_r_L_g              "Reynold number of refrigerant from the
pump, generator inlet"
 mu_r_L_g1 = viscosity(Fluid$, T = T_c, P = P_p) "Dyn. viscosity at the generator inlet"
mu_r_L_g2 = viscosity(Fluid$, T = T_g_tp, x = 0) "Dyn. viscosity at the end of liquid phase"
 mu_r_L_g = (mu_r_L_g1+mu_r_L_g2)/2
 Pr_r_l_g = prandtl(Fluid$,T = T_c, P = P_p)     "Prandtl number  at the generator inlet - or
pump outlet"

"Usually Reynold number at generator inlet is small, because it is in liquid state. Muley correlation for
Re < 400 is applied"
Nu_r_L_g= 0.44*((theta/30)^0.38)*(Re_r_l_g^0.5)*(Pr_r_l_g^(1/3))"equa. 11.10 in heat exchanger book
"

k_r_l_g = conductivity(Fluid$, P= P_p, T= T_c)   "Thermal conductivity of  ref. at generator
inlet"

he_r_l_g = Nu_r_L_g*k_r_l_g/(D_h_g)              "Heat transfer convection coefficient of  ref.
at generator inlet"


 "Superheat - from saturated vapor to required superheating point"

Re_r_sh_g = G_r_ch_g*D_h_g/mu_r_sh_g             "Refrigerant, super heat section"

mu_r_sh_g1 = viscosity(Fluid$, T = T_g_tp, P = P_g-0.5 [Pa])"dyn. viscosity at the begining of
generator's supeheated flow  "
mu_r_sh_g2 = viscosity(Fluid$, T = T_g, P = P_g)  "dyn. viscosity at the generator outlet"
2*mu_r_sh_g = mu_r_sh_g1 + mu_r_sh_g2

 Pr_r_sh_g = prandtl(Fluid$,T=T_g,P=P_g )        "Prandtl number  vapor state - DeltaP_g is
the refrigerant pressure drop as it goes through generator "
```

```
Nu_r_sh_g = (2.668-0.006967*theta+7.244*10^(-5)*theta^2 )*(20.78-
50.94*phi_pl_g+41.16*phi_pl_g^2-10.51*phi_pl_g^3
)*Re_r_sh_g^((0.728+0.0543*sin((pi*theta/45)+3.7)) ) *Pr_r_sh_g^(1/3)*("mu_g/mu_wall"1)^0.14

"mu_g/mu_wall = 1"                              "assumed- because the flows'  temperature
at wall and at the plate pitch are equal, steady flow"

k_r_sh_g = conductivity(Fluid$, P= P_g, T= T_g)           "Thermal conductivity of  ref. at generator
outlet"

he_r_sh_g = Nu_r_sh_g*k_r_sh_g/D_h_g                  "Heat transfer convection coefficient of  ref.
at generator inlet"

"velocity of superheated vapor"
Ve_sh_g = G_r_ch_g/density(Fluid$, T = T_g, P = P_g)

"Phase-change - Refrigerant reaches to saturated vapor point - the formula for two-phase Fanning
friction coeff. and Nu are completely different. therefore, the new correlation of Amalfi is applied in
two-phase."
Re_r_tp_g = Re_r_sh_g*(mu_r_sh_g/mu_r_L_g)*(rho_r_g_l/rho_r_g_sh)^0.5 + Re_r_l_g "equivalent
 Reynold number (average) at phase-change section"
Pr_r_tp_g = (prandtl(Fluid$,T=T_g_tp,x = 0 ) + prandtl(Fluid$,T=T_g_tp,x = 1))/2 "the equivalent
Prandtl value of phase-change section."
Nu_r_tp_g_Mul = (2.668-0.006967*theta+7.244*10^(-5)*theta^2 )*(20.78-
50.94*phi_pl_g+41.16*phi_pl_g^2-10.51*phi_pl_g^3
)*Re_r_tp_g^((0.728+0.0543*sin((pi*theta/45)+3.7)) ) *Pr_r_tp_g^(1/3)*("mu_g/mu_wall" 1 )^0.14
      "Mulley correlation"

Nu_r_tp_g = 18.495*theta_star^0.248*Re_vap_g^0.351
*Re_lo_g^0.351*Bd_g^0.235*Bo_g^0.198*rho_star_g^(-0.223)
      "tp stands for two phase"

k_r_tp_g = (conductivity(Fluid$,T=T_g_tp,x = 0 ) + conductivity(Fluid$,T=T_g_tp,x = 1))/2

 he_r_tp_g = Nu_r_tp_g*k_r_tp_g/D_h_g
he_r_tp_g_Mul = Nu_r_tp_g_Mul*k_r_tp_g/D_h_g

      "==============two-phase by Amalfi=========="
"Bond number"
Bd_g = DeltaRho_g*gravity*D_h_g^2/Stension_g            "g for generator here"
DeltaRho_g = density(Fluid$, T = T_g_tp, x = 0) - density(Fluid$, T = T_g_tp, x = 1)
gravity = 9.81 [m/s^2]                                  "gravity acceleration"
Stension_g = surfacetension(Fluid$, T= T_g_tp)

"Boiling number"

q_r_tp_g  = Q_dot_g_tp/A_tp_g                           "heat flux of the two-phase (phase change)
is the ratio of heat load over the area of this section "
 h_g_lv = h_g_tpv - h_g_tpl
Bo_g = q_r_tp_g/(G_r_ch_g*h_g_lv)


"Weber number (We) - note that this is a simple assumption for the two phase "
 We_m_g = G_r_ch_g^2*D_h_g/(Stension_g*rho_m_g)
rho_m_g = ((x_qua_g/density(Fluid$, T = T_g_tp, x = 1) + (1- x_qua_g)/density(Fluid$, T = T_g_tp, x =
0)))^(-1) "homogeneous model of density / series liquid-vapor arrange"
x_qua_g  =  0.5                                         " assumption"
```

```
"Dimensionless parameters"
Re_vap_g = G_r_ch_g*x_qua_g*D_h_g/mu_r_tpv_g                "tpv : two phase - vapor : the end of two-
phase section"
 mu_r_tpv_g = viscosity(Fluid$, T = T_g_tp, x = 1)
"dimensionless chevron angle"
theta_star = theta/theta_max                                 " base on the correlation from the work of
Raffaele"
theta_max = 70 [deg]
 rho_star_g =  density(Fluid$, T = T_g_tp, x = 0)/ density(Fluid$, T = T_g_tp, x = 1)
"reference: heat exchangers, selection, rating, and thermal design. Table 11.5 Muley and Manglik
chevron plates with theta = 30)"
 Re_lo_g = G_r_ch_g*D_h_g/mu_r_tpL_g
mu_r_tpL_g = viscosity(Fluid$, T = T_g_tp, x = 0)            "tpL : two phase - Liquid: the beginning of
two-phase section"
"========================================"

"Overall Heat transfer  coefficient U"
 1/U_sh_g = 1/he_w_g + 1/he_r_sh_g + t/k_pl_g + fou_tot_g   "Superheat section"
1/U_L_g = 1/he_w_g + 1/he_r_l_g + t/k_pl_g + fou_tot_g       "liquid section"
1/U_tp_g = 1/he_w_g + 1/he_r_tp_g + t/k_pl_g + fou_tot_g     "phase-change section"


 "Logarithmic mean temperature difference"
LMTD_tp_g = (T_w_g_in_tp - T_w_g_out_tp) / ln((T_g_tp -T_w_g_in_tp)/(T_g_tp -T_w_g_out_tp))"
logarithmic mean temperature difference of the phase change section - the compact heat exchanger
book "
LMTD_L_g = ((T_w_g_out_tp - T_c) - (T_w_g_out  - T_g_tp))/ln((T_w_g_out_tp - T_c)/ (T_w_g_out  -
T_g_tp))
LMTD_sh_g = ((T_w_g_in - T_g_tp) - (T_w_g_out_tp - T_g))/ln(((T_w_g_in - T_g_tp)/ (T_w_g_out_tp -
T_g)))

"Areas of each section"
Q_dot_g_sh{*convert('kW','W' )} = U_sh_g*A_sh_g*LMTD_sh_g "Area required for heat transfer for
superheating section"
 Q_dot_g_tp{*convert(kW,W) }= U_tp_g*A_tp_g*LMTD_tp_g  "Area required for heat transfer for phase-
change section"
 Q_dot_g_L{*convert(kW,W)}  = U_L_g*A_L_g*LMTD_L_g       "Area required for heat transfer for
sensitive heat gain section"
 Q_dot_g = Q_dot_g_L + Q_dot_g_sh +Q_dot_g_tp

"Ratio between required and actual area"
A_ratio_g = A_tot_g/(A_sh_g+A_tp_g+A_L_g)


 "======Average heat transfer coefficient and Average Overall heat transfer coefficient U======="
he_r_g_ave = R_Q_g_sh*he_r_sh_g +  R_Q_g_tp*he_r_tp_g +  R_Q_g_L*he_r_l_g
U_g_ave =   R_Q_g_sh*U_sh_g +  R_Q_g_tp*U_tp_g +  R_Q_g_L*U_L_g

 "Average Fanning friction factor "

f_r_g_ave = R_Q_g_sh*f_r_sh_g + R_Q_g_tp*f_r_tp_g + R_Q_g_L*f_r_L_g

"Channel Pressure drop per length unit"
 DeltaP_r_g_ch_perUnit = DeltaP_r_g_ch/L_v_g

"============= the UA is known previously, this calculation is for hx rating purpose========="
"EFFECTIVENESS of the generator"
```

```
    "The heat flow rate ratio"
R_Q_g_sh*A_tot_g = A_sh_g_avail                          "A_sh_g_available, based on the total heat
transfer area of the hx"
R_Q_g_L*A_tot_g = A_L_g_avail
R_Q_g_tp*A_tot_g =  A_tp_g_avail

 epsilon_g_tp_real = 1 - exp(-(U_tp_g*A_tp_g_avail)/(Cp_w_g_tp*m_dot_w_g))  "for estimating the
effectiveness - does not work"

 epsilon_g_L_real = (1 - exp(-(U_L_g*A_L_g_avail/C_min_g_L)*(1 - Cr_g_L)))/(1 - Cr_g_L*exp(-
(U_L_g*A_L_g_avail/C_min_g_L)*(1 - Cr_g_L)))             "effectiveness for Liquid zone"

epsilon_g_sh_real = (1 - exp(-(U_sh_g*A_sh_g_avail/C_min_g_sh)*(1 - Cr_g_sh)))/(1 - Cr_g_sh*exp(-
(U_sh_g*A_sh_g_avail/C_min_g_sh)*(1 - Cr_g_sh)))         "effectiveness for superheated zone"

epsilon_g_real = (epsilon_g_sh_real*R_Q_g_sh  + epsilon_g_L_real*R_Q_g_L  + epsilon_g_tp_real*R_Q_g_tp
)


"Effectiveness of hx when the required heat transfer area is met (not oversized)"

epsilon_g_tp = 1 - exp(-(U_tp_g*A_tp_g)/(Cp_w_g_tp*m_dot_w_g))

 epsilon_g_L = (1 - exp(-(U_L_g*A_L_g/C_min_g_L)*(1 - Cr_g_L)))/(1 - Cr_g_L*exp(-
(U_L_g*A_L_g/C_min_g_L)*(1 - Cr_g_L)))                   "effectiveness for Liquid zone"
 "where"
C_min_g_L = min(m_dot_g_r*cp(Fluid$,T=(T_g+T_c)/2,P=p_p), m_dot_w_g*C_w_g_L)
 C_max_g_L = max(m_dot_g_r*cp(Fluid$,T=(T_g+T_c)/2,P=p_p), m_dot_w_g*C_w_g_L)
Cr_g_L = C_min_g_L/C_max_g_L

epsilon_g_sh = (1 - exp(-(U_sh_g*A_sh_g/C_min_g_sh)*(1 - Cr_g_sh)))/(1 - Cr_g_sh*exp(-
(U_sh_g*A_sh_g/C_min_g_sh)*(1 - Cr_g_sh)))               "effectiveness for superheated zone"
 "where"
C_min_g_sh = min(m_dot_g_r*cp(Fluid$,T=T_g,P=p_g), m_dot_w_g*C_w_g_sh)
 C_max_g_sh = max(m_dot_g_r*cp(Fluid$,T=T_g,P=p_g), m_dot_w_g*C_w_g_sh)
Cr_g_sh = C_min_g_sh/C_max_g_sh

epsilon_g = (epsilon_g_sh*R_Q_g_sh + epsilon_g_L*R_Q_g_L + epsilon_g_tp*R_Q_g_tp)

NTU_g_L = A_L_g_avail*U_L_g/C_min_g_L
NTU_g_sh = A_sh_g_avail*U_sh_g/C_min_g_sh
NTU_g_tp = A_tp_g_avail*U_tp_g/(Cp_w_g_tp*m_dot_w_g)
NTU_g = NTU_g_tp + NTU_g_sh +NTU_g_L
 epsilon_g_tpA =  NTU_g_tp/(1+NTU_g_tp)
 epsilon_g_shA = (1-exp(-NTU_g_sh*(1-Cr_g_sh)))/(1-Cr_g_sh*exp(-NTU_g_sh*(1-Cr_g_sh)))
 "=============================================================="


"===Define f (Fanning friction Factor)==="

 f_r_L_g = (theta/30)^(0.83)*((30.2/Re_r_l_g)^5 +(6.28/Re_r_l_g^0.5)^5)^0.2 "Muley colleration for Re
< 400"

f_r_sh_g = (2.917-0.1277*theta+2.016*10^(-3)*theta^2 )*(5.474-19.02*phi_pl_g+18.93*phi_pl_g^2-
5.341*phi_pl_g^3)*Re_r_sh_g^(-(0.2+0.0577*sin((pi*theta/45)+2.1))) "Muley colleration for Re >
1000, turbulent flow)"

f_r_tp_g = C_coef*15.698*We_m_g^(-0.475)*Bd_g^0.255*rho_star_g^(-0.571)
```

```
C_coef = 2.125*theta_star^9.993 + 0.955                    "C_coef is the leading coefficient for
prediction methods"

"Frictional channel Pressure drops"
DeltaP_r_g_sh = 4*f_r_sh_g*L_v_g*N_p*G_r_ch_g^2/(2*rho_r_g_sh*D_h_g) "equ. 11.20 in heat
exchangers- sadik book - at refrigerant side - Superheated"
DeltaP_r_g_tp = 4*f_r_tp_g*L_v_g*N_p*G_r_ch_g^2/(2*rho_m_g*D_h_g)
DeltaP_r_g_L = 4*f_r_L_g*L_v_g*N_p*G_r_ch_g^2/(2*rho_r_g_L*D_h_g)
DeltaP_r_g_ch = DeltaP_r_g_sh + DeltaP_r_g_tp + DeltaP_r_g_L "The Total frictional channel Pressure
drop at refrigerant side"

" connection and Port pressure drops in the ref. side"
DeltaP_r_g_p = (1.5*N_p*G_p_r_g^2/(2*density(Fluid$, T =T_c, P = P_p) ) +
1.5*N_p*G_p_r_g^2/(2*density(Fluid$, T = T_g, P = P_g) ))/2 "Port pressure drop at refrigerant side,
inlet is liquid, outlet is vapor"

G_p_r_g = m_dot_g_R/(pi*(D_p_g^2)/4)

    "Total pressure drop in ref. side is sum of channel and port pressure "
 DeltaP_g_cal = DeltaP_r_g_ch + DeltaP_r_g_p                 "total  presssure drop in refri. side through
the generator"


 "===============EVAPORATOR - counterflow====================="
N_cp_e = (N_pl_e - 1)/(2*N_p)                               "Number of channel per pass ( for each
working fluid)"

x_e = pi*b_e/lambda_e
 phi_pl_e = (1+(1+x_e^2)^0.5+4*(1+(x_e^2)/2)^0.5)/6        " enlargement factor of plate"

 "Define the D_h_e"
 D_h_e = (4*b_e*L_w_e)/(2*(b_e+L_w_e*phi_pl_e))

 "The quality at the ex. valve outlet"
x_qua_v = quality(Fluid$, h = h_c, p = p_v)                "assumed that the enthalpy of the fluid
before and after the ex. valve are constant (without enthalpy loss)"

rho_r_v= x_qua_v*density(Fluid$, x= 0, P = P_v) +(1- x_qua_v)*density(Fluid$, x= 1, P = P_v) "density at
the evaporator inlet"
 rho_r_e_sh = density(Fluid$, T = T_e, P = P_e)             "density at the evaporator outlet"

"The second  working fluid "
T_w_e_in = T_e +2
T_w_e_out = T_e +1

 P_w_e = 320000 [Pa]                                        "absolute pressure in the heat supply cycle,
~ 3.2 Bara"
 h_w_e_in = enthalpy(F2$, P= P_w_e, T=T_w_e_in)             "w stand for water, but also for the second
working fluid here"
 h_w_e_out = enthalpy(F2$, P= P_w_e, T=T_w_e_out)
 mu_w_e = viscosity(F2$,P= P_w_e, T= (T_w_e_in+T_w_e_out)/2) "dyna. viscosity of water, average
value"
Pr_w_e = prandtl(F2$, T = (T_w_e_in+T_w_e_out)/2, P = P_w_e)
Q_dot_e_tot = m_dot_w_e*(h_w_e_in - h_w_e_out)

"Heat capacity rates"
Q_dot_e_sh = m_dot_e_R*(h_e - h_e_tpv)                     "heat transfer rate of superheat section"
Q_dot_e_sh = m_dot_w_e*C_w_e_sh*(converttemp('C', 'K', T_w_e_in) - converttemp('C', 'K', T_w_e_tp))
"T_w_e_in_tp is the water temp at refri. vapor saturatured temperature"
```

```
Q_dot_e_tp = m_dot_e_R*( h_e_tpv - h_v)                    "heat flow rate of phase-change process, "
Q_dot_e_tp = m_dot_w_e*C_w_e_tp*(T_w_e_tp - T_w_e_out) "T_w_e_out_tp is the water temp at refri.
Liquid saturatured temperature"

"T_w_Rsatv is the water temp at the saturature"
C_w_e_sh = cp(F2$, T = (T_w_e_in + T_w_e_in_tp)/2,P = P_w_e)
C_w_e_tp = cp(F2$, T = (T_w_e_tp + T_w_e_out)/2,P = P_w_e)

"The heat flow rate ratio"
R_Q_e_sh = Q_dot_e_sh/Q_dot_e_tot                          "Ratio of heat flow rate at super heat
section"
R_Q_e_tp = Q_dot_e_tp/Q_dot_e_tot                          "Ratio of heat flow rate at phase change
section"


 "============Heat transfer and pressure drop analysis - Water side=========="

"Re in water side is usual from 1000 - 2000, depends mostly on the temperature difference between
outlet and inlet, thus the required flow rate. Applying the Muley correlation for Re > 1000"
Nu_w_e = (2.668-0.006967*theta+7.244*10^(-5)*theta^2 )*(20.78-50.94*phi_pl_e+41.16*phi_pl_e^2-
10.51*phi_pl_e^3 )*Re_w_e^((0.728+0.0543*sin((pi*theta/45)+3.7)) ) *Pr_w_e^(1/3)

f_w_e =   (2.917-0.1277*theta+2.016*10^(-3)*theta^2 )*(5.474-19.02*phi_pl_e+18.93*phi_pl_e^2-
5.341*phi_pl_e^3)*Re_w_e^(-(0.2+0.0577*sin((pi*theta/45)+2.1)))  "Muley colleration for Re > 1000,
turbulent flow)"

     "Frictional channel Pressure drops"
DeltaP_w_e = 4*f_w_e*L_v_e*N_p*G_w_ch_e^2/(2*rho_w_e*D_h_e)  "equ. 11.20 in heat exchanger"
rho_w_e = density(F2$, T = T_w_e_in/2+T_w_e_out/2, P = (P_w_e ))  "Caution, the pressure!!"
DeltaP_w_e_sh = DeltaP_w_e*R_Q_e_sh
 DeltaP_w_e_tp = DeltaP_w_e*R_Q_e_tp
{DeltaP_w_e_L = DeltaP_w_e*R_Q_e_L}

     "Port pressure drop"
DeltaP_w_e_p = 1.4*N_p*G_P_w_e^2/(2*density(F2$, T = (T_w_e_in+ T_w_e_out)/2, P = P_w_e))

G_P_w_e = m_dot_w_e/(pi*D_p_e^2/4)

     "Total pressure drop in water side is sum of channel and port pressure, others can be ignored "
DeltaP_w_e_tot = DeltaP_w_e + DeltaP_w_e_p

 "HEAT TRANSFER ANALYSIS"

"Mass flow rate per channel"
m_dot_w_e_ch = m_dot_w_e/N_cp_e                            "mass flow rate per channel"
G_w_ch_e = m_dot_w_e_ch/A_ch_e                             "The mass velocity"
Re_w_e = G_w_ch_e*D_h_e/mu_w_e                             "Reynold number (Assumed that Re_w_e
does not vary by much)"
k_w_e = conductivity(F2$, P= P_w_e, T= (T_w_e_in+T_w_e_out)/2) "Thermal conductivity of water"

he_w_e = Nu_w_e*k_w_e/D_h_e                                "Heat transfer convection coefficient in
water side"

 "============ Heat transfer and pressure drop analysis - Coolant side=========="

m_dot_e_R_ch = m_dot_e_R/N_cp_e                            "flow rate per channel (refrigerant)"
G_r_ch_e = m_dot_e_R_ch/ A_ch_e                            " Mass velocity of refrigerant, superheat
section"
```

```
 "Refri. inlet state  - The pressure is the pump outlet pressure"
 Re_r_v_e = G_r_ch_e*D_h_e/mu_r_v_e                          "Reynold number of refrigerant from the
pump, evaporator inlet"
 mu_r_v_e = x_qua_v*viscosity(Fluid$, x=0, P = P_v) +(1-x_qua_v)*viscosity(Fluid$, x=1, P = P_v)
"average Dyn. viscosity of the superheated flow"

 "Superheat - from saturated vapor to required superheating point"

Re_r_sh_e = G_r_ch_e*D_h_e/mu_r_sh_e                          "Refrigerant, super heat section"
mu_r_sh_e = viscosity(Fluid$, T = T_e, P = P_e)               "dyn. viscosity at the evaporator outlet"
 Pr_r_sh_e = prandtl(Fluid$,T=T_e,P=P_e )                     "Prandtl number  vapor state - DeltaP_e is
the refrigerant pressure drop as it goes through evaporator "

Nu_r_sh_e = (2.668-0.006967*theta+7.244*10^(-5)*theta^2 )*(20.78-
50.94*phi_pl_e+41.16*phi_pl_e^2-10.51*phi_pl_e^3
)*Re_r_sh_e^((0.728+0.0543*sin((pi*theta/45)+3.7)) ) *Pr_r_sh_e^(1/3)*("mu_g/mu_wall" 1 )^0.14
 k_r_sh_e = conductivity(Fluid$, P= P_e, T= T_e)              "Thermal conductivity of  ref. at evaporator
outlet"

he_r_sh_e = Nu_r_sh_e*k_r_sh_e/D_h_e                          "Heat transfer convection coefficient of  ref.
at evaporator inlet"


 "Phase-change - Refrigerant reaches to saturated vapor point"
Re_r_tp_e = Re_r_sh_e*(mu_r_sh_e/mu_r_v_e)*(rho_r_v/rho_r_e_sh)^0.5 + Re_r_v_e "equivalent
Reynold number (average) at phase-change section"
Pr_r_tp_e = ( x_qua_v*prandtl(Fluid$,T=T_e_tp,x = 0 ) + (1- x_qua_v)*prandtl(Fluid$,T=T_e_tp,x = 1))
"the equivalent Prandtl value of phase-change section"
 k_r_tp_e = (conductivity(Fluid$,T=T_e_tp,x = 0 ) + conductivity(Fluid$,T=T_e_tp,x = 1))/2
he_r_tp_e = Nu_r_tp_e*k_r_tp_e/D_h_e

  Nu_r_tp_e_Mul = (2.668-0.006967*theta+7.244*10^(-5)*theta^2 )*(20.78-
50.94*phi_pl_e+41.16*phi_pl_e^2-10.51*phi_pl_e^3
)*Re_r_tp_e^((0.728+0.0543*sin((pi*theta/45)+3.7)) ) *Pr_r_tp_e^(1/3)*( 1 )^0.14


 " Nusselt number for two phase -  Raffaele Luca AMALFIcorrelation - Macro scale as Bond number is
greater than 4"
 Nu_r_tp_e = 18.495*theta_star^0.248*Re_vap_e^0.351
*Re_lo_e^0.351*Bd_e^0.235*Bo_e^0.198*rho_star_e^(-0.223)
"-------------------------------------"
"Bond number"
Bd_e = DeltaRho_e*gravity*D_h_e^2/Stension_e                  "e for evaporator"
DeltaRho_e = density(Fluid$, T = T_e_tp, x = 0) - density(Fluid$, T = T_e_tp, x = 1)

Stension_e = surfacetension(Fluid$, T= T_e_tp)

"Boiling number"
q_r_tp_e  = Q_dot_e_tp/A_tp_e                                 "heat flux of the two-phase (phase change)
is the ratio of heat load over the area of this section"
 h_e_lv = h_e_tpv - h_v
Bo_e = q_r_tp_e/(G_r_ch_e*h_e_lv)

 h_e_tpv = enthalpy(Fluid$, P= P_e, x=1)


"Weber number (We) - note that this is a simple assumption for the two phase "
 We_m_e = G_r_ch_e^2*D_h_e/(Stension_e*rho_m_e)
```

```
rho_m_e = ((x_qua_e/density(Fluid$, T = T_e_tp, x = 1) + (1- x_qua_e)/density(Fluid$, T = T_e_tp, x =
0)))^(-1) "homogeneous model of density / series liquid-vapor arrange"
x_qua_e  =  (x_qua_v + 1)/2                                    " the average quality from the beginning to
the end (x = 1)  of the two-phase in the evaporator "


"Dimensionless parameters"
Re_vap_e = G_r_ch_e*x_qua_e*D_h_e/mu_r_tpv_e
 mu_r_tpv_e = viscosity(Fluid$, T = T_e_tp, x = 1)
"dimensionless chevron angle"
 rho_star_e =  density(Fluid$, T = T_e_tp, x = 0)/ density(Fluid$, T = T_e_tp, x = 1)

"reference: heat exchangers, selection, rating, and thermal design. Table 11.5 Muley and Manglik
chevron plates with theta = 30)"
 Re_lo_e = G_r_ch_e*D_h_e/mu_r_tpL_e
mu_r_tpL_e = viscosity(Fluid$, T = T_e_tp, x = 0)

"----------------------------"

"Overall Heat transfer  coefficient U"
 1/U_sh_e = 1/he_w_e + 1/he_r_sh_e + t/k_pl_e + fou_tot_e   "Superheat section"
1/U_tp_e = 1/he_w_e + 1/he_r_tp_e + t/k_pl_e + fou_tot_e    "phase-change section"


 "Logarithmic mean temperature difference"
LMTD_tp_e = (T_w_e_tp - T_w_e_out) / ln((T_e_tp -T_w_e_tp)/(T_e_tp -T_w_e_out))
LMTD_sh_e = ((T_w_e_in - T_e_tp) - (T_w_e_tp - T_e))/ln((T_w_e_in - T_e_tp)/ (T_w_e_out - T_e))

"Areas of each section"
Q_dot_e_sh{*convert('kW','W' )} = U_sh_e*A_sh_e*LMTD_sh_e "Area required for heat transfer for
superheating section"
 Q_dot_e_tp{*convert(kW,W)} = U_tp_e*A_tp_e*LMTD_tp_e  "Area required for heat transfer for phase-
change section"

"Ratio between required and actual area"
A_ratio_e = A_tot_e/(A_sh_e+A_tp_e)

 "==================Average heat transfer coefficient and Average Overall heat transfer
coefficient U================="
he_r_e_ave = R_Q_e_sh*he_r_sh_e +  R_Q_e_tp*he_r_tp_e
U_e_ave =   R_Q_e_sh*U_sh_e +  R_Q_e_tp*U_tp_e

 "Average Fanning friction factor "

f_r_e_ave = R_Q_e_sh*f_r_sh_e + R_Q_e_tp*f_r_tp_e

"Channel Pressure drop per length unit"
 DeltaP_r_e_ch_perUnit = DeltaP_r_e_ch/L_v_e

 "=============================================================="
"EFFECTIVENESS of the evaporator"

R_Q_e_sh*A_tot_e = A_sh_e_avail                                "A_sh_e_available, based on the total heat
transfer area of the hx"

R_Q_e_tp*A_tot_e =  A_tp_e_avail

 epsilon_e_tp_real = 1 - exp(-(U_tp_e*A_tp_e_avail)/(C_w_e_tp*m_dot_w_e))  "for estimating the
effectiveness "
```

```
epsilon_e_sh_real = (1 - exp(-(U_sh_e*A_sh_e_avail/C_min_e_sh)*(1 - Cr_e_sh)))/(1 - Cr_e_sh*exp(-
(U_sh_e*A_sh_e_avail/C_min_e_sh)*(1 - Cr_e_sh)))            "effectiveness for superheated zone"



epsilon_e_real = (epsilon_e_sh_real*R_Q_e_sh  + epsilon_e_tp_real*R_Q_e_tp)

"Effectiveness of hx when the required heat transfer area is met (not oversized)"
 epsilon_e_tp = 1 - exp(-(U_tp_e*A_tp_e)/(C_w_e_tp*m_dot_w_e))

 epsilon_e_sh = (1 - exp(-(U_sh_e*A_sh_e/C_min_e_sh)*(1 - Cr_e_sh)))/(1 - Cr_e_sh*exp(-
(U_sh_e*A_sh_e/C_min_e_sh)*(1 - Cr_e_sh)))                  "effectiveness for superheated zone"
 "where"
C_min_e_sh = min(m_dot_e_r*cp(Fluid$,T=T_e,P=p_e), m_dot_w_e*C_w_e_sh)
 C_max_e_sh = max(m_dot_e_r*cp(Fluid$,T=T_e,P=p_e), m_dot_w_e*C_w_e_sh)
Cr_e_sh = C_min_e_sh/C_max_e_sh

epsilon_e = (epsilon_e_sh*R_Q_e_sh  + epsilon_e_tp*R_Q_e_tp)
 "=============================================================="

"Define f (Fanning friction Factor)"
f_r_sh_e = (2.917-0.1277*theta+2.016*10^(-3)*theta^2 )*(5.474-19.02*phi_pl_e+18.93*phi_pl_e^2-
5.341*phi_pl_e^3)*Re_r_sh_e^(-(0.2+0.0577*sin((pi*theta/45)+2.1))) "Muley colleration for Re >
1000, turbulent flow)"

 " Amalfi correlation"
 f_r_tp_e = C_coef*15.698*We_m_e^(-0.475)*Bd_e^0.255*rho_star_e^(-0.571)

"Frictional channel Pressure drops"

DeltaP_r_e_sh = 4*f_r_sh_e*L_v_e*N_p*G_r_ch_e^2/(2*rho_r_e_sh*D_h_e) "equ. 11.20 in heat exchanger -
at refrigerant side - Superheated"
DeltaP_r_e_tp = 4*f_r_tp_e*L_v_e*N_p*G_r_ch_e^2/(2*(rho_r_e_sh + rho_r_v)/2*D_h_e) "equ. 11.20 in
heat exchanger - at refrigerant side - phase-change"

DeltaP_r_e_ch = DeltaP_r_e_sh + DeltaP_r_e_tp               "The Total frictional channel Pressure drop
at refrigerant side"

      "Connection and Port pressure drops"
DeltaP_r_e_p = 1.5*N_p*G_p_r_e^2/(2*density(Fluid$, T = (T_e_tp+ T_e)/2, P = P_v)) "Port pressure
drop at refrigerant side"
G_p_r_e = m_dot_e_R/(pi*D_p_e^2/4)

      "Total pressure drop in ref. side is sum of channel and port pressure "
 DeltaP_e_cal = DeltaP_r_e_ch + DeltaP_r_e_p                "total  presssure drop in refri. side through
the evaporator"


 "=================CONDENSER - counterflow======================"
 N_cp_c = (N_pl_c - 1)/(2*N_p)                              "Number of channel per pass ( for each
working fluid)"

x_c = pi*b_c/lambda_c
 phi_pl_c = (1+(1+x_c^2)^0.5+4*(1+(x_c^2)/2)^0.5)/6         " enlargement factor of plate"

"Define the D_h"
 D_h_c = (4*b_c*L_w_c)/(2*(b_c+L_w_c*phi_pl_c))
```

```
m_dot_c =  m_dot_g_R + m_dot_e_R                          " refrigerant flow rate from diffusor outlet -
total flow rate"


rho_r_c_l = density(Fluid$, T = T_c, P = P_c)             "density at the condenser outlet - 'c' for
condenser"
 rho_r_c_sh = density(Fluid$, T = T_d, P = P_d)           "density at the condenser inlet"

 "The second  working fluid "
T_w_c_in = T_c-2
T_w_c_out = T_c-1
 P_w_c = 320000 [Pa]                                      "absolute pressure in the chilling cycle"
 h_w_c_in = enthalpy(F2$, P= P_w_c, T=T_w_c_in)           "w stands for water, it can be understood as
second working fluid "
 h_w_c_out = enthalpy(F2$, P= P_w_c, T=T_w_c_out)
 mu_w_c = viscosity(F2$,P= P_w_c, T= (T_w_c_in+T_w_c_out)/2) "dyna. viscosity of water, average
value"

Pr_w_c = prandtl(F2$, T = (T_w_c_in+T_w_c_out)/2, P = P_w_c)

"Enthalpies of the fluids"
 h_r_c_tpv = enthalpy(Fluid$, P= P_d - 10 [Pa] , x=1)      "refrigerant enthalpy at beginning of phase-
change process, assuming that the pressure at the condenser inlet and pressure at this point is the
same"

h_r_c_tpL =  enthalpy(Fluid$, P= P_c { - DeltaP_r_c_sh - DeltaP_r_c_tp}, x= 0) "enthalpy of SATurated
liquid - at the end of phase-change process"


      "water side"
Q_dot_c_tot = m_dot_w_c*(h_w_c_out - h_w_c_in)            "Make sure the value is positive"

"Heat capacity rates"
Q_dot_c_sh = m_dot_c*(h_d - h_r_c_tpv)                    "heat transfer rate of superheat section"

 Q_dot_c_sh = m_dot_w_c*C_w_c_sh*(converttemp('C', 'K',T_w_c_in_tp) - converttemp('C', 'K',
T_w_c_in) ) "T_w_c_in_tp is the water temp at refri. vapor saturatured temperature"

Q_dot_c_tp = m_dot_c*(  h_r_c_tpv -  h_r_c_tpL)           "heat flow rate of phase-change section"

Q_dot_c_tp = m_dot_w_c*C_w_c_tp*(T_w_c_out_tp  - T_w_c_in_tp ) "T_w_c_out_tp is the water temp when
the refri. state is  Liquid saturated "
      "T_w_c_Rsatv is the water temp at the saturature"

Q_dot_c_L = m_dot_c*(h_r_c_tpL - h_c)                     "heat flow rate at the section where the
coolant gains tempurature to saturated T_g_tpL: process"
Q_dot_c_L = m_dot_w_c*C_w_c_L*( T_w_c_out - T_w_c_out_tp )
 C_w_c_tp = cp(F2$, T = (T_w_c_in_tp + T_w_c_out_tp)/2,P = P_w_c) "specific heat capacity"
C_w_c_L = cp(F2$, T = (T_w_c_out_tp + T_w_c_out)/2,P = P_w_c)

      "The heat flow rate ratio"
R_Q_c_sh = Q_dot_c_sh/Q_dot_c_tot                         "Ratio of heat flow rate at super heat
section"
R_Q_c_tp = Q_dot_c_tp/Q_dot_c_tot                         "Ratio of heat flow rate at phase change
section"
R_Q_c_L = Q_dot_c_L/Q_dot_c_tot                           "Ratio of heat flow rate at senitive heat
(temperature gain at liquid state) section"
```

```
 "=============Heat transfer and pressure drop analysis - Water side================"
"Pressure drop at water side, "
f_w_c = (2.917-0.1277*theta+2.016*10^(-3)*theta^2 )*(5.474-19.02*phi_pl_c+18.93*phi_pl_c^2-
5.341*phi_pl_c^3)*Re_w_c^(-(0.2+0.0577*sin((pi*theta/45)+2.1))) "Muley colleration for Re > 1000,
turbulent flow)"


 Re_w_c = G_w_c_ch*D_h_c/mu_w_c                          "Reynold number (Assumed that Re_w_c
does not vary much)"

 Nu_w_c = (2.668-0.006967*theta+7.244*10^(-5)*theta^2 )*(20.78-50.94*phi_pl_c+41.16*phi_pl_c^2-
10.51*phi_pl_c^3 )*Re_w_c^((0.728+0.0543*sin((pi*theta/45)+3.7)) )
*Pr_w_c^(1/3)*("mu_g/mu_w_call" 1 )^0.14


G_w_c_ch = m_dot_w_c_ch/A_ch_c                           "The mass velocity"

"Mass flow rate per channel"
m_dot_w_c_ch = m_dot_w_c/N_cp_c                          "mass flow rate per channel"

    "Frictional channel Pressure drops"
DeltaP_w_c = 4*f_w_c*L_v_c*N_p*G_w_c_ch^2/(2*rho_w_c*D_h_c)

rho_w_c = density(F2$, T = T_w_c_in/2+T_w_c_out/2, P = (P_w_c ))

DeltaP_w_c_sh = DeltaP_w_c*R_Q_c_sh
 DeltaP_w_c_tp = DeltaP_w_c*R_Q_c_tp
DeltaP_w_c_L = DeltaP_w_c*R_Q_c_L

    "Port pressure drop"
DeltaP_w_c_p = 1.5*N_p*G_p_w_c^2/(2*density(F2$, T = (T_w_c_in+ T_w_c_out)/2, P = P_w_c))
  G_p_w_c = m_dot_w_c/(pi*D_p_c^2/4)


    "Total pressure drop in water side is sum of channel and port pressure, others can be ignored "
DeltaP_w_c_tot = DeltaP_w_c + DeltaP_w_c_p

 "HEAT TRANSFER ANALYSIS"
 k_w_c = conductivity(F2$, P= P_w_c, T= (T_w_c_in+T_w_c_out)/2) "Thermal conductivity of water"

he_w_c = Nu_w_c*k_w_c/D_h_c                              "Heat transfer convection coefficient in
water side"

"============Heat transfer and pressure drop analysis - refrigerant side=========="


m_dot_c_ch = m_dot_c/N_cp_c                              "flow rate per channel (refrigerant)"


G_r_ch_c = m_dot_c_ch/ A_ch_c                            " Mass velocity of refrigerant, superheat
section"


 "Liquid state - Refrigerant reaches to saturated liquid point - The pressure is the pump outlet
pressure"
 Re_r_l_c = G_r_ch_c*D_h_c/mu_r_c_l                      "Reynold number of refrigerant at
condenser outlet"
 mu_r_c_l = viscosity(Fluid$, T = T_c, P = p_c)          "Dyn. viscosity at the condenser outlet"
```

```
 Pr_r_c_l = prandtl(Fluid$,T = T_c, P = p_c)                    "Prandtl number  at the condenser outlet"

"Usually Reynold number at condenser outlet is small. Thus,  Muley correlation for low Re is applied"
Nu_r_c_l = 0.44*((theta/30)^0.38)*(Re_r_l_c^0.5)*(Pr_r_c_l^(1/3)) "equa. 11.10 in heat exchanger book
"
k_r_c_l = conductivity(Fluid$, P= P_c, T= T_c)                  "Thermal conductivity of  ref. at condenser
outlet"

he_r_c_l = Nu_r_c_l*k_r_c_l/D_h_c                               "Heat transfer convection coefficient of  ref.
at condenser outlet"

 "Superheat - from saturated vapor to required superheating point"

Re_r_c_sh = G_r_ch_c*D_h_c/mu_r_c_sh                            "Refrigerant, super heat section"
mu_r_c_sh = viscosity(Fluid$, T = T_d, P = P_d)                 "dyn. viscosity at the diffuser outlet"
 Pr_r_c_sh = prandtl(Fluid$,T=T_d,P=P_d )                       "Prandtl number  vapor state - DeltaP_g is
the refrigerant pressure drop as it goes through condenser "

Nu_r_c_sh = (2.668-0.006967*theta+7.244*10^(-5)*theta^2 )*(20.78-
50.94*phi_pl_c+41.16*phi_pl_c^2-10.51*phi_pl_c^3
)*Re_r_c_sh^((0.728+0.0543*sin((pi*theta/45)+3.7)) ) *Pr_r_c_sh^(1/3)*("mu_g/mu_w_call" 1 )^0.14

{mu_g/mu_w_call = 1}                                            "assumed- because the flows'  temperature
at wall and at the plate pitch are equal, steady flow"

k_r_c_sh = conductivity(Fluid$, P= P_d, T= T_d)                 "Thermal conductivity of  ref. at diffuser
outlet"

he_r_c_sh = Nu_r_c_sh*k_r_c_sh/D_h_c                            "Heat transfer convection coefficient of  ref.
at diffuser outlet"


 "Phase-change - Refrigerant reaches to saturated vapor point"
Re_r_c_tp = Re_r_c_sh*(mu_r_c_sh/mu_r_c_l)*(rho_r_c_l/rho_r_c_sh)^0.5 + Re_r_l_c  "equivalent
Reynold number (average) at phase-change section"
Pr_r_c_tp = (prandtl(Fluid$,T=T_c_tp,x = 0 ) + prandtl(Fluid$,T=T_c_tp,x = 1))/2  "the equivalent
Prandtl value of phase-change section. Double check!"

 Nu_r_c_tp_Mul = (2.668-0.006967*theta+7.244*10^(-5)*theta^2 )*(20.78-
50.94*phi_pl_c+41.16*phi_pl_c^2-10.51*phi_pl_c^3
)*Re_r_c_tp^((0.728+0.0543*sin((pi*theta/45)+3.7)) ) *Pr_r_c_tp^(1/3)*("mu_g/mu_w_call" 1 )^0.14

k_r_c_tp = (conductivity(Fluid$,T=T_c_tp,x = 0 ) + conductivity(Fluid$,T=T_c_tp,x = 1))/2
he_r_c_tp = Nu_r_c_tp*k_r_c_tp/D_h_c

 "------------Dimensionless number----------------"
     "Bond number"
Bd_c = DeltaRho_c*gravity*D_h_c^2/Stension_c                    "c for condenser"
DeltaRho_c = density(Fluid$, T = T_c_tp, x = 0) - density(Fluid$, T = T_c_tp, x = 1)

Stension_c = surfacetension(Fluid$, T= T_c_tp)

     "Boiling number"
q_r_tp_c  = Q_dot_c_tp/A_tp_c                                   "heat flux of the two-phase (phase change)
is the ratio of heat load over the area of this section"
 h_c_lv = h_c_tpv - h_c_tpL
Bo_c = q_r_tp_c/(G_r_ch_c*h_c_lv)

 h_c_tpv = enthalpy(Fluid$, P= P_d, x=1)
```

```
 h_c_tpL = enthalpy(Fluid$, P= P_c, x=0)


"Weber number (We) - note that this is a simple assumption for the two phase "
 We_m_c = G_r_ch_c^2*D_h_c/(Stension_c*rho_m_c)
rho_m_c = ((x_qua_c/density(Fluid$, T = T_c_tp, x = 1) + (1- x_qua_c)/density(Fluid$, T = T_c_tp, x =
0)))^(-1) "homogeneous model of density / series liquid-vapor arrange"
x_qua_c  =  0.5                                              "assumed, because the phase change
process in this heat exchanger starts from saturated liquid and ends at  saturated gas, a completed
phase change process"

" Nusselt number for two phase -  Raffaele Luca AMALFIcorrelation - Macro scale as Bond number is
greater than 4"
 Nu_r_c_tp = 18.495*theta_star^0.248*Re_vap_c^0.351
*Re_lo_c^0.351*Bd_c^0.235*Bo_c^0.198*rho_star_c^(-0.223)
    "tp is phase change "


 "Fanning friction coefficient - Amalfi"
 f_r_c_tp = C_coef*15.698*We_m_c^(-0.475)*Bd_c^0.255*rho_star_c^(-0.571)

"Dimensionless parameters"
Re_vap_c = G_r_ch_c*x_qua_c*D_h_c/mu_r_tpv_c
 mu_r_tpv_c = viscosity(Fluid$, T = T_c_tp, x = 1)

    "dimensionless chevron angle"
  rho_star_c =  density(Fluid$, T = T_c_tp, x = 0)/ density(Fluid$, T = T_c_tp, x = 1)
"reference: heat exchangers, selection, rating, and thermal design. Table 11.5 Muley and Manglik
chevron plates with theta = 30)"
 Re_lo_c = G_r_ch_c*D_h_c/mu_r_tpL_c
mu_r_tpL_c = viscosity(Fluid$, T = T_c_tp, x = 0)


    "Overall Heat transfer  coefficient U"
 1/U_sh_c = 1/he_w_c + 1/he_r_c_sh + t/k_pl_c + fou_tot_c   "Superheat section"
1/U_L_c = 1/he_w_c + 1/he_r_c_l + t/k_pl_c + fou_tot_c       "liquid section"
1/U_tp_c = 1/he_w_c + 1/he_r_c_tp + t/k_pl_c + fou_tot_c     "phase-change section"

 "Logarithmic mean temperature difference"
LMTD_sh_c = (( T_d - T_w_c_out) - (T_d_tp - T_w_c_out_tp))/ln((( T_d - T_w_c_out)/ (T_d_tp -
T_w_c_out_tp)))

LMTD_tp_c = (T_w_c_out_tp - T_w_c_in_tp  ) / ln((T_d_tp -T_w_c_in_tp)/(T_d_tp -T_w_c_out_tp))"
logarithmic mean temperature difference of the phase change section - the compact heat exchanger
book ."
LMTD_L_c = ((T_d_tp - T_w_c_in) - (T_c  - T_w_c_in_tp))/ln(((T_d_tp - T_w_c_in) / (T_c  - T_w_c_in_tp)))

"Areas of each section"
Q_dot_c_sh = U_sh_c*A_sh_c*LMTD_sh_c                         "Area required for heat transfer for
superheating section"
 Q_dot_c_tp = U_tp_c*A_tp_c*LMTD_tp_c                        "Area required for heat transfer for phase-
change section"
 Q_dot_c_L  = U_L_c*A_L_c*LMTD_L_c                           "Area required for heat transfer for
sensitive heat gain section"

    "Ratio between required and actual area"
A_ratio_c = A_tot_c/(A_sh_c+A_tp_c+A_L_c)

"===========Average heat transfer coefficient and Average Overall heat transfer coefficient U====="
```

```
he_r_c_ave = R_Q_c_sh*he_r_c_sh +  R_Q_c_tp*he_r_c_tp +  R_Q_c_L*he_r_c_l
U_c_ave =    R_Q_c_sh*U_sh_c +  R_Q_c_tp*U_tp_c +  R_Q_c_L*U_L_c


 "Average Fanning friction factor "
f_r_c_ave = R_Q_c_sh*f_r_c_sh +  R_Q_c_tp*f_r_c_tp +  R_Q_c_L*f_r_c_L

"Channel Pressure drop per length unit"
 DeltaP_r_c_ch_perUnit = DeltaP_r_c_ch/L_v_c

"========================== EFFECTIVENESS of the condenser ===================="
R_Q_c_sh*A_tot_c = A_sh_c_avail                          "A_sh_c_available, based on the total heat
transfer area of the hx"
R_Q_c_L*A_tot_c = A_L_c_avail
R_Q_c_tp*A_tot_c =  A_tp_c_avail

 epsilon_c_tp_real = 1 - exp(-(U_tp_c*A_tp_c_avail)/(C_w_c_tp*m_dot_w_c))  "for estimating the
effectiveness - does not work"

 epsilon_c_L_real = (1 - exp(-(U_L_c*A_L_c_avail/C_min_c_L)*(1 - Cr_c_L)))/(1 - Cr_c_L*exp(-
(U_L_c*A_L_c_avail/C_min_c_L)*(1 - Cr_c_L)))              "effectiveness for Liquid zone"

 epsilon_c_sh_real = (1 - exp(-(U_sh_c*A_sh_c_avail/C_min_c_sh)*(1 - Cr_c_sh)))/(1 - Cr_c_sh*exp(-
(U_sh_c*A_sh_c_avail/C_min_c_sh)*(1 - Cr_c_sh)))          "effectiveness for superheated zone"
 epsilon_c_real = (epsilon_c_sh_real*R_Q_c_sh  + epsilon_c_L_real*R_Q_c_L  + epsilon_c_tp_real*R_Q_c_tp)

 "Effectiveness of hx when the required heat transfer area is met (not oversized)"
 epsilon_c_tp = 1 - exp(-(U_tp_c*A_tp_c)/(C_w_c_tp*m_dot_w_c))

 epsilon_c_L = (1 - exp(-(U_L_c*A_L_c/C_min_c_L)*(1 - Cr_c_L)))/(1 - Cr_c_L*exp(-
(U_L_c*A_L_c/C_min_c_L)*(1 - Cr_c_L)))                    "effectiveness for Liquid zone"
 "where"
C_min_c_L = min((m_dot_e_r+m_dot_g_r)*cp(Fluid$,T=T_c,P=p_c), m_dot_w_c*C_w_c_L)
 C_max_c_L = max((m_dot_e_r+m_dot_g_r)*cp(Fluid$,T=T_c,P=p_c), m_dot_w_c*C_w_c_L)
Cr_c_L = C_min_c_L/C_max_c_L

epsilon_c_sh = (1 - exp(-(U_sh_c*A_sh_c/C_min_c_sh)*(1 - Cr_c_sh)))/(1 - Cr_c_sh*exp(-
(U_sh_c*A_sh_c/C_min_c_sh)*(1 - Cr_c_sh)))                "effectiveness for superheated zone"
 "where"
C_min_c_sh = min((m_dot_e_r+m_dot_g_r)*cp(Fluid$,T=T_d,P=p_d), m_dot_w_c*C_w_c_sh)
 C_max_c_sh = max((m_dot_e_r+m_dot_g_r)*cp(Fluid$,T=T_d,P=p_d), m_dot_w_c*C_w_c_sh)
Cr_c_sh = C_min_c_sh/C_max_c_sh

epsilon_c = (epsilon_c_sh*R_Q_c_sh + epsilon_c_L*R_Q_c_L + epsilon_c_tp*R_Q_c_L)
 "============================================================="

"Define f (Fanning friction Factor)"
f_r_c_sh = (2.917-0.1277*theta+2.016*10^(-3)*theta^2 )*(5.474-19.02*phi_pl_c+18.93*phi_pl_c^2-
5.341*phi_pl_c^3)*Re_r_c_sh^(-(0.2+0.0577*sin((pi*theta/45)+2.1))) "Muley colleration for Re >
1000, turbulent flow)"
f_r_c_L = (theta/30)^(0.83)*((30.2/Re_r_l_c)^5 +(6.28/Re_r_l_c^0.5)^5)^0.2 "Muley colleration for Re
< 400"

      "Port pressure drop"
DeltaP_r_c_p = 1.5*N_p*G_p_r_c^2/(2*density(Fluid$, T = (T_c+ T_d)/2, P = P_d)) "Port pressure drop
at refrigerant side"

G_p_r_c = m_dot_c/(pi*D_p_c^2/4)
```

```
"Frictional channel Pressure drops"

DeltaP_r_c_sh = 4*f_r_c_sh*L_v_c*N_p*G_r_ch_c^2/(2*rho_r_c_sh*D_h_c) "equ. 11.20 in heat exchanger -
at refrigerant side - Superheated"

DeltaP_r_c_tp = 4*f_r_c_tp*L_v_c*N_p*G_r_ch_c^2/(2*(rho_r_c_sh + rho_r_c_L)/2*D_h_c) "equ. 11.20 in
heat exchanger - at refrigerant side - phase-change"
DeltaP_r_c_L = 4*f_r_c_L*L_v_c*N_p*G_r_ch_c^2/(2*rho_r_c_L*D_h_c) "equ. 11.20 in heat exchanger - at
refrigerant side - liquid phase"
DeltaP_r_c_ch = DeltaP_r_c_sh + DeltaP_r_c_tp + DeltaP_r_c_L "The Total frictional channel Pressure
drop at refrigerant side"


"Total pressure drop in ref. side is sum of channel and port pressure "
 DeltaP_c_cal = DeltaP_r_c_ch + DeltaP_r_c_p                         "total  presssure drop in refri. side through
the condenser"

  "========================================="
```

APPENDIX 2 DIAGRAM WINDOW OF THE LABVIEW PROGRAM

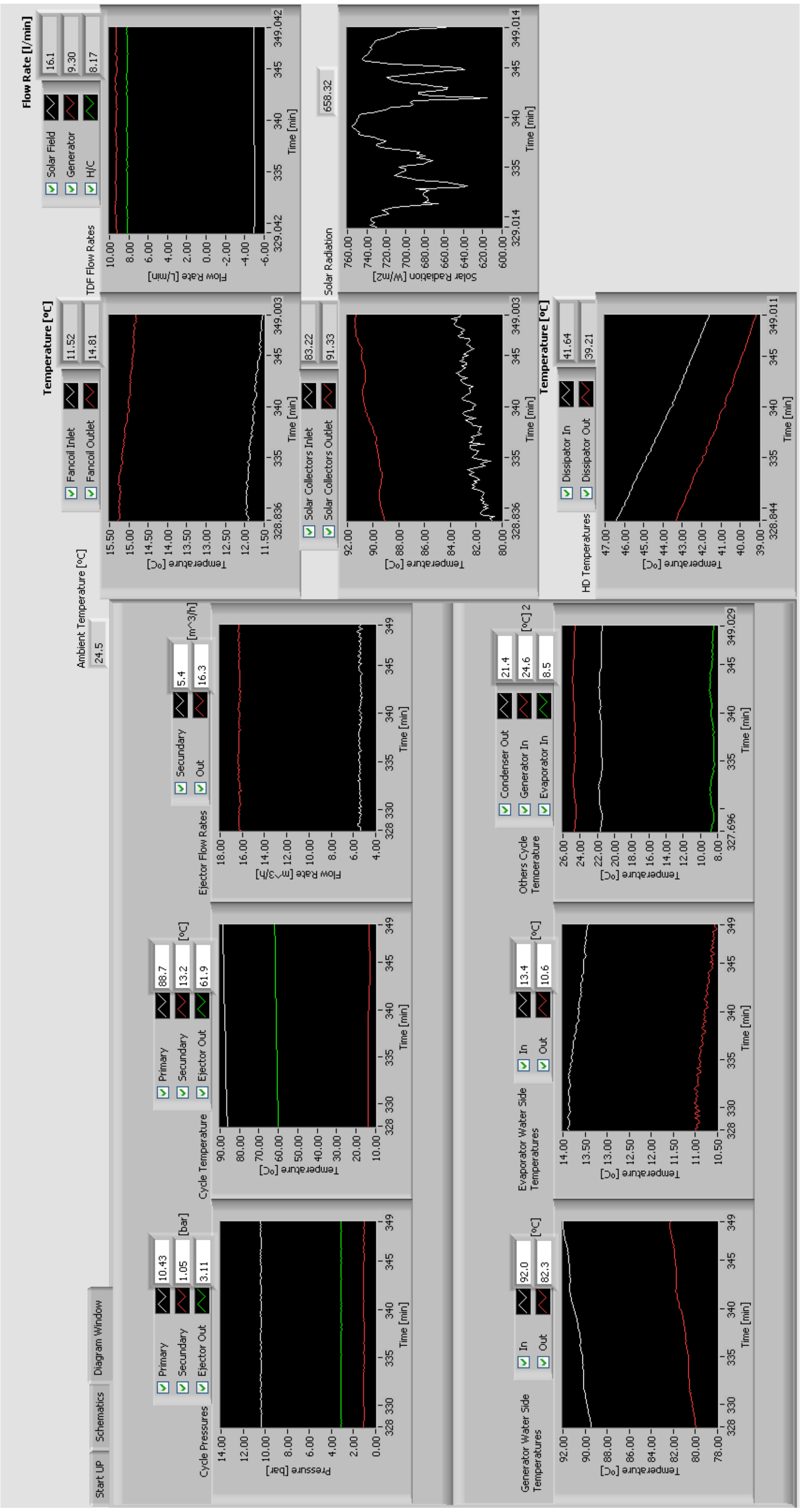

APPENDIX 3 ADDITIONAL RESULTS OF THE STUDY

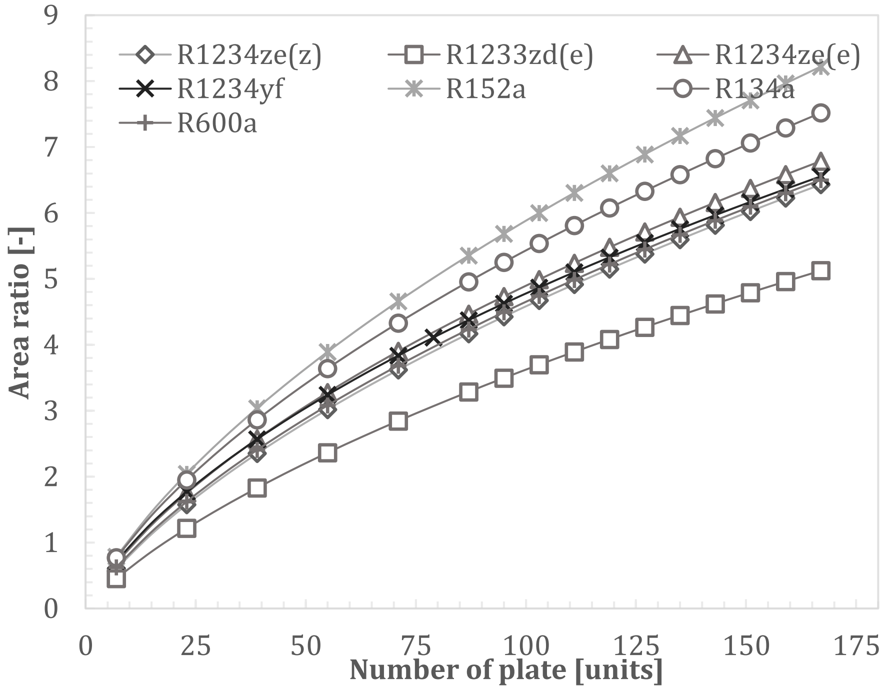

Figure 0.1 Heat transfer area ratio of the generator

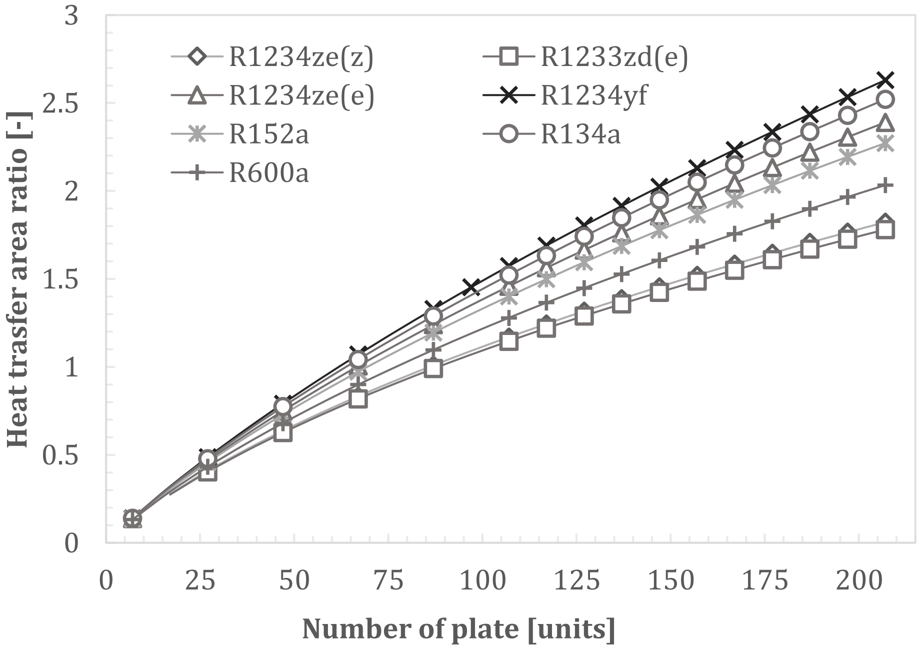

Figure 0.2 Heat transfer area ratio of the evaporator

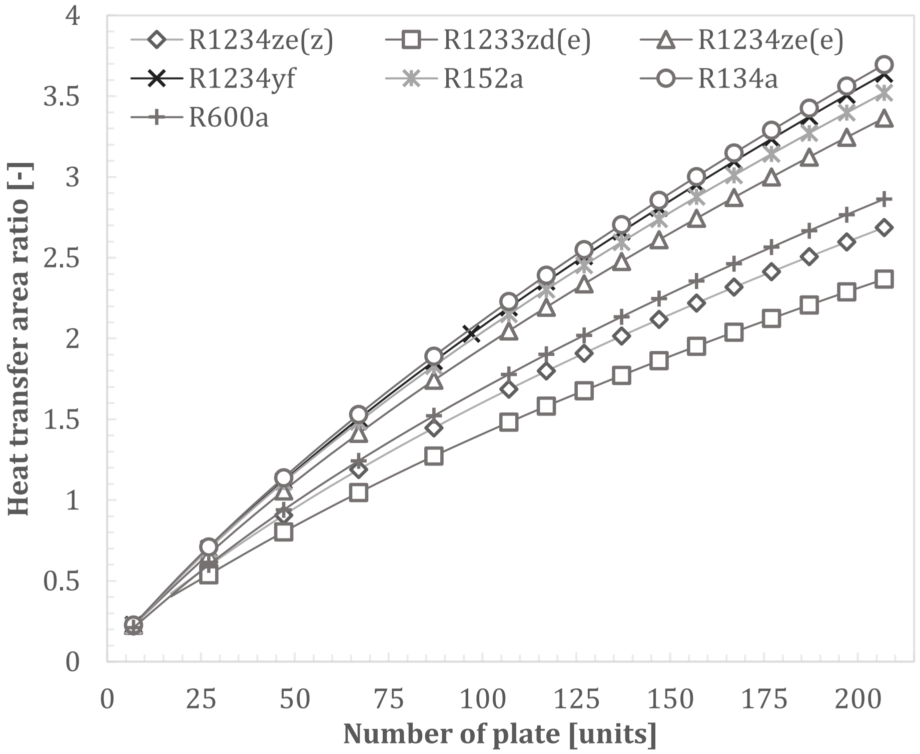

Figure 0.3 Heat transfer area ratio of the condenser

APPENDIX 4 SIMPLIFIED WORKING CYCLES IN PRESSURE-ENTHALPY DIAGRAM OF EJECTOR COOLING CYCLE

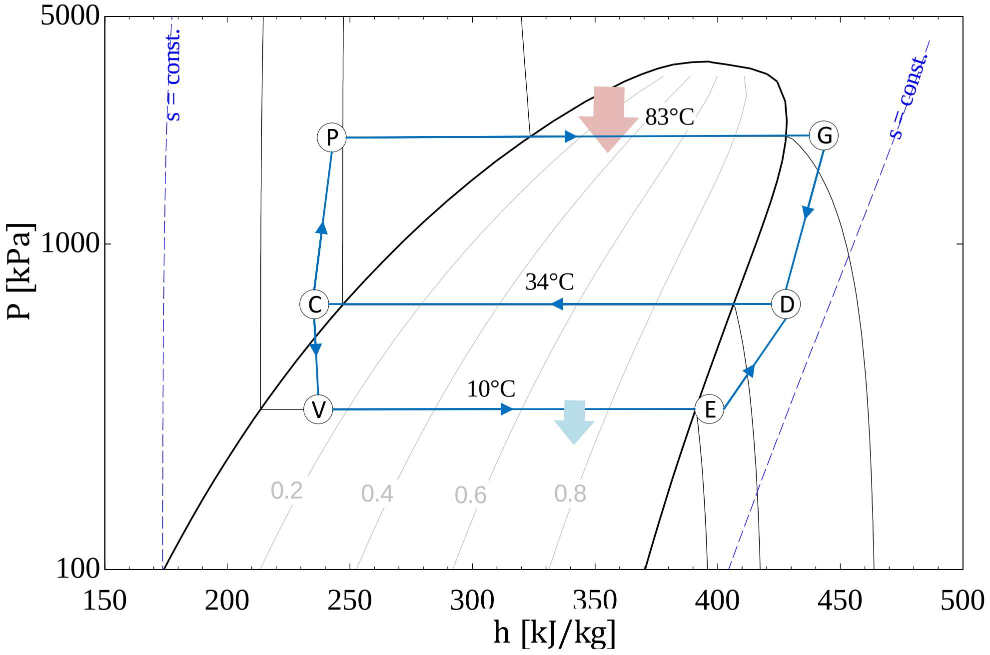

Figure 0.4 Simplified working cycles in pressure-enthalpy diagram of ejector cooling cycle with R1234ze(e) as the working fluid.